Towards using seismic anisotropy to interpret ductile deformation in mafic lower crust

Daniel John Tatham

Submitted in accordance with the requirements for the degree of PhD.

The University of Leeds
School of Earth and the Environment
May 2008

The candidate confirms that the work submitted is his own and that appropriate credit has been given where reference has been made to the work of others. This copy has been supplied on the understanding that it is copyright material and that no quotation from the thesis may be published without proper acknowledgement.

For Nipa.

Fortitudine vincimus

Acknowledgements

I would like to start by thanking Geoff Lloyd and Rob Butler for the opportunity of this research project.

I would also like to give my utmost thanks to Martin Casey who has selflessly provided support and guidance, both academic and otherwise, far beyond the call of duty.

James Wookey is thanked for his time, advice, patience and enthusiasm during collaborative research in seismic modelling.

Thanks to Dr. Eric Condliffe for technical support with electron optics.

I am forever in debt to my wife Nipa for her support, patience and understanding throughout my research degree.

Also, thanks to my office-mate and friend, Jamie Maddock, for his advice and support.

Thanks to Scottish Natural Heritage and Dr. J. Balfour for licence to collect rock samples from the Badcall estate.

Thanks to Dr. K. Brodie and Dr. G. Stuart for agreeing to act as examiners.

Abstract

The lower crust forms an important geodynamic control in continental tectonics and the communication and coupling of kinematics between surface and deep-Earth processes. An understanding of the relationship between seismic properties, finite strain and fabric orientation thus provides a useful tool in the remote sensing and interpretation of deformation in the lower crust.

This thesis outlines a work-flow model by which the seismic properties of a single and representative lower crustal lithology can be calculated and calibrated against finite strain from petrofabric development across a strain gradient. The work-flow model constitutes a multi-disciplinary approach, incorporating field mapping and sample collection, experimental petrofabric determination, and seismic modelling.

A review of compositional estimates of the deep crust, including xenoliths, exposed sections and estimates from wide-angle seismic profiles, indicates the importance of mafic lithologies.

The Laxfordian-age high-grade shear zone at Upper Badcall, NW Scotland, exhibits a strain gradient in a deformed doleritic Scourie dyke (Lewisian complex) that intersects the zone at a high angle. From an analysis of field data from detailed mapping, the shear zone is shown to be characterised by generally simple shear, but where the tectonic movement direction varies transversely across the shear zone. Calculation of the strain profile across the deformation zone gives shear strains, γ up to 57, but with $\gamma < 15$ being perhaps more realistic. Cumulative displacements total $\sim 1000m$ left-laterally, and $\sim 600m$ vertical displacement, north-side up. Nine samples were collected across the shear zone in the mafic dyke, representing a strain gradient from undeformed protolith to the highest recorded stains.

The sample suite is characterised as a hornblende-plagioclase-quartz aggregate

that develops macroscopic planar and linear fabrics with strain, from an essentially isotropic protolith. Quantification of the aggregate lattice preferred orientation (LPO) using electron backscatter diffraction (EBSD) showed the dominance of fabric development in the hornblende phase, with (100) poles clustering forming normal to the foliation plane and [001] axes parallel to the tectonic X direction. Plagioclase and quartz retained random fabrics from the wall-rock protolith with increasing finite strain. The hornblende LPO fabric, described by the texture index, J, shows a positive logarithmic relationship with strain, where LPO intensity saturated by $\gamma \approx 10$.

The strain-calibrated quantitative petrofabric description of each sample is used to calculate their aggregate elasticity tensors (C_{ij}) via a Voigt-Reuss-Hill average, and from which seismic properties are derived using Christoffel's equation. Hence, a framework of petrofabric- and strain-calibrated seismic properties is described for a strain gradient in a representative high-grade mafic lithology. P-wave anisotropies up to ~10% are recorded in the most deformed samples with $V_p max$ typically between 6.42-6.63kms^{-1}. S-wave anisotropies record up to 7.23% AV_s in the most deformed samples, with $V_s max$ ranging between 3.62-3.75kms^{-1} for all samples. The relationship between petrofabric-derived seismic anisotropy and finite strain across the sample suite show a positive relationship, approximated by a logarithmic function, whereby P- and S-wave anisotropy exhibit a steep positive gradient with strain up to $\gamma \approx 10$.

The sample-wise framework of petrofabric- and strain-calibrated seismic properties is interpolated to estimate the continuum relationship between seismic properties, finite strain and petrofabric orientation. In a move to illustrate the application of results in seismic and structural modelling, case study models of crustal deformation are presented for the eastern Basin and Range province, the North Sea rift, and Tibet. Models are promising in their ability to differentiate between regions of lower crust characterised by a uniform mafic composition but different finite strain state and/or petrofabric geometry, although multiple seismic survey methods may be needed to fully interpret results in terms of strain and fabric orientation.

In summary, a multidisciplinary approach combining field mapping and sam-

pling, petrofabric characterisation with EBSD, and seismic modelling provides an efficient and reproducible work-flow for the determination of petrofabric-derived strain-calibrated seismic properties of lower crustal materials.

Contents

Acknowledgements iii
Abstract iv
Contents ix
List of Tables x
List of Figures xvi

1 Introduction **1**
1.1 Why study the lower crust? 2
1.2 Defining the lower crust 3
1.3 State of the lower crust 6
1.4 Material properties and seismic anisotropy 17
1.5 Model of the lower crust 18
1.6 Thesis outline 20

2 The Lewisian Terrane **23**
2.1 The Lewisian complex, NW Scotland 24
2.2 The Laxfordian shear zone at Upper Badcall 34
2.2.1 Field data 35
2.2.2 Discussion of field data 39
2.3 Strain analysis 47
2.3.1 Stereographic determination of γ 48
2.3.2 Restoration of the dyke 53
2.3.3 Error analysis 56
2.4 Conclusions 56

3 Experimental techniques **61**

3.1 Sample preparation 61

3.2 Scanning electron microscopy 62

3.3 Quantitative microgeochemistry by EMPA 65

3.4 Petrofabric determination by EBSD 69

4 Analysis of petrofabric **75**

4.1 Petrology & microgeochemistry 76

4.1.1 Undeformed material 76

4.2 Further strain analysis 91

4.2.1 Approximating γ from shape fabric parameters 92

4.2.2 Discussion of errors 98

4.3 The texture index, J 104

4.4 Petrofabric 106

4.4.1 LPO development 107

4.4.2 Texture index analysis 129

4.5 Discussion of petrofabric results:

Deformation in a polyphase aggregate 130

4.6 Conclusions 137

5 Seismic properties **139**

5.1 Elastic and seismic anisotropy 139

5.1.1 Single crystal seismic properties 147

5.2 Seismic property results 151

5.2.1 Seismic properties of samples and correlation to strain . . . 151

5.2.2 The effect of varying modal composition 161

5.3 Conclusions 167

6 Modelling **170**

6.1 Reaffirmation of some physical assumptions 170

6.2 Seismic signature of strain intensity

& petrofabric orientation 172

6.3 Application in crustal modelling 185

6.3.1 Model assembly 186
6.3.2 Eastern Basin and Range Province 189
6.3.3 North Sea 196
6.3.4 Tibet 205
6.4 Conclusions 215

7 Conclusions **217**
7.1 Approximations in studying the lower continental crust 218
7.2 Strain gradient in a mafic lower crustal analogue 218
7.3 Characterising petrofabric 219
7.4 Calibration of seismic attributes with strain 221
7.5 Seismic and structural modelling 222
7.6 Work-flow model 223
7.7 The contribution of this research to science 223
7.8 Future work 225

A Publications **227**

B Detailed fair copy map, Upper Badcall **228**

C Data **229**

D Sample Numbers **230**

List of Tables

2.1 Summary of data used in the calculation of strain and cumulative displacement across the deformation zone at Upper Badcall. 54
2.2 Coordinates and displacements used in the restoration of part of the western margin of the deformed dyke at Upper Badcall. Based on a field data-derived strain profile. 57

3.1 EMPA crystal mirror *d*-spacing. 68
3.2 References to unit cell structures and elemental compositions used in EBSD. 72

4.1 Modal fractions of mineral phases for Sample 1-9. 79
4.2 Finite shear strain data from shape fabric parameters. 96
4.3 Coordinates and displacements used in the restoration of part of the western margin of the deformed dyke at Upper Badcall. Based on a shape fabric-derived strain profile. 101
4.4 Potential error in the calculation of finite strain for Sample 3 due to error in measuring linear fabrics. 103
4.5 Texture index values, J, for the sample suite. 132

5.1 The complete description of P-wave seismic properties for the sample suite. 151
5.2 The complete description of S-wave seismic properties for the sample suite. 153

List of Figures

1.1 Schematic rheology profile of the lithosphere: the 'jelly sandwhich' model. 4
1.2 Schematic lithospheric rheology profiles for a compositionally layered crust. 5
1.3 Schematic rheology profile corresponding to the crustal model employed in this project. 19
1.4 Thesis work-flow. 21

2.1 Sketch map of northwest Scotland showing the Lewisian complex. . 25
2.2 Simplified map showing the structural relationships in the region of the Laxford front. 28
2.3 Simplified structural map of Farhead Point, Upper Badcall, NW Scotland. 36
2.4 Field data from the deformation zone at Upper Badcall. 38
2.5 Isogons of strike of gneissic banding. 40
2.6 A schematic illustration how a steeply dipping dyke can be sheared to generate an antithetic kink in its outcrop trace. 42
2.7 Geometries of pure shear deformation. 44
2.8 A pure shear model for the deformation zone at Upper Badcall. . . 44
2.9 Material lines deforming in a pure shear zone. 45
2.10 Map showing the data points used for calculating the strain profile. 50
2.11 Stereographic calculation of finite strain from field data. 51
2.12 Strain profile for the deformation zone at Upper Badcall, as calculated from field data. 52

2.13 Restoration of the deformed dyke at Upper Badcall according to the stereographic determination of the finite strain profile. 58

3.1 Sample reference frame. 63
3.2 Schematic SEM column. 64
3.3 Bragg's condition. 67
3.4 EMPA crystal mirror wavelength coverage. 68
3.5 The principle of the focussing circle. 69
3.6 Schematic SEM column for EBSD. 70
3.7 Diffraction cones and Kikuchi bands. 71

4.1 Optical and BSE micrographs of pertinent microstructures, Sample 1. 77
4.2 Core-rim EMPA data for Sample 1 amphiboles. 79
4.3 Plagioclase composition across the sample suite. 80
4.4 EMPA data for Sample 1 clinopyroxene. 80
4.5 EMPA data for Sample 1 plagioclase. 83
4.6 EMPA data for Samples 2-9 amphiboles. 83
4.7 Core-rim EMPA data for Samples 2-9 amphiboles. 84
4.8 Optical and BSE micrographs of pertinent microstructures, Sample 2. 85
4.9 Optical and BSE micrographs of pertinent microstructures, Sample 4. 88
4.10 Optical and BSE micrographs of pertinent microstructures, Sample 8. 89
4.11 Image processing steps in the determination of shape fabric parameters for strain analysis. 94
4.12 Comparison of results of both field data- and shape fabric-based strain analyses. 97
4.13 Restoration of the deformed dyke at Upper Badcall according to the shape fabric determination of the finite strain profile. 99
4.14 Stereogram to illustrate the sensitivity of the field data-based strain calculation to potential angular error. 101
4.15 Sensitivity in the calculation of finite strain to potential angular error in the measurement of planar fabrics. 103

4.16 Single crystal pole figures for hornblende, plagioclase, quartz and clinopyroxene. 109
4.17 Hornblende phase pole figures for the sample suite. 110
4.18 Quartz phase pole figures for the sample suite. 111
4.19 Plagioclase phase pole figures for the sample suite, crystallographic axes. 112
4.20 Plagioclase phase pole figures for the sample suite, crystallographic poles. 113
4.21 Clinopyroxene phase pole figures. 114
4.22 The relationship of pfJ with strain for hornblende. 115
4.23 The relationship of pfJ with strain for quartz. 117
4.24 The relationship of pfJ with strain for plagioclase. 119
4.25 Phase map to show plagioclase subsets for Sample 1. 121
4.26 Plagioclase pole figures for Sample 1 subsets. 122
4.27 Phase map to show plagioclase subsets for Sample 5. 123
4.28 Plagioclase pole figures for Sample 5 subsets. 124
4.29 Phase map to show plagioclase subsets for Sample 9. 125
4.30 Plagioclase pole figures for Sample 9 subsets. 126
4.31 The relationship between the pole figure texture index, pfJ, and strain for plagioclase subsets of Samples 1, 5 and 9. 127
4.32 The relationship between texture index, J, and finite strain, γ. . . . 131
4.33 Microstructures in deformed two-phase aggregates. 133

5.1 Single crystal seismic properties for constituent mineral phases of the sample suite. 148
5.2 Seismic properties of the sample suite. 152
5.3 Relationship between seismic velocity and finite strain exhibited by the sample suite. 158
5.4 Relationship between seismic anisotropy and finite strain exhibited by the sample suite. 159
5.5 Relationship between seismic anisotropy and the texture index, J, exhibited by the sample suite. 160

5.6 The sensitivity of P-wave velocity to modal composition across the sample suite. 163
5.7 The sensitivity of P-wave anisotropy to modal composition across the sample suite. 164
5.8 The sensitivity of S-wave anisotropy to modal composition across the sample suite. 165

6.1 Continuum relationship between P-wave velocity, finite strain and petrofabric orientation, rotated about the kinematic X-axis. 174
6.2 Continuum relationship between P-wave velocity, strain ellipse major axis length and petrofabric orientation, rotated about the kinematic X-axis. 174
6.3 Continuum relationship between P-wave velocity, finite strain and petrofabric orientation, rotated about the kinematic Y-axis. 175
6.4 Continuum relationship between P-wave velocity, the strain ellipse major axis length, S_1, and petrofabric orientation, rotated about the kinematic Y-axis. 175
6.5 Continuum relationship between shear-wave splitting time delay, δt_s, finite strain and petrofabric orientation, rotated about the kinematic X-axis. 176
6.6 Continuum relationship between shear-wave splitting time delay, δt_s, the strain ellipse major axis length, S_1, and petrofabric orientation, rotated about the kinematic X-axis. 176
6.7 Continuum relationship between shear-wave splitting time delay, δt_s, finite strain and petrofabric orientation, rotated about the kinematic Y-axis. 177
6.8 Continuum relationship between shear-wave splitting time delay, δt_s, the strain ellipse major axis length, S_1, and petrofabric orientation, rotated about the kinematic Y-axis. 177
6.9 Relationship between the fast shear-wave orientation, V_{s1}, finite strain and petrofabric orientation, rotated about the kinematic X-axis. 178

6.10 Relationship between the fast shear-wave orientation, V_{s1}, the strain ellipse major axis length, S_1, and petrofabric orientation, rotated about the kinematic X-axis. 178
6.11 Relationship between the fast shear-wave orientation, V_{s1}, finite strain and petrofabric orientation, rotated about the kinematic Y-axis. 179
6.12 Relationship between the fast shear-wave orientation, V_{s1}, the strain ellipse major axis length, S_1, and petrofabric orientation, rotated about the kinematic Y-axis. 179
6.13 Schematic representation of a vertical teleseismic ray-path passing through the crust. 180
6.14 Schematic representation to aid in the visualisation and interpretation of continuum relationships of seismic properties 180
6.15 Reference frame rotations for use in seismic modelling. 181
6.16 Normal simple shear model of the lithosphere, by Wernicke (1985). . 192
6.17 Uniform stretch in the lower crustal beneath the Basin and Range Province, according to Smith & Bruhn (1984). 192
6.18 P-wave velocity model and zero-offset seismic reflection profile of the eastern Basin and Range Province for normal sense simple shear. 194
6.19 P-wave velocity model and zero-offset seismic reflection profile of the eastern Basin and Range Province for uniform pure shear stretching of the lower crust. 195
6.20 Pure shear stretching models of the lower crust of the northern North Sea, summarised by Brun & Tron (1993). 198
6.21 Normal sense simple shear model of the lower crust of the northern North Sea, according to Beach (1986). 198
6.22 P-wave velocity model and zero-offset seismic reflection profile of the northern North Sea basin for non-uniform pure shear stretching of the lower crust. 201
6.23 P-wave velocity model and zero-offset seismic reflection profile of the northern North Sea basin for uniform pure shear stretching of the lower crust. 202

6.24 *P*-wave velocity model and zero-offset seismic reflection profile of the northern North Sea basin for a crustal penetrating simple shear zone. 203
6.25 Models of continental deformation for the Tibetan Plateau region. . 208
6.26 *P*-wave velocity model and zero-offset seismic reflection profile of the Tibetan Plateau for uniform pure shear vertical stretching. . . . 209
6.27 *P*-wave velocity model and zero-offset seismic reflection profile of the Tibetan Plateau for the 'hydraulic pump' model. 210

7.1 Work-flow model. 224

Chapter 1

Introduction

Our understanding of ductile flow in the lower continental crust is far from complete (McKenzie & Jackson, 2002). Furthermore, the need for high resolution seismic data that is calibrated against the geometry and intensity of deformation for realistic lower crustal lithologies is consistently documented (e.g. Molnar, 1988; Mainprice & Nicolas, 1989; Rudnick & Fountain, 1995; Handy et al., 2001).

In a review of research in rheology and geodynamic modelling, Handy et al. (2001) stress the importance for future work in these disciplines in the compilation of crustal deformation models developed from integrated geological and geophysical studies that are fundamentally based upon, and tested against, field studies and experimentation of naturally occurring shear zones and deformed polyphase rocks.

Presented is a first-step investigation into the calibration of seismic anisotropic properties of rock materials against strain, from petrofabric. This contribution outlines a practical and reproducible work-flow for future research by relating the strain in lower crustal materials to their seismic properties, and demonstrates how such results can be easily applied in crustal modelling.

1.1 Why study the lower crust?

Recent decades have seen extensive research in characterising seismic anisotropy in the mantle (Hess, 1964; Christensen, 1984; Kendall, 2000; Vauchez et al., 2000) and in the upper crust, particularly sedimentary basins associated with hydrocarbon exploration and exploitation (Thomsen, 1986; Sayers, 1994, 1998; Vernik & Liu, 1997). Such studies have permitted a certain degree of simplification in their inputs. For example, mantle lithology is commonly modelled as a single-phase olivine aggregate whose anisotropic characteristics are such that they allow a direct correlation to kinematic inferences, such as mantle flow. Moreover, sedimentary sequences have generally been studied in terms of individually isotropic layers whose anisotropy is controlled by extrinsic properties such as lithological layering.

Structural complexity and compositional heterogeneity on a variety of scales has left the lower crust comparatively less well understood in terms of its seismic anisotropic properties, with research generally being case-study specific on the manifold lithologies and the specific physical states observed there (Siegesmund & Kern, 1990; Percival et al., 1992; Khazanehdari et al., 2000; Mazzoli et al., 2002; Pros et al., 2003; Waters et al., 2003; Smithson & Johnson, 2003; Kitamura, 2006).

This research aims to go some way in supplementing our knowledge base by providing a generalised scheme for calibrating seismic properties against ductile strain and petrofabric orientation for lower crustal materials. These data can thus be integrated into any model lower crustal section with any structure, strain state, and potentially, combination of lithology.

The main aims of the work are to evaluate the effects on seismic anisotropy of changes in microstructure due to strain. Field data and experimentally-derived microstructural information are integrated for naturally deformed samples collected across a strain gradient in a macro-scale deformation zone and are used to illustrate the continuum change in seismic anisotropy with strain and petrofabric for a single, typical lower crustal lithology.

1.2 Defining the lower crust

Throughout this project, the lower crust is defined as that part of the crust beneath the brittle-ductile transition, and above the Moho, that is rheologically weak and capable of deforming by ductile behaviour. That is, strain is accommodated by dominantly crystal plastic processes, in contrast to the upper crust which is characterised by brittle or frictional behaviour (Byerlee, 1978; Sibson, 1977, 1984; Scholz, 1988; Snoke & Tullis, 1998). The ductile lower crust is considered aseismic, and hence due to the dependence of the position of the brittle-ductile transition on composition and geothermal gradient, it is often practically defined by the base of upper crustal seismicity (Chen & Molnar, 1983; Sibson, 1984; Scholz, 1988; Cloetingh & Burov, 1996).

This two-layer scenario corresponds to the long established and accepted 'jelly sandwich' model of crustal strength or rheology profiles (Brace & Kohlstedt, 1980; Chen & Molnar, 1983; Ranalli & Murphy, 1987; Burov & Diament, 1995; Cloetingh & Burov, 1996). This model is generally highly simplified, assuming a constant composition throughout the whole crust, commonly approximated as the properties of quartz, feldspar or a simple quartzo-feldspathic aggregate, and where the underlying lithospheric mantle is represented by the properties of olivine (e.g. Goetze, 1978; Chen & Molnar, 1983).

The jelly sandwich model has recently been subject to review based on observed depth distributions of earthquakes that are not congruent with the ductile or aseismic lower crust advocated by this model (Maggi et al., 2000; Jackson, 2002). Specifically, they present evidence of deep earthquakes in a selection of cratonic regions and a generally aseismic lithospheric mantle to support a model (dubbed the crème brûlée model, Burov & Watts, 2006) comprising a relatively strong, brittle lower crust and a weak, ductile upper mantle, where the jelly sandwich scenario is only acceptable under conditions where fractional volumes of water or melt are present in the lower crust, acting to weaken it.

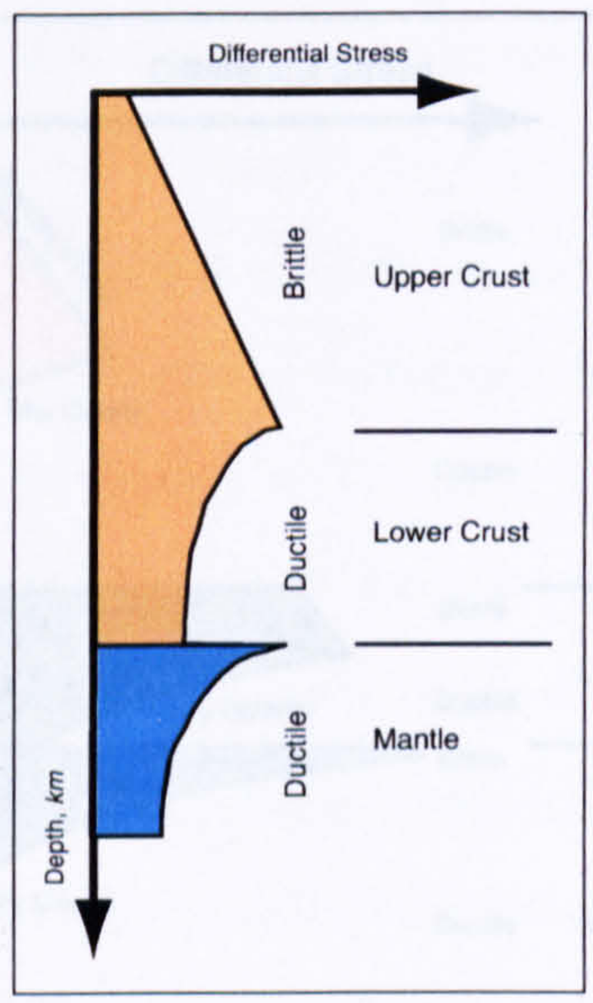

Figure 1.1: Schematic rheology profile of the lithosphere, corresponding to the basic 'jelly sandwich' model. A weak lower crust is sandwiched between a relatively strong upper crust and mantle. From Mainprice & Nicolas (1989).

Furthermore, the jelly sandwich model has been called upon for refinement from workers wishing to achieve a more realistic vertical compositional stratification of the crust (Ranalli, 2000; Afonso & Ranalli, 2004), although the effect of lithology on idealised rheology profiles has been considered to varying degrees in many earlier papers (e.g. Smith & Bruhn, 1984; Kirby, 1985; Carter & Tsenn, 1987; Meissner & Kuznir, 1987; Ranalli & Murphy, 1987; Rutter & Brodie, 1991; Burov & Diament, 1995; Cloetingh & Burov, 1996). Those rheology profiles that include a compositionally stratified crust, particularly with a mafic layer representing the lower crust, tend to introduce a step-like increase in ductile strength in the lower crust, which, depending on the tectonothermal setting and stress state, may or may not represent a ductile zone. Such mafic layers are often approximated by anhydrous feldspar-supported lithologies, or have the properties of monomineralic feldspar (Ranalli, 2000; Watts & Burov, 2003). This gross approximation may not necessarily be representative, for example, where relatively softer hydrous mafic phases may constitute the dominant phase, or where strain is preferentially parti-

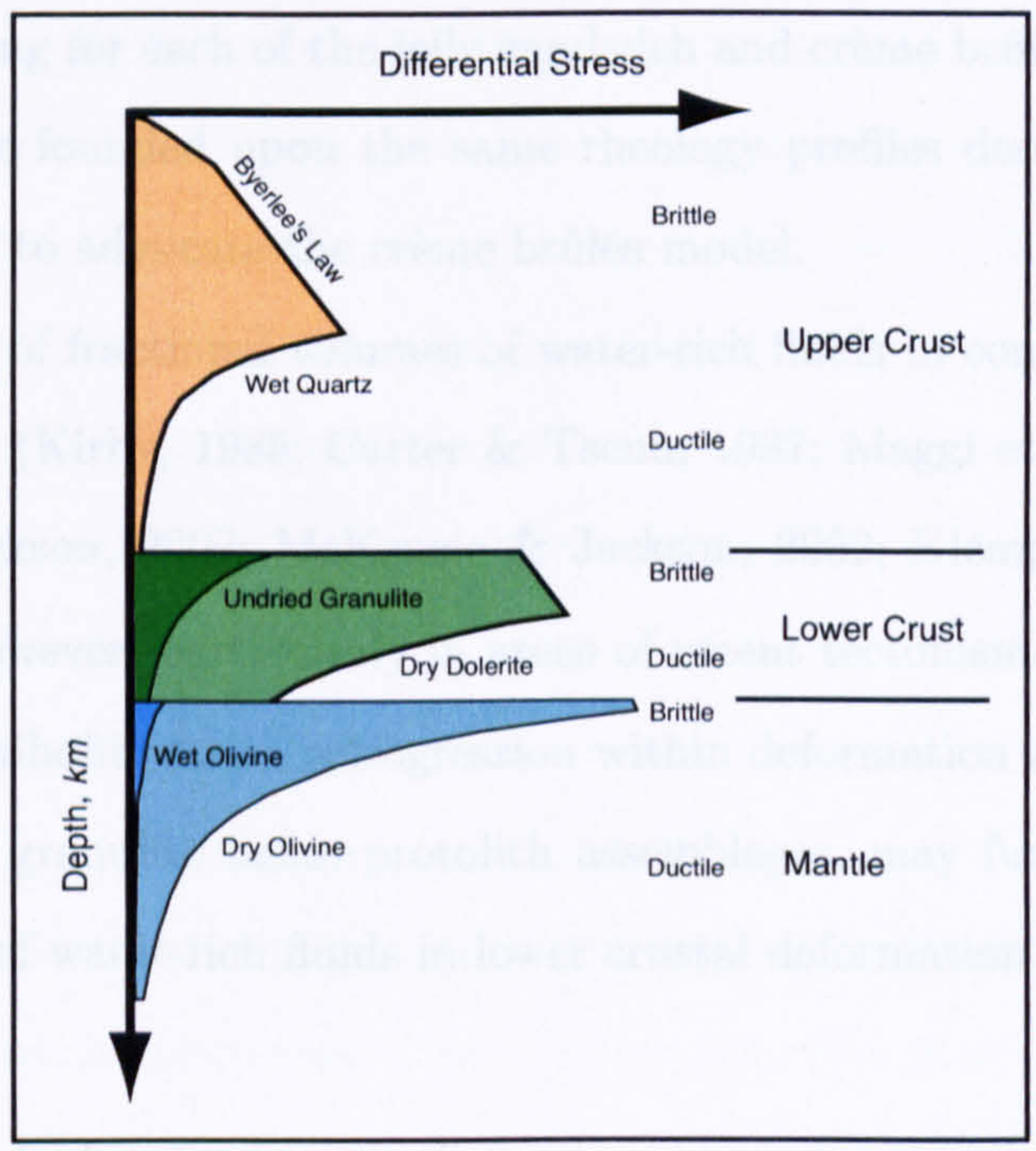

Figure 1.2: Schematic lithospheric rheology profiles for a compositionally layered crust. Both relatively weak and strong lithologies are depicted for the lower crust and mantle. The crème brûlée model corresponds to the scenario of a strong lower crust (dry dolerite) and a weak upper mantle (wet olivine). Note that a mafic lower crust need not necessarily result in a mid-crustal strong, brittle zone, particulary where diffuse fluids are present, or the geothermal gradient is greater than represented here. From Jackson (2002).

tioned into them (see Chapter 4). As highlighted by Handy et al. (2001) however, flow laws describing the plastic behaviour of such mineral phases are notably lacking. Afonso & Ranalli (2004) go some way in accounting for variation in lower crustal lithologies by including wet and dry dolerite, in addition to a range of felsic and mafic granulite compositions, in their rheological calculations. Their models exhibit a generally weak lower crust, where hydrous mafic compositions occur, relative to the mantle.

Despite recent and extensive criticism of the jelly sandwich model, Burov & Watts (2006) continue to promote it as the most widely applicable crustal rheology profile for explaining the long-term stability of the lithosphere. Their conclusions are based on observations of lithospheric flexure, and results of thermal and me-

chanical modelling for each of the jelly sandwich and crème brûlée models, which, interestingly, are founded upon the same rheology profiles described in Jackson (2002, Figure 5) to advocate the crème brûlée model.

The presence of fractional volumes of water-rich fluids in contributing to lower crustal ductility (Kirby, 1985; Carter & Tsenn, 1987; Maggi et al., 2000; Rutter et al., 2001; Jackson, 2002; McKenzie & Jackson, 2002; Klemperer, in press) is not ruled out however, particularly in areas of recent tectonism. The observation of hydrous amphibolite facies retrogression within deformation zones, from essentially dry mafic granulite facies protolith assemblages, may further substantiate the importance of water-rich fluids in lower crustal deformation (Chapter 4).

1.3 State of the lower crust

Commonly employed methods for inferring the composition or characteristic lithology of the lower continental crust include the following (Rudnick & Fountain, 1995; Afonso & Ranalli, 2004, and references therein). (1) Seismic velocity analysis from controlled-source and teleseismic events (Christensen & Mooney, 1995), where velocity estimates are compared against those determined experimentally. These are generally ultrasonic measurements calibrated against relevant lithologies collected from and characteristic of exposed high-grade terranes and xenoliths (Christensen & Fountain, 1975; Christensen & Wepfer, 1989; Fountain & Christensen, 1989; Jackson et al., 1990; Holbrook et al., 1992; Rudnick & Jackson, 1995). (2) Observation and analysis of the frequency distribution or volume fraction of lithologies in currently-outcropping high-grade terranes (Weaver & Tarney, 1984; Percival et al., 1992). (3) Evidence from deep-sourced xenoliths (Jackson et al., 1990; Rudnick, 1992; Rudnick & Jackson, 1995).

An accurate description of the bulk composition of the lower continental crust remains uncertain however (Holbrook et al., 1992; Rudnick & Fountain, 1995). Traditionally, seismic velocity analysis employs wide-angle seismic reflection and

refraction profiling (Holbrook et al., 1992) whereby iterative forward modelling of travel-times of identified seismic phases are refined to converge on a final velocity model. Commonly, this is done via raytracing techniques (Holbrook et al., 1992). In order for seismic velocity estimates to be useful in inferring the bulk composition of the deep crust, they are correlated against a catalogue of laboratory-determined velocities for a plethora of common rock types including those sampled from high-grade terranes (Siegesmund & Kern, 1990; Percival et al., 1992; Rudnick, 1992; Rutter & Brodie, 1992; Weiss et al., 1999; Khazanehdari et al., 2000; Rutter et al., 2003), and deep crustal xenoliths (Rudnick, 1992).

Seismic velocities in the deep crust are controlled by lithology (and intrinsic anisotropy), pressure, temperature, and the presence of intergranular fluids (Holbrook et al., 1992). Deep crustal lithostatic pressures can easily be calculated and supported with estimates from mineral geobarometers (e.g. Hammarstrom & Zen, 1986; Kohn & Spear, 1990). Control on deep crustal temperatures is more difficult, but geothermometry using mineral assemblages can give quite reliable estimates (e.g. Graham & Powell, 1984; Blundy & Holland, 1990). Pressure increase tends to correlate with velocity increase (Christensen & Wepfer, 1989; Holbrook et al., 1992). This effect is most significant at relatively low pressure associated with the closure of microcracks (0.5-1.0$km/s/100MPa$ up to $200MPa$), beyond which velocity change is less significant with further increase in pressure (0.02-0.06$km/s/100MPa$ for most rock types) (Birch, 1961; Christensen, 1965; Christensen & Wepfer, 1989; Fountain & Christensen, 1989; Holbrook et al., 1992; Barruol & Kern, 1996). In contrast, temperature increase correlates with a velocity decrease (2.0-6.0$\times 10^{-4} km/s/°C$) (Kern, 1978; Christensen, 1979; Holbrook et al., 1992; Barruol & Kern, 1996). For a typical geotherm of $15°C/km$ and uniform lithology, beneath the depth at which microcracks seal, the competing effects of pressure and temperature on velocity tend to cancel, giving a constant velocity through mid- to lower crustal depths (Holbrook et al., 1992; Christensen &

Mooney, 1995). The pressure and temperature derivatives of seismic velocity have been laboratory-determined for most major rock types (e.g. Kern, 1978; Christensen, 1979). Hence, velocity measurements at ambient conditions can be places in a deep crustal context along with direct velocity measurements on rock specimens at confining pressure and elevated temperature (Kern, 1978; Christensen, 1979; Rutter et al., 2003).

The presence and effect of free pore fluid in the deep crust remains an ongoing debate (Yardley, 1986; Hyndman & Shearer, 1989; Holbrook et al., 1992; Percival et al., 1992). It is often used to explain observations of relatively low resistivity in the lower crust and P-wave reflections in the deep crust (Yardley, 1986; Hyndman & Shearer, 1989; Holbrook et al., 1992; Jones, 1992). Observations of exposed high-grade terranes do not support the widespread presence of fluids in the deep crust although they may be locally important (Percival et al., 1992). Indeed, electromagnetic observations of the deep crust can be explained in terms of observed graphitic grain boundary films, which at deep crustal conditions would form a continuous conductive network (Frost et al., 1989; Percival et al., 1992). Furthermore, the details of S-wave reflections corresponding to those if P-waves in the deep crust do not support a pore-fluid origin to reflectors (Holbrook et al., 1988, 1992). Most studies (as reviewed by Holbrook et al., 1992) assume a dry crust, absent of intergranular pore-fluid phases, although this statement may not always be true in nature.

Seismic velocity is therefore a function of lithology (i.e. mineralogical composition and their modal fractions), adjusted for pressure and temperature conditions via appropriate pressure and temperature derivatives of velocity. Seismic velocity is therefore a used as an indicator of lithology (Christensen & Fountain, 1975; Holbrook et al., 1992; Christensen & Mooney, 1995; Rudnick & Fountain, 1995).

The correlation between seismic velocity and lithology is non-unique however, leading to potential ambiguity in resolving composition from velocity data (Hol-

brook et al., 1992; Christensen & Mooney, 1995; Rudnick & Fountain, 1995). Furthermore, metamorphic grade can affect the velocity of a given composition (Holbrook et al., 1992). For example, considerable P-wave velocity overlap exists between high-grade mafic rocks and metapelites (6.8-7.2kms^{-1}) (Holbrook et al., 1992). Such ambiguity may be reduced by the use of S-wave data (and hence Poison's ratio) where it is available, in addition to other geological and geophysical controls, such as borehole data (Holbrook et al., 1992).

The wide range of P-wave velocities observed both within and between tectonic environments suggests that the deep crust is compositionally diverse (Holbrook et al., 1992; Christensen & Mooney, 1995; Rudnick & Fountain, 1995). Velocities from 6.4-7.5kms^{-1} with peaks at 6.7-6.8kms^{-1} and 7.2-7.5kms^{-1} mean that plausible compositions include metapelites, intermediate to mafic granulites, anorthosites and amphibolites (Holbrook et al., 1992). Mid-crustal velocity peaks at 6.5-6.8kms^{-1} correlate with velocities measured for metagabbro, amphibolite or metapelite (Holbrook et al., 1992). Such velocities represent the bulk average of the materials along the raypath. As such, the lithologies that they correlate with should be considered a modal average of a potentially compositionally diverse and heterogeneous deep crust (Holbrook et al., 1992; Rudnick & Fountain, 1995). Such an average is, however, useful in order to place compositional bounds on deep crustal material.

Holbrook et al. (1992) conclude from their compilation of >90 seismic reflection and refraction experiments (weighted to account for sampling bias of certain tectonic environments) with laboratory-derived velocity data for deep crustal lithologies (corrected for pressure and temperature), that the deep crust is in general close to a gabbroic composition.

One obvious method of estimating the composition of the deep crust is direct observation of the widespread high-grade terranes (Fountain & Salisbury, 1981; Weaver & Tarney, 1984; Bohlen & Mezger, 1989; Percival et al., 1992; Rutter et

al., 2003). Of particular interest however, are where complete, or at least partial continuous sections of the crust can be identified. Lower crustal sections can become exposed via compressional uplifts, extensional complexes, transpressive regimes, and more rarely in the vicinity of bolide impact sites (Fountain & Salisbury, 1981; Percival et al., 1992; Rutter et al., 2003). Wide high-grade terranes whose uplift mechanism remains spurious are also observed (Percival et al., 1992).

Compressional uplifts expose perhaps the most dramatic and convincing deep crustal sections, which often expose a full section from upper crustal assemblages through the deep crust to the Moho (Percival et al., 1992), with associated changes in pressure, temperature, metamorphic grade and composition. Compressional uplifts occur where full-crustal over-thrusting has occurred, with up-ending of the previously horizontal column and followed by erosion. Where they are available, seismic reflection profiles across exposed sections can often trace deep reflectors to the exposed section (Geis et al., 1990). Two commonly cited examples of compressional uplifts are the Kapuskasing uplift, Canada, affecting Precambrian rocks (Percival & Card, 1983; Percival & McGrath, 1986; Percival et al., 1992), and the Ivrea zone, Italian Alps, of Phanerozoic origin (Fountain, 1976; Percival et al., 1992; Rutter et al., 2003). Other examples include the Calabrian massif, southern Italy, and the Kohistan arc, Pakistan (see review in Percival et al., 1992). Features common to each include increasing mafic composition with depth associated with an increasing magmatic origin of units relative to supracrustal, and increasing metamorphic grade from greenschist to granulite facies (Fountain & Salisbury, 1981; Percival et al., 1992; Rutter et al., 2003). Where mineral assemblage geobarometry is available, maximum inferred pressures from basal sections are consistently in the range 7-9*kbars*, although 12-14*kbars* has been suggested for some localities such as the Kohistan arc (Percival et al., 1992). Geothermometers consistently record metamorphic temperatures between 700-850°C (Percival et al., 1992). Compressional uplifts expose crustal sections constructed in a variety

of tectonic environments, including accretionary prisms, magmatic arcs and rifts (Fountain & Salisbury, 1981; Percival et al., 1992; Handy et al., 1999).

The third method of inferring deep crustal composition, is from deep-sourced xenoliths. Two notable differences are observed between deep-sourced xenoliths and exposed high-grade terranes (Rudnick, 1992). Firstly, while high-grade terranes have a significant portion of more evolved, felsic to intermediate compositions, xenolith suits tend to be dominated by more primitive mafic compositions (Rudnick, 1992). Secondly, while many exposed high-grade terranes are of Precambrian origin, most xenolith suits are observed in igneous assemblages that have traversed through Phanerozoic crust (Rudnick, 1992). Such differences may be a function of differences in sampling depth between terranes and xenoliths, compositional evolution of the crust through time, or an issue of how representative either samples are of deep crustal material (Rudnick, 1992). Observation of metamorphic textures (Frey & Prinz, 1978), in addition to chemical and isotopic analyses (Rudnick, 1992), indicate that high-grade xenoliths are often distinct from their host basalt or kimberlite, and have in fact resided in the deep crust for sufficient time, post-crystallisation, to develop metamorphic textures (Rudnick, 1992). Common mineral assemblages include pyroxene, plagioclase and garnet, where pargasitic amphibole is the dominant hydrous phase, both primary (Wass & Hollis, 1983) and secondary (Okrusch et al., 1979). Geobarometry suggests that most granulite facies xenoliths equilibrated at pressures in excess of $8kbars$, supporting a deep crustal origin (van Calsteren et al., 1986; Downes & Leyreloup, 1986; Rudnick, 1992), although equilibration pressures of many xenolith suits cannot be determined due to the absence of key indicative minerals in the assemblage (Rudnick, 1992). Furthermore, decompression features, including fracturing and alteration, the coexistence of lherzolite, and primitive composition of host magmas suggest that xenoliths were plucked from deep structural levels and were transported quickly to the surface (Rudnick, 1992). In a review of 336 high-grade xenolith samples from 20 suites,

Rudnick (1992) concludes an average mafic composition, corresponding to a variety of basaltic melts and their cumulates. Laboratory-determined seismic velocities of mafic granulite xenoliths at $4kbars$ of 7.2-8.0kms^{-1} by Jackson & Arculus (1984) are consistent with those from exposed high-grade terranes, e.g. 7.0-7.3kms^{-1} at $10kbars$ (Manghnani et al., 1974) and 7.5kms^{-1} at $10kbars$ (Christensen & Fountain, 1975), and of deep crustal velocity estimates from wide-angle seismic profiles (6.61-7.25kms^{-1} for average crust at 35 km depth, Christensen & Mooney, 1995). Most simply, it seems likely that xenoliths are samples of the deepest part of the crust that represent previous episodes of deep basaltic intrusions and their cumulates (mafic underplating), and have become entrained by more recent magmatic events (Rudnick, 1992). This is supported by the observation of an increase in mafic material and magmatic origin of units with increasing depth (increasing pressure and temperature) as exposed in crustal sections (Fountain & Salisbury, 1981; Percival et al., 1992).

Rudnick & Fountain (1995) present a comprehensive review and study into the lithological composition of the lower crust, including a review of the aforementioned techniques of its determination. Laboratory-based ultrasonic measurements on a plethora of lower crustal materials, including high-grade mafic, felsic, intermediate and metapelitic compositions, are combined with continental heat flow observations and analyses of the average heat producing elemental composition of the aforementioned lithologies, and compared against the pressure and temperature calibrated seismic profile velocity measurements. Further to discussion of field observations from currently exposed high-grade terranes, the authors conclude the importance of mafic material in the deep crust in accounting for its bulk average properties, comprising between 40% and 90% of its total volume and approximating the composition of amphibolite- to granulite facies metabasalt or metagabbro. Rudnick & Fountain (1995) stress, however, that the average seismic properties of a lower crustal layer are indicative of the average properties of the constituent rock

types, and recognise that such an average may be caused by a heterogenous package of materials. The results of Rudnick & Fountain (1995) are supported by an extensive heritage of seismic velocity observations that suggest mafic composition in the lower continental crust (e.g. Fountain & Christensen, 1989; Christensen & Mooney, 1995).

The structure of the lower crust has been shown to be complex in both deep seismic reflection profiles (Mooney & Meissner, 1992) and exposed crustal sections (Fountain & Salisbury, 1981).

One of the most significant and consistent structural features to be observed on deep seismic reflection profiles globally is that of a reflective and laminated lower crust (e.g. Meissner & Rabbel, 1999). Whereas the upper crust and upper mantle tend to be seismically transparent in deep wide-angle surveys, the lower crust is often characterised by a dense package of strongly reflective subhorizontal lamellae (Allmendinger et al., 1987; Cheadle et al., 1987; Mooney & Meissner, 1992; Meissner & Rabbel, 1999). Reflective lower crust is a feature of (albeit in varying strength and distribution) almost all tectonic environments including compressional belts and ancient shields, although is most prominent in young extensional zones characterised by extensional tectonics and thermal events in their recent tectonothermal history (Meissner & Rabbel, 1999).

A widely cited mechanism for the origin of lower crustal reflectivity calls on compositional and metamorphic layering coupled with ductile creep (Allmendinger et al., 1987; Cheadle et al., 1987; Mooney & Meissner, 1992; Meissner & Rabbel, 1999). Acoustic impedance contrasts between multi-scale compositional and metamorphic layering, and tabular igneous intrusions provide the primary origin of reflections (Meissner & Rabbel, 1999; Smithson & Johnson, 2003). Reflectivity may be further enhanced by an ordering process, notably viscous creep under an extensional stress field, augmented by heating from mafic intrusions or upwelling mantle (Mooney & Meissner, 1992; Meissner & Rabbel, 1999; Waters et al., 2003).

This would further enhance subhorizontal fabrics and the development of lattice preferred orientations in minerals, and thus enhancing subhorizontal reflectivity (Mooney & Meissner, 1992). This mode of genesis supports the observation of strong and pervasive lower crustal reflection lamellae in extensional environments, e.g. the Basin and Range province (Allmendinger et al., 1983, 1987; Hamilton, 1987) and the U.K. continental shelf (Matthews, 1986; Beach et al., 1987; Cheadle et al., 1987; Blundell, 1990), and rejuvinated mobile lower crust during post-orogenic extension (Meissner & Rabbel, 1999). Furthermore, lower crustal reflectivity in cold Archaean cratons can call on the primary causes of reflectivity (e.g. compositional layering) without necessarily requiring secondary ordering by ductile processes (Mooney & Meissner, 1992). Observations and modelling of borehole data from deep crustal materials, and from where deep crustal reflectors can be traced to the surface outcrop, support this thesis (Allmendinger et al., 1983; Mooney & Meissner, 1992; Rabbel & Mooney, 1996).

Alternatively, deep crustal reflections may be due to mylonitic fault zones (Jones & Nur, 1982; Fountain et al., 1984; Ji et al., 1993, 1997). Modelling of the seismic response to mylonitic lamellae in the deep crust Fountain et al. (1984); Ji et al. (1997) have shown that compositional, petrofabric and petrophysical characteristics of mylonite zones can be responsible for reflectivity observed in the deep crust. The often pervasive nature of reflectivity in the deep crust suggests that a multi-causal origin is most likely, incorporating compositional and metamorphic layering, intrusion, ductile ordering processes and deep mylonitic shear zones (Mooney & Meissner, 1992).

A number of studies have used direct observation of exposed crustal sections and high-grade samples collected from them to forward model the expected seismic reflection profile that would result from such a crustal assemblage (Fountain & Christensen, 1989; Pohl et al., 1999; Khazanehdari et al., 2000; Rutter et al., 2003).

As mentioned above, the Ivrea crustal section provides an accessible example of

a mid- to lower crustal exposed section in the Italian Alps (Rutter & Brodie, 1990; Percival et al., 1992; Handy et al., 1999; Khazanehdari et al., 2000; Rutter et al., 2003). Prior to final uplift and exposure in a compressional uplift, the Ivrea section records accretion, metamorphic and magmatic processes, orogeny, magmatic underplating, and post-orogenic thinning and extension (Handy et al., 1999; Rutter et al., 2003) and is considered typical of thinned late Variscan continental crust within the Tethyan and Atlantic passive margins (Handy et al., 1999).

The Ivrea deep crustal section can be broadly considered in terms of two tectonically juxtaposed blocks, the Ivrea-Verbano zone (IVZ) and the Strona-Ceneri zone (including the Scisti dei Laghi)(SCZ), separated by the Cossato-Mergozzo-Brissago (CMB) line (Khazanehdari et al., 2000; Rutter et al., 2003).

The IVZ represents the deepest, higher-grade part of the section, and is characterised by high-grade paragneiss and metavolcanics (Handy et al., 1999; Khazanehdari et al., 2000; Rutter et al., 2003). With increasing grade, mafic intrusives and associated cumulates become increasingly important such that they dominate the deepest parts of the section (Handy et al., 1999; Khazanehdari et al., 2000; Rutter et al., 2003). Polyphase folding is widely evident in the IVZ resulting in complex structures that can be broadly considered isoclinal with, what would have been horizontal limbs prior to uplift (Handy et al., 1999; Khazanehdari et al., 2000; Rutter et al., 2003). Gneissic banding and schistosity would have been horizontal prior to up-ending, and mafic intrusives are roughly concordant with banding (Handy et al., 1999; Khazanehdari et al., 2000; Rutter et al., 2003).

The SCZ is characterised by an assemblage of metasedimentary gneisses and schists cut by orthogneiss and undeformed granitic intrusives (Boriani et al., 1990; Handy et al., 1999; Khazanehdari et al., 2000; Rutter et al., 2003). Again, units are multiply folded but with metamorphic fabrics lying subhorizontal in the crust prior to uplift of the section (Handy et al., 1999; Rutter et al., 2003).

In order to assess the effect of complex and heterogeneous deep crustal structure

and composition, Rutter et al. (2003) produced a synthetic seismic reflection profile of the Ivrea section by forward modelling from a 2D velocity profile derived from a simplified geological map of the Ivrea section (appropriately back-rotated to a pre-uplift crustal section) and laboratory determined velocities from 23 rock samples across 90 localities covering the range of lithologies included in the model.

Strong reflections are noted on their migrated synthetic reflection profile that can be correlated with both lithological and tectonic contacts across the entire section. Of particular interest however is the generation of a package of reflection lamellae in the lower crust. These spatial interference composites are the result of reflections from a package of structures whose resolution is less than that of the seismic wavelength and represent finely layered paragneiss and mafic intrusions in recumbent isoclinal folds of the IVZ (Rutter et al., 2003). Hence, the individual reflections in this zone cannot be directly correlated with a particular structure or interface (Rutter et al., 2003). Furthermore, steep components of recumbent isoclinal folds are not imaged, hindering a true interpretation of the structure (Rutter et al., 2003). Reflection seismology is successful therefore in identifying zones of compositional and metamorphic layering with intrusions, as in the IVZ, but may fail to resolve the true detail.

In most respects, the deterministic forward modelling of Rutter et al. (2003) supports the model of a layered lower crust with ductile ordering processes as inferred from seismic reflection profiling (Mooney & Meissner, 1992; Meissner & Rabbel, 1999).

The continental lower crust is thus extremely heterogeneous, both compositionally and structurally, and at all scales. It exhibits an assemblage of metamorphic (meta-igneous and metasedimentary) and igneous rocks that span a range of compositions from felsic to ultramafic, often multiply reworked, and which represent the different stages and different tectonic settings in the crusts complex tectonothermal history. This complex history is also reflected structurally, where

polyphase deformation and structural overprinting is common. The importance of mafic compositions in the deep crust is recognised however, both as observed lithologies, and as an average, bulk composition. Ductile structures are also considered as an important structural feature of the deep crust, notably multi-scale layering whether it be compositional, metamorphic or structural.

1.4 Material properties and seismic anisotropy

Seismic anisotropy describes the azimuthal dependance of seismic wave velocity (P- and S-wave velocity anisotropy), and the differential velocity of orthogonally polarised waves during shear-wave birefringence (shear-wave splitting anisotropy) (see Chapter 5).

Seismic anisotropy can result from a number of micro- and macroscopic rock properties, and can be considered in two broad groups (Crampin et al., 1984; Kendall, 2000).

Intrinsic anisotropy is independent of seismic wavelength and is a function of the physical properties inherent to the transmitting material. The most important of these is preferred orientation of crystal lattices of constituent mineral phases in a rock aggregate deforming by ductile deformation. This is termed lattice preferred orientation, or LPO. Some of the first observations of seismic anisotropy due to LPO were for the oceanic upper mantle, where anisotropy is attributed to olivine crystals aligned with plate spreading directions or upwelling in the proximity of spreading centres (e.g. Hess, 1964; Blackman et al., 1993; Kendall, 2000). Subsequently, intrinsic anisotropy has been shown to be important in crustal materials where the development of LPO is due to crystal-plastic processes under ductile deformation (Nicolas & Poirier, 1976; Mainprice & Nicolas, 1989; Khazanehdari et al., 1998; Lloyd & Kendall, 2005). Lithological anisotropy occurs where inequidimensional grains of anisotropic minerals are deposited with a preferred orientation, thus generating a strong intrinsic anisotropy in that material (Sayers, 1994; Vernik

& Liu, 1997).

In contrast, extrinsic anisotropy refers to that resulting from a periodicity in material heterogeneity, and is dependant on seismic wavelength. It has been shown that compositional layering (that is, a stack of periodically varying isotropic or anisotropic layers) can be modelled as a homogeneous anisotropic unit where the seismic wavelength is longer than that of the periodicity of the heterogeneity (Backus, 1962; Crampin, 1984*a*). The anisotropic expression is a function of the physical properties of the layered material and the nature of the layering itself.

Media containing cracks, fractures or inclusions with a preferred orientation have also been shown possess effective anisotropy (Crampin, 1978, 1984*b*; Leary et al., 1990). The magnitude and symmetry of such anisotropy is a function of crack geometry, density, and the material properties of inclusions, whether they be vapour- or fluid-filled (Crampin, 1978; Leary et al., 1990; Knight & Nolen-Hoeksema, 1990). Fractures are often shown to be related to local or regional stresses (Crampin et al., 1990; Shih & Meyer, 1990; Shepherd, 1990). The dependance of fracture dilatancy on confining pressure means that their contribution to anisotropy is commonly considered negligible beneath a few kilometers depth in the Earth (Crampin et al., 1984; Christensen & Wepfer, 1989; Fountain & Christensen, 1989; Leary et al., 1990; Siegesmund & Kern, 1990).

The effect of pressure and temperature on seismic velocity is outlined in Section 1.3. As concluded there, the competing effects can be thought to cancel for moderate thermal gradients

1.5 Model of the lower crust

For the purpose of providing a compositional and structural framework for this project, a practically applicable crustal model is constructed which integrates both generalisations and specific intricacies from the above discussions.

The importance of mafic compositions in the lower crust is addressed by con-

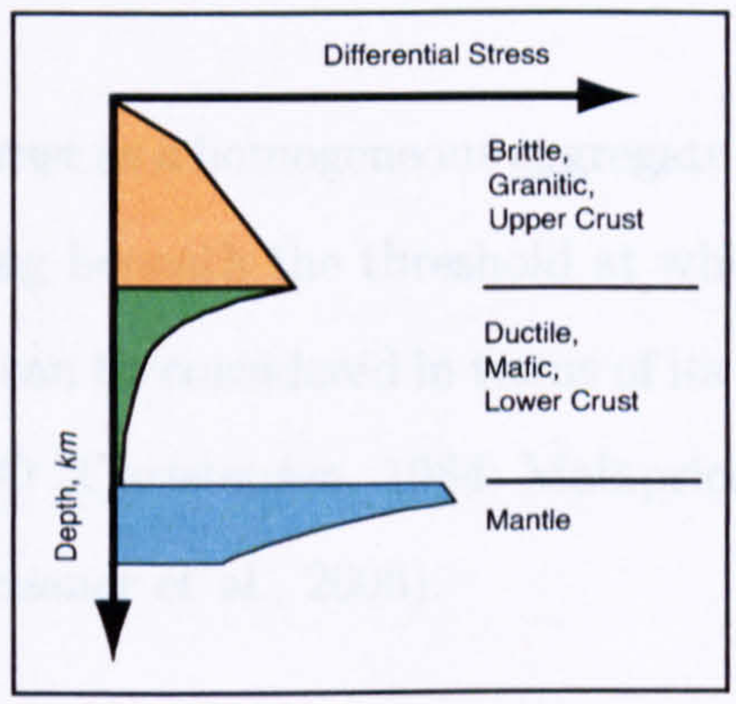

Figure 1.3: Schematic rheology profile corresponding to the crustal model employed in this project. The crust is approximated as two-layer system with a brittle, granitic upper crust, passing to a ductile, mafic lower crust beneath the brittle-ductile transition.

sidering it in terms of a macroscopically homogeneous mafic lithology. The upper crust is represented as an isotropic and homogeneous unit of granitic composition. This is combined with the rheological approximation described by the jelly sandwich model, whereby the lower crust is defined as that part characterised by solid-state ductile deformation, practically identified as the region beneath the base of seismicity (characteristic of the brittle-frictional upper crust) and above the Moho. The transition to the lower crust is hence marked by a compositional and rheological boundary in this model. Complexities such as a mid-crustal strong-zone at the transition from quartzo-feldspathic upper crustal lithology and rheology to relatively stronger mafic lithologies of the lower crust are ignored in this simplification.

The principal aim of this research project is to outline a reproducible workflow for the calibration of seismic properties against material strain, rather than attempting to provide a unifying answer to complex structural and petrological observations in zones of continental deformation. Hence, provided that the limitations and fundamental generalisations in the rheological modelling and determination of average lower crustal composition are considered (Rutter & Brodie, 1991) the proposed two-layer approximation of crustal structure and properties is

considered acceptable.

Modelling the lower crust as a homogeneous aggregate deforming by crystal plastic processes, and existing beneath the threshold at which cracks or fractures are prevalent, means that it can be considered in terms of its intrinsic anisotropic properties alone, namely LPO (Christensen, 1984; Mainprice & Nicolas, 1989; Siegesmund & Kern, 1990; Meissner et al., 2006).

1.6 Thesis outline

The aims of this project are to illustrate a practical and reproducible procedure for determining the seismic properties of a typical lower crustal lithology, calibrated to strain via calculation from petrofabric (LPO).

Research objectives include:

1. To identify and sample a strain gradient in a representative high-grade mafic lithology.

2. To characterise the collected sample suite in terms of its finite strain and petrofabric.

3. To illustrate the dependence of seismic velocity and anisotropy with strain intensity and petrofabric orientation.

4. To show how such information can be included in simple structural models of the crust.

A thesis work-flow is shown in Figure 1.4.

Chapter 2 opens by introducing the Lewisian complex high-grade terrane of northwest Scotland as a suitable analogue for the lower crust in terms of its lithology, structure and inferred deformation processes. The specific field area at Upper Badcall, comprising an amphibolite-facies ductile shear zone cutting amphibolite- to granulite-facies mafic protolith is then described, including a discussion of its

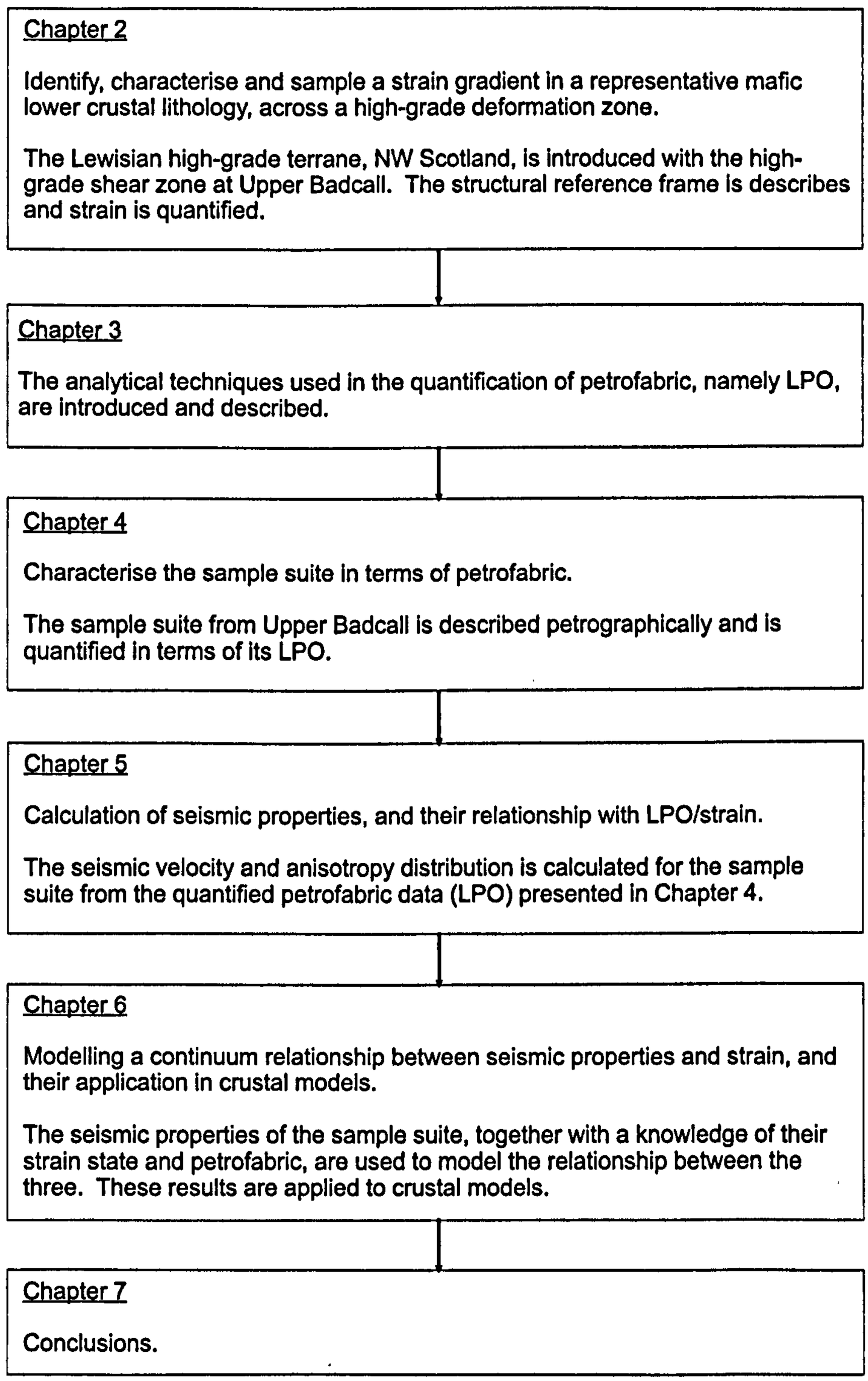

Figure 1.4: Thesis work-flow.

strain history. A suite of nine samples collected across the deformation zone at Upper Badcall are correlated to its finite strain profile.

The analytical and experimental techniques used in the microgeochemical and microstructural characterisation and quantification of collected samples (Section 4) are summarised in Chapter 3.

Chapter 4 examines the results of such analyses of the sample suite, describing its petrology, microstructure and and petrofabric. A further, microstructurally-based method of calculating the finite strain profile is presented here and critically discussed.

An introduction to seismic anisotropy and its calculation from material properties is recounted in Chapter 5. In addition, seismic velocity and anisotropy results for the strain-calibrated sample suite are presented, together with an analysis of the dependance of seismic properties on aggregate modal composition.

Strain-calibrated, sample-wise seismic properties are interpolated across a continuum of finite strain and petrofabric orientations in Chapter 6. In a move to illustrate the application of petrofabric- and strain-calibrated seismic properties in integrated geological and geophysical studies of crustal deformation, results are incorporated into a selection of simplified crustal models representative of competing theories in zones of contemporary or recent continental deformation.

Chapter 7 summarises the pertinent conclusions to this study.

Chapter 2

The Lewisian high-grade terrane: A deep crust analogue

The primary step in the work-flow model outlined in this project is to identify and sample rock materials representative of mafic lower crust. Numerous exposures of deep crustal material exist worldwide including high-grade terranes (Weaver & Tarney, 1984; Newton & Hansen, 1986; Park & Tarney, 1987) and crustal sections (Fountain & Salisbury, 1981; Percival et al., 1992), and provide an opportunity to sample rocks that were once stable in, and representative of the deep crust. Examples include the Kapuskasing uplift, Canada, the Kohistan arc, Pakistan, the Calabrian massif, southern Italy, and the Ivrea section, Italy (as described in Section 1.3) (see review of deep crustal sections in Percival et al., 1992). This chapter presents the Lewisian high-grade terrane of northwest Scotland with a summary of its structure, composition and tectonic history. The latter part of the chapter concerns the specific field locality studied at Upper Badcall. Here, a high-grade ductile shear zone cutting initially isotropic mafic protolith is observed. In view of the discussion of lower crustal bulk composition in Section 1.3 and the crustal model of Section 1.5 used herein, this lithology is taken as a suitable lower crustal analogue material, and a suite of samples were collected across this deformation zone representative of a strain gradient in that lithology. Sampling

a strain gradient in a mafic lower crustal lithology forms the foundation to the work-flow model presented in this project, and constitutes the core materials for petrofabric and petrophysical characterisation in succeeding chapters.

2.1 The Lewisian complex, NW Scotland

The Lewisian gneiss complex of northwest Scotland forms a relatively narrow and well exposed strip of Precambrian basement to the Caledonian foreland (Figure 2.1). The Archaean to Proterozoic Lewisian gneiss complex shows evidence of a protracted and complex history including multiple phases of deformation and intrusion (e.g. Sutton & Watson, 1951). Moreover, the length of the Lewisian outcrop crosses the strike of the major tectonic features, permitting a variety of structures and lithologies from different crustal levels to be observed. These features make the Lewisian a particularly useful resource for identifying and studying strain in the mid- to lower crust.

The tectonic and metamorphic history of the Lewisian is complex and has been the subject of debate for over a century (e.g. Peach et al., 1907; Sutton & Watson, 1951; Friend & Kinny, 2001). Advancements in the understanding of structural geology, particularly in the context of global tectonics, together with increased accuracy of isotopic dating techniques have constrained the argument to a more universally accepted model.

A range of lithologies can be identified in the Lewisian complex (e.g. Sutton & Watson, 1951). Mafic and ultramafic material form metre- to kilometre-scale enclaves and masses hosted in lithologically diverse acid to intermediate gneisses. The distribution and relative proportion of each lithology represented in a particular locality is a function of its structural position in the complex, as is the intensity of metamorphic or tectonic fabric observed. It should also be noted that some supracrustal and metasedimentary material is observed within the complex (Sutton & Watson, 1951; Cartwright et al., 1985). Although these represent a

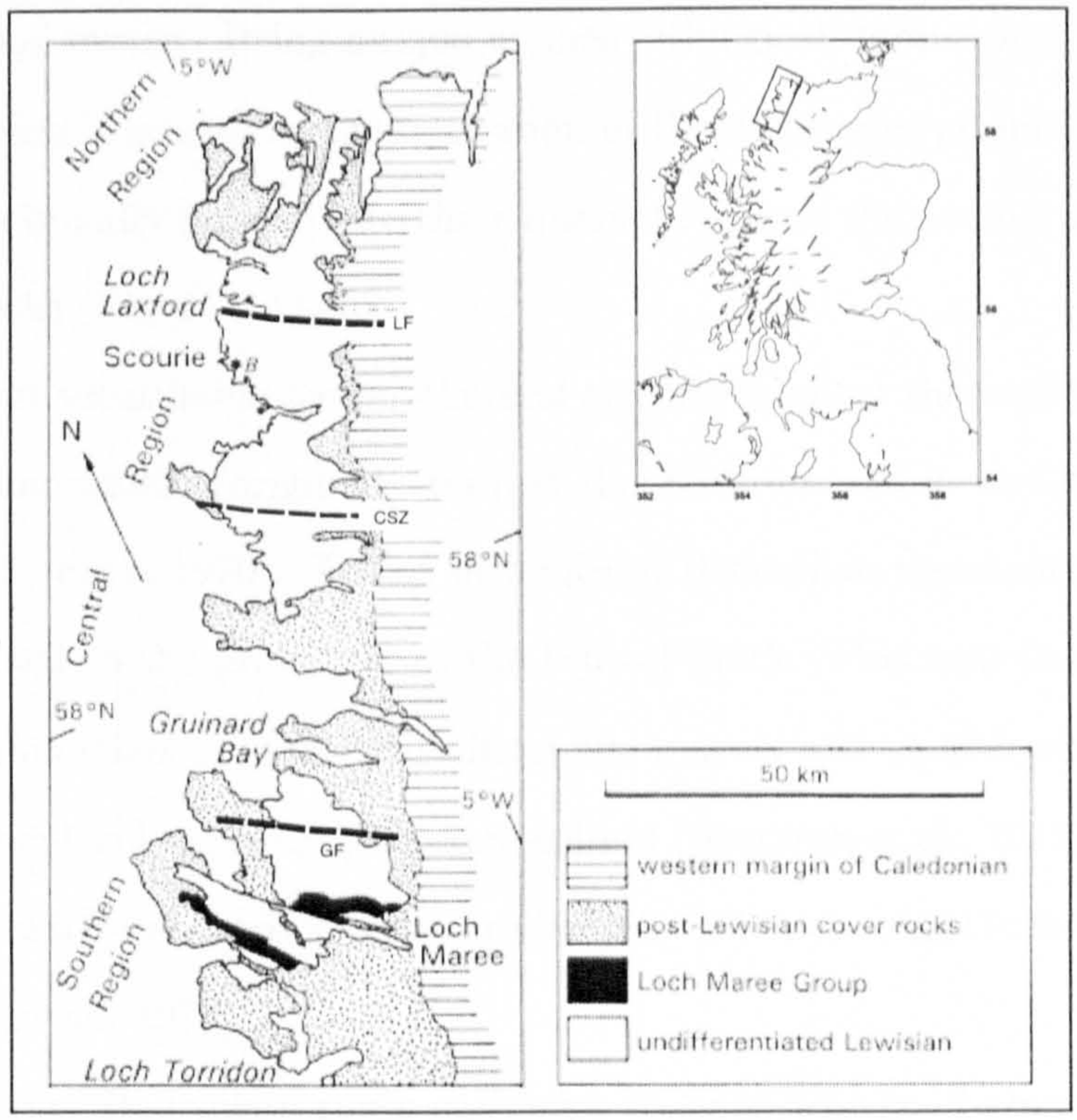

Figure 2.1: A sketch map of northwest Scotland showing the outcrop of Lewisian gneiss complex including the Loch Maree supracrustal group. The Lewisian can be broadly divided into the northern block, north of the Laxford front (LF), the central block, and the southern block, south of the Gruinard front (GF). The locations of Upper Badcall (B) and the Canisp shear zone (CSZ) are included for reference. The Inverian Tarbet and Gairloch-Diabaig shear zones are reactivated by the Laxford front and Gruinard front respectively. The insert highlights the location of the sketch map within Scotland. Modified from Friend & Kinny (1995).

minor component of the lithologies of the complex, they are often observed in association with mafic or ultramafic masses — a feature that may be important in understanding the petrogenesis of the complex, and indeed, the evolution of high-grade terranes and the lower crust globally.

On a gross scale, the Lewisian complex can be considered in terms of four major tectonothermal events. Being unique in their lithlogical, metamorphic and structural expression, the outcrop manifestation of these episodes permit the Lewisian terrane to be broadly divided into three distinct regions: the northern, central and southern blocks (Figure 2.1).

The earliest identifiable tectonothermal episode to affect the region is the Badcallian metamorphism (originally termed the Scourian *sensu stricto*, Sutton & Watson, 1951; Park, 1970). Today, evidence of Badcallian metamorphism is generally restricted to the granulites of the central block. This zone is characterised by a high proportion of mafic and ultramafic masses and smaller enclaves. Host gneisses are acid to intermediate in composition (Sheraton et al., 1973). Badcallian deformation can be recognised structurally by broad open folds (Sutton & Watson, 1951; Beach et al., 1974).

The dating of Badcallian rocks continues to be a subject of great controversy. Longstanding debates prevail over issues ranging from proper nomenclature and terminology, to representative lithologies for dating particular events (see discussion in Friend & Kinny, 2001). Moreover, problems of element mobility with respect to grain size within gneisses at high-grade conditions, and heterogeneous metamorphism, retrogression and deformation within the Lewisian complex as a whole cause countless problems for workers and often result in an over-complication of a potentially much simpler tectonothermal history. Nevertheless, a relatively firm and widely accepted geochronological framework does exist for the Lewisian. Radioisotope systematics have been widely and intensively used over the past few decades in dating Lewisian rocks, and have proved invaluable in understanding the

evolution of the complex (see review in Rollinson, 1996). Genesis of Lewisian crust occurred *c.*2950*Ma* (Hamilton et al., 1979; Friend & Kinny, 1995) and appears to have been proceeded in continuous succession by over 300*Myrs* of granulite facies metamorphism to *c.*2650*Ma* (e.g. Pidgeon & Bowes, 1972; Holland & Lambert, 1975; Chapman & Moorbath, 1977; Weaver & Tarney, 1980; Corfu et al., 1998) — the Badcallian event.

Estimates of the *P-T* conditions of Badcallian metamorphism record high-grade conditions, although absolute values vary. It is generally accepted that peak metamorphism exceded 700-800°C and 7-8*kb* (Sills & Rollinson, 1987).

The Badcallian event was followed by a further high-grade episode identified in the central zone of the complex (Tarney, 1963) and named the Inverian by Evans (1965). Inverian movements led to the development of steep NW-SE striking shear belts several kilometers wide (Attfield, 1987; Coward & Park, 1987). During this episode, central zone granulites were cut by three major shear belts with associated and locally restricted retrogressive high-grade amphibolite-facies hydrous metamorphism (Attfield, 1987; Coward & Park, 1987; Park et al., 1987; Wheeler et al., 1987). The Tarbet and Gairloch-Diabaig shear zones border the central zone to the north and south respectively, both dipping towards it, and form wide belts in excess of 2-4*km* (Beach et al., 1974; Coward & Park, 1987; Park et al., 1987; Wheeler et al., 1987) (Figure 2.1). The third major Inverian structure is the 2*km* wide, WNW-ESE trending Canisp shear zone (Attfield, 1987), bisecting the central zone just north of its centre, near Lochinver (Figure 2.1). Fabric elements indicate a thrust sense in Inverian structures (Coward & Park, 1987). That is, right-lateral and south-side up on the Tarbet and Canisp zones, and right-lateral north-side up across the Gairloch-Diabaig system.

Geochronologically, the Inverian was noted during early isotopic studies (Giletti et al., 1961; Evans & Lambert, 1974; Humphries & Cliff, 1982), although the interpretation of the event of that age has been debated. Continued study and

reinterpretation marked it as a high-grade event in its own right with peak conditions at *c.*2490*Ma* (Corfu et al., 1994; Friend & Kinny, 1995) of 550-650°C and 3-7 *kbars* (e.g. Sills & Rollinson, 1987; Cartwright & Barnicoat, 1989).

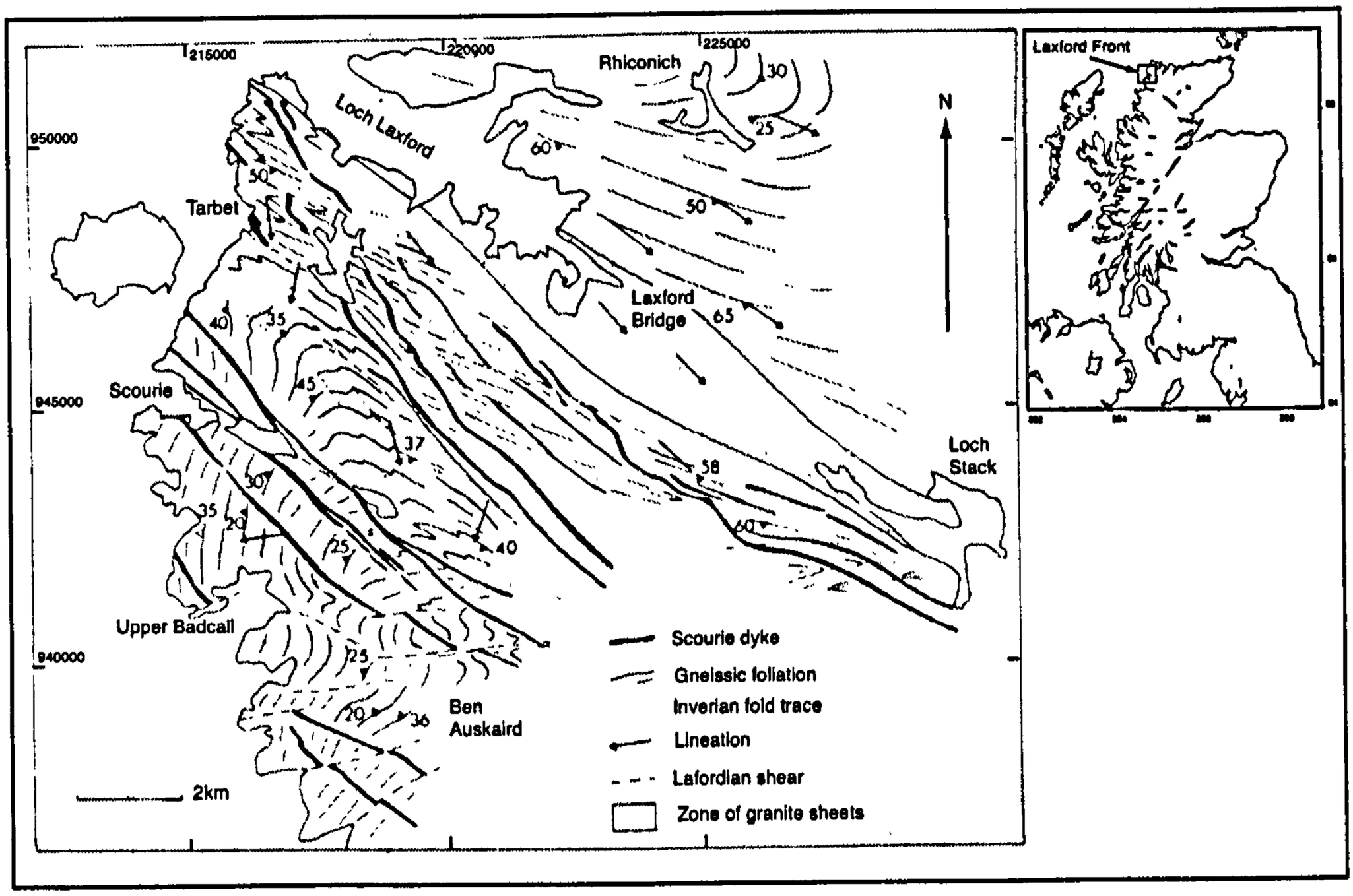

Figure 2.2: Simplified map of the region between Upper Badcall and Rhiconich, highlighting the main relationships between Scourian, Inverian and Laxfordian structures, in addition to the Scourie dyke suite. The broad open folds typical of the Scourian near Scourie and Upper Badcall can be seen to rotate into the steep, parallel fabric of the Inverian shear zone near Tarbet. This region is also marked by an increase in Laxfordian deformation, with left-laterally offset Scourie dykes. North of the granite sheets of Laxford Bridge, marking the Laxford front, intense Laxfordian deformation is pervasive. The insert highlights the location of the map within Scotland. Modified from Coward & Park (1987).

The demise of the Inverian event saw the onset of a period of dyke intrusion. The Scourie dykes form a suite of steep (dipping approximately 50°-60°NE), NW-SE trending, laterally extensive, tabular intrusions that can be observed and inferred throughout the Lewisian complex (Teall, 1885; Sutton & Watson, 1951, 1962; Beach et al., 1974; Park & Tarney, 1987; Waters et al., 1990). They represent an important unit given their emplacement between major regional deformation episodes, providing workers with a marker and hence some control over the protracted de-

formation and metamorphic history of the complex. Dykes vary from a few centimetres in width (e.g. Cleit Mhor, U.K. grid reference NC14124418) to tens of metres (e.g. at Poll Eorna, Scourie, U.K. grid reference NC14954560). Radiometric dating has now confirmed that the dykes were intruded over a period of time between 2400Ma and 2000Ma (Chapman, 1979; Heaman & Tarney, 1989; Waters et al., 1990; Cohen et al., 1991). Structural relationships with country rock and inferences from metamorphic assemblages in certain areas of the complex clarify that the onset of intrusion began prior to the termination of Inverian deformation and metamorphism (Tarney, 1973; Park & Cresswell, 1973). Although up to four distinct lithologies have been identified within the Scourie dyke suite (quartz-dolerite, bronzite-picrite, olivine-gabbro, tholeiite-norite, Weaver & Tarney, 1981a; Tarney & Weaver, 1987b), the quartz-dolerite dykes dominate, accounting for 95% of the total. O'Hara (1961) described this lithology as one- or two-pyroxene quartz-dolerite, variably amphibolitised. A garnetiferous chilled margin to the dykes is sometimes observed and taken as evidence for intrusion into country rock gneisses at amphibolite facies P-T conditions of 5-7 *kbars* and 450-500°C (O'Hara, 1961). This is supported by Tarney (1963) who used mineral associations in picrite dykes to estimate dyke intrusion into rocks at 500°C at pressures in excess of 5-6 *kbars* (15-20 *km* depth).

The final major tectonothermal event to affect the Lewisian crust was the Laxfordian, *c.*1750Ma (Moorbath et al., 1969; Corfu et al., 1994; Kinny & Friend, 1997). Laxfordian deformation is heterogeneous and is characterised by ductile shears with associated amphibolite facies retrogression. In the north, the southern limit of intense and pervasive Laxfordian deformation is termed the Laxford front (Sutton & Watson, 1951; Beach et al., 1974) and marks the boundary between the central and the northern zones (Figure 2.1). Structural observations including southwest-plunging linear fabrics and left-lateral dyke offsets suggest that south-side down oblique extension prevailed during the Laxfordian (Beach

et al., 1974). Although an early period of south-side up and right-lateral oblique trusting has been suggested (Coward, 1990), it is not clear whether or not this is independent of late Inverian movements. The Laxford front represents a wide ductile shear zone with intense fabric development. Beach et al. (1974) and Davies (1978) described the zone as $8km$ wide, trending NW-SE and dipping 50-60° to the southwest. South of the Laxford front, to Tarbet (Figure 2.2), Laxfordian deformation affects are manifest in an anastamosing network of ductile shears that enclose unaffected Scourian and, nearer the front, Inverian gneiss (Beach et al., 1974; Coward, 1990). South of Tarbet, Laxfordian deformation is represented by discrete ENE to ESE-trending shear zones with localised retrogression (Figure 2.2). A similar structure is mirrored further to the south at the boundary of the central and southern blocks, the Gruinard front (Park et al., 1987) (Figure 2.1). The difficulty to workers arises in the fact that the trend and intensity of Laxfordian fabrics are very similar to those developed during Inverian metamorphism: steep zones of intense fabric development trending NW-SE and lineations plunging to the SE. This is further complicated in view of the fact that Inverian structures are commonly reactivated during Laxfordian deformation. For example, the Laxford front reactivates the Tarbet shear zone, and similarly the Guinard front overprints the Gairloch-Diabaig system. Deconvolution of the two events is possible where Scourie dykes cross-cut the assemblage and delimit the deformation history.

There are few $P-T$ estimates of Laxfordian deformation. From metapelites of the Loch Maree Group, Droop et al. (1999) calculate a peak of metamorphism at 630±30°C and 6.5±1.5 *kbars*, and 530±20°C from other metasedimentary lithologies (24±5 *km* depth). Fettes et al. (1992) use mineral associations in a metadolerite in the Outer Hebrides to calculate 620-640°C at 4-7 *kbars*.

It is worth noting here that a significant geochemical dichotomy also exists between the granulite facies gneisses of the central block, and the amphibolite facies material to the north and south. This dichotomy is marked by a pervasive

depletion of mobile large ion lithophile elements (LIL's) relative to the global crustal average (e.g. Sheraton et al., 1973; Tarney & Weaver, 1987a), and is a common feature of many high grade terranes (Heier, 1973). A detailed description of the complex bulk and trace element geochemical relationships exhibited by the Lewisian is beyond the scope of this study, and the interested reader is referred to thorough accounts in e.g. Weaver & Tarney (1980, 1981a,b); Park & Tarney (1987); Tarney & Weaver (1987a); Rollinson (1996).

A wealth of structural and petrological observations in the Lewisian complex allows us to draw inferences on the petrogenesis and tectonic assembly of the Lewisian crust. A valid tectonic model for the assembly of, and movements within, the Lewisian crust was developed by Park & Tarney (1987), although in part postulated by Weaver & Tarney (1980). In their model, the Scourian crust is the result of protracted and extreme tectonic reworking in the deep crust of an essentially Andean-style active margin. Geochemical characteristics, such as REE patterns and Fe/Mg ratios (Weaver & Tarney, 1980), are cited as support for mafic gneisses being the product of tholeittic low-pressure fractionation. Moreover, their common association in the complex with metasedimentary units suggests that they represent tectonically obducted and intercalated subducting ocean crust at an active margin. This melange of accreted and stacked ocean crust and ocean floor sediment was then intruded at deep structural levels by tonalitic gneisses, derived from partially melted, shallowly subducting ocean crust, which augmented and became involved in prevailing intense ductile deformation and reworking. Originating and residing within the deep crust for hundreds of millions of years, this assemblage underwent granulite facies metamorphism by equilibration on a cooling path from magmatic temperatures at its genesis and the crystallisation of the tonalitic gneisses (Weaver & Tarney, 1980, 1981a).

Uplift and cooling is associated with the Inverian event, whereby the central block became up-thrust between major through-crustal fore- and back-thrusts

marked by the relatively steep oblique slip shear zones of Tarbet, Canisp and Gairloch-Diabaig. This event segmented the Scourian crust along discrete zones and led to the juxtaposition of granulite facies material of the deepest crust with rocks residing and deformed at higher structural levels, in the mid-crust. The nature of Inverian structures suggest a less intense geotherm than that characteristic of Archaean crustal genesis (Tarney & Weaver, 1987a).

As mentioned earlier, the close of the Inverian event is associated with the onset of Scourie dyke intrusion. Notably, they appear to be emplaced under a dilational regime, indicating crustal extension. Of interest are the inferences of Weaver & Tarney (1981b) who note a relative LIL enrichment in the Scourie dykes which are attributed to mantle source. They propose this LIL enriched upper mantle is the byproduct of Archaean subduction processes, notably those that led to the production of the LIL-depleted Scourian tonalites. This suggests that during, or immediately after, crustal generation $c.3000Ma$, the lithospheric mantle was sufficiently isolated from the convecting upper mantle to maintain trace element heterogeneities produced by enrichment processes. Supporting a model of crustal extension at this time is the Loch Maree Group (Park & Tarney, 1987). These comprise a supracrustal sequence of dominantly metavolcanics and metasediments in excess of $3km$ thick, deposited towards the end of dyke emplacement, $c.2000Ma$ (O'Nions et al., 1983). Park & Tarney (1987) postulate that a period of slow crustal extension led to the intrusion of the early Scourie dykes $c.2400Ma$, which was proceeded by a more localised and accelerated period of extension in the Loch Maree region where greater lower crustal thinning was accomplished by upper crustal rifting and basin development.

The stress and strain fields prevalent during Laxfordian times were complex and varied temporally (Park & Tarney, 1987; Park et al., 1987; Wheeler et al., 1987), where interactions of structural blocks were important locally and may have contradicted predictions based on the regional stress field. The dominant

mechanism for crustal restructuring during this time, however, appears to have involved an extensional regime that incorporated significant strike-slip motion, whereby the central block subsided relative to those to the north and south, and moved to the southeast along serially reactivated Inverian ramp and mid-crustal flat structures (Coward & Park, 1987). Although this strain field is similar to that suggested for the Inverian, it does not necessarily represent a temporal continuation of it.

Kinny & Friend (1997); Friend & Kinny (2001) and Love et al. (2004) propose an alternative model for the structural history of the Lewisian crust. Recently developed isotopic dating techniques, such as SHRIMP (sensistive high-mass resolution ion microprobe), image micron-scale zoned complexities in metamorphic zircons and have provided a plethora of dates for tectonothermal events that were previously not seen or resolved. Their evidence support a model whereby the Lewisian crust is composed of at least four disparate terranes that each show a unique Archaean history of crustal genesis and metamorphism prior to the Laxfordian. At this time, separate blocks accreted along the major Laxfordian shear zones (or rather, sutures) and after which, tectonothermal histories are shared. Although this model seems attractive and suitably supported based on modern understanding of accreted terranes at active margins, a number of field relationships question its integrity. Firstly, the Scourie dyke suite predates the proposed terrane accretion, yet is common to both the northern and central blocks (Rhiconich and Assynt terranes, respectively, Friend & Kinny, 2001). From evidence of sheared dykes in the central block, and in particular the Tarbet shear zone immediately south of the Laxford front, the NW-SE trend of the dykes upon intrusion was also common to both zones. If the northern and southern zones represented disparate terranes at the time of dyke intrusion, then one would have to assume a stress-strain field constant over a wide area and covering multiple crustal blocks and plate boundaries, in addition to negligible block rotation upon docking along

the suture. Furthermore, the model suggests that the granite sheets that mark the Laxford front are associated with the northern block (Rhiconich terrane) in terms of pre-Laxfordian provenance. However, immediately south of the Laxford front, the granite sheets make a sharp boundary and slightly cross-cut the fabric of deformed and amphibolitised gneisses of the central block (Assynt terrane): an observation not expected at a major crustal suture. Finally, as mentioned earlier, Laxfordian deformation is generally associated with crustal extension, contrary to a model of terrane accretion.

2.2 The Laxfordian shear zone at Upper Badcall

Section 1.3 described how the deep crust is characterised by compositional and structural heterogeneity, showing evidence of polyphase deformation and reworking of material through time. Access to examples of discrete high-grade shear zones affecting undeformed protolith (igneous, or undeformed meta-igneous) thus provides a unique opportunity to study the effects of strain on petrofabric. Such studies are available in the literature based a variety of localities, for example the Lower Pennine Nappes of Switzerland (Ramsay & Graham, 1970) where the effects of Alpine deformation are manifest in shear zones with fabric development in pre-Triassic igneous intrusives and xenoliths.

Of particular interest here however, are studies of Laxfordian-age high-grade shears cutting doleritic Scourie dykes of the Lewisian complex (Teall, 1885; Ramsay & Graham, 1970; Beach, 1974; Coward, 1976; Ramsay, 1980). These studies give insight into the effects of strain in otherwise isotropic mafic material, as is being envisioned to represent the bulk composition of the deep continental crust (Section 1.5). These studies will be referred to appropriately in the proceeding sections.

The following discussion describes such a Laxfordian shear zone affecting a Scourie dyke near Upper Badcall, NW Scotland, and is abstracted from Tatham

& Casey (2007) (see Appendix A). The work presented in Section 2.2.2 is the product of collaborative discussion with Dr. Martin Casey.

Upper Badcall is situated in the central block of the Lewisian complex and is the type area for the Badcallian event (Park 1970). Farhead Point is a small promentory located on the northern coast of Badcall Bay (U.K. grid reference NC153413) (Figure 2.2). As illustrated in Figure 2.3, the area is characterised by an assemblage of banded granulite-facies Badcallian gneisses intruded by a Scourie dyke which retains original mineral associations and igneous textures. This assemblage is dissected by a discrete ENE-WSW trending Laxfordian-age shear zone with an apparent sinistral offset as suggested by the deflection of the dyke and gneissic fabric (Figure 2.3). A detailed map from Upper Badcall is available in Appendix B.

To fully resolve the contribution of Laxfordian deformation to the observed microstructure and petrofabric of the multiply deformed country-rock gneisses would prove difficult and unreliable. The Scourie dyke, however, shows a deformation gradient, from an isotropic protolith to highly sheared material, that is the product of one deformation event only. It is hence the simplest and most sensible unit for studying the petrophysical properties across a strain gradient. The shear zone at Farhead Point was mapped in detail and studied with an emphasis on fabric development across a high strain zone. For the purpose of petrophysical experimentation, a total of nine samples were collected, numbered serially from north to south, representing the strain gradient evident in the dyke across the deformation zone (Figure 2.3). A full lithological description of the sample suite is given in Section 4.1.

2.2.1 Field data

The NW-SE trending, steeply dipping Scourie dyke intersects the northern boundary of the shear zone at a high angle (Figure 2.3). From this point southwards,

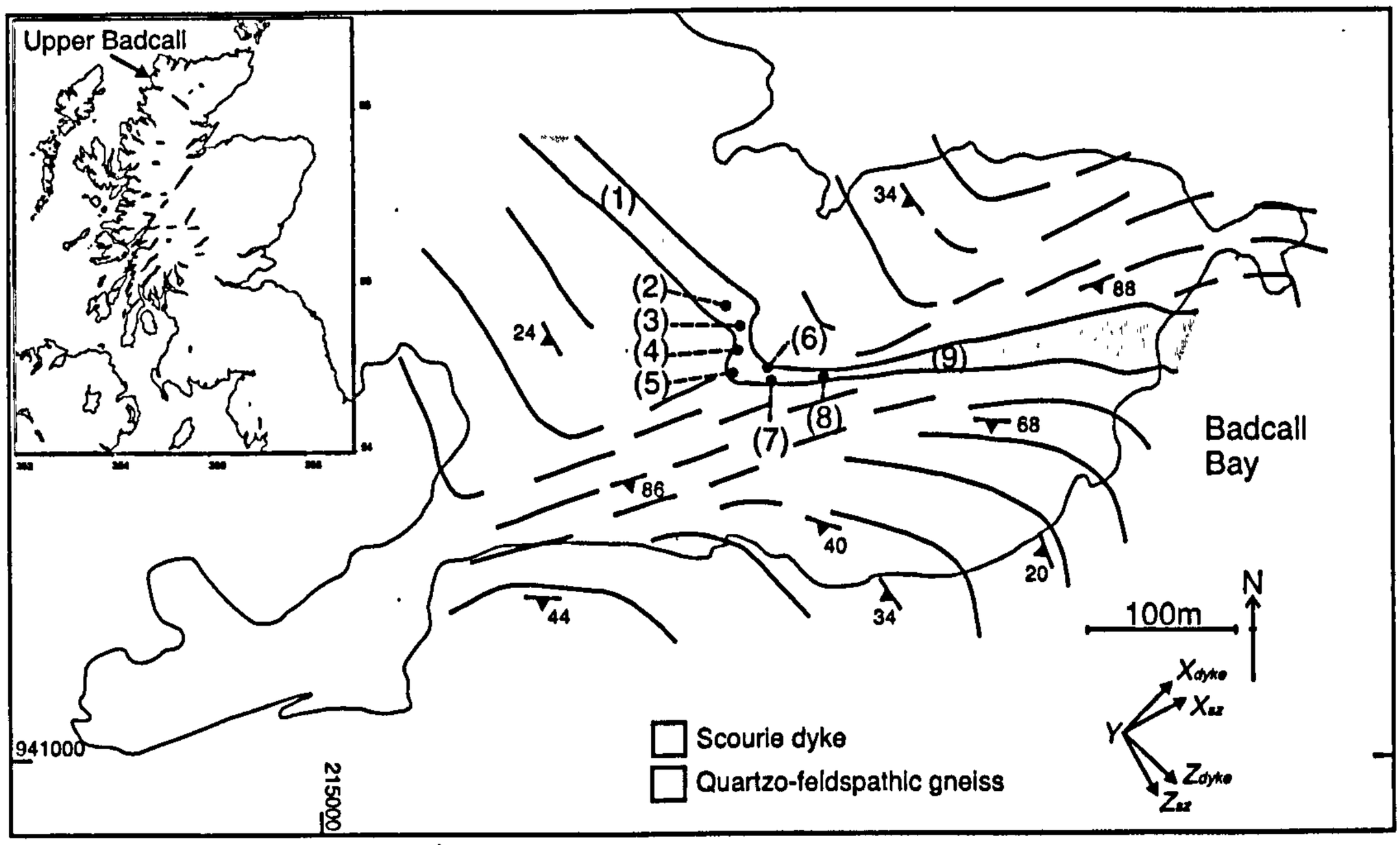

Figure 2.3: Simplified structural map of Farhead Point, Upper Badcall, NW Scotland. The Scourie dyke and the orientation and formed-surface gneissic banding are shown. Scourie dyke is shaded. Numbers in parentheses refer to sample numbers and the locations from where they were collected. Both the shear zone (x_{sz}, y_{sz}, z_{sz}) and undeformed dyke $(x_{dyke}, y_{dyke}, z_{dyke})$ reference frames are illustrated. A detailed fair copy map is available in Appendix B. Field data is available in Appendix C.

the dyke is deflected left-laterally through the high strain zone, in which it is offset by approximately $190m$ in map view, before returning to an undeformed state at its most southeastern outcrop in Badcall Bay. Note that the apparently antithetic kink in the deflection of the dyke at the northern boundary of the shear zone is a real feature and not an artifact of topographic interference.

The poles to gneissic banding, plotted in Figure 2.4(a), show a steady migration from the undeformed wall rock orientation at the southern coast of Farhead Point (e.g. 145/27W, Figure 2.4(b)) to a zone of intense and sub-vertical fabric development (e.g. 075/84S, Figure 2.4(c)) (Figure 2.3).

Figure 2.4(d) illustrates the orientation of mineral lineations measured within the dyke material. In order to increase spatial accuracy, fabric elements presented here from within the dyke were measured not *in situ*, where apparent orientations

may have mistakenly been measured, but from collected and dissected oriented samples. Dyke lineations are shown for samples collected between the northern boundary of the shear zone and the central band of intense shear fabric development (Figure 2.3). North of the shear zone, the dyke material is undeformed and hence shows no tectonic fabric. Poor exposure of the dyke towards the southern boundary of the shear zone prevented sample collection there. Note that all lineation orientations can be approximately contained within the average orientation of the shear zone (Figure 2.4(d)). Thus, lineation data indicate the absence of a broad zone of fabric development with a strain trajectory from 45° to parallelism with the shear zone, as predicted by conventional simple shear models (Ramsay & Huber, 1983). Instead, the strain fabric appears to saturate over a narrow zone at the boundary of the shear zone (a feature also observed in a Laxfordian shear zone at Castell O'Dair by Coward, 1976).

Figure 2.4(e) is a plot of mineral lineations measured in the quartzo-feldspathic country rock gneiss between the central band of intense shear fabric development and the southern coast of Farhead Point (Figure 2.3).

It can be seen from Figure 2.4(d) and (e) that quartzofeldspathic gneiss and dyke mineral lineations can be broadly contained within a girdle that, intuitively, approximates the shear zone (Figure 2.4(b)). This is most clearly developed in the dyke lineations, Figure 2.4(d), where the undeformed dyke material outside the shear zone is isotropic. Therefore, all mineral lineations plotted from within the dyke are the result of the Laxfordian deformation associated with the mapped shear zone. This is in contrast to mineral lineations from the quartzo-feldspathic country rock gneiss where a pre-existing mineral lineation is observed outside the shear zone, a remnant from some earlier tectonothermal event, most likely Scourian. Hence, mineral lineations representative of the Laxfordian shear within the quartzo-feldspathic gneiss may have some memory of an earlier orientation and progressively rotate to the orientation of the new deformation field. These data,

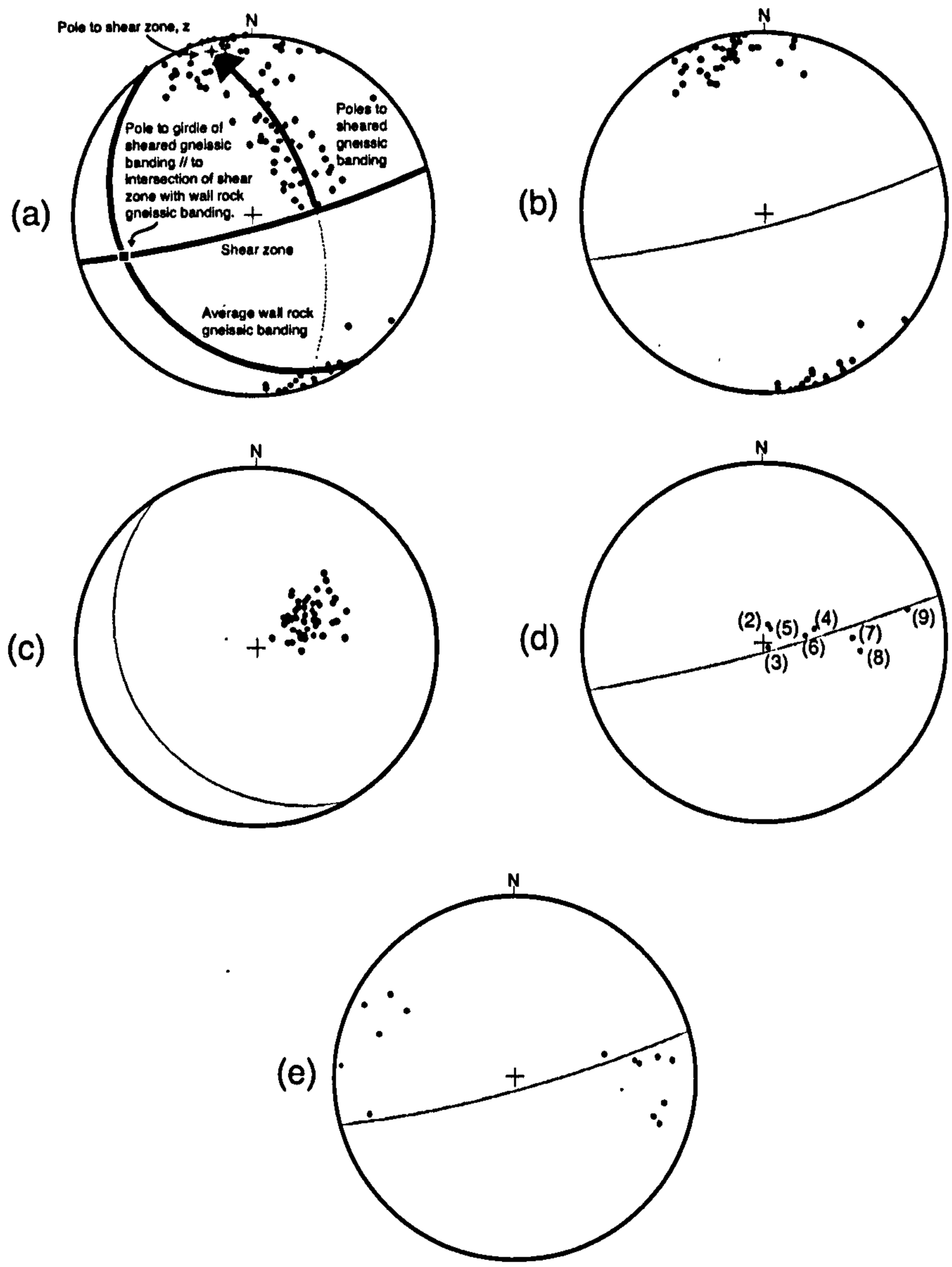

Figure 2.4: Field data. (a) Stereogram illustrating the parallelism of the line of intersection between the average shear zone orientation (b) and the average wall-rock gneissic banding orientation (c), and the pole to the girdle of sheared gneissic banding. The trace of the arrow indicates the migration of poles to gneissic banding with increasing deformation towards the centre of the deformation zone. (b) Average orientation of the deformation zone, 075/84S, from measurements of gneissic banding (shown as poles) in the central band of intense fabric development. (c) Average orientation of the wall-rock planar fabric, 145/27W, from measurements of gneissic banding (shown as poles) north and south of the deformation zone. (d) Lineations in the Scourie dyke. Numerical annotations refer to the sample number from which they were derived. Sample 1 is not included due to its undeformed state and therefore no linear tectonic fabric. (e) Lineations in the quartzo-feldspathic gneiss. The average orientation of the shear zone ((b), 075/84S) is shown in (d) and (e) for reference. Lower hemisphere, equal-area projections.

therefore, have significantly more scatter, especially away from the band of greatest shear fabric development. Most of the west-plunging lineations in the gneiss (Figure 2.4(e)) refer to locations south of the zone of intense shear fabric development and include pre-existing linear fabrics and those from the low-strain shear zone margin. Eastward plunges (Figure 2.4(e)) mark mineral lineations from within the zone of intense fabric development, although there is no ordered correlation between the individual orientation of east-plunging lineations and the location of that data transversely across the zone. In contrast, dyke mineral lineations migrate from a sub-vertical plunge near the northern boundary of the shear zone to a sub-horizontal plunge in the zone of intense fabric development (Figure 2.4(d)).

2.2.2 Discussion of field data

Though the heterogeneous strain field of a shear zone undisputedly is the result of mechanical effects, we can study the reorientation of linear and planar features in shear zones as a consequence of the heterogeneous deformation field alone. Thus the distinction of the active or passive nature of linear or planar fabric elements is not relevant. The left-lateral sense of shear, inferred from the deflection of the dyke, is supported by the apparent deflection of gneissic banding as shown in Figure 2.3. According to the method of determining true shear sense from the deflection of passive markers, described by Wheeler (1987), this inference of left-lateral shear from the gneissic fabric is a correct one.

As described by Ramsay (1967), hinge lines and fold axes in a simple shear zone are always parallel to the line of intersection of the shear plane with the surface being folded. Hence, the line of intersection between the undeformed gneissic banding in the wall rock and the simple shear zone itself should remain constant in spatial orientation during deformation. As shown in Figure 2.4(a) the pole to the girdle containing poles to gneissic banding lies parallel to the line of intersection between the representative undeformed gneissic banding orientation and the shear

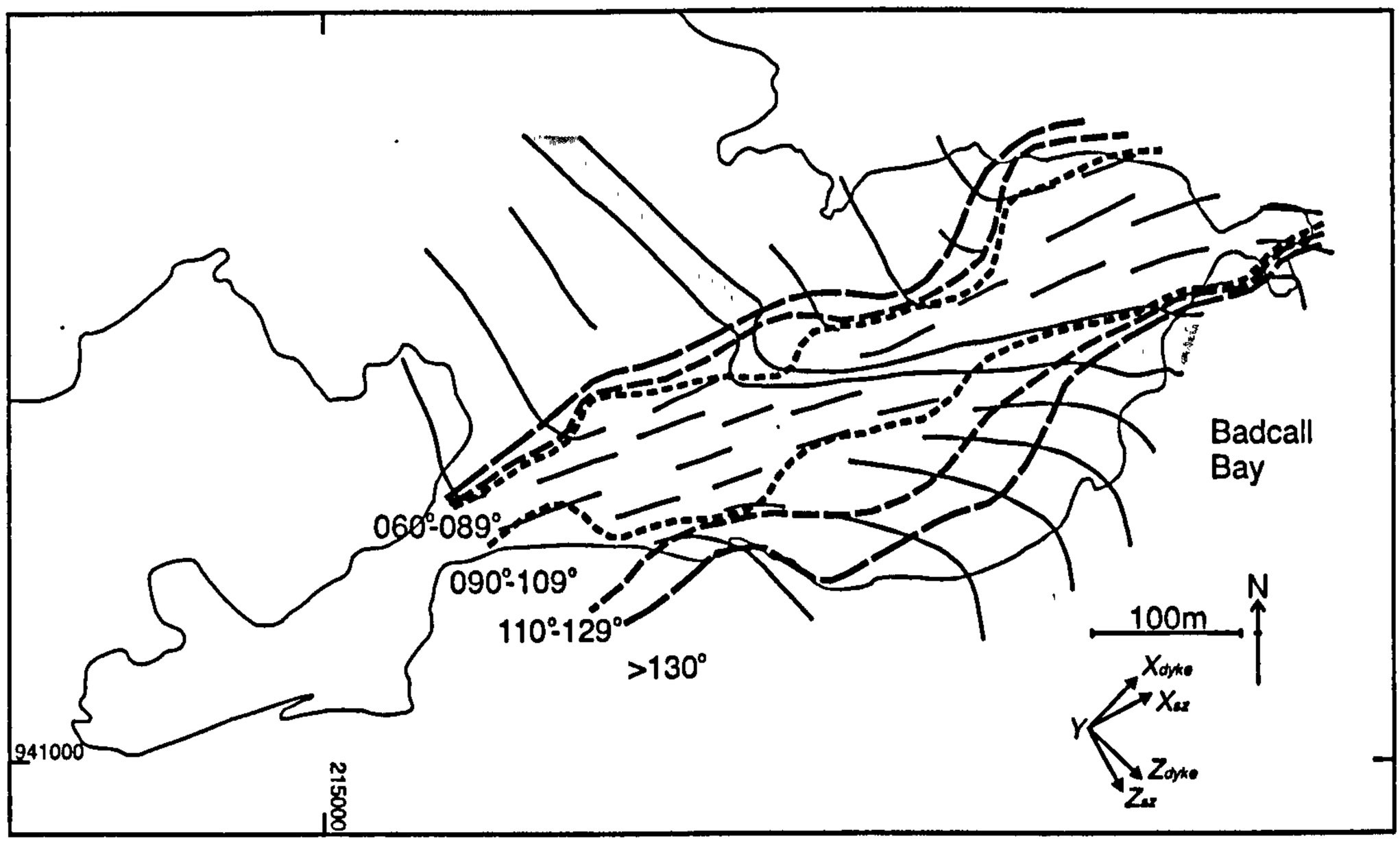

Figure 2.5: Isogons of strike of gneissic banding. Isogons are parallel and laterally continuous. Given that the profile plane (XZ) to the deformation zone is not transversely constant, this isogon pattern is only an approximation based on the surface expression of reoriented marker planes at that transverse level in the deformation zone. However, it is the lateral, or longitudinal, continuity of reoriented planes that is important here, for which the kinematic X-direction is constant.

zone. Note also that during simple shear, poles to planes are deformed along a great circle that contains the pole to the shear plane (kinematic Z-direction), and they eventually approach that pole (Figure 2.4(a)). The field data support both of these tests for simple shear.

It has also been shown that the behaviour of linear fabrics can be used to infer the kinematics of deformation prevalent in a shear zone. Wheeler (1987) suggests that passive linear markers, when deformed under simple shear, deform along great circles that contain the movement direction and ultimately approach parallelism with that direction. Figure 2.4(d) and (e) show that to some degree of accuracy, this rule is upheld. Scatter in the data may be due to a number of factors. For example, the varying mineral lineation directions from the dyke, within a fixed foliation orientation (Figure 2.4(d)), suggest that the tectonic movement direction across the shear zone varies. Undeformed dyke material in the wall-rock

is isotropic and shows no fabric development; however dyke mineral lineations migrate from sub-vertical at the northern boundary of the shear zone to sub-horizontal in the zone of intense shear fabric development. This may indicate either spatial partitioning of the strain field or temporal variations in the movement direction and magnitude of strain.

Parallelism of gneissic banding strike isogons (as measured in the field) supports the quality of the approximation of a concentrated zone deforming by simple shear (Figure 2.5). This satisfies the condition that deformation is laterally constant at each level transversely across the dyke, normal to the shear zone boundary.

The inference of a variable tectonic movement direction is supported by the apparently antithetic 'kink' in the deflection of the dyke at the northern boundary of the shear zone (by the location of Sample 5, Figure 2.3). This can be explained by a number of mechanisms. The most simple explanation is that the entire shear zone is deforming under simple shear with the tectonic movement direction spatially partitioned, or temporal variation in the strain field, transversely across the shear zone. This concept is cartooned in Figure 2.6. The exact three-dimensional orientation of the undeformed dyke could not be measured directly although it was clear that it dipped steeply (50°-60°) to the northeast. The dyke could hence assume the geometry depicted in Figure 2.6 under the condition that it dipped more shallowly than the mineral lineations/movement directions measured in, for example, Sample 5 (Figures 2.3 and 2.4(d)). Note that the anomalously shallower lineation plunge measured in Sample 4 (Figure 2.4(d)) amongst the steep plunges of Samples 3 and 5 close to its location in the shear zone (Figure 2.3) suggest that the sample may not be representative.

It could also be suggested that this outcrop geometry could have developed under pure shear. Escher et al. (1975) depict a selection of outcrop geometries that can prevail when a unit of rock, cross-cut by a sub-vertical marker, is deformed by a pure shear zone with different boundary conditions (Figure 2.7). Upon initial

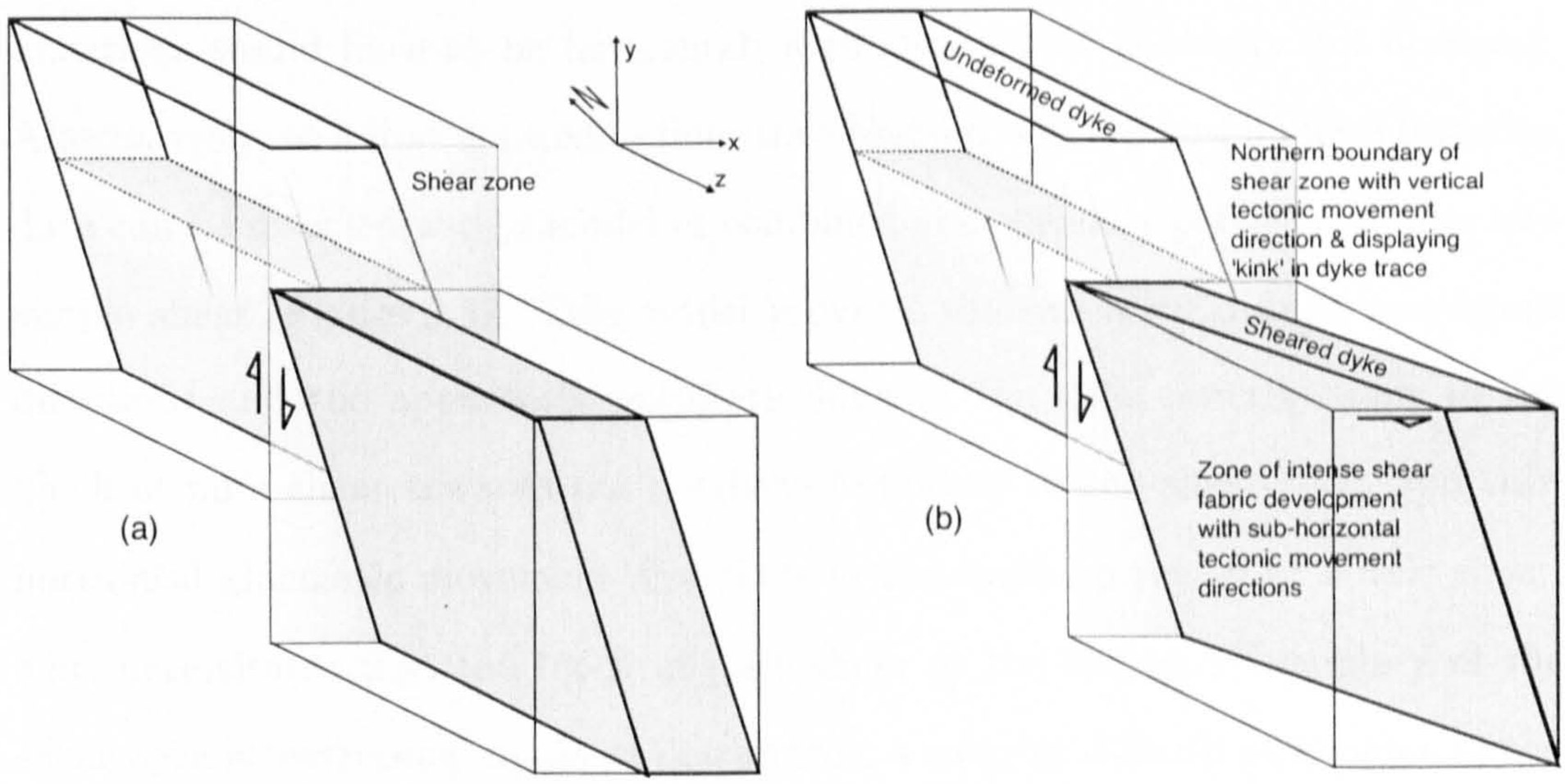

Figure 2.6: (a) A schematic illustration how a steeply dipping dyke can be sheared to generate a kink in its outcrop trace. A vertical shear zone with a vertical shear direction can create an apparently right-lateral outcrop trace. (b) Model for the shear zone at Upper Badcall. Vertical shear on a vertical shear zone at the northern boundary of the deformation zone provides the sub-vertical linear fabric and kink in the dyke trace observed. Simple shear with a horizontal displacement vector in the southern block gives a left-lateral offset geometry of the dyke and sub-horizontal linear fabric.

inspection there is an almost convincing similarity between the unusual geometry mapped at the northern boundary of the shear zone at Upper Badcall and the patterns depicted in Figure 2.7(b) and (c). However, there are a number of factors that invalidate this theory. The variation in lineation directions across the shear zone from sub-horizontal to sub-vertical (Figure 2.4(d)) suggests that a single pure shear plane strain field does not exist. In order to generate the observed map-view outcrop pattern from such a spatially consistent pure shear strain field, all mineral lineations would have to be horizontal; a condition that is clearly not observed. Alternatively, to a first approximation, the observed outcrop and mineral lineation data can be satisfied with a model of combined and spatially partitioned pure and simple shear (Figure 2.8). This model provides the sub-vertical finite movement directions and the apparently antithetic kink in the dyke outcrop trace in the block of pure shear towards the northern boundary of the shear zone, and sub-horizontal kinematic movement directions in the southern region of simple shear. This necessitates that the block of pure shear at the northern boundary of the shear zone is 'extruding' material downwards, a concept difficult to imagine at the amphibolite-facies conditions of Laxfordian deformation. Moreover, any pure shear would change the orientation of the line of intersection between the undeformed gneissic banding in the wall-rock and the shear zone. This is not observed, and hence suggests that pure shear deformation does not occur in this shear zone.

Furthermore, pure shear necessitates that the displacement and strain in the shear zone varies along its length. That is, about some centre point of the shear zone, strain and displacement increase cumulatively longitudinally outwards. Figure 2.9 illustrates transverse material lines deforming in a pure shear zone. This prediction is not supported by field observations (Figure 2.5). In addition, Figure 2.7(b) and (c) suggest, respectively, an equivalent and opposite kink in the outcrop geometry or a discrete discontinuity on the southern boundary of the shear zone. Again, these are not observed.

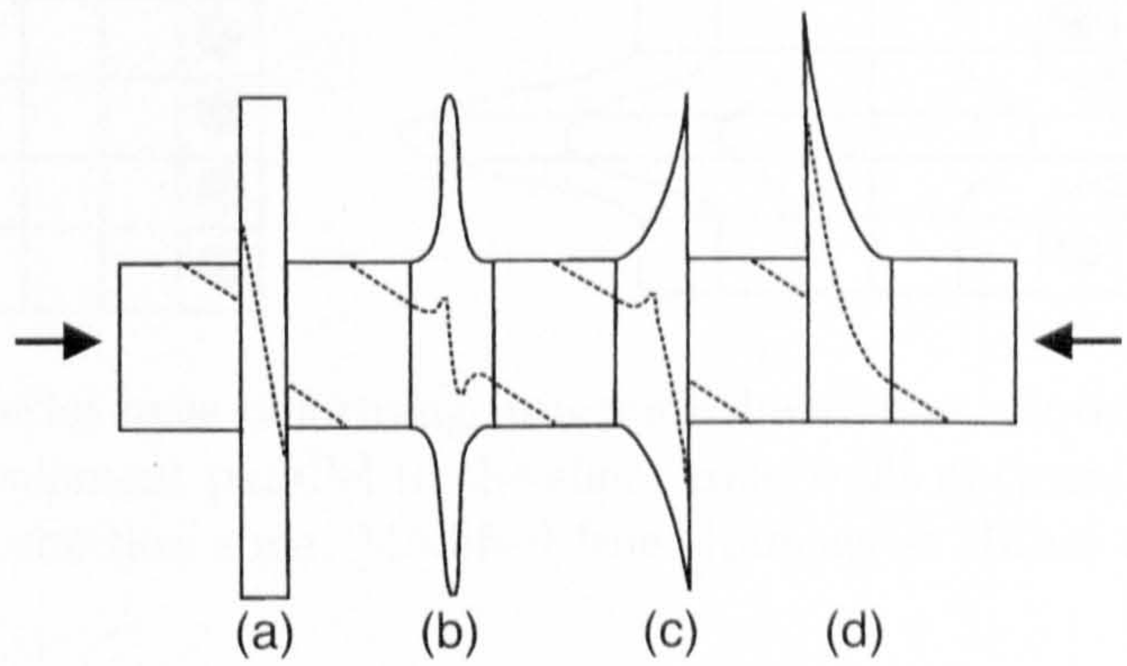

Figure 2.7: Expected geometries under pure shear deformation as described by Escher et al. (1975). Geometries (a)-(d) refer to situations with different boundary conditions where the shear zone-wall rock interface switches between no-slip and free-slip.

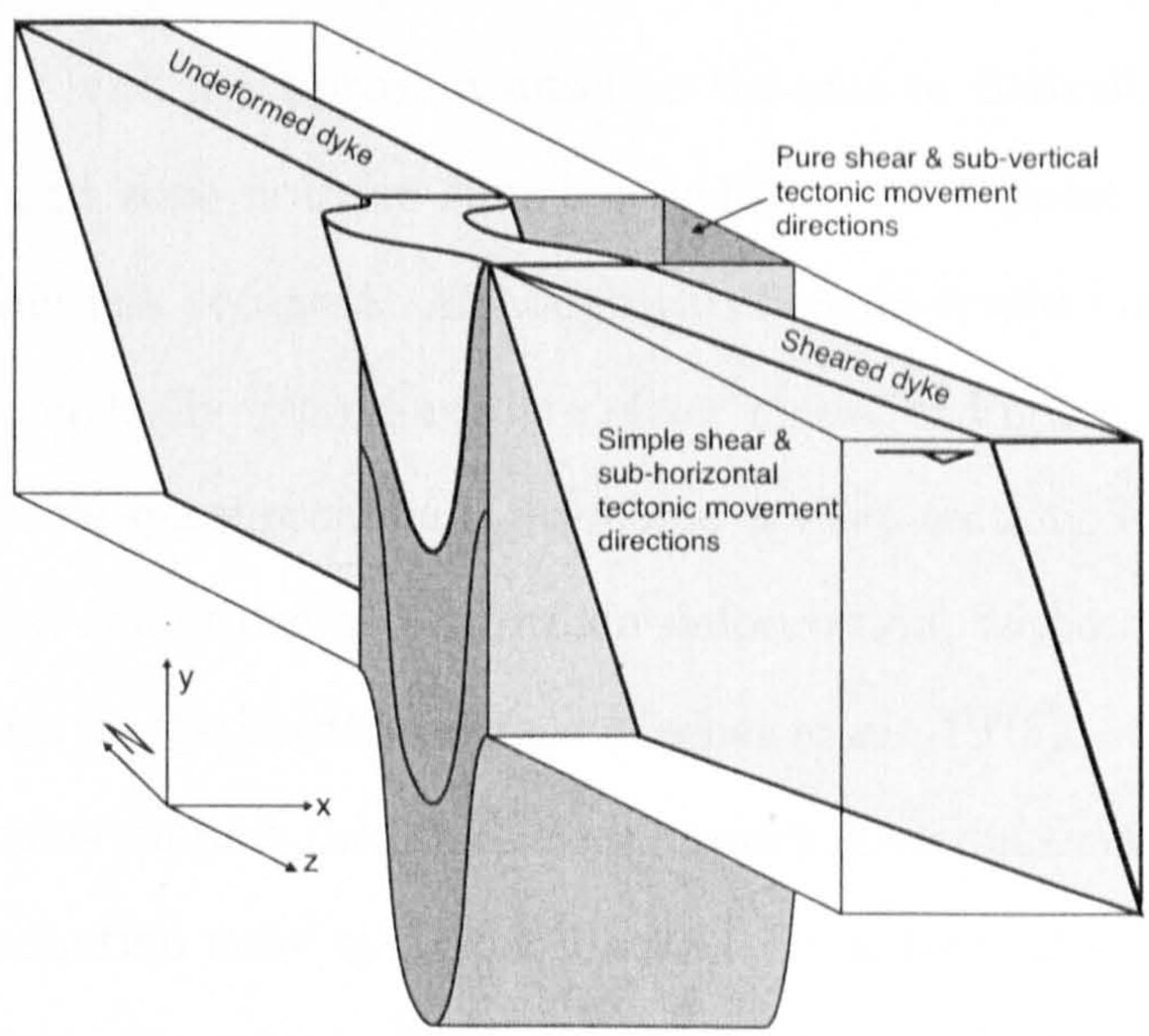

Figure 2.8: An alternative hypothesis of deformation in the dyke including pure shear near the northern boundary of the shear zone.

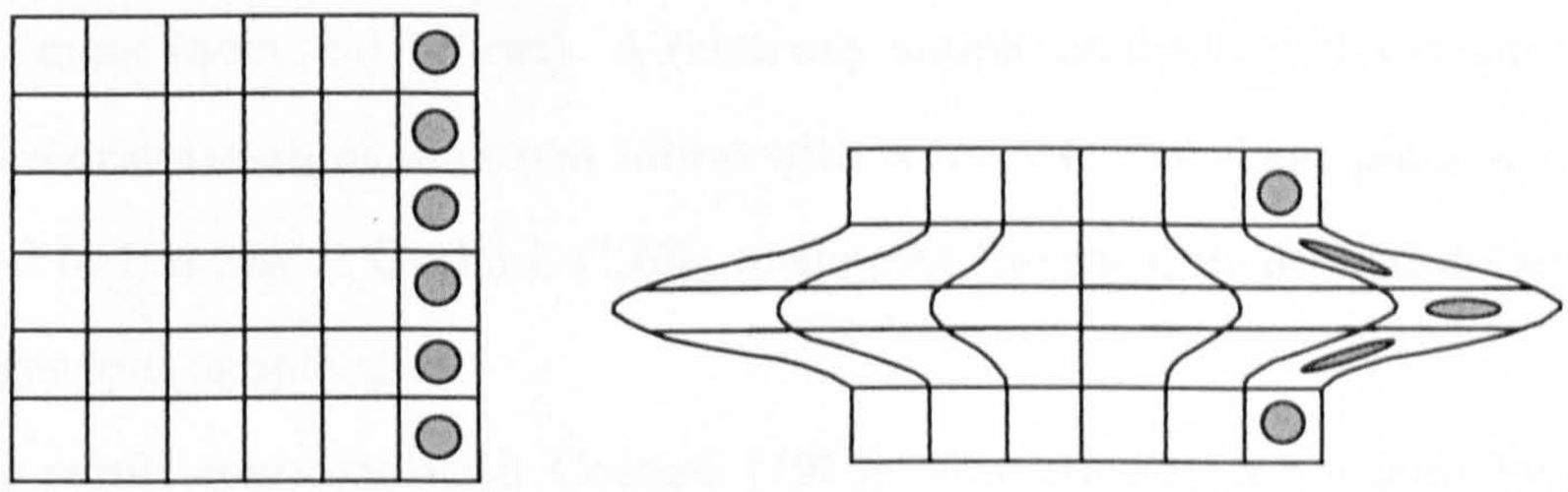

Figure 2.9: Material lines deforming in a pure shear zone. Notice the cumulative increase in displacement parallel to the shear zone walls outward from the centre-point of the deformation zone. Modified from Ramsay & Huber (1983).

The problem of strain compatibility and increasing differential shear parallel to the shear zone highlights a further problem, one of space. A shear zone of finite length must show evidence for the extrusion of the 'filling' at its lateral terminations if it is to be modelled by pure shear. The main high-strain segment of the deformation zone at Upper Badcall is considered to be of relatively finite length parallel to the zone boundary, although Beach (1974); Barber et al. (1978) and the original survey field maps of the area (Peach et al., 1892) link the zone to one or two shears with less apparent offset to the east of Badcall Bay. At neither end of the mapped zone is there sufficient evidence to suggest that this lateral extrusion of filling has occurred. Although this feature would not be observed in outcrop for the vertically extruding pure shear model of Figure 2.8, it is difficult to conceive how this space problem is overcome at deep tectonic levels, such as the amphibolite-facies conditions of Laxfordian deformation, without the presence of a free surface such as the Earth's surface (Escher et al., 1975).

These limitations support the inference that pure shear deformation is not prevalent in the deformation zone at Upper Badcall. It is instead best approximated as an overall simple shear zone, with a transversely varying kinematic movement direction.

Ramsay & Graham (1970) describe two Laxfordian shear zones in an isotropic mafic body at Castell O'Dair, North Uist, Scotland, each with relatively minor

displacement ($8cm$ and $140cm$). A relatively simple analysis of the strain profiles from the orientation of the shear fabric with respect to the shear plane across the zone led to Ramsay & Graham (1970) to suggest the shear zones had deformed by heterogeneous simple shear.

This result contrasts with Coward (1976) who investigated a $20m$ long Laxfordian shear in a Scourie Dyke body from Castell O'Dair. Coward (1976) used analysis of mineral fabric distributions to compare against those expected for ideal simple shear, including the analysis of shape fabrics of mineral clusters, and their orientation with respect to the shear zone, together with fabric development and orientation analysis of hornblende grains using magnetic susceptibility. Coward (1976) concluded that deformation was not by simple shear alone, but included a pure shear component. Evidence from the length of the Y component of ellipsoidal mineral clusters (orthogonal to the shear direction and shear plane normal) indicated that any non-plane strain is minimal (Coward, 1976). The result is attributed to complex flow patterns induced by boundary effects at the end of a shorter, incipient shear zone (Coward, 1976), rather than resulting from a regional transpressive stress field. As such, it is not considered significant for the larger shear zone at Upper Badcall, where incipient fabrics have like been destroyed and any boundary effects (Coward & Potts, 1983) are remote from the main body of the shear zone.

A larger scale study by Beach (1974) provides estimates of offset along Laxfordian shears over the northern Central block of the Lewisian terrane. Beach (1974) adopts the simple shear model of Ramsay & Graham (1970) in his strain and displacement calculations, although pursues a simpler method of calculating displacement from the offset of marker dykes, given their orientation, the orientation of the shear zone and the movement direction within the shear zone. Beach (1974) recognises that shear zones in the Badcall area often have a transversely varying movement direction, as is concluded in this study, but uses an average movement

direction for simplicity. It is noted that such an approximation may give erroneous results (Beach, 1974).

Existing literature is therefore non-conclusive for the existence of a pure shear component in Laxfordian shear zones, but observations by Beach (1974) do support the proposed model for a generally simple shear zone with transversely varying shear direction at Upper Badcall.

2.3 Strain analysis

A number of methods are available to determine the finite shear strain, γ, of a deformed rock sample in a shear zone, e.g. Ramsay (1967), Ramsay & Huber (1983). Techniques include macro-scale analyses relating field data to the finite strain across a transect of a deformation zone, such as the reorientation of passive lines or planes within a shear zone (Ramsay, 1967; Ramberg & Ghosh, 1977; Ramsay & Huber, 1983). Alternatively, microstructural techniques have been proven to provide quantitative estimates of finite strain in deformed materials. Such an analysis will be presented in Section 4.2.1 subsequent to a description of the petrography and microstructure of the sample suite.

Methods of determining strain from the reorientation of fabrics can be broadly divided into those that assume reorientation of an existing fabric or marker intersecting the shear zone at some angle (Ramsay, 1967, 1980; Ramsay & Huber, 1983), and those that trace the reorientation of incipient fabrics from an isotropic protolith (Ramsay, 1967; Coward, 1976; Ramsay, 1980; Ramsay & Huber, 1983). The approximate parallelism of all the measured dyke lineation data with the average shear zone orientation (Figure 2.4(d)) makes analyses involving reorientation of incipient fabrics undesirable here. Reorientation of gneissic banding which intersects the shear zone at a high angle presents a more suitable solution to approximating the shear strain profile in this example.

This section outlines a method of calculating the finite shear strain profile across

the deformation zone at Upper Badcall using macro-structural field data. Furthermore, restoration of displacements across the shear zone, based on the calculated strain profile, provides a test of the methods validity.

2.3.1 Stereographic determination of γ

Following the method outlined in Ramsay (1967), the reorientation of passive planes from the country rock into the highest strain portion of the shear zone is used to calculate the finite shear strain profile in three dimensions. Thus, the transversely varying finite movement direction, X, and hence the non-constant profile plane, XZ, is considered and accounted for.

A coordinate system is established, the shear zone reference frame, in which the x_{sz}-axis is parallel to the strike of the average orientation of the shear zone (positive to the east), the y_{sz}-axis is positive up, and the z_{sz}-axis is oriented transversely across the shear zone, normal to the average orientation of the shear plane (positive to the south). The origin lies at the intersection of the northern shear zone boundary with the western margin of the dyke.

A transect of arbitrary width was chosen transversely across the shear zone and in the vicinity of the coordinate system origin (Figure 2.10). The length of the transect was defined by the northern and southern boundaries of the deformation zone. A series of 13 data points were chosen across the transect (Table 2.1), where data points consist of lineation and gneissic banding pairs, derived from the dyke and quartzo-feldspathic gneiss respectively. Sufficient data points were used to account for the non-constant tectonic movement direction and to give a representative approximation of the integrated shear strain across the deformation zone. The finite shear strain was then calculated for each data point across the shear zone stereographically, as follows (Figure 2.11; Ramsay, 1967):

1. Plot the shear zone boundary orientation as a plane and a pole (here 075/84S).

2. Plot a representative orientation of the gneissic banding outside the shear

zone (e.g. 145/27W in Figure 2.11).

3. For each data point (lineation-banding pair):

   (a) Plot the lineation direction, X.

   (b) Plot the great circle containing the lineation/shear direction, X, and the pole to the shear zone, Z.

   (c) Plot the gneissic banding representative for this level across the shear zone.

   (d) Read α and α' as the respective angles between the unsheared and sheared gneissic banding orientations and the average orientation the shear zone along the great circle containing the lineation/shear direction, X, and the pole to the shear zone, Z (as constructed in Step (b)). Also, θ is the angle between positive x_{sz} of the reference frame and the lineation, X, measured along the great circle of the average shear zone orientation (the $x_{sz}y_{sz}$ plane).

The results of the stereograph are related to the strain by the equation (Ramsay, 1967, Equation 3-71, p 88) (Table 2.1, Figure 2.12):

$$\gamma = \cot\alpha' - \cot\alpha \tag{2.1}$$

And hence the x_{sz}- and y_{sz}-parallel components of the resultant shear strain are (Table 2.1):

$$\gamma_{x_{sz}} = \gamma\cos\theta \tag{2.2}$$

$$\gamma_{y_{sz}} = \gamma\sin\theta \tag{2.3}$$

where θ is the angle of pitch from positive x_{sz} to the lineation, X, measured in the $x_{sz}y_{sz}$ plane.

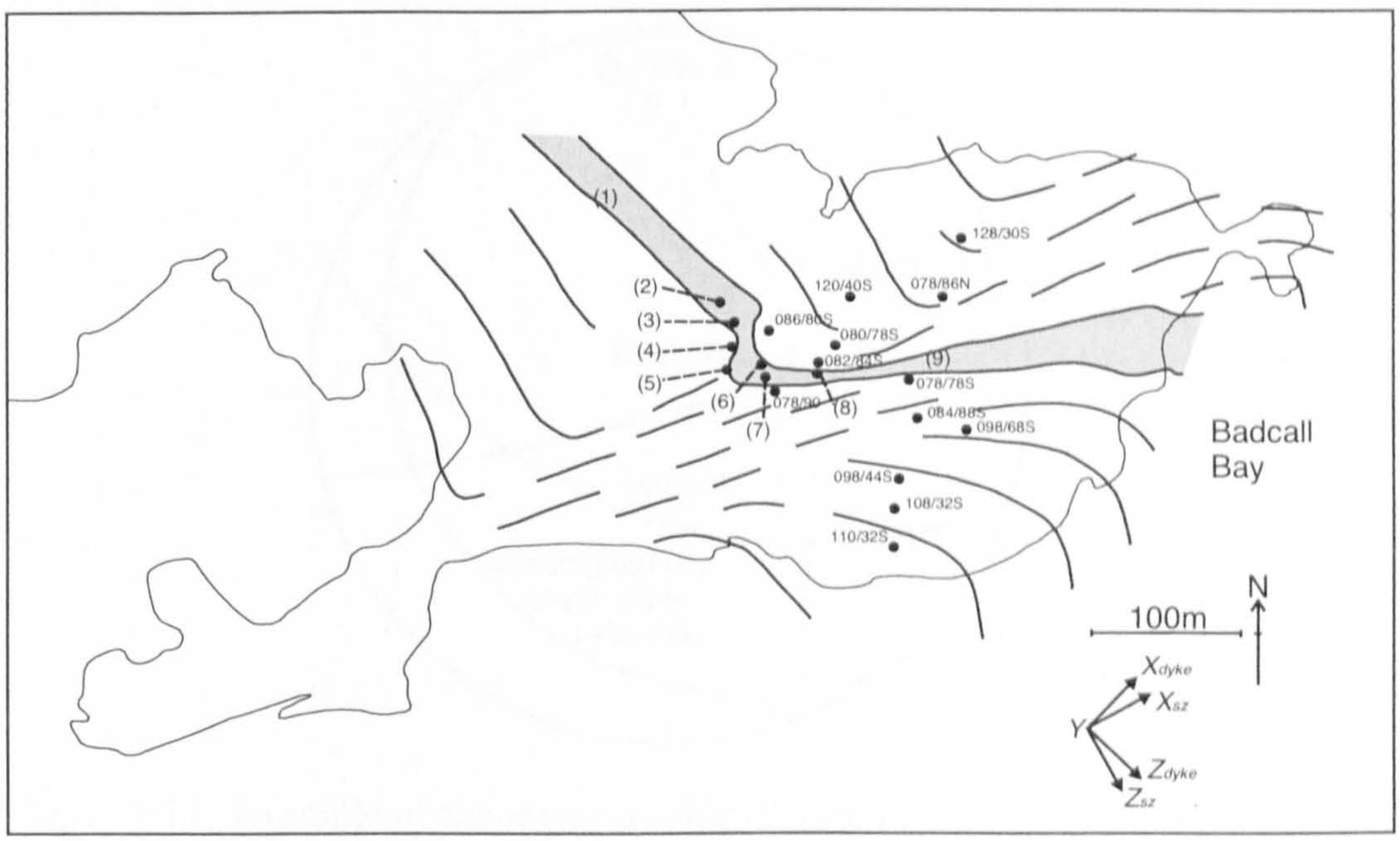

Figure 2.10: The location of data points for the calculation of the strain profile from field data. Strain is calculated using gneissic banding and mineral lineation (tectonic movement direction) pairs (Section 2.3.1, Table 2.1). Mineral lineation data was taken from collected dyke samples (shown 1-9). Banding-lineation pairs were chosen to lie on the same $x_{sz}y_{sz}$ plane as closely as possible.

The length of the transect is divided into a number of segments delimited by half the distance between successive data points. Coordinates of data points were rotated into the shear zone reference frame from observed map-view coordinates (i.e. x_{map} and z_{map} horizontal, and z_{map} vertical) by the rotation matrix about the horizontal x_{map}-axis:

$$\begin{pmatrix} x_{sz} \\ y_{sz} \\ z_{sz} \end{pmatrix} = \begin{pmatrix} 1 & 0 & 0 \\ 0 & \cos\theta & \sin\theta \\ 0 & -\sin\theta & \cos\theta \end{pmatrix} \begin{pmatrix} x_{map} \\ y_{map} \\ z_{map} \end{pmatrix} \tag{2.4}$$

where $\theta = -6°$ is the angle of clockwise rotation between vertical and maximum dip of the shear zone, 84°, effectively making y parallel to the maximum dip of the average shear zone orientation. Each data point marks the centre of each segment, and the value of the finite shear strain, γ, calculated there (Equations 2.1-2.3)

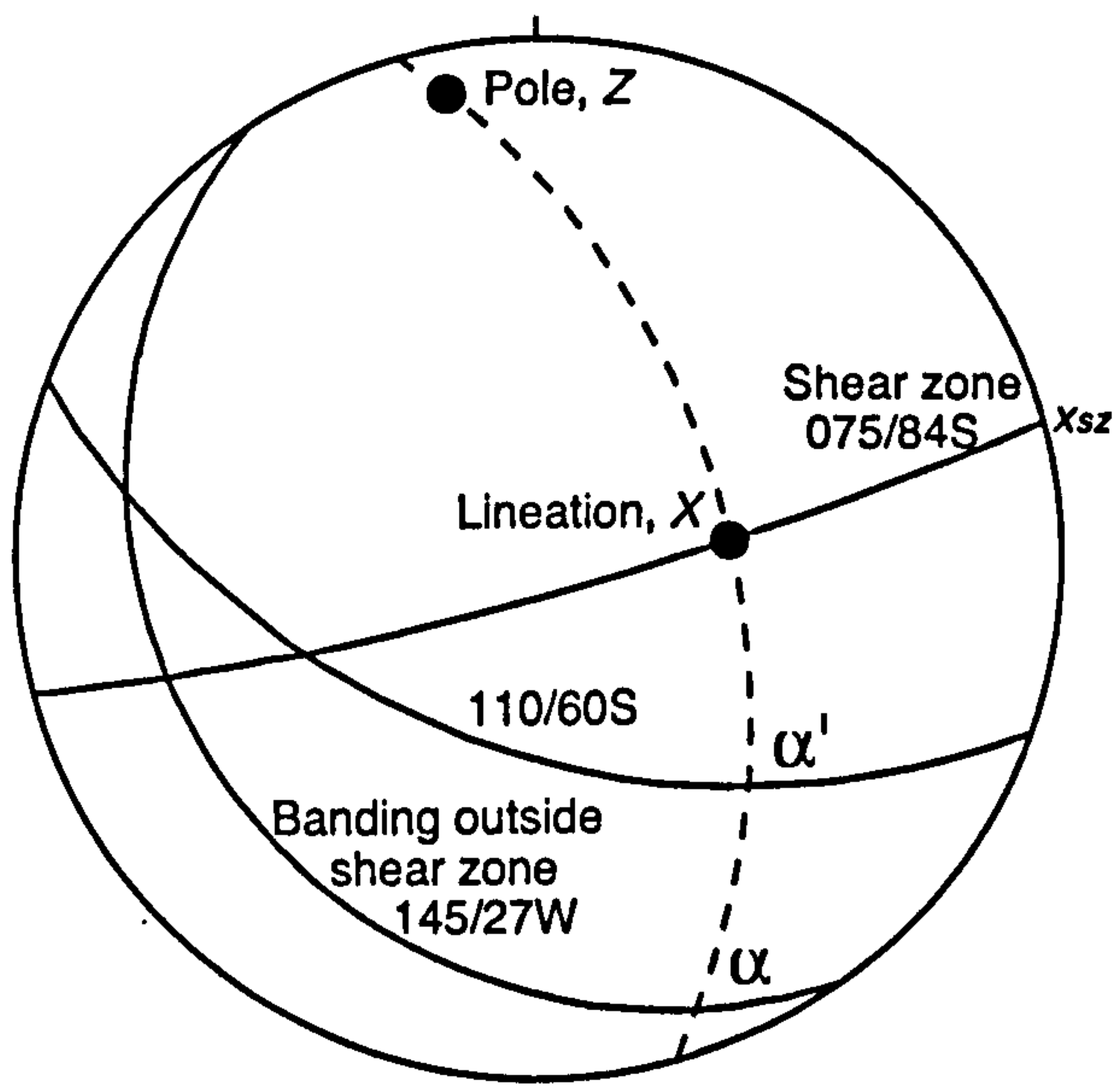

Figure 2.11: Example of the stereographic determination of α and α'. Values for structural data are included as an example. The angle X-α is α and the angle X-α' is α'. The angle x_{sz}-X is θ, and in this case is negative in reference to the lower hemisphere plot.

is considered constant over that finite width of shear zone. Hence, the relative displacements ($\Delta U_{x_{sz}}, \Delta U_{y_{sz}}$) across each transverse segment of the deformation zone (Δz_{sz}) is calculated from:

$$\Delta U_{x_{sz}} = \gamma_{x_{sz}} \Delta z_{sz} \tag{2.5}$$

$$\Delta U_{y_{sz}} = \gamma_{y_{sz}} \Delta z_{sz} \tag{2.6}$$

The cumulative displacements can be obtained by summing the contributions of each segment across the shear zone from north to south, totalling $999m$ left-laterally in x_{sz} and $594m$ north-side up in y_{sz} (Table 2.1). The resolution of Δz used in the integration of γ and U across the shear zone influences the associated computational error (Ramsay & Huber, 1983). That is, reducing the size of Δz (increasing the resolution), will give a more spatially and numerically accurate result of the integrated shear strain across the deformation zone. However, this may also include shear zone heterogeneities, such as isolated high- or low-strain

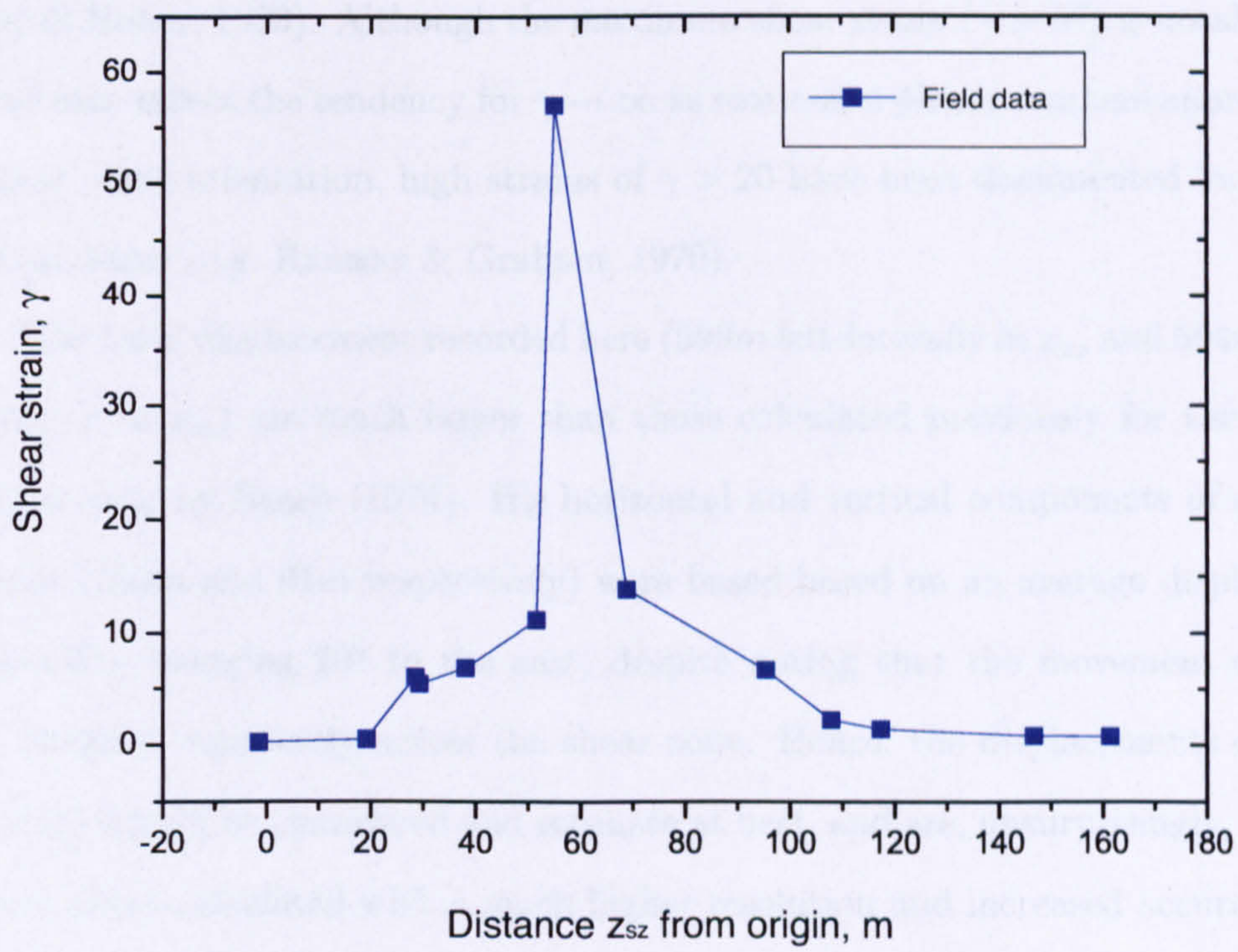

Figure 2.12: Strain profile for the deformation zone at Upper Badcall, calculated from field data. Shear strain (γ) is plotted against the position, transversely across the shear zone, at which that value was calculated. See Section 2.3.1 for details of its derivation.

zones that may not necessarily be representative of the shear zone as a whole, and may not be included in a lower resolution and more generalised model of the shear zone strain profile. The resolution chosen here was primarily controlled by the spatial resolution of the field mapping data and dyke sampling, and appears to have provided a good compromise between accuracy and smoothing localised heterogeneities in shear strain.

The strain profile of Figure 2.12 is typical of heterogeneous simple shear (Ramsay & Huber, 1983). Although the maximum shear strain ($\gamma = 57$) is notably high, and may reflect the tendency for $\gamma \rightarrow \infty$ as reoriented planar markers approach the shear plane orientation, high strains of $\gamma > 20$ have been documented for natural shear zones (e.g. Ramsay & Graham, 1970).

The total displacement recorded here ($999m$ left-laterally in x_{sz} and $594m$ north-side up in y_{sz}) are much larger than those calculated previously for the Badcall shear zone by Beach (1974). His horizontal and vertical components of displacement ($250m$ and $91m$ respectively) were based based on an average displacement direction plunging 20° to the east, despite noting that the movement direction is variable transverely across the shear zone. Hence, the displacements of Beach (1974) should be considered and estimate at best, and are, unsurprisingly, different from those calculated with a much higher resolution and increased accuracy here.

2.3.2 Restoration of the dyke

To test the stereographic method of determining finite shear strain, coordinates from within the sheared portion of the dyke were restored to their pre-deformation geometry.

This procedure has two purposes. Firstly, it tests the method of γ and displacement calculation through a simple observation of the continuity between the unsheared wall-rock dyke and the restored dyke coordinates. Secondly, it estimates the spatial orientation of the undeformed dyke where direct field measurements

Sample	Gneissic banding	Lineation	$\alpha(°)$	$\alpha'(°)$	$\theta(°)$	γ	$\gamma_{x_{sz}}$	$\gamma_{y_{sz}}$	$\Delta z_{sz}(m)$	$Cum.U_{x_{sz}}(m)$	$Cum.U_{y_{sz}}(m)$
2	128/30S	78/012	75	66	-81	0.18	0.03	-0.18	14.30	0.40	-2.50
3	120/40S	86/135	75	54	-84	0.46	0.05	-0.46	14.98	1.11	-9.33
4	086/80S	58/075	75	9	-58	6.05	3.20	-5.13	5.02	17.21	-35.10
5	078/86N	80/027	75	10	-81	5.40	0.85	-5.34	4.82	21.28	-60.80
6	080/78S	64/080	75	8	-64	6.85	3.00	-6.15	11.19	54.87	-129.66
7	082/84S	38/087	75	5	-38	11.16	8.80	-6.87	8.44	129.11	-187.66
8	078/90	34/095	74	1	-38	57.00	44.92	-35.09	8.65	517.65	-491.22
9	078/78S	12/077	67	4	-12	13.88	13.57	-2.89	20.25	792.52	-549.65
-	084/88S	12/077	67	8	-12	6.69	6.54	-1.39	19.52	920.30	-576.81
-	094/68S	12/077	67	21	-12	2.18	2.13	-0.45	10.93	943.60	-581.76
-	098/44S	12/077	67	29	-12	1.38	1.35	-0.29	19.37	969.74	-587.32
-	108/32S	12/077	67	40	-12	0.77	0.75	-0.16	21.96	986.22	-590.82
-	110/32S	12/077	67	41	-12	0.73	0.71	-0.15	18.39	999.27	-593.60

Table 2.1: Summary of data used in the calculation of strain and cumulative displacement across the deformation zone. See Section 2.3.1 for discussion and definition of terms. Note that the combined gneissic banding data from the country-rock gneiss and an associated, strike-parallel lineation from the dyke material define a data point. Axes are in the shear zone reference frame.

were sparse and approximate.

A series of coordinates were documented along the western dyke margin that, parallel to the average strike of the shear zone, were representative of a particular γ, $\Delta U_{x_{sz}}$ and $\Delta U_{y_{sz}}$ calculated for successive data points described in Section 2.3.1.

Coordinates were restored by removing the cumulative displacement, as calculated in Table 2.1, from the coordinate values, in metres, at that point in the shear zone reference frame, x_{sz}, y_{sz}, z_{sz} (Table 2.2). Coordinates were rotated into the shear zone reference frame from their observed map-view points (i.e. x_{map} and z_{map} horizontal, and y_{map} vertical) by a rotation about the x_{map}-axis as given in Equation 2.4, again, where $\theta = -6°$ is the angle of clockwise rotation between vertical and maximum dip of the shear zone, 84°.

In general, points moved to the west and upwards upon restoration. To determine the geometry of the undeformed dyke, the restored coordinates were viewed in a new reference frame, relative to the wall-rock dyke, with the x_{dyke}-axis horizontal and perpendicular to the strike of the dyke, the z_{dyke}-axis parallel to the strike of the dyke, and the y_{dyke}-axis vertically up (Table 2.2). Coordinate points were transformed from the shear zone reference frame (x_{sz}, y_{sz}, z_{sz}) to the wall-rock dyke reference frame $(x_{dyke}, y_{dyke}, z_{dyke})$ by sequential anticlockwise rotations about x_{sz} and the y_{dyke}-axis produced by that rotation, of $\theta = 6°$ and $\phi = 32°$ respectively.

$$\begin{pmatrix} x_{dyke} \\ y_{dyke} \\ z_{dyke} \end{pmatrix} = \begin{pmatrix} x_{sz} \\ y_{sz} \\ z_{sz} \end{pmatrix} \begin{pmatrix} 1 & 0 & 0 \\ 0 & \cos\theta & \sin\theta \\ 0 & -\sin\theta & \cos\theta \end{pmatrix} \begin{pmatrix} \cos\phi & 0 & \sin\phi \\ 0 & 1 & 0 \\ -\sin\phi & 0 & \cos\phi \end{pmatrix} \tag{2.7}$$

The angles $\theta = 6°$ and $\phi = 32°$ transform z_{dyke} parallel to, and x_{dyke} perpendicular to the strike of the wall-rock dyke respectively. Figure 2.13 shows restored coordinates projected onto the plane x_{dyke}, y_{dyke}. The best-fit line of Figure 2.13 represents the trace of the planar dyke in the section plane which has the strike

direction of the wall-rock dyke as its pole. It suggests an original dip close to 50° to the northeast. This value compares well with field data of the wall-rock dyke orientation, although sparse. The relatively minor deviations of restored points from the best-fit line shows that the model of bulk simple shear with a varying shear direction (Figure 2.6) is a reasonable one, considering the irregularity of the shear zone (see Figures 2.4 and 2.5). Furthermore it gives support to inferences made in Section 2.2.2 on the simple shear origin of the kink in the trace of the dyke, near the northern boundary of the shear zone. Any deviations from a perfect linear fit may also be attributed to the fact that dyke wall coordinates were often projected some distance (up to 130m) from the data points (Section 2.3.1) where the kinematics for that transverse level in the deformation zone were calculated. Across such distances, minor variations in the shear zone width are observed (Figure 2.5), leading to a more condensed or expanded strain profile parallel to z_{sz}. Hence the strain profile along the transect of Section 2.3.1 may not be precisely congruent along the shear zone.

2.3.3 Error analysis

An investigation into the potential error in the calculation of finite strain is presented in Section 4.2.2, subsequent to the discussion of a further method of calculating strain. This alternative calculation is based on microstructural parameters, and requires a knowledge of the petrology and microstructure of the sample suite. This method and a combined error analysis are thus presented in Chapter 4.

2.4 Conclusions

1. The Lewisian gneiss complex introduced herein represents a currently exposed high-grade terrane. Although the Lewisian terrane in itself is compositionally heterogeneous and shows evidence of a protracted period of com-

(x_{sz}, y_{sz}, z_{sz})	$Cum.U_{x_{sz}}$	$Cum.U_{y_{sz}}$	$(x_{sz}, y_{sz}, z_{sz}) - Cum.U_{x_{sz},y_{sz}}$	(x_{dyke}, y_{dyke})
(0.00, 0.00, 0.00)	0.40	-2.50	(-0.40, 2.50, 0.00)	(-0.48, 2.49)
(10.00, -0.36, 22.59)	1.11	-9.33	(8.89, 8.97, 22.59)	(18.94, 11.28)
(2.50, -1.41, 32.53)	17.21	-35.10	(-14.71, 33.69, 32.53)	(2.80, 36.91)
(0.00, -1.70, 35.02)	21.28	-60.80	(-21.28, 59.13, 35.02)	(-2.87, 62.47)
(0.00, -4.18, 39.78)	54.87	-129.66	(-54.87, 125.48, 39.78)	(-32.52, 128.95)
(22.50, -15.69, 53.65)	129.11	-187.66	(-106.61, 171.97, 53.65)	(-71.66, 176.63)
(37.50, -17.94, 55.93)	517.65	-491.22	(-480.15, 473.28, 55.93)	(-403.93, 476.53)
(132.50, -15.53, 71.27)	792.52	-549.65	(-660.02, 534.11, 71.27)	(-551.75, 538.64)
(242.50, -35.32, 96.84)	920.30	-576.81	(-677.80, 541.49, 96.84)	(-553.76, 548.65)

Table 2.2: Coordinates and displacements used in the restoration of part of the western margin of the deformed dyke at Upper Badcall. Displacements calculated from γ values determined via the stereographic method (Section 2.3.1 and Table 2.1). Notice that in the rotated coordinate scheme of the dyke reference frame, data is projected onto the $x_{dyke}y_{dyke}$ plane, and so the z_{dyke} coordinate is not necessary.

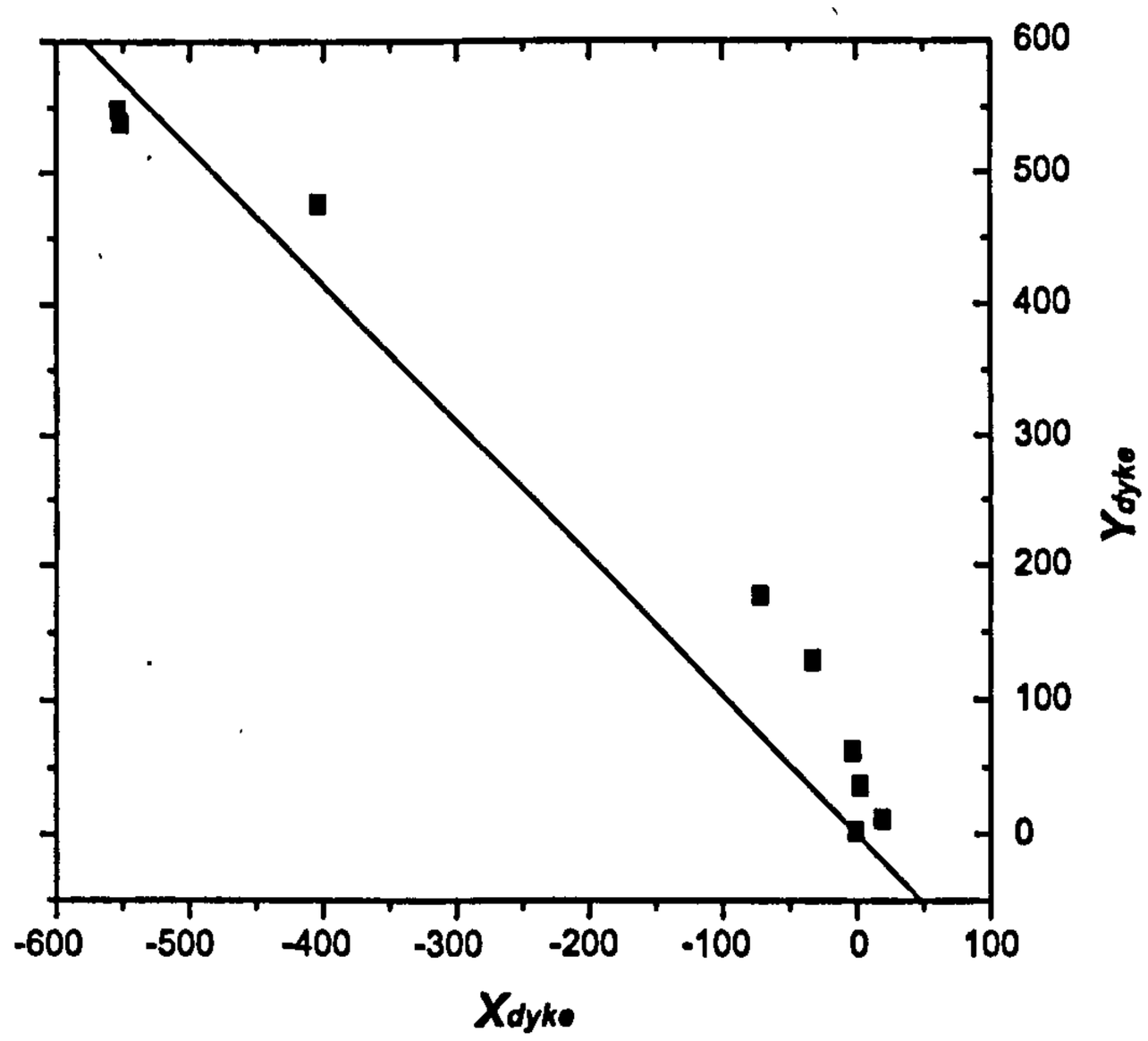

Figure 2.13: Coordinates from the western margin of the deformed portion of the Scourie dyke at Upper Badcall after U_x and U_y have been subtracted in the shear zone reference frame, x_{sz}, y_{sz}, z_{sz} (Section 2.3.1). Data are plotted in the dyke reference frame, whereby coordinates are projected onto x_{dyke}, y_{dyke}, the plane normal to the strike of the dyke. The best-fit line through the origin suggests an original, undeformed dyke dip of close to 50°.

plex polyphase deformation, one unit in particular is useful in providing a representative analogue material for this study. Being intruded prior to the finial major tectonothermal event interpreted in the Lewisian complex, the Scourie dyke suite is present as both an undeformed igneous protolith of doleritic composition, equilibrated to amphibolite facies conditions, and also in strain gradients where dykes are cross-cut by discrete, ductile, amphibolite-facies shear zones of Laxfordian age.

2. The deformation zone at Upper Badcall is shown to provide an accessible and useful example of where a Scourie dyke is deformed by a Laxfordian shear zone. From it, a suite of nine rock samples were collected across a strain gradient from undeformed protolith to highly strained material.

3. Detailed structural mapping is shown to be an important resource in establishing a structural reference frame, in characterising a deformation history, and in providing a means of calculating a quantitative strain profile of the deformation zone and sample suite. Analysis of field data shows that the deformation zone at Upper Badcall is complex, and is best described as an overall simple shear zone, with a transversely varying shear direction. Nevertheless, calculation of a three-dimensional strain profile for the deformation zone, based on the reorientation of planar gneissic fabrics, shows a relatively simple and typical transverse strain profile, from undeformed wall rock, through a broad and increasingly deformed flanking zone ($\gamma \leq 13$) to a narrow and highly deformed central zone ($\gamma \leq 57$). A successful restoration of displacements across the shear zone, resulting in a pre-deformation geometry of the sheared Scourie dyke, suggests that the outlined stereographic method of strain calculation is valid.

Thus, the result of field work in the work-flow model is to obtain a sample suite representing a strain gradient in a typical high-grade lithology. Moreover,

that sample suite is calibrated against finite strain, and can be considered in a structural reference frame.

Chapter 3

Experimental & analytical techniques

As discussed in Chapter 1, the main contributor to the anisotropic properties of the lower crust is the intrinsic rock property, LPO. Hence, a series of analytical and experimental techniques are employed for the purpose of petrofabric characterisation and quantification. Subsequent to a note on sample preparation and declaration of a reference frame convention, the fundamental concepts of scanning electron microscopy (SEM, Section 3.2) are introduced, forming the basis for electron microprobe analysis (EMPA, Section 3.3) and electron backscatter diffraction techniques (EBSD, Section 3.4), which permit the accurate quantitative description of rock composition and microstructure, respectively. These data, presented in Chapter 4, are key to the determination of the petrophysical, and particulary seismic properties of the strain-calibrated rock aggregates (Chapter 5 and 6).

3.1 Sample preparation

Much of the experimental procedures employed in petrofabric determination are based on electron microscopic techniques. Such methods necessitate specialised sample preparation, and so are worth noting here. The foremost requirement for maximising results in the electron microprobe and electron diffraction techniques, described in Sections 3.3 and 3.4, is a flat and highly polished surface.

Rock samples of approximately $10\times10mm$ square (Figure 3.1(a)) are mounted in a $30mm$ diameter cylindrical polyester resin block (Figure 3.1(b)) and polished with increasingly fine suspended abrasives from $60\mu m$ silicon carbide grit to $1\mu m$ diamond paste. These lapping and polishing procedures, however, introduce crystal lattice damage and distortion to the sample near-surface, giving lattice orientation data that are not representative of the original unpolished grains, or no data at all. Therefore, a further polishing procedure is used that provides a damage-free and highly polished sample surface. This chemo-mechanical polish uses a $0.05\mu m$ colloidal silica abrasive suspended in an alkaline (pH 8-9) fluid (Lloyd, 1987).

Electrical conductivity of the sample surface is provided by 10-$20nm$ of vacuum evaporated carbon. This coating prevents the buildup of charge on the sample surface under an electron beam, which may distort the sample image.

In order to maintain consistency throughout experimental samples and results, a convention of reference frame is declared. A sample reference frame coincident with the local kinematic reference frame, as illustrated in Figure 3.1(a), is adopted. This makes the direct comparison of experimental results, field data and strain information possible and straight-forward. Furthermore, it is much simpler to translate a data series presented in this reference frame to a geographic, or shear zone spatial reference frame, using lineation and foliation field data, than *vice versa*. In general, the XZ plane was chosen as the study surface as it is commonly considered to contain the most quantitative kinematic features (Passchier & Trouw, 1998).

3.2 Scanning electron microscopy

The scanning electron microscope (SEM) forms the central apparatus upon which the analytical and experimental techniques used herein are based, and so is briefly described here. This summary is derived from more exhaustive accounts in e.g. Lloyd (1985, 1987); Reed (1996); Goldstein et al. (2003).

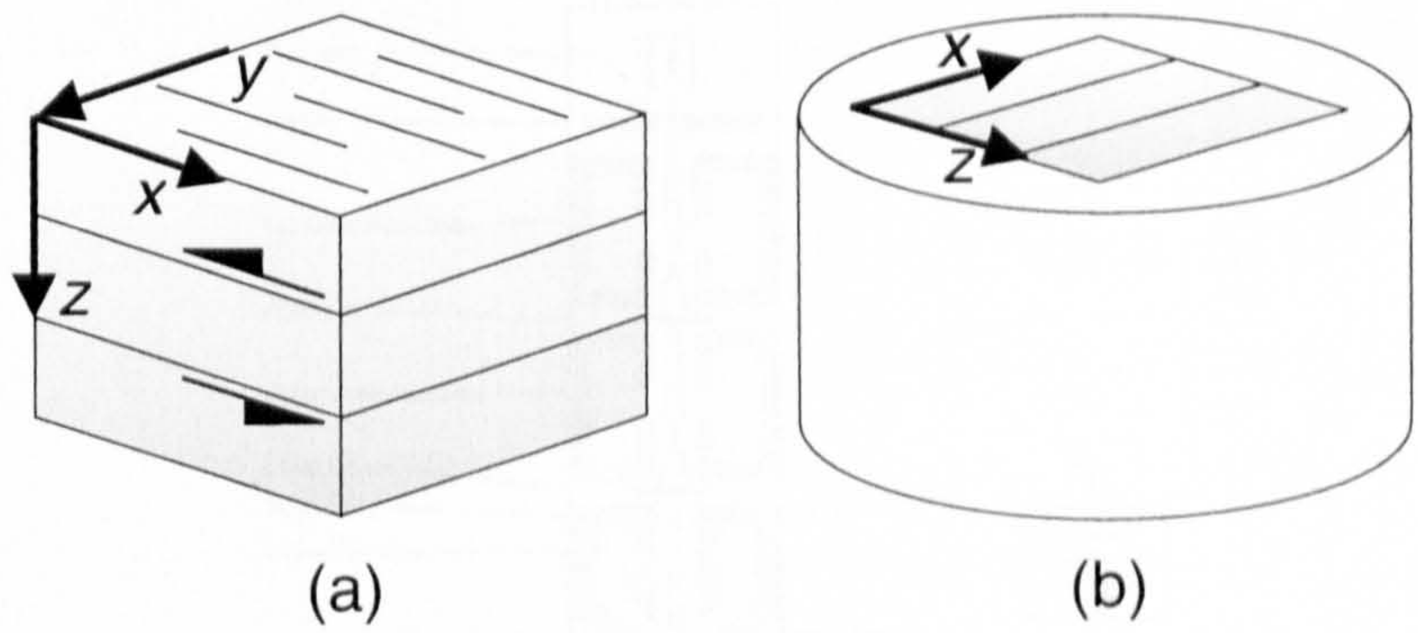

Figure 3.1: An illustration of the chosen sample reference frame. (a) Samples are cut in a kinematic reference frame whereby X is parallel to the mineral stretching lineation, and XY is parallel to the plane of foliation. (b) Samples are mounted into SEM blocks exposing the XZ plane, the profile plane to the shear zone for that sample.

The scanning electron microscope (SEM) is a versatile tool in high resolution imaging. The SEM is capable of imaging rock samples in a number of modes including topographic (secondary electron imaging, SE), qualitative lattice orientation (orientation contrast imaging, OC), and authigenic grain evolution and overgrowths (cathodoluminescence imaging, CL), in addition to microstructural imaging, or so-called atomic number, or Z-contrast imaging. Both OC and Z-contast modes utilise backscatter electron imaging (BSE). Such imaging modes can resolve detail to 10-100nm, highlighting the advantage over optical microscopy.

The standard setup of an electron microscope column for imaging modes is illustrated in Figure 3.2. In its most simplest, the SEM consists of an electron source, and a series of apertures and electromagnetic lenses that control the intensity and size of the electron beam through the column prior to interaction with the specimen.

Incident electrons undergo a series of elastic and inelastic scattering events within the sample surface as electrons interact with target atoms. Such interactions alter the trajectory and energy of electrons such that they diffuse through a volume of the specimen until their energy falls and they are 'absorbed' by the sample material, or they are ejected at the free surface. The envelope of zero en-

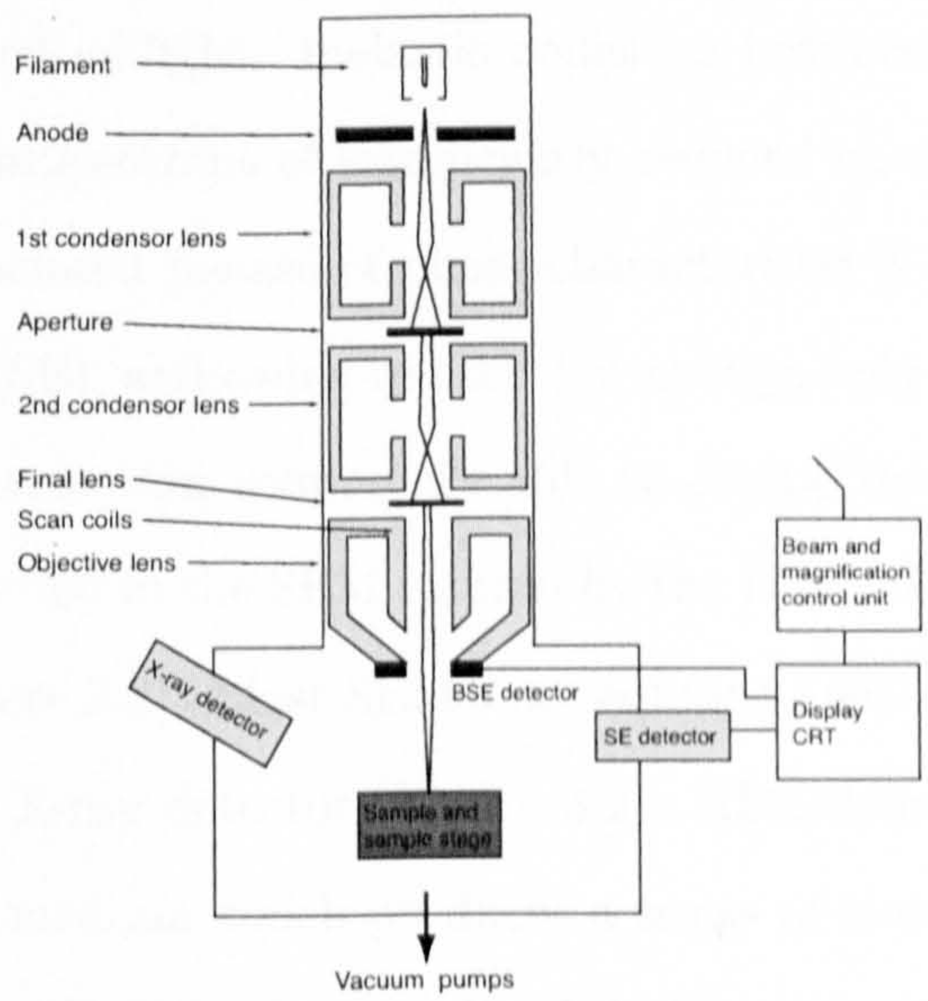

Figure 3.2: A schematic representation of a standard SEM column configured for normal imaging modes.

ergy incident electrons defines the 'interaction volume', whose exact diameter is a function of the energy of the incident beam electrons and the composition of the target, and is typically 1-3μm. A number of interactions between incident electrons can be distinguished within this volume. Elastic collisions alter the trajectory of beam electrons without significant change in energy. Where the deflection of the electron trajectory is large, in excess of 90° in a single event or a series of smaller deflections, then they can escape the sample surface as high energy backscatter electrons (BSE). The degree to which high energy beam electron trajectories are altered, and hence the fraction of BSE electrons leaving the sample, is a function of the sample composition, in particular the average atomic mass, Z, and to some degree its crystal lattice orientation. Hence, BSE imaging is often referred to as either Z-contrast imaging or orientation contrast imaging (OC), where it is used to map compositional phases within a sample or to provide a qualitative indication of their lattice orientations relative to one another, respectively. Cathodoluminescence (CL) is visible light emitted due to the action of incident electrons raising bound electrons to higher energy levels. On returning to their original shell, ex-

cess energy is released as light. Inelastic collisions between beam electrons and target atoms result in electrons of significantly reduced energy in an altered trajectory, and the associated release of phase-characteristic X-radiation. These are secondary electrons (SE), and owing to their low energy, only those generated near the surface of the interaction volume are able to escape the sample free surface. Such signals are recorded in the SEM column by the BSE, SE and X-ray detectors respectively (see Figure 3.2). Most SEM's are equipped with an energy dispersive spectrometer (EDS) X-ray detector (Figure 3.2). EDS detectors employ a solid-state semiconductor medium which produces a series of electrical pulses that are proportional in size to the X-ray energy (Reed, 1996). X-ray energy is proportional to the elemental composition of target sample. Thus, pulses are sorted according to their energy and flux to give a spectrum of peaks which provides an essentially qualitative indication of elemental abundance. The use of X-ray data are discussed further in Section 3.3.

3.3 Quantitative microgeochemistry by EMPA

Quantitative characterisation of aggregate LPO by EBSD (Section 3.4), requires the input of data pertaining to the crystal structure and elemental composition of constitutive mineral phases of the sample aggregate. Increased accuracy in EBSD can thus be attained where these phases are tightly constrained such that the most representative crystallographic data can be used. Electron microprobe analysis (EMPA) forms an accurate and efficient means of microgeochemical analysis for this purpose, and is thus summarised here, sourced from a thorough account in Reed (1996) and discussions with Dr. Eric Condliffe, University of Leeds.

The electron microprobe is similar to the SEM but is designed specifically for compositional analysis.

As the incident electron beam strikes the sample surface, it penetrates the interaction volume. Within the this volume, the combination of electron interactions

with target atoms generate a range of X-ray radiation. Two main groups of X-rays are produced: background or continuous X-rays, and characteristic X-rays. The former group are non-specific and pose a hinderance to the accuracy of EMPA by masking the signature and intensity of characteristic X-rays. They are produced by the quantum jump of an incident electron to a lower energy state, during elastic scattering, which is associated with the release of an X-ray photon. As unbound electrons occupy a continuum of energy levels, the released photon may also possess any energy in a continuum, up to the energy of the initial electron, E_0. Characteristic X-rays are produced during the inelastic interaction of incident electrons with target atom electrons. Most important in EMPA are those involving the innermost, or K-shell electrons. Where the energy of an incident electron is greater than that of the critical excitation energy of the K-shell, E_K, then the bombarding electrons have the potential to ionise an atom. The critical excitation energy is a function of the atomic mass of an atom, and represents the energy required to overcome the attractive force between an atomic nucleus and its shell electrons. Where a K-electron is removed, the net positive charge is balanced by the jump of an electron from a lower energy shell: a process associated with the release of an X-ray photon whose energy is equivalent to the energy difference between the two electron shells involved, for example K and L, and is characteristic of that elemental atom. The jump of electrons between energy shells continues between increasingly lower energy levels, until the charge is balanced by a captured free electron. Hence, quantification of characteristic X-rays has the potential for quantifying elemental composition of the target material.

Quantitative EPMA thus records mineral phase composition from the measurement of the abundance of its fractional elemental components, as recorded by the characteristic X-ray distribution. This is most accurately and efficiently achieved through wavelength dispersive spectrometry (WDS). The EPMA column is fitted with at least three WDS detectors that each record the X-ray emissions from the

target sample with high spectral resolution over a specific wavelength range. Each WDS detector comprises a crystal mirror and X-ray detector which are geometrically coupled to the X-ray source, i.e. the sample.

X-rays will be reflected by the crystallographic planes of the crystal mirrors, where the angle of incidence of the radiation (θ) and the interplanar spacing of the reflecting crystal (d) are such that the Bragg condition is satisfied:

$$n\lambda = 2d\sin\theta \tag{3.1}$$

where n is an integer, the so-called order of diffraction, and λ is the wavelength of the incident electron beam energy, an inverse function of the SEM accelerating voltage. That is, the difference in wavepath length between two rays reflected off adjacent crystallographic planes must be an integer multiple of the wavelength for Bragg reflection (Figure 3.3). Reflections of the first order, where $n = 1$ are most intense and therefore important in WDS analysis.

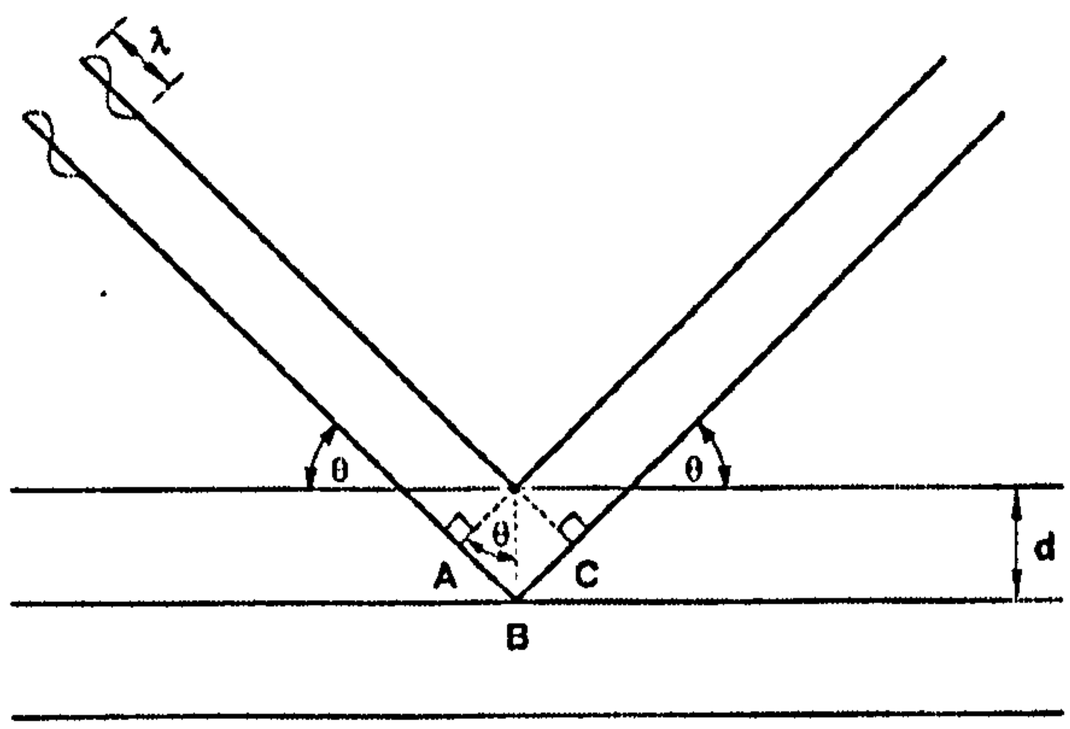

Figure 3.3: Diagrammatic representation of Bragg's condition. Highest intensity reflection on crystallographic planes of interplanar spacing d will occur at an angle of incidence θ, where the distance ABC is an integral number of X-ray wavelength $n\lambda$. From Goldstein et al. (2003)

It can be seen from Equation 3.1 that for a given value of n and d, there is a limited range of wavelengths that can be analysed. That is, limiting ($\sin\theta$) to a

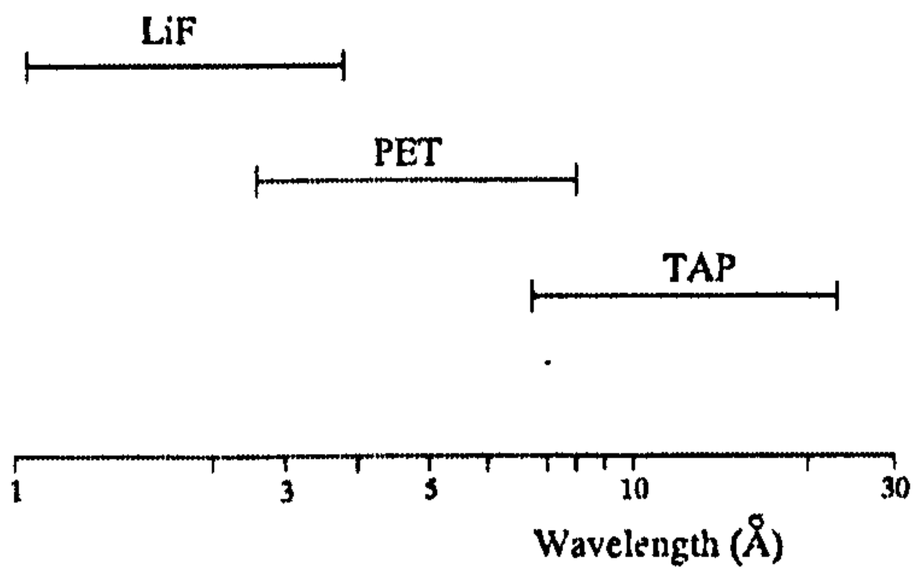

Figure 3.4: A graphical presentation of the wavelength coverage of crystal mirrors used for Bragg reflection in wavelength dispersive spectrometers. From Reed (1996).

Crystal	*d*(Å)
LiF	2.013
PET	4.371
TAP	12.95

Table 3.1: Crystal mirrors and their associated interplanar *d*-spacings commonly used in wavelength dispersive spectrometry. From Reed (1996).

maximum of 1 restricts the longest diffracted wavelength to $2d$. Hence, a number of different WDS reflecting crystals of pure and specific composition are used, each with a unique and known d-spacing (Table 3.1), which collectively permit a range of X-ray wavelengths to be measured. These are shown in Figure 3.4, illustrating the full spectrum of wavelength coverage. Within each of the three WDS detectors, the reflecting crystal and detector are coupled and able to move along a motorised linear track whilst satisfying the condition that the sample, crystal reflector, and detector lie on the circumference of a so-called focussing circle, or Rowland circle, providing a constant Bragg angle. This effectively varies the incident angle, increasing the range of wavelengths detected with that crystal (Figure 3.5). Furthermore, spectrometer crystal surfaces are ground to a radius of curvature of the focussing circle, r, with crystal planes bent to a raduis of curvature $2r$. This geometry permits X-rays to have the same angle of incidence over the entire surface of the crystal, and focussing on a single point at the detector. Clearly, this increases detector efficiency and signal detection. The intensity of the reflected signals are recorded by a proportional counter and processed to provide quantitative compositional data.

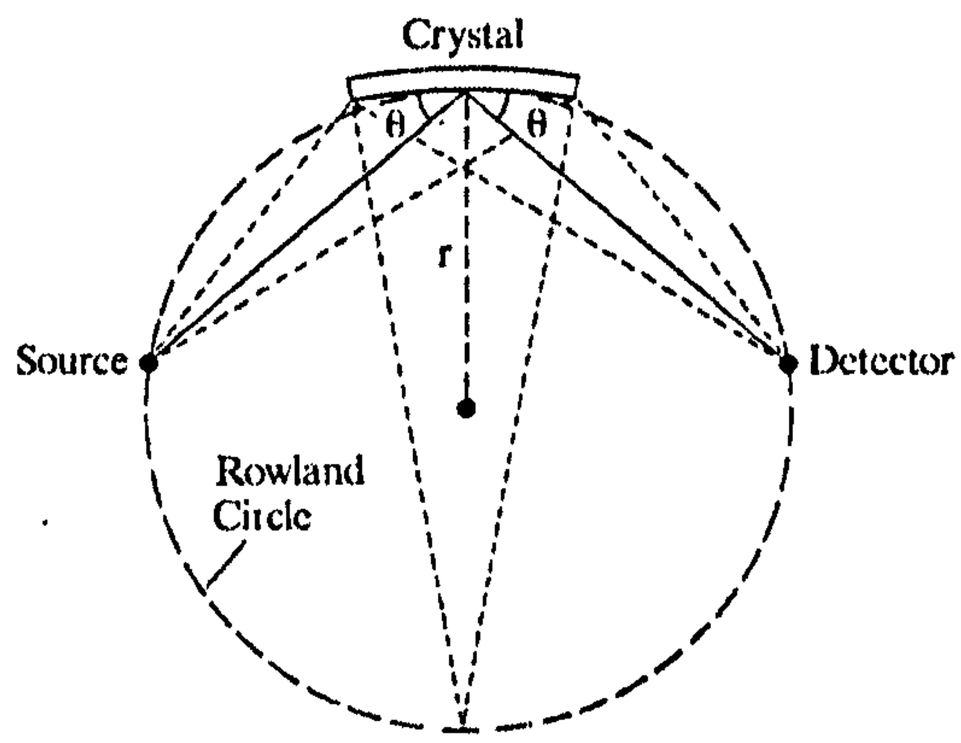

Figure 3.5: The principle of the focussing, or Rowland, circle in WDS detectors (see text). θ is the Bragg angle and r is the radius of the focussing circle. From Reed (1996).

3.4 Petrofabric determination by EBSD

Electron backscatter diffraction (EBSD) in the SEM provides a time-efficient method of retrieving high-resolution and accurate crystallographic orientation data for the constituent mineral phases of rock aggregates. Prior et al. (1999); Lloyd (2000); Randle (2003); Wendt et al. (2003) provide exhaustive accounts of EBSD procedure and application, and form the resource from which the following overview is sourced.

The experimental setup for EBSD is very different from that of more routine imaging modes in the SEM, and is illustrated in Figure 3.6. Within the interaction volume a percentage of electrons interact with target atoms in elastic and inelastic scattering events to generate, essentially, point sources of divergent electrons. Scattered electrons that interact with lattice planes at an angle such that the Bragg condition is satisfied will be diffracted by those planes (Equation 3.1).

In three dimensions, the trajectories of scattered electrons that satisfy the Bragg condition, i.e. those that are diffracted along lattice planes, form paired large angle cones (Figure 3.7). Bragg angles of diffraction are typically small (~0.5°) and so cone opening angles approach 180° and can hence be approximated as planes. The manifestation of this phenomenon upon interception with the phosphor screen

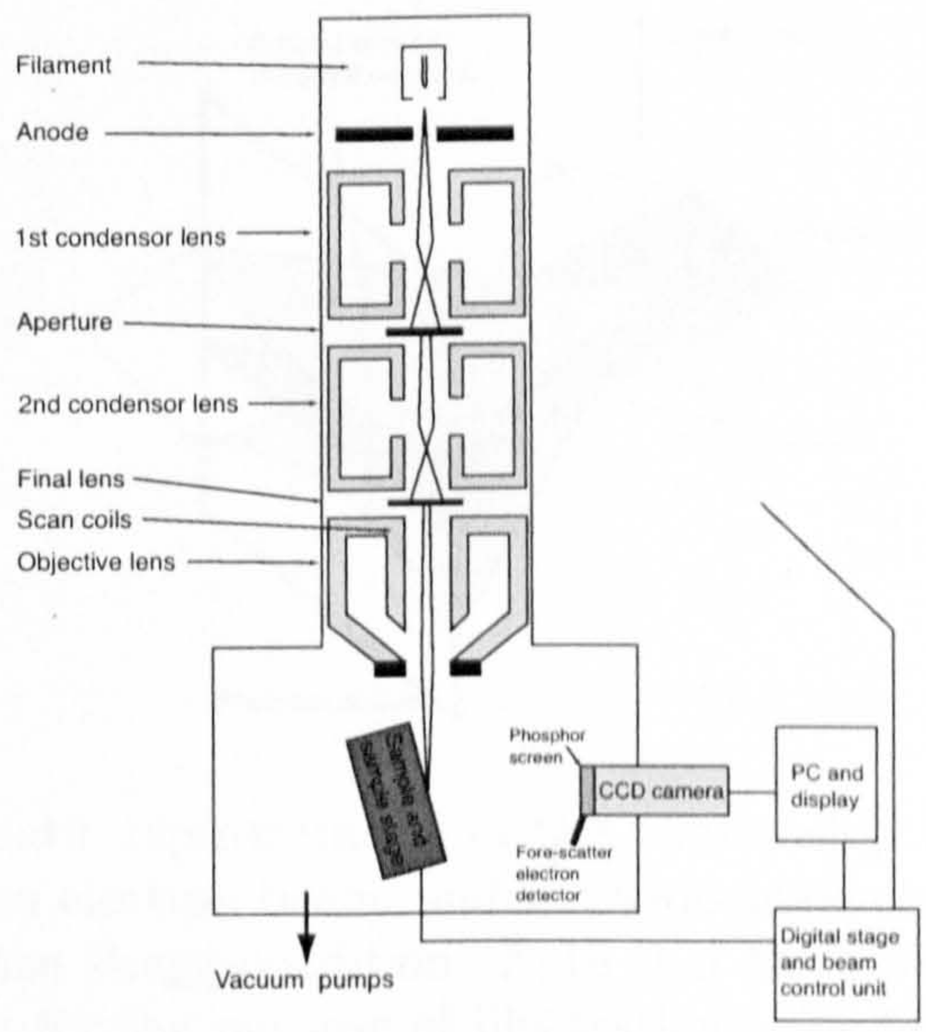

Figure 3.6: A schematic representation of the configuration of an SEM for EBSD. A phosphor screen and CCD camera are wound into the sample chamber for the purpose of EBSP capture. The sample and stage are held at a high angle (75°) to the incident electron beam to maximise diffraction. Fore-scatter electron (FSE) detectors detect BSE when the sample surface is at a high angle to the BSE detectors.

within the SEM are the so-called Kikuchi bands: pairs of apparently parallel and straight lines that define a band, the bisector of which is a projection of a lattice plane (Figure 3.6 and 3.7). In a crystalline target, diffraction of scattered electrons may occur on multiple lattice planes simultaneously. These form a complex pattern of intersecting Kikuchi bands called electron backscatter diffraction patterns (EBSP's), whereby bands represent lattice planes and band intersections are projections of crystallographic axes. Each EBSP is unique for a particular target material and for the lattice orientation in space of the infinitesimal interaction volume of material beneath the electron beam.

A digital image of the EBSP is captured from the phosphor screen by a sensitive charge coupled device (CCD) video camera. From these, bespoke commercially available software (e.g. *Channel*, from HKL Technologies) provide an efficient and user-friendly interface for the acquisition and processing of crystallographic phase and orientation data.

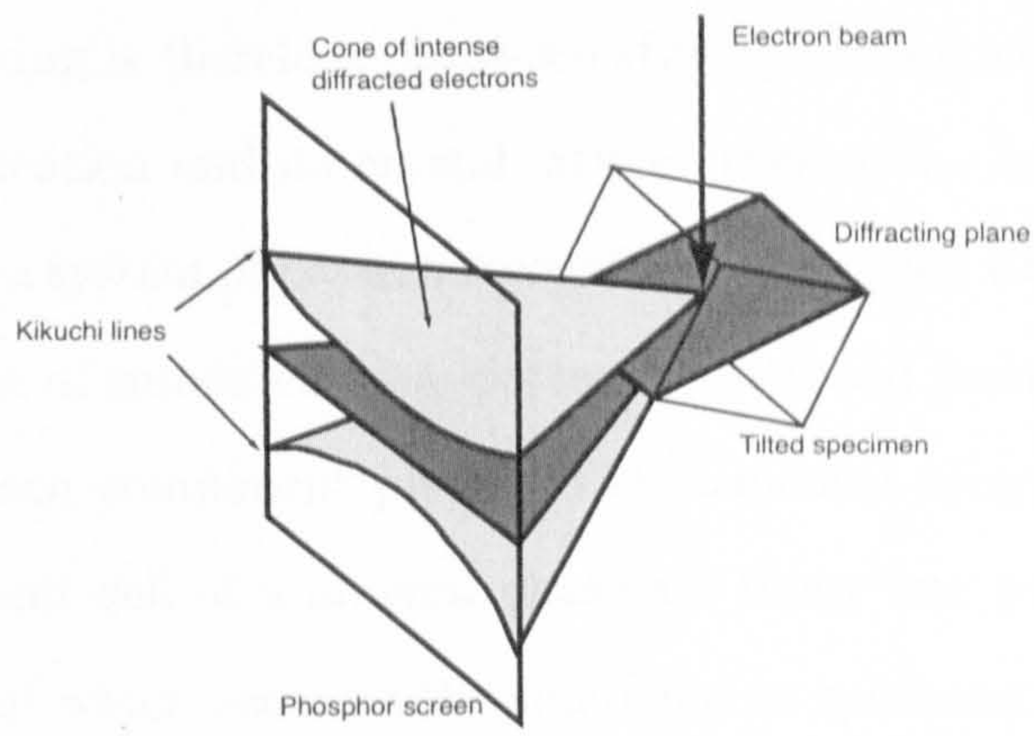

Figure 3.7: A schematic representation of the relationship between a diffracting lattice plane under an electron beam, and the wide-angle cones of diffracted electrons which satisfy the Bragg condition. Note that the curvature of the Kikuchi bands is exaggerated for the purpose of illustration. The bisector of the Kikuchi lines is the projection of the diffracting plane, (hkl). Modified from Day (1993).

The EBSP is analysed by the software via the Hough Transform. This converts lines in EBSP space (x,y) to points in Hough space (ρ,θ) according to:

$$\rho = x\cos\theta + y\sin\theta \tag{3.2}$$

where a line or band in EBSP space can be considered in terms of the perpendicular distance (ρ) between that band and the origin, and the angle (θ) that the perpendicular makes with the x-axis.

Point maxima in Hough space are more easily localised by the software than raw EBSP bands, and are used to reconstruct the original EBSP. Together with system calibrations such as specimen-to-screen distance and specifics of the screen and sample reference frames, the angular relations between sets of Kikuchi bands, band intensity and band width are included in algorithms to determine the orientation of the crystal lattice at the point under the electron beam for that target material. This process of EBSP analysis to determine crystallographic orientation is termed 'indexing'. Because EBSP's are a function of specific unit cell structure and composition, they are therefore unique to the target material in addition to its

orientation. Indexing is therefore phase-sensitive, providing coupled data of mineral phase identification and its crystal lattice orientation. In its most simplest, indexing relies on a system of pattern recognition. Recorded EBSP's are compared against a database of simulated ideal patterns calculated from atomic and lattice information for each component phase. The elemental composition and atomic structure of the unit cell of a mineral phase are input into software (e.g. *Twist*, HKL Technologies) which generate the simulated or synthetic EBSP's for the full three-dimensional range of possible orientations of that phase in space. By characterising the precise elemental composition of component mineral phases in a rock sample using EMPA, a database of simulated EBSP's can be created and uploaded into the EBSD indexing software prior to experimentation. This provides a more constrained, accurate and sample-specific database of Kikuchi band patterns for the indexing software to compare experimental EBSP's against, further increasing the efficiency, accuracy and speed of EBSD analysis. Thus, subsequent to EMPA analysis of the sample suite, a set of new theoretical EBSP files were generated via *Twist* for each of the major component phases of the aggregates, specific to the mineral composition and structure in their respective solid solution series (see Section 4.1). References to crystal structures and compositions used in generating EBSP database files for this research are given in Table 3.2. Petrological and microgeochemical support is provided in Chapter 4.

Mineral phase	Reference to unit cell parameters
Hornblende (ferropargasite)	Oberti et al. (1993)
Plagioclase (An38, andesine)	Steurer & Jagodzinski (1988)
Plagioclase (An25, oligoclase)	Phillips et al. (1971)
Quartz (α-phase)	Sands (1969)
Clinopyroxene (diopside)	HKL Technologies

Table 3.2: References to unit cell structures and elemental compositions used in EBSP database (*Twist*) files for EBSD.

The crystal lattice orientation is described by three Euler angles (Bunge, 1982):

three sequential angular rotations that describe the spatial transformation from the fixed sample reference frame and the unfixed lattice reference frame. The three rotations are order specific: (1) φ_1 about z_s ($\leq 360°$), (2) Φ about x_s ($\leq 180°$) and (3) φ_2 about z_s ($\leq 360°$), where the subscript s refers to axes in the sample reference frame, and sequential axial rotations must be considered in terms of the previous rotation(s). All rotations are clockwise when viewed towards the origin from positive x_s or z_s, in a left-handed coordinate system with x_s at 'north' and y_s 'east'.

Modern EBSD analysis is fully automated. Limiting coordinates defining the sample area of interest are input by the user, in addition to the step size between indexing points, depending on the desired relsolution. The indexing software then controls the mechanised sample-mounting stage in the SEM, analysing points at defined intervals within the desired sample coordinates. Although rock samples used in EBSD are relatively small in area at $10\times10mm$, they are considered large enough with respect to grain size (where grain size is $\ll 1mm$, Section 4.1) for compositionally homogeneous samples such that the mineral phase and lattice orientation distribution is sufficiently quantified. An automated-EBSD experiment can result in the acquisition of hundreds of thousands of lattice orientation data across a single $10\times10mm$ sample, depending on step size.

The output of an automated-EBSD experiment using the *Channel* indexing software is a Channel-version text file (**.ctf*). This file contains data on phase identification (from a user-defined list) and lattice orientation (as Euler angles) at each coordinate point in the grid defined by the sample area and analysis step size. A selection of statistical data is also provided, such as the band contrast — a grey-scale value pertaining to the physical quality of the EBSP image, where increasingly white shades represent better quality captured EBSP images. This test allows apparently erroneous data to be assessed against the quality of the captured EBSP image from which it is derived. Where the EBSP image quality

is very poor, the indexing software may be unable to match that EBSP with a theoretical one, and the coordinate is either not indexed or more problematically is 'mis-indexed'. A further statistic, the mean angular deviation (MAD) indicates the angular difference between the experimentally observed EBSP and the best-fit theoretical pattern for that phase and lattice orientation. MAD's > 1 are considered erroneous. Mis-indexed patterns tend to have relatively high MAD's (> 1) and can hence be removed from the data set.

EBSD analysis at the University of Leeds employs a CamScan Series 4 vertical column SEM, where the sample stage is tilted to 75° to optimise electron diffraction. Experiments are conducted with a $20keV$ accelerating voltage and a sample current of $20nA$ (note that beam current cannot be measured directly in the SEM at Leeds). EBSD experiments are conducted with a indexing step size of $25\mu m$ over the sample area, which provides a significant data set with which to accurately assess the bulk LPO of constituent mineral phases of the rock aggregates.

Combining EMPA and EBSD thus provides an efficient and accurate means of collecting statistical data sets of petrofabric information, or more specifically, characterising the crystal lattice orientation distribution of constituent mineral phases of aggregates. Chapter 4 continues the work-flow model by presenting observations and results of petrofabric for the sample suite, including those derived from techniques described here.

Chapter 4

Analysis of petrofabric

A comprehensive qualitative and quantitative description of the petrology and petrofabric for the suite of study samples is presented herein. Section 4.1 provides a petrographic description of the sample suite. This is not a detailed account of the igneous and metamorphic history of the unit, but rather a qualitative indication of the compositional and petrofabric development across the sampled strain gradient in order to provide the reader with context for the quantitative LPO data of Section 4.4. It is also considered appropriate here to present and discuss a further method of calculating a strain profile across the deformation zone and sample suite at Upper Badcall, from microstructural data. This method, and the approach outlined in Section 2.3, are discussed critically. In addition, an error analysis in the calculation of strain is investigated. The chapter closes with a discussion of deformation and strain partitioning in polyphase and polycrystalline aggregates in the context of petrofabric results presented herein. Chapters 5 and 6 follow with the application of the quantitative evaluation of petrofabric acquired here in the calculation of seismic properties for the sample suite, and hence the calibration of seismic properties against finite strain.

4.1 Petrology & microgeochemistry

4.1.1 Undeformed material

Sample numbers refer to those of Figure 2.3. The undeformed wall-rock Sample 1 is characterised by an original igneous granular texture of subhedral 1-3mm grains (Figure 4.1). The rock is dominated by hornblendic (*s.l.*) amphibole (Figure 4.2) and andesinic plagioclase feldspar (Figure 4.3), with a lesser percentage of quartz and remnant salitic clinopyroxene (Figure 4.4). Accessory phases include ilmenite, titanite, apatite, and chlorite, which together constitute a fractional contribution of the total modal distribution and can be ignored for the purpose of this work, whereby their contribution to the bulk physical and seismic properties of the rock will be insignificant. Relative modal fractions for the major mineral phases, determined by phase-sensitive EBSD indexing (Section 3.4) are shown in Table 4.1. The aggregate is best described as a quartz-dolerite and can be approximated as a hornblende-plagioclase-quartz±clinopyroxene aggregate (consistent with Sutton & Watson, 1951; O'Hara, 1961).

A texture is often observed in amphibole phase grains whereby a core of partially recrystallised amphibole with anhedral and very fined grained ($10 - 50\mu m$) quartz is mantled by a more pristine amphibole phase (Figure 4.1(b)). The rim phase appears to have a different composition to that of the core, as suggested by a deeper green colour and more extreme pleochroism in plane polarised light. Electron microprobe analysis of amphibole grains for this sample (Figure 4.2) provides support to this observation, indicating magnesiohornblendic grain cores that are relatively deficient in Al and Fe^{2+}, and relatively enriched in Mg, compared to ferropargasitic grain mantles and rims. This texture and elemental distribution is likely a manifestation of disequilibrium during the retrogressive P-T history of the dyke since intrusion. That is, initial breakdown of clinopyroxene to hornblende proceeds with uninhibited elemental exchange between grain and matrix,

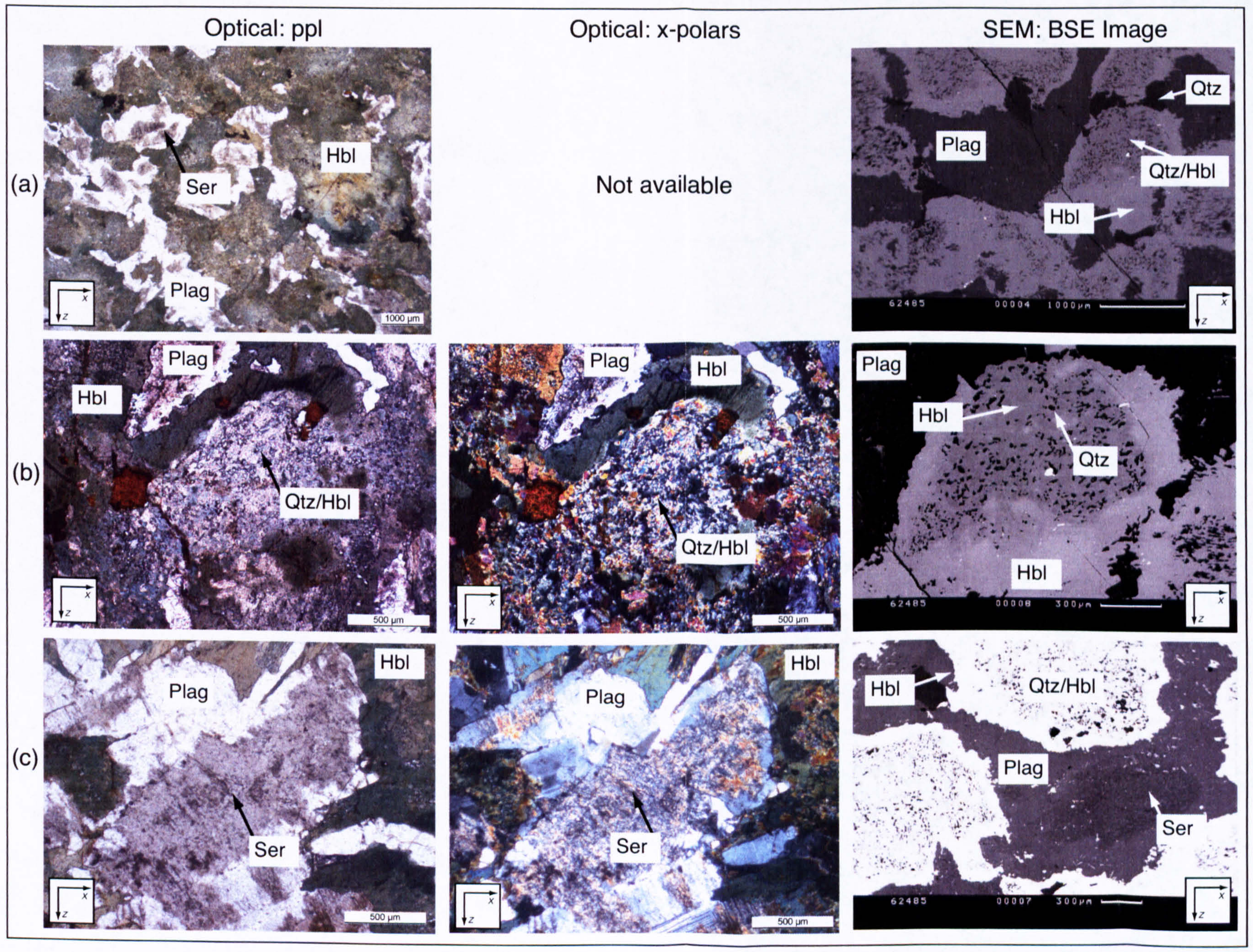

Figure 4.1: Optical and BSE micrographs of pertinent microstructures, Sample 1. (a) Original igneous texture. Crossed-polar images are not available for low-magnification optics. (b) Disequilibrium texture of hornblende grains with cores of fine-grained magnesiohornblende and quartz, and ferropargasitic rims. This compositional variation is particularly clear in the Z-contrast SEM image. (c) Example of sericitised plagioclase grain cores. Scale and the kinematic reference frame is indicated on each figure. Hbl = hornblende, Plag = plagioclase, Qtz = quartz, and Ser = sericite.

with silica released as quartz. The balance of calcium and aluminium during this complex reaction cannot be fully accounted for by elemental exchange with plagioclase, whereby excess calcium from clinopyroxene, and the requirement for extra aluminium necessary in reaction from clinopyroxene to hornblende is not substantiated in the core to rim chemical variation in the plagioclase phase (Figure 4.5). An open system must therefore have prevailed, with elemental exchange with a fluid phase.

At some point, the boundary between clinopyroxene and hornblende stability fields must have been sufficiently overstepped such that remaining clinopyroxene reacted to hornblende relatively rapidly, with the length scale of diffusion becoming limited, giving a grain core texture of much finer grain size relative to the rim, with *in situ* crystallisation of quartz and comparatively Al-deficient magnesiohornblendic amphibole. Occasionally, relict clinopyroxene can be observed in grain cores. EMPA analysis indicates a composition in the salite field (Figure 4.4).

Whether the driving force for this clinopyroxene breakdown to hornblende is due to post-crystallisation auto-metamorphism, or more regional Laxfordian retrogression (Sutton & Watson, 1951; O'Hara, 1961), is not clear. Indeed, it may be some combination of the two.

Core-to-rim compositional variation in plagioclase is commonly observed (Figure 4.5) although the magnitude and direction between more sodic and calcic varieties is not consistent. This may be a reflection of the influence of fluid phases in an open system during or after metamorphism, selectively altering an original igneous normal zoning. Alternatively, it may reflect localised cation exchange between clinopyroxene and plagioclase in its breakdown to hornblende. Discrimination between the two hypotheses cannot be fully substantiated without further detailed analysis, which is beyond the scope of the objectives here. Repeated albite twinning is also observed.

Sericitisation of plagioclase cores is a common feature (Figure 4.1(c)), where

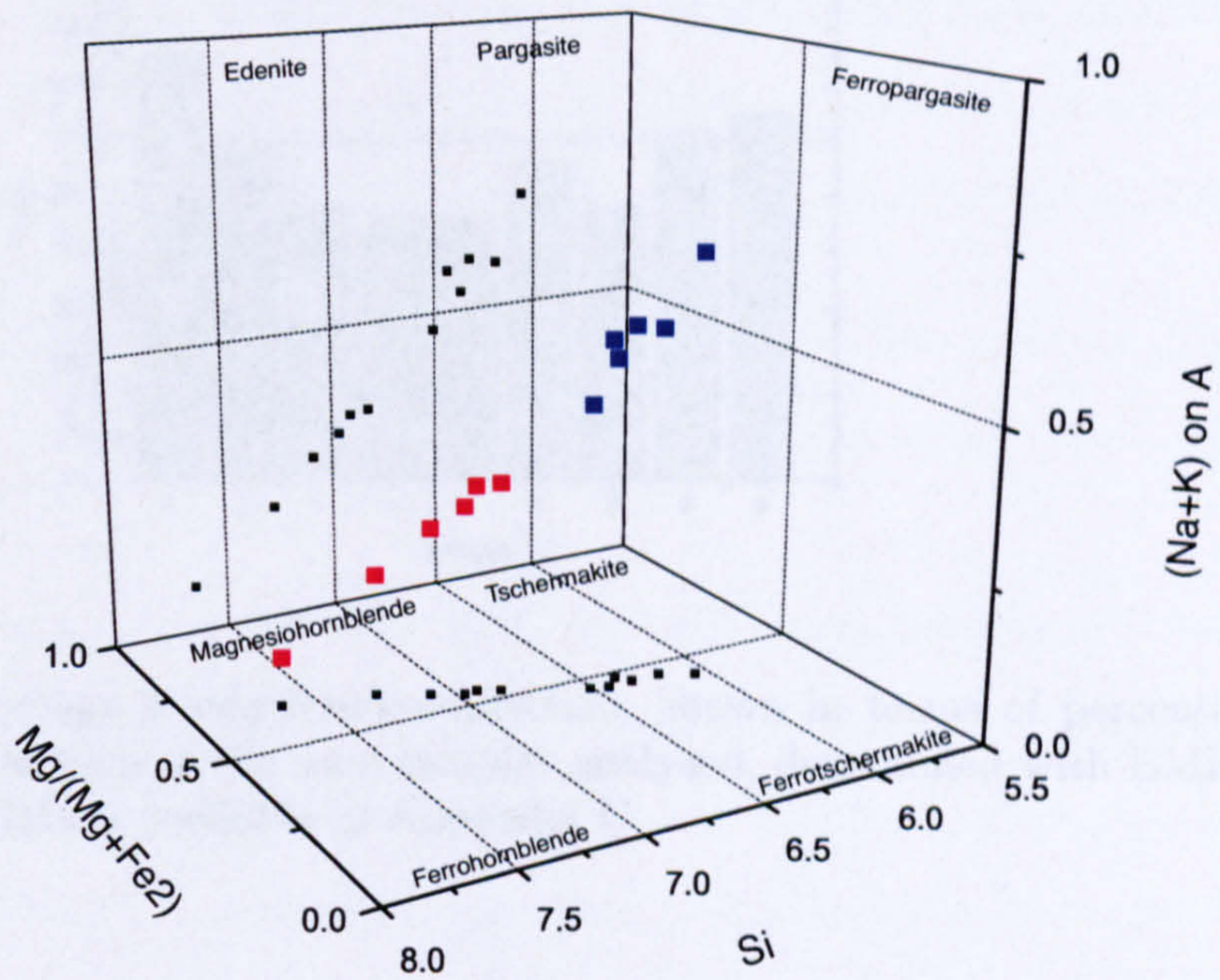

Figure 4.2: A plot of EMPA data for Sample 1 amphiboles. Red and blue points represent analyses from grain cores and rims respectively. Data points in black are 2D projections of the data. Amphibole chemistry is expressed as a function of (Na+K) in *A* sites, Mg/(Mg+Fe^{2+}), and Si atoms per formula unit. In accordance with IMA nomenclature of calcic amphiboles (Leake et al., 1997), grain core chemistry is that of magnesiohornblende, whilst rim compositions indicates ferropargasite. Tabulated EMPA data is available in Appendix C.

Sample	% Hbl	% Plag	% Qtz	%Cpx
1	52.47	26.56	6.92	14.05
2	71.55	17.73	10.72	-
3	61.13	28.90	9.98	-
4	66.72	21.66	11.62	-
5	77.77	15.54	6.69	-
6	42 38	41.83	15.80	-
7	54.70	24.72	20.57	-
8	62.42	24.78	12.80	-
9	50.64	26.05	23.30	-

Table 4.1: Modal fractions of constituent major mineral phases for Samples 1-9. Values are those determined from phase-sensitive EBSD indexing (see Section 3.4).

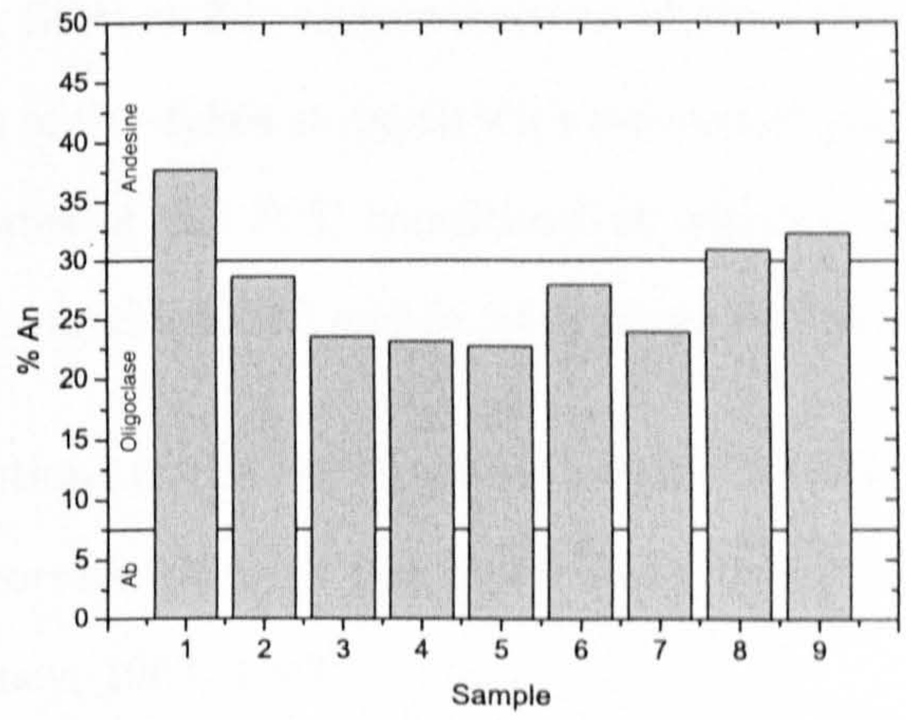

Figure 4.3: The average plagioclase composition, shown in terms of percentage anorthite (%An), for each of the nine samples analysed, determined with EMPA. Tabulated EMPA data is available in Appendix C.

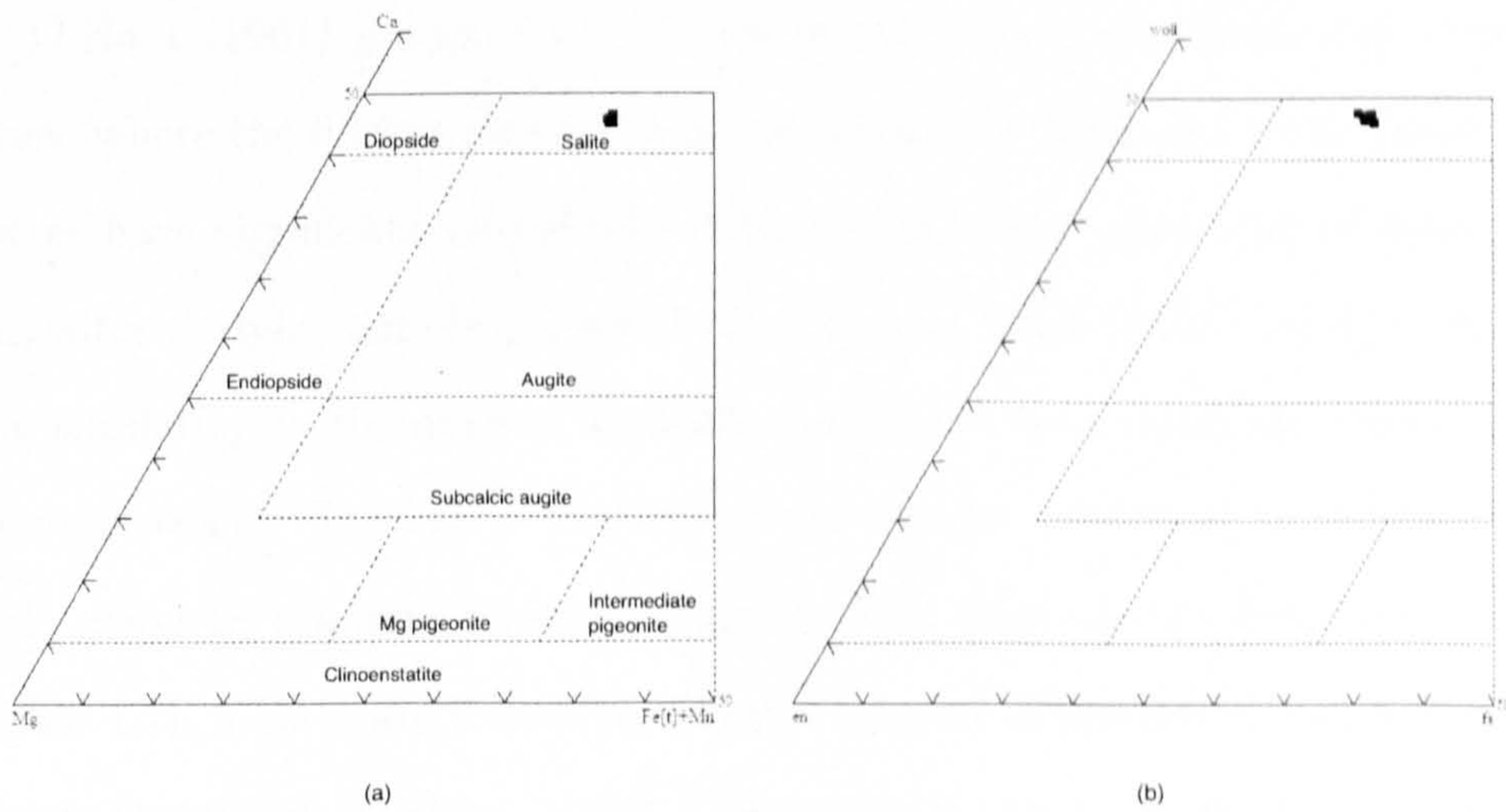

Figure 4.4: A plot of EMPA data for Sample 1 clinopyroxene. Normalised data are plotted on partial ternary plots for pyroxene composition between Ca-Mg-Fe^{2+} (a), and Wollastonite-Enstatite-Ferrosilite end-members (b). Field labels in (a) apply to both plots. The six data cluster in the salite field. Tabulated EMPA data is available in Appendix C.

more anorthitic cores may be preferentially susceptible.

As addressed in Section 2.1, metamorphism of the undeformed dykes is likely related to intrusion of the dykes at depth with associated post-crystallisation metamorphism. Estimates of the P-T conditions at which dykes were intruded and crystallised range from 300-500°C and in >5-6 *kbars* (O'Hara, 1961; Tarney, 1963).

Existing descriptions of the undeformed doleritic Scourie dyke material in this area are in close correlation with the observations described above (Teall, 1885; O'Hara, 1961; Tarney, 1963, 1973).

Teall (1885) describes a fresh sample of dolerite dyke from Scourie, documenting andesinic feldspar, clinopyroxene and secondary minerals including amphibole, with a coarsely crystalline texture, up to $2mm$ diameter. He notes, however, that at the same locality samples show a range of alteration states between clinopyroxene-plagioclase-quartz and hornblende-plagioclase-quartz, where hornblende first mantles and ultimately replaces clinopyroxene.

O'Hara (1961) groups the dolerites in this region into fresh and altered varieties, where the former retain clinopyroxene as the dominant mafic phase, and the latter have significant amphibole at the expense and alteration of clinopyroxene. An altered dyke sample collected close to the Teall (1885) locality bears striking similarity to the dyke at Badcall, dominated by hornblende, plagioclase, and clinopyroxene. The mafic fraction of the sample described in O'Hara (1961) is still richer in remnant clinopyroxene (24.7%) than observed at Badcall (14.1%, Table 4.1). This is attributed to different degrees of alteration and metamorphism across the region (O'Hara, 1961). Observed structures are similar to those seen at Badcall however, including hornblende mantling remnant clinopyroxene.

Tarney (1963, 1973) support the observations of O'Hara (1961) with the additional description of the quartz sieve texture in amphibole cores, where amphibole-quartz pseudomorph original igneous clinopyroxene, as noted for Sample 1. Variation in alteration of dykes across the region, between "fresh" clinopyroxene-

plagioclase assemblages and "altered" amphibole-plagioclase±clinopyroxene assemblages (where plagioclase is typically An20-60, Tarney, 1973) is a function of the metamorphic conditions into which the dykes were intruded and cooled, and the length of time that they remained at those conditions, rather than a later regional metamorphism (O'Hara, 1961; Tarney, 1963, 1973). Details and arguments on the topic of relative dyke alteration are complex and beyond the scope of this thesis, which considers the Badcall rock suite as a deep crustal material in its rawest sense. The finer complexities of Lewisian intrusive and metamorphic history, and detailed regional geochemical comparisons of the Scourie dykes are are generally not required.

Deformed material

Observation of the deformed quartz-dolerite material of the dyke shows a number of textural changes with increasing deformation, towards the high-strain part of the shear zone.

The major and accessory mineral assemblage is as that for the undeformed Sample 1, with the exception of clinopyroxene which is no longer observed. Again, phase-sensitive EBSD indexing (Section 3.4) is considered to be a sufficiently accurate determination of modal distribution, and results for Samples 2-9 are given in Table 4.1. The modal composition is close to that for the wall-rock protolith, Sample 1. EMPA analysis of Samples 2-9 indicates a marginally more sodic composition (oligoclase) for the plagioclase phase in most of the deformed material than that of Sample 1 (Figure 4.3). Amphibole compositions, although clustered, are borderline to each of the subclassifications of hornblende (*s.l.*) (Figure 4.6), where the chemical dichotomy between core and rim presented for Sample 1 is no longer apparent (Figure 4.2 and 4.7). Furthermore, the texture of quartz-rich fine grained cores to amphibole grains (pseudomorphing clinopyroxene) disappears.

Marginal samples at the northern boundary of the shear zone, such as Sample 2,

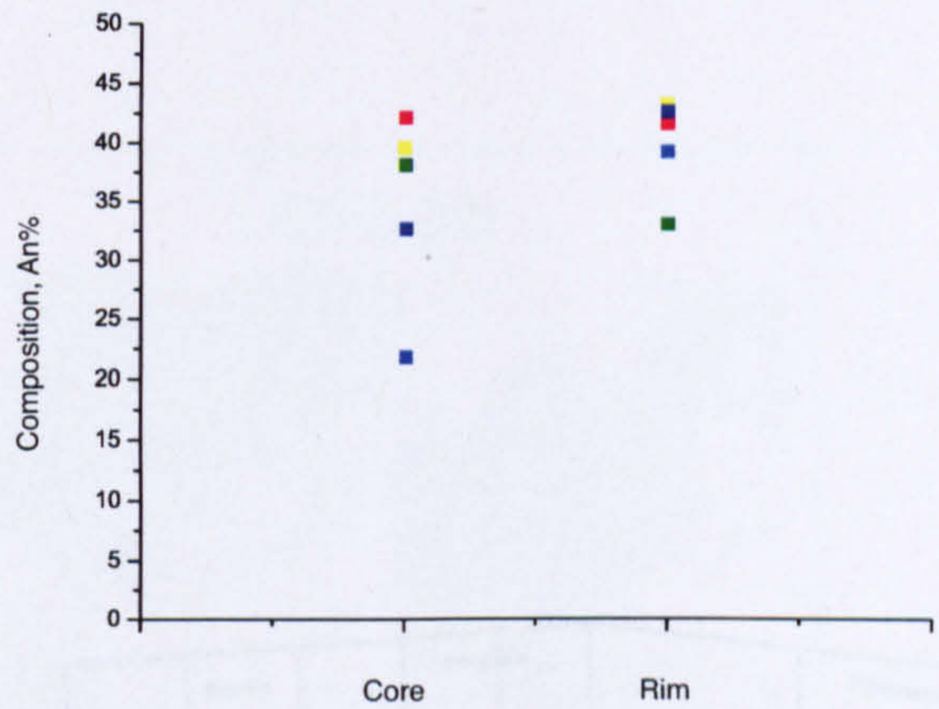

Figure 4.5: A plot of EMPA data for Sample 1 plagioclase. Colours are unique for core-rim analysis pairs in single grains. It can be seen that, in general, grain rims are at least fractionally more anorthitic than their cores, although it is not a strict condition. Tabulated EMPA data is available in Appendix C.

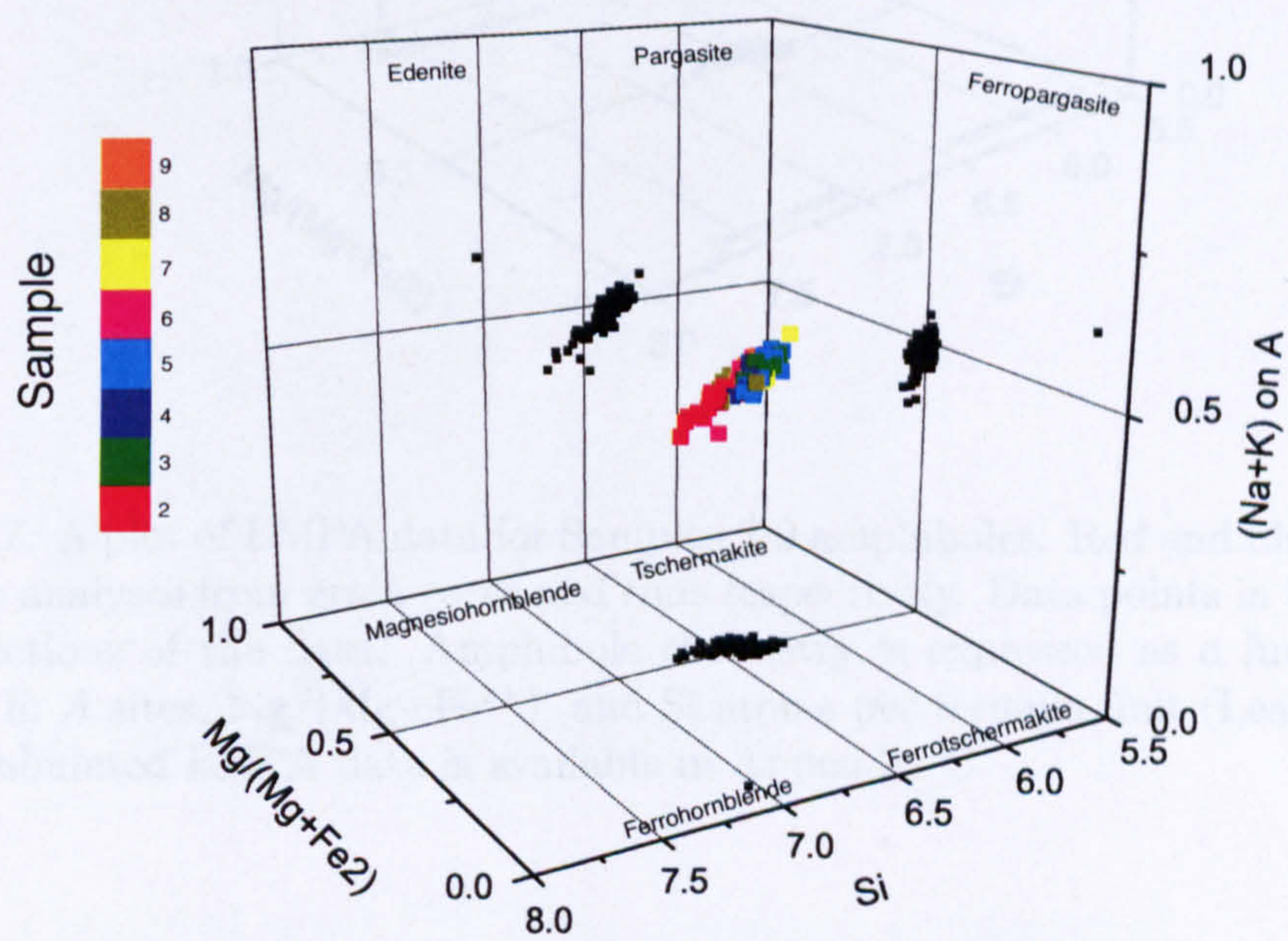

Figure 4.6: A plot of EMPA data for Samples 2-9 amphiboles. Colour scale refers to sample numbers. Data points in black are 2D projections of the data. Amphibole chemistry is expressed as a function of (Na+K) in A sites, Mg/(Mg+Fe^{2+}), and Si atoms per formula unit (Leake et al., 1997). Tabulated EMPA data is available in Appendix C.

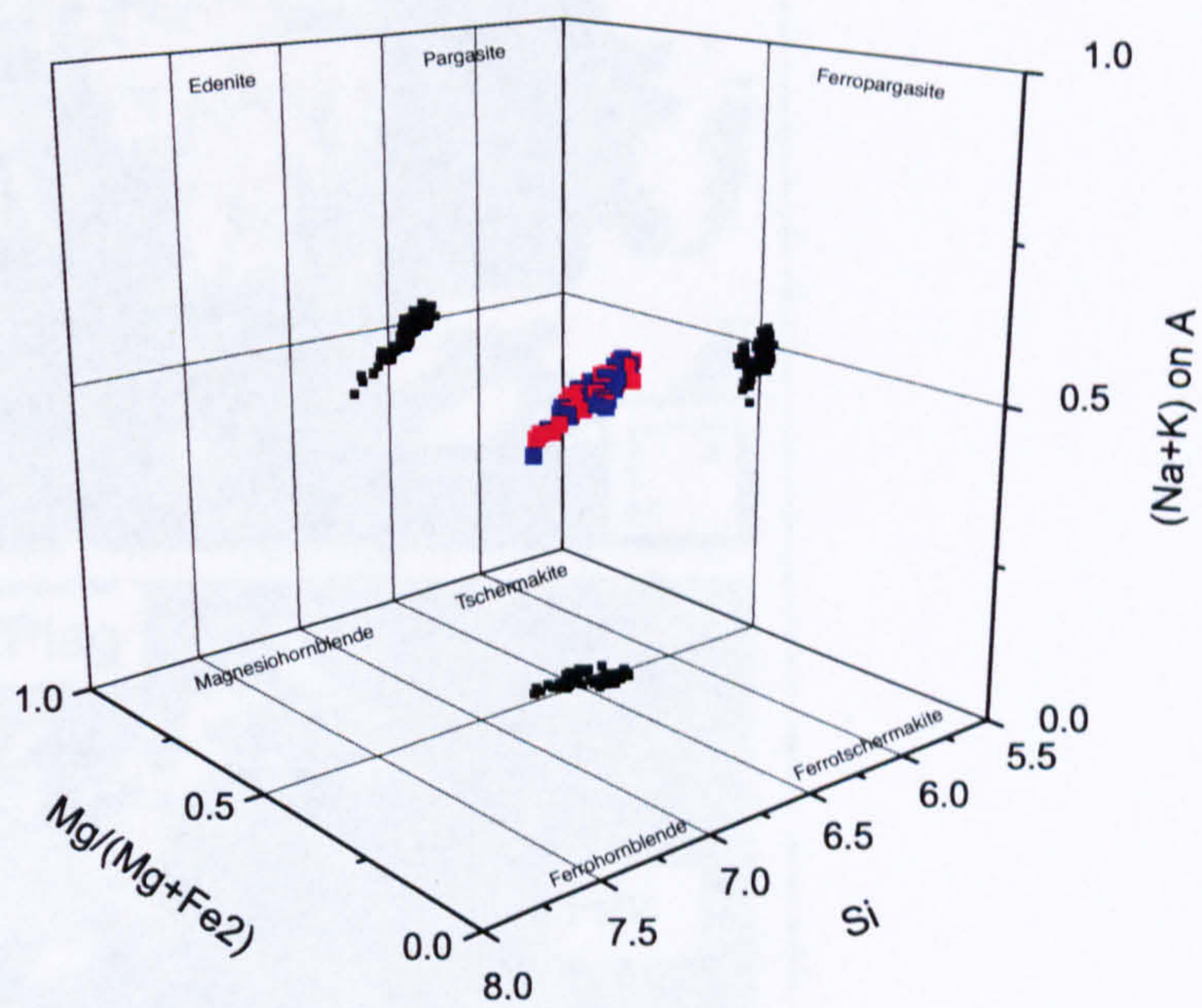

Figure 4.7: A plot of EMPA data for Samples 2-9 amphiboles. Red and blue points represent analyses from grain cores and rims respectively. Data points in black are 2D projections of the data. Amphibole chemistry is expressed as a function of (Na+K) in *A* sites, Mg/(Mg+Fe^{2+}), and Si atoms per formula unit (Leake et al., 1997). Tabulated EMPA data is available in Appendix C.

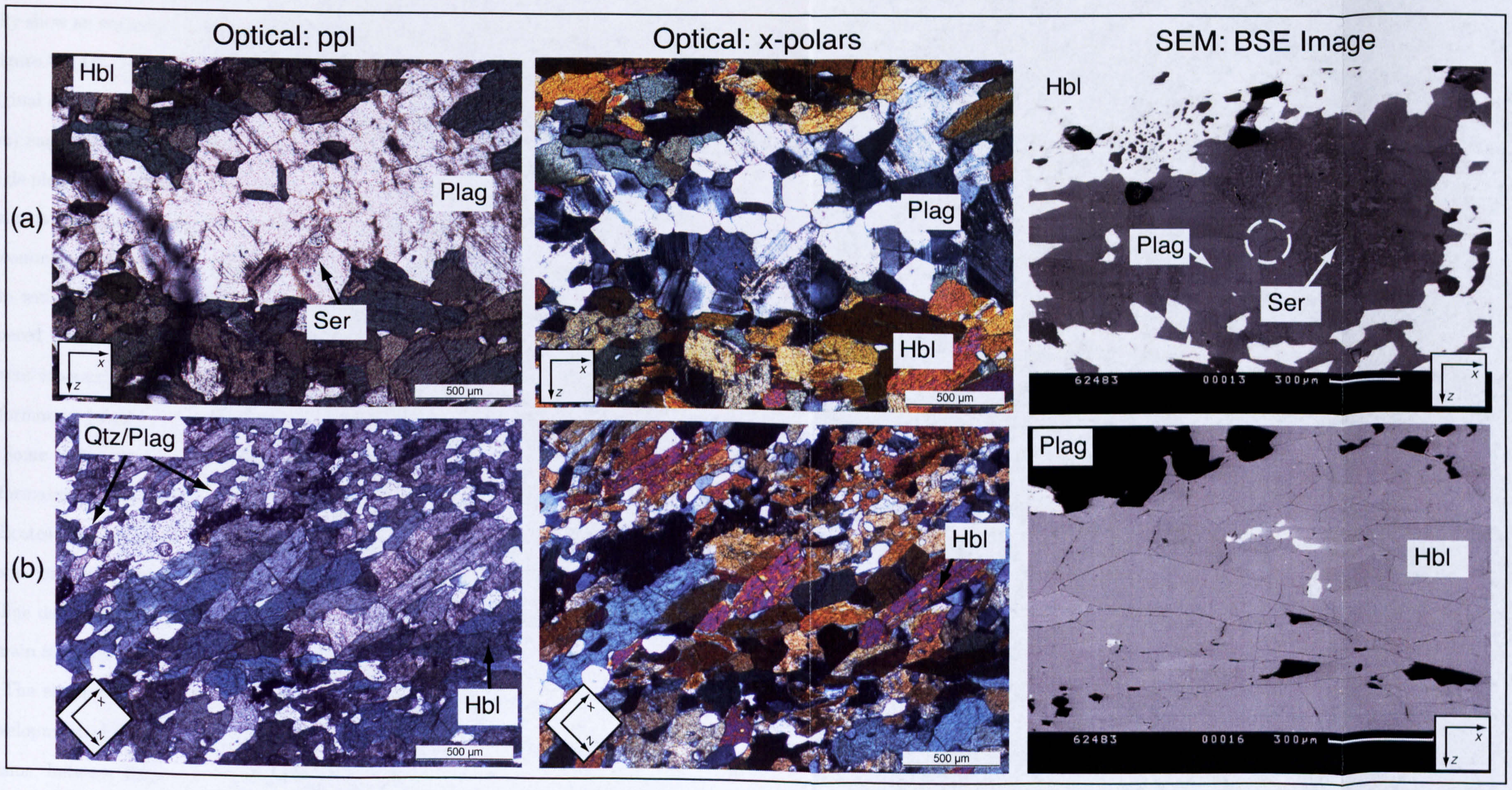

Figure 4.8: Optical and BSE micrographs of pertinent microstructures, Sample 2. (a) Felsic clot showing internally equant polygonal texture, with 120° interfacial angles (circled). The clot as a whole shows a weak X-parallel shape fabric. Patchily sericitised plagioclase grains can be observed. (b) The development of shape fabric in the hornblende phase. Note that the disequilibrium texture and compositional heterogeneity of Sample 1 is not longer evident. A polygonal texture is clearly observed. Scale and the kinematic reference frame is indicated on each figure. Hbl = hornblende, Plag = plagioclase, Qtz = quartz, and Ser = sericite.

show transitional characteristics. Felsic clots clearly define a weak shape fabric (ellipticity of felsic clots is documented in Table 4.2) (Figure 4.8(a)). Clots comprise a reduced grain size aggregate (100-250μm) of plagioclase (± quartz) and internally show an equant, polygonal texture with characteristic 120° interfacial angles (Figure 4.8(a)). The size and ellipticity of such felsic aggregates corresponds to an original circular grain size of $3mm$ (given constant volume plane strain deformation) suggesting that they represent recrystallised aggregates of original igneous single plagioclase crystals. Full and partial sericitisation of individual recrystallised grains is documented (Figure 4.8). Repeated albite twinning in plagioclase is not uncommon, although twin orientations appear random with no unique relationship with the kinematic axes. Moreover, twins are generally straight rather than tapered and may therefore represent growth twins, perhaps inherited from the parent igneous grain, or developed during static recrystallisation, rather than a deformation feature.

Some undulatory extinction in quartz suggests the activity of intracrystalline deformation and recovery processes. Its restriction to the quartz phase, however, indicates that it may be a late feature, representing, say regional uplift, at lower-grade conditions where the quartz phase is particularly susceptible to intracrystalline deformation with respect to the plagioclase and hornblende phases which remain internally undeformed.

The shape fabric noted in felsic clots is also manifest to some degree by the development of a shape fabric and preferred orientation in elongate hornblende prisms, between 100μm-1mm parallel to the grain long axis (Figure 4.8(b)). A polygonal texture is also manifest in the hornblende phase (Figure 4.8(b)).

Between Samples 3 and 6, a strengthening of the tectonic fabric is documented, again defined by the shape ellipticity and preferred orientation of both the hornblende prisms and felsic aggregate clots (see Section 4.2, Table 4.2) (Figure 4.9(a)(b)). Grain size remains relatively constant from Sample 2, with individual recrystallised

and refined plagioclase grains between 100-250μm (Figure 4.9(a)(c)), and hornblende long axes between 100μm and 1.5mm (Figure 4.9(b)). Plagioclase sericitisation is patchy and grain-localised within the aggregates (Figure 4.9(c)). The equant, polygonal texture within felsic clots is consistently observed through to Sample 9, retaining the same range of grain size as seen in Sample 2 (Figure 4.9(c)). Again, a polygonal texture is observed in the hornblende phase, although better developed than in Sample 2 (Figure 4.9(b)).

A transition to higher strain conditions is recorded in Samples 7-9 with a saturation of the shape fabric in terms of the ellipticity and preferred orientation of felsic aggregate clots (Table 4.2) and hornblende prisms (Figure 4.10(a)(b)). Hornblende prisms develop axial ratios between 2 and 6, with long axes typically up to 1.5mm, but 500μm being more typical (Figure 4.10(b)). Some hornblende porphyroblasts (<5 per thin section) of approximately 1mm persist. Felsic clots are strained such that the term ribbon is probably more appropriate (Figure 4.10(a)). In these high strain samples, they become stretched to a degree such that they become dissected and incorporated into the matrix, so shape fabric analysis of felsic clots to approximate finite shear strain may yield underestimated, erroneous values (as tested in Section 4.2.1).

Grain size reduction mechanisms and the development of grain-shape fabrics accommodated by crystal-plasticity have no doubt prevailed during deformation. However, much of the microstructural evidence indicative of the deformation mechanisms by which this occurred appear to have been lost to subsequent static recrystallisation. An equant to prismatic polygonal texture (in plagioclase and hornblende phases respectively) is observed throughout each of the deformed samples with straight to gently curved grain boundaries and 120° interfacial angles, generally encompassing internally unstrained grains. Furthermore, the reduced grain size established by Sample 2 persists, particularly in the plagioclase phase, until sample 9. This suggests that the observed texture represents some sort of

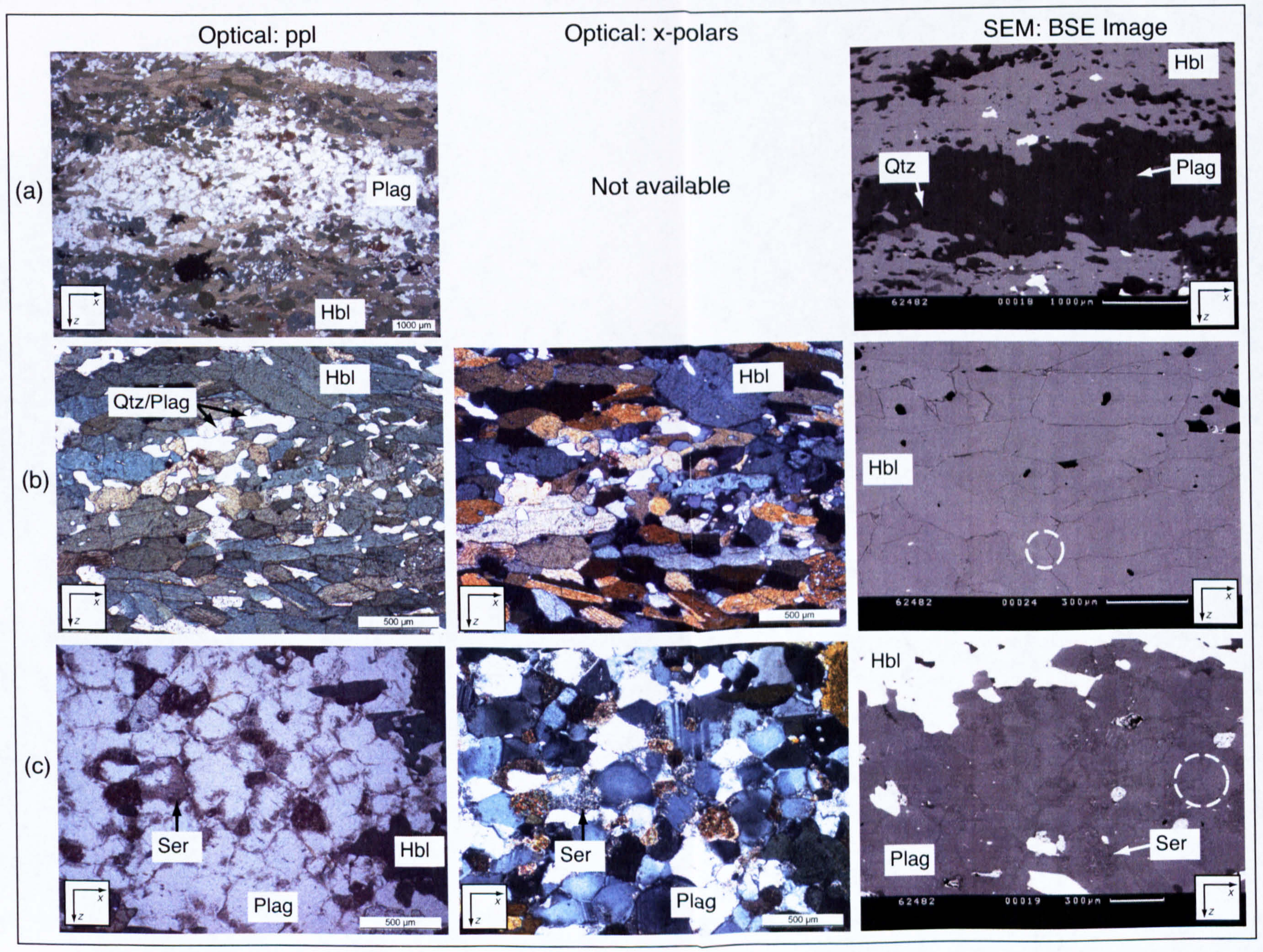

Figure 4.9: Optical and BSE micrographs of pertinent microstructures, Sample 4. (a) Felsic clot showing shape fabric parallel to X. (b) X-parallel shape fabric in hornblende grains. Polygonal texture with 120° interfacial angles can be observed (BSE image, circled). (c) Internal texture of a felsic clot, showing polygonal texture and 120° interfacial angles (circled). Sericitisation is notably patchy. Scale and the kinematic reference frame is indicated on each figure. Hbl = hornblende, Plag = plagioclase, Qtz = quartz, and Ser = sericite.

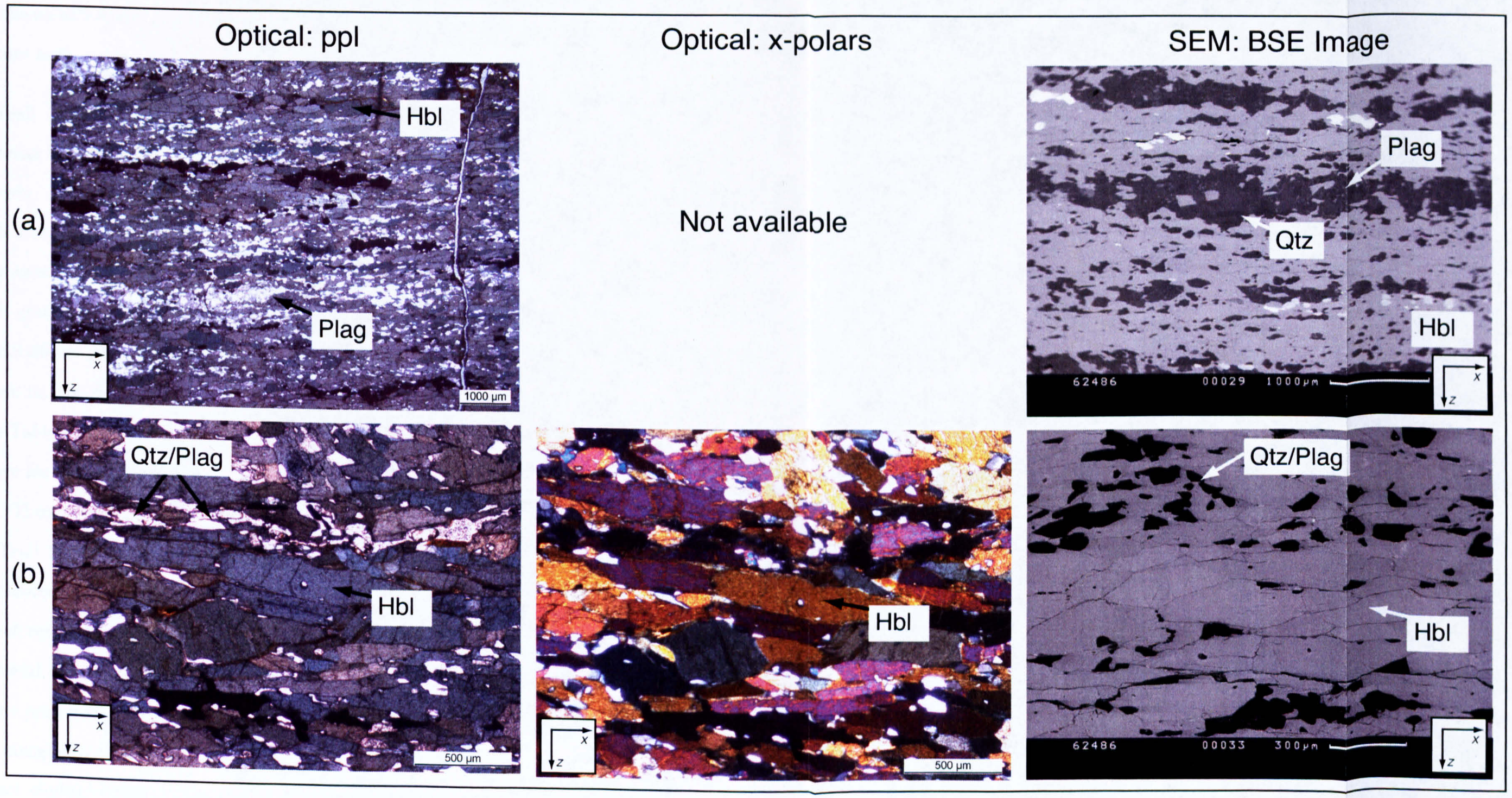

Figure 4.10: Optical and BSE micrographs of pertinent microstructures, Sample 8. (a) Highly developed X-parallel shape fabric in felsic clots. (b) X-parallel shape fabric in hornblende grains. Polygonal texture with 120° interfacial angles can be observed. Scale and the kinematic reference frame is indicated on each figure. Hbl = hornblende, Plag = plagioclase, and Qtz = quartz.

minimum-energy equilibrium grain size and texture developed during static recrystallisation, rather than a 'frozen-in' deformation texture, although the bulk LPO characteristic of the crystal-plastic deformation will still be retained (Section 4.4).

The common occurrence of sericitised plagioclase across the entire suite, including the undeformed material, suggests that sericitisation is a late, post-deformational feature here.

Teall (1885) first noted the deformation of originally isotropic Scourie dyke material in a Laxfordian shear zone in his description of a hornblende schist at Scourie. He noted alternating lenticular bands of hornblende and quartz+feldspar with a shape preferred orientation in the plane of the schistosity, and hornblende long axes 150-400μm. Teall (1885) observes that the hornblende schist is associated with grain size reduction with respect to the undeformed protolith. Interestingly he details an increase in the quartz fraction relative to the undeformed material which he associates with the conversion of remnant clinopyroxene to hornblende (see Table 4.1). These observations are in close agreement with those documented above for Upper Badcall.

O'Hara (1961) describes a foliated and lineated rock from the same locality as Teall (1885) in a Scourie dyke. Modal fractions (hbl 70.4%, plag 22.7% + accessories) is similar to those observed at Badcall (Table 4.1), although quartz is not represented by O'Hara (1961). Despite this, O'Hara (1961) describes this material as a hornblende-plagioclase-quartz schist, characterised by strong grain shape preferred orientation parallel to schistosity. Plagioclase compositions (An36) are marginally higher than than observed in Samples 2-9 (see Figure 4.3) and may reflect slightly different deformation conditions. Hornblende compositions are in agreement with those at Badcall, and a lattice preferred orientation (LPO) with (100) parallel to schistosity and [001] parallel to the elongation direction os noted.

In the more general overview of deformed Scourie dolerite dykes by Sutton & Watson (1951), some key features which are observed in the undeformed and de-

formed dolerite at Badcall are described. Notably, hornblende rims around clinopyroxene, hornblende-quartz entirely replacing and pseudomorphing clinopyroxene. Within shear zone, they describe the development of schistosity and shape preferred orientation, and the replacement of original igneous feldspar grains with granular aggregates — each of which are described above for the Badcall sample suite.

As summarised in Section 2.1, the sparse estimates of Laxfordian *P-T* estimates, range from 530-640°C and 4-7 *kbars* (Fettes et al., 1992; Droop et al., 1999). These estimates are in agreement with the amphibolite facies assemblage described at Upper Badcall.

Thus, the Scourie dyke at Upper Badcall was likely intruded into gneisses at amphibolite facies conditions, where subsequent to crystallisation of an igneous assemblage that included clinopyroxene with plagioclase, equilibration to ambient conditions was associated with alteration of clinopyroxene to amphibole. Laxfordian shearing appears to be a later event that affected the hornblende-plagioclase-quartz±clinopyroxene assemblage and is associated with the development of planar and linear shear fabrics, grain size reduction, recrystallisation, and minor changes in mineral chemistry.

The whole rock aggregate can be considered as a three-phase system with isolated felsic clots in an interconnected matrix of hornblende, plus isolated and distributed 100-200μm grains of quartz and plagioclase.

4.2 Further strain analysis

A method of strain analysis based on macro-scale structural data was presented in Section 2.3. As indicated there however, microstructural techniques have also been proven to provide quantitative estimates of finite strain in deformed materials. Methods include the analysis of shape fabric parameters (such as the aspect ratio

of the best-fit ellipse and its orientation relative to some reference plane) as a proxy for the finite strain ellipse (Coward, 1976; Ramsay & Huber, 1983). Correlation of strain with the distribution and intensity of a lattice preferred orientation in constituent minerals of rock aggregates has also been attempted (e.g. Lister & Paterson, 1979; Lister & Hobbs, 1980; Schmid & Casey, 1986; Law, 1990; Law et al., 1990; Passchier & Trouw, 1998). Such attempts on a limited range of mineralogies have proved, at best, qualitative, due to the recognition of multiple possible crystallographic slip systems which can be variably active depending on the conditions of deformation, or act together or sequentially to unpredictably alter any pre-developed fabric.

Based on the petrography and microstructure described in Section 4.1, this section presents an alternative, microstructural method for determining the finite shear strain across the deformation zone at Upper Badcall, and highlights its validity with respect to that determined from field data (Section 2.3).

4.2.1 Approximating γ from shape fabric parameters

The microstructural method presented here uses the shape fabric of originally circular constituent mineral grains as a proxy for the finite strain ellipse.

As outlined in Section 4.1, the quartz-dolerites of the Scourie dyke at Upper Badcall chiefly comprise an aggregate of hornblende, plagioclase and quartz (± remnant clinopyroxene). Although the hornblende phase defines a strong grain shape fabric, the interplay of dynamic and static recrystallisation on the inherently prismatic crystal form is not clear, and may therefore not provide a representative proxy for the bulk shear strain ellipse.

It was decided, therefore, to use the felsic aggregates or clots (see Section 4.1) as microstructural strain markers. Such aggregates present as single igneous parent grains in the wall-rock protolith, and deform as a reduced grain size aggregate, developing shape fabric within the deformation zone.

Optical photomicrographs for each of the specimens were imported into the image analysis software, *Scion Image* (©Scion Corporation). Images were then processed according to the following procedure:

1. Photomicrographs are cropped to 512×1024 pixels and greyscaled – requisites in Scion Image software for this image processing. Figure 4.11(a).

2. Define upper and lower *thresholds* within the greyscale representative of felsic aggregates, and make the new image binary in black and white. Figure 4.11(b).

3. Process the binary image with a *closure* function. This action performs a *dilation* operation followed by an *erosion* – essentially smoothing object outlines, filling holes, and removing wildspikes. Figure 4.11(c).

4. Load and run the macro *Averagepore*, developed by Dr. Martin Casey. This macro analyses particles of a user-defined minimum and maximum area, via a tensor average method, similar to that outlined in Wheeler (1984). A particle area range of 500-∞ pixels was used here as a compromise between reducing noise from very small non-representative grain and maintaining a statistically significant data set. Particles are assigned a best-fit ellipse, the spatial properties of which give a moment of inertia equal to that of the real particle. Figure 4.11(d).

For each sample, the best-fit ellipse is related to the finite shear strain by (Ramsay, 1967):

$$R = \lambda_1 = \frac{2 + \gamma^2 + \gamma\sqrt{(\gamma^2 + 4)}}{2} \tag{4.1}$$

where R refers to the ellipticity of the finite strain ellipse:

$$R = \left(\frac{\lambda_1}{\lambda_2}\right)^{\frac{1}{2}} = \frac{1 + e_1}{1 + e_3} \geq 1 \tag{4.2}$$

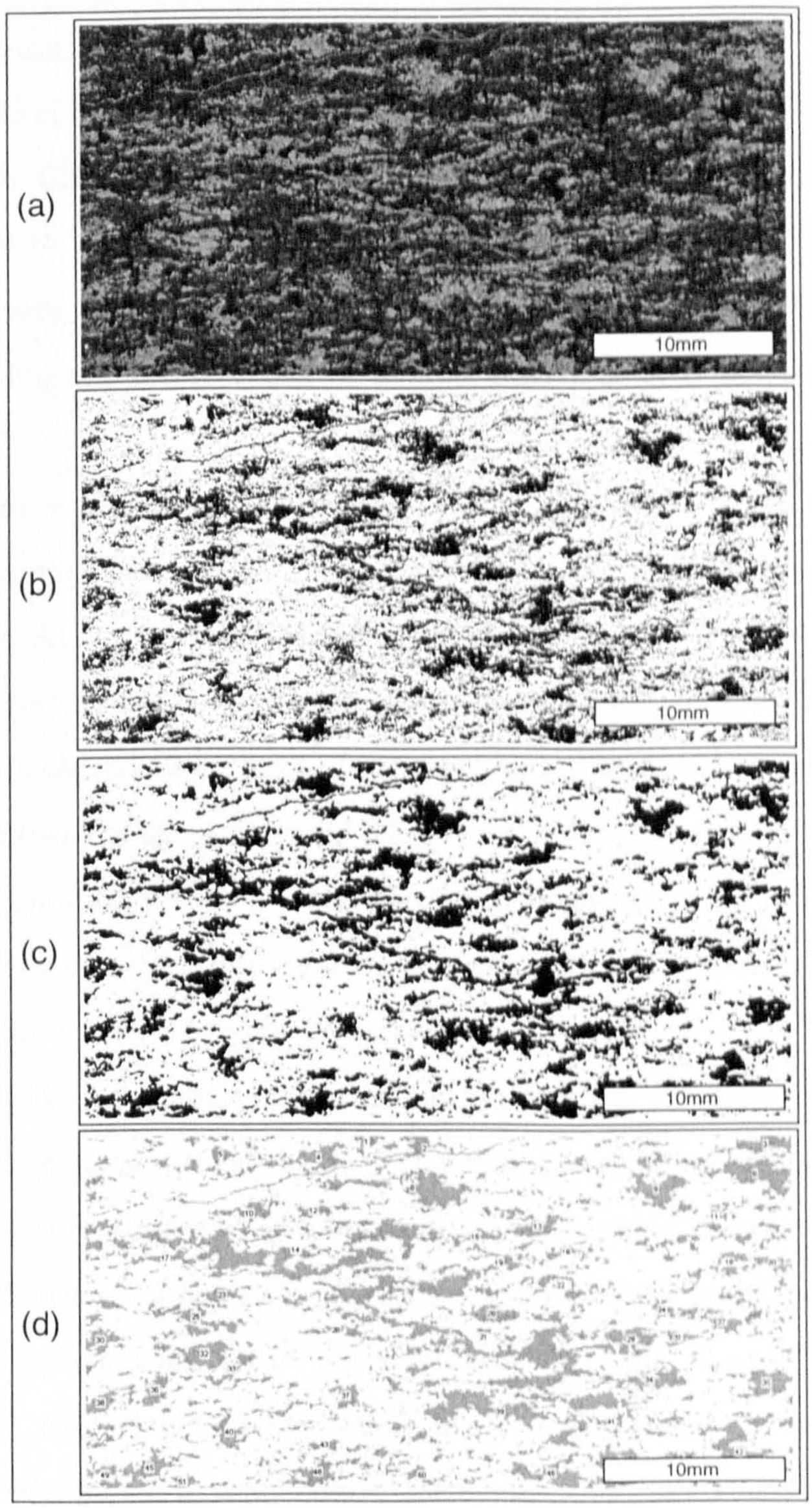

Figure 4.11: Graphical results of the sequence of image processing steps using the software *Scion Image* in the determination of shape fabric parameters (Section 4.2.1) using Sample 6 as an example. Numbered grains in (d) are those grains determined to be within the user-defined grain-size limits and can be directly correlated with quantitative output data.

and $\lambda_{1,2}$ are the square of the ellipse long and short axes, respectively; and e_n is the axial extension.

The results of the shape fabric determination of finite shear strain, γ, are shown in Table 4.2. Given that samples are cut in a kinematic reference frame where X is parallel to the mineral stretching lineation defined by felsic clots, best-fit ellipse long-axes are generally parallel to the kinematic X-direction. Potential errors regarding the measurement of mineral lineations are discussed further in Section 4.2.2.

A comparison of Table 2.1 and Table 4.2, and illustrated in Figure 4.12, highlights a clear discrepancy in the magnitude of the values of γ in the finite shear strain profile. At its most extreme, the difference between the value of γ calculated between the two methods exceeds 55, although, more realistically, the maximum discrepancy is around 12 for most of the more highly strained samples.

Clearly, either the shape fabric of felsic clots in the deformed dyke aggregate, or the re-orientation of the macro-scale fabric as measured in the field in the country-rock quartzo-feldspathic gneiss, does not deform in a predictable way such that it can be used to provide representative values of the finite shear strain. For example, it may be that strain in the shear zone is partitioned between the country-rock gneiss and the dyke, such that more strain is accommodated in the gneiss, accounting for greater values of strain. This would, however, necessitate some sort of strain concentration at the country rock-dyke interface, such as an accommodating boundary shear — a feature which is not observed in the field. Alternatively, felsic clots may not deform like a single particle by internal plastic processes. Deformation as a polycrystalline aggregate by, for example, a granular flow mechanism, may give erroneous estimates of the strain ellipse, calculations of which traditionally assume homogeneous internal deformation of a single particle with a viscosity contrast of unity with the enveloping matrix (Ramsay & Huber, 1983; Freeman, 1987). The mechanical complexity of many polyphase aggregates,

Sample	R	$\theta(°)$	γ	$\gamma_{x_{sz}}$	$\gamma_{y_{sz}}$	$\Delta z_{sz}(m)$	$Cum.U_{x_{sz}}(m)$	$Cum.U_{y_{sz}}(m)$
1	1.08	-	0.08	-	-	-	-	-
2	2.36	-81	0.89	0.14	-0.88	8.50	1.18	-7.48
3	3.28	-84	1.26	0.13	-1.25	15.13	3.18	-26.43
4	2.83	-58	1.09	0.58	-0.92	17.40	13.23	-42.52
5	1.92	-81	0.66	0.10	-0.65	6.99	13.95	-47.07
6	2.61	-64	1.00	0.44	-0.90	4.45	15.90	-51.07
7	3.87	-38	1.46	1.15	-0.90	6.06	22.87	56.52
8	4.83	-38	1.74	1.37	-1.07	7.56	33.24	-64.62
9	5.72	-12	1.97	1.93	-0.41	110.83	246.80	-110.02

Table 4.2: Results of the calculation of finite shear stain, γ, for samples across the deformation zone from shape fabric parameters (see Section 2.3.1 and 4.2.1 for a definition of symbols). The wall-rock protolith, Sample 1, is included to illustrate its axial ratio close to unity, and hence is not used for further strain analysis.

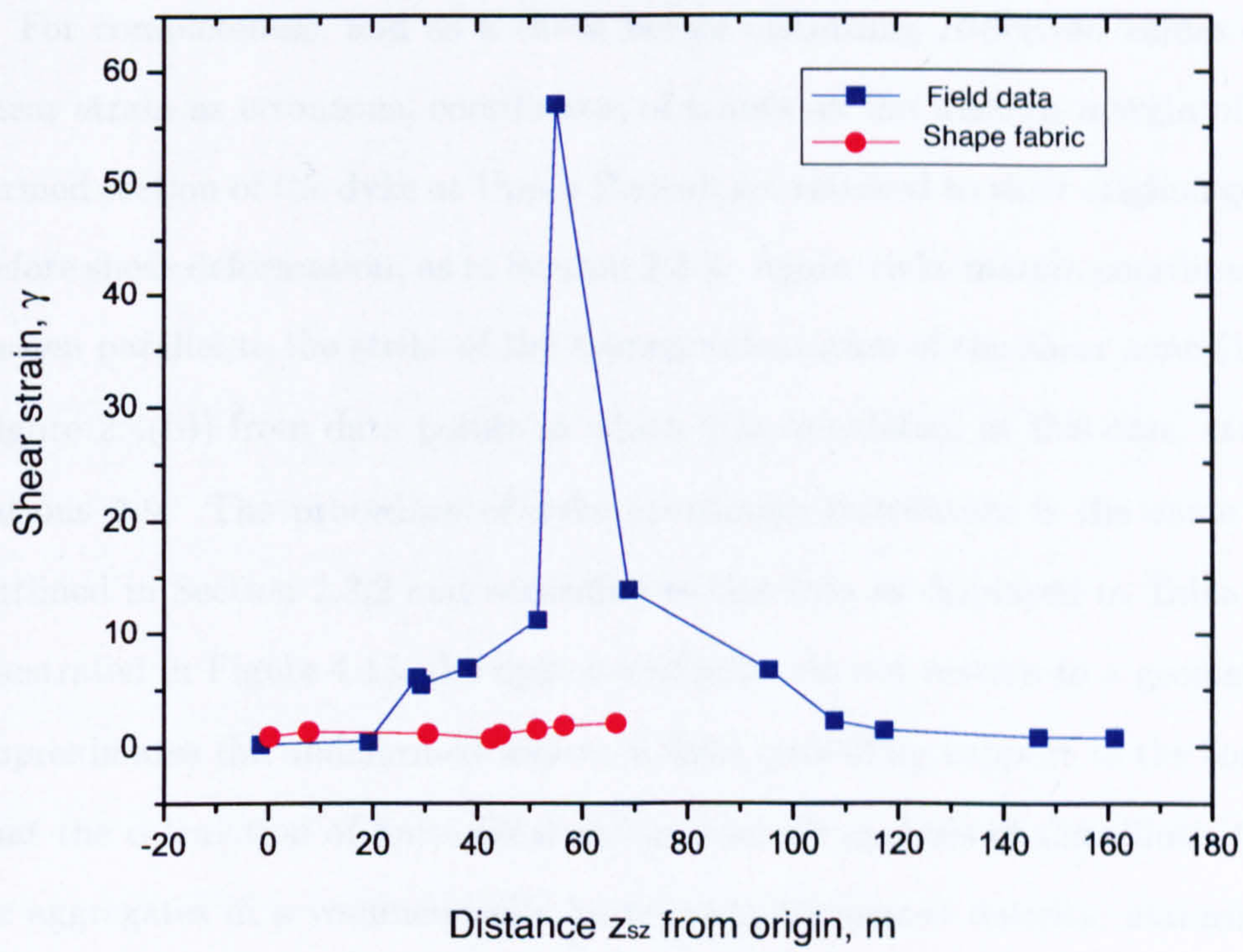

Figure 4.12: Graph to illustrate the discrepancies in the values of γ calculated from the two described methods using field data (Section 2.3.1), and shape fabric ellipticities (Section 4.2.1). Strain is plotted against the position, transversely across the shear zone, at which that value was calculated.

although supported to some degree in the literature (e.g. Lister & Price, 1978; Passchier & Trouw, 1998; Siegesmund et al., 1994; Stünitz & FitzGerald, 1993; Bruhn & Casey, 1997; Ji & Xia, 2002) remains relatively poorly constrained for many lithologies. Strain partitioning in polyphase aggregates is further discussed in Section 4.5. What is important to understand here, however, is that the aggregate clots of dominantly plagioclase (± quartz) do not deform in such a way as to realistically estimate the strain ellipse.

For completeness, and as a check before discarding R-derived values of finite shear strain as erroneous, coordinates of points on the western margin of the deformed section of the dyke at Upper Badcall are restored to their original geometry before shear deformation, as in Section 2.3.2. Again, dyke margin coordinates were chosen parallel to the strike of the average orientation of the shear zone (175/84S, Figure 2.4(b)) from data points at which γ is calculated, in this case, sample locations 2-9. The procedure of dyke coordinate restoration is the same as that outlined in Section 2.3,2 and according to the data as displayed in Table 4.3. As illustrated in Figure 4.13, the dyke coordinates do not restore to a geometry that approximates the undeformed wall-rock dyke, providing support to the conclusion that the calculation of finite shear strain from an analysis of the ellipticity of felsic aggregates in a volumetrically hornblende-dominated doleritic material is not representative of the bulk deformation in the shear zone.

4.2.2 Discussion of errors

In order to gain an appreciation of the errors in the calculation of strain, investigation into the confidence of both lineation and foliation measurements are shown. This error analysis refers to the methods of both Sections 2.3.1 and 4.2.1.

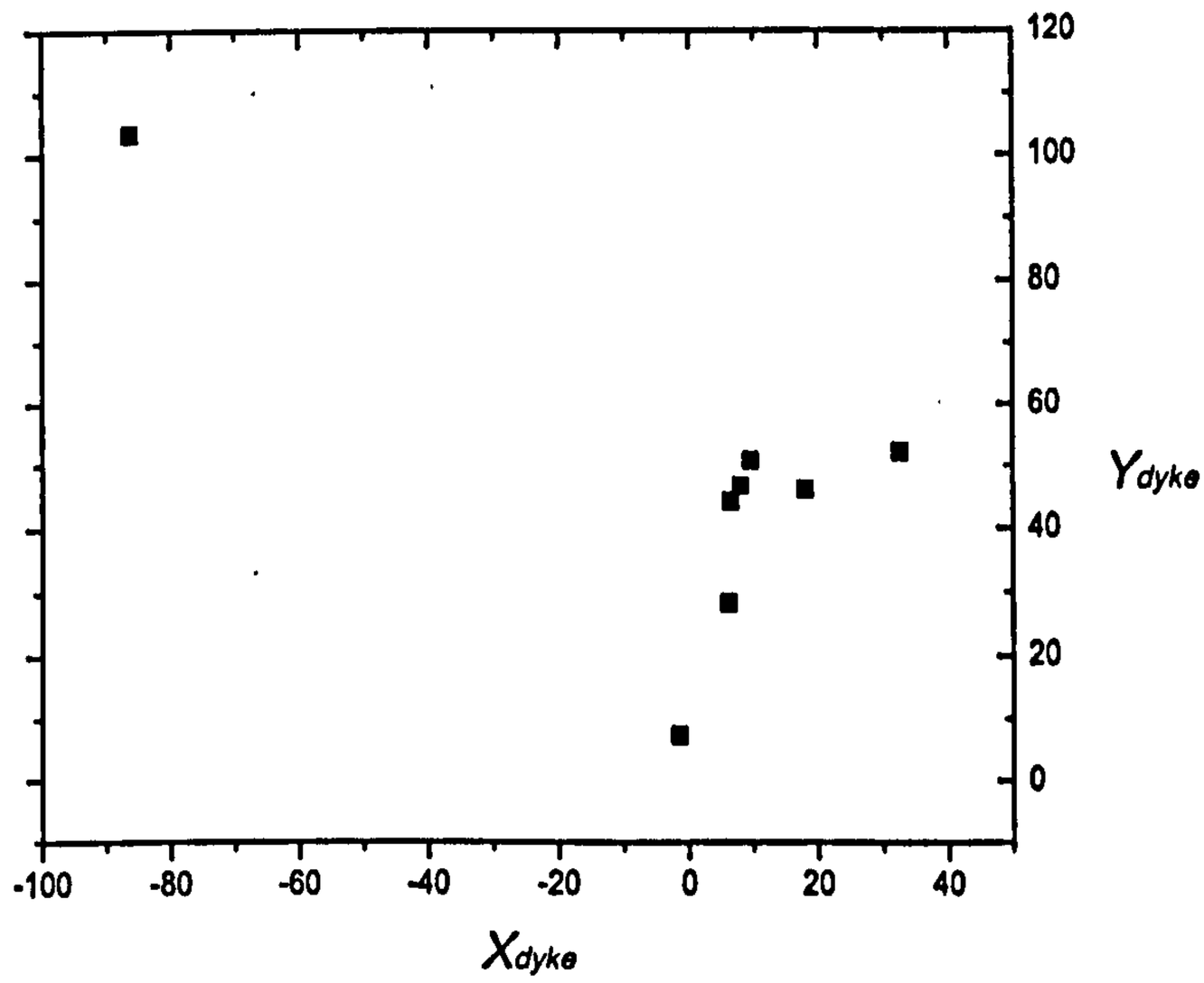

Figure 4.13: Coordinates from the western margin of the deformed portion of the Scourie dyke at Upper Badcall after U_x and U_y, determined from shape fabric parameters, have been subtracted in the shear zone reference frame, x_{sz}, y_{sz}, z_{sz} (Section 4.2.1). Data are plotted in the dyke reference frame, whereby coordinates are projected onto x_{dyke}, y_{dyke}, the plane normal to the strike of the dyke.

Accuracy of lineation observation

The lineation measurements used in the calculation of strain from the reorientation of planar fabrics (Section 2.3.1) was defined by the shape preferred orientation (SPO) of plagioclase or felsic clots (Section 4.1). Although the utmost effort was taken to ensure the accuracy of measurement, and that a representative lineation direction was chosen, natural variation of the lineation direction about the measured value is inevitable.

As described in Section 4.2.1, image analysis of photomicrographs using macros such as *Averagepore* in image processing packages such as *Scion Image* can provide a statistical data set of rock fabric parameters. An additional output of the *Averagepore* macro is a full list of ellipse long axis and short axis lengths, and the angle made between the long axis and the reference horizontal (kinematic X-axis),

for each of the particles digitised between the user-defined particle area bounds (e.g. 500-∞ pixels), and from which the average or best-fit ellipse (as used as a proxy for the strain ellipse in Section 4.2.1) was calculated. Hence, a data set of the spread in lineation orientation about the chosen and measured value (reference horizontal, X) is available.

To quantify an upper bound on this natural variation, one of the most undeformed (lowest γ-value) samples was chosen for analysis — Sample 3. Exhibiting only fractional strain ($\gamma = 0.46$, Table 2.1), this sample would be expected to have the most poorly defined SPO and hence a relatively large angular error in its estimation.

Processing indicates a standard deviation $\sigma = \pm 12°$ in the foliation plane (XY) about the measured lineation (X) where deviations $> 2\sigma$ (often pertaining to small, non-representative grains) were considered erroneous. This is without doubt an upper bound estimate of the angular discrepancy in the observation of the true lineation and measurement error was consistently much less. Table 4.4 and Figure 4.14 show the effect of such a potential angular variation in lineation on the calculated strain for Sample 3, via the stereographic method (Section 2.3.1).

Sensitivity analysis of reoriented fabric

In addition to the lineation direction, the calculation of γ is a function of the reoriented planar fabric elements of the shear zone (Section 2.3.1, Equation 2.1). For simplicity, these will be considered here in terms of α and α' (Equation 2.1), the angular relationships between the undeformed country-rock fabric and the sheared fabric respectively, relative to the shear zone orientation, projected onto the girdle containing the lineation, X, at that position transversely across the shear zone, and the shear zone normal (i.e. the kinematic XZ plane).

Given that the sheared planar fabric elements should be recorded parallel to the kinematic Y-direction, or perpendicular to the lineation, X, the orientation

(x_{sz}, y_{sz}, z_{sz})	$U_{x_{sz}}$	$U_{y_{sz}}$	$(x_{sz}, y_{sz}, z_{sz}) - U_{x_{sz}, y_{sz}}$	(x_{dyke}, y_{dyke})
(0.00, 0.00, 0.00)	1.18	-7.48	(-1.18, 7.48, 0.00)	(-1.42, 7.43)
(7.50, 1.21, 7.67)	1.99	-18.96	(4.32, 27.64, 7.67)	(6.18, 22.29)
(5.00, -1.15, 30.04)	10.05	-16.09	(-8.23, 41.37, 30.04)	(6.56, 44.29)
(0.00, -4.44, 42.27)	0.72	-4.56	(-13.95, 42.63, 42.27)	(8.08, 46.82)
(2.50, -4.70, 44.75)	1.95	-4.00	(-13.40, 46.37, 44.75)	(9.65, 50.79)
(15.00, -15.43, 51.17)	6.97	-5.45	(-7.87, 41.09, 51.17)	(18.01, 46.21)
(40.00, -17.94, 55.93)	10.37	-8.10	(6.76, 46.68, 55.93)	(32.62, 52.27)
(110.00, -13.02, 66.50)	213.56	-45.39	(-136.80, 96.99, 66.50)	(-86.34, 103.41)

Table 4.3: Coordinates and displacements used in the restoration of part of the western margin of the deformed dyke at Upper Badcall. Displacements, U, calculated from γ values determined from shape fabric parameters (Section 4.2.1, Table 4.2). Notice that in the rotated coordinate scheme, data is projected onto the $x_{dyke}y_{dyke}$ plane, and so the z_{dyke} coordinate is not necessary.

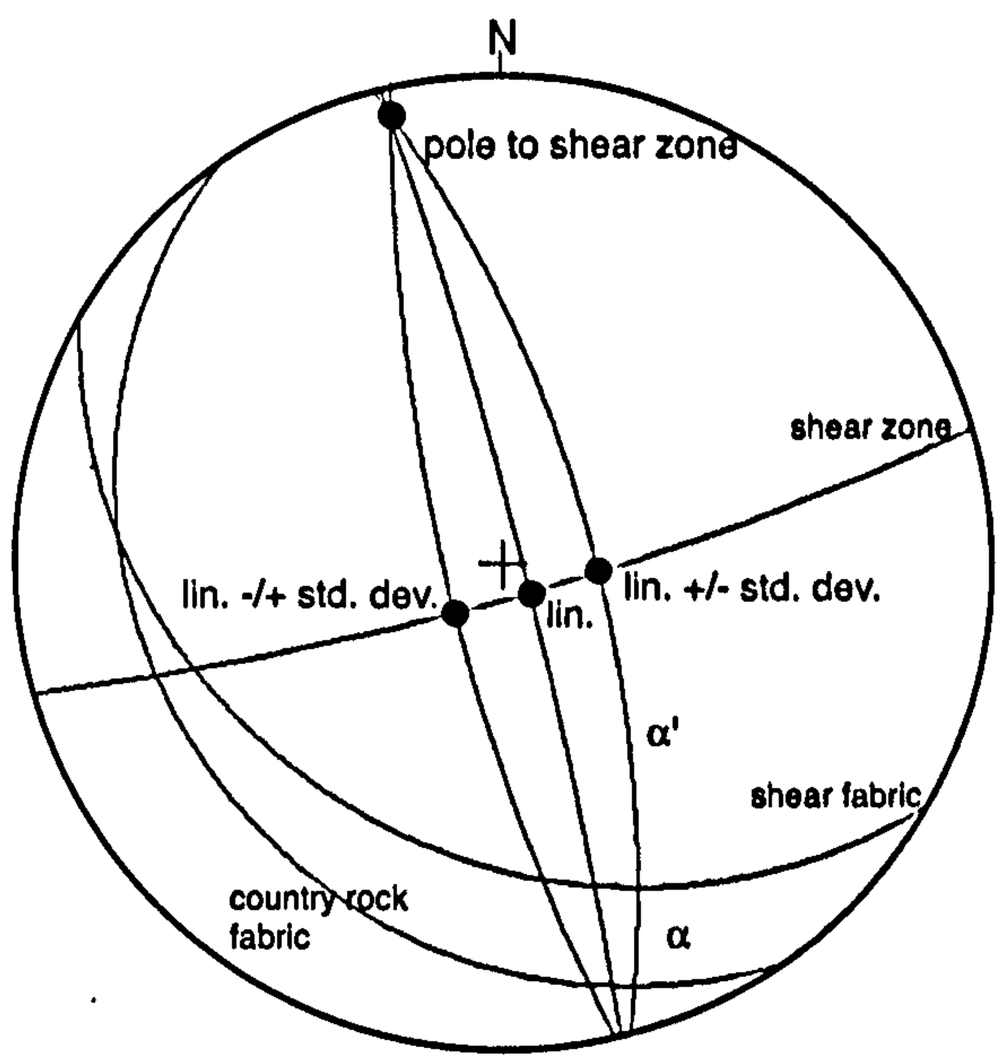

Figure 4.14: Stereogram based on the data of Sample 3 (Table 2.1) and illustrating the effects of 1σ angular deviation in the observation and measurement of the lineation direction for the calculation of strain via the parameters α and α'. The calculated strain of $\gamma = 0.46$ is shown to vary by $\pm \leq 18.5\%$ in γ due to a standard deviation in the lineation measurement of $\pm 12°$ in the shear plane XY (Table 4.4).

of the outcrop with respect to the kinematic axes (Y in-and-out of the outcrop surface) means that in the construction of a strain profile across the shear zone it is necessary to use fabric orientations that are located in close proximity to the taken lineation (for this exercise, sample locations).

It is therefore not a representative approximation of the error in the measurement of planar fabric elements to observe the angular deviation in fabric orientations parallel to the strike of the shear zone at successive levels along the z_{sz}-parallel strain profile.

Presented, therefore, is a sensitivity analysis providing an indication of the potential error in the calculation of γ across the range of values of α' between shear zone-parallel and wall-rock fabric-parallel, and for a selection of assumed errors in orientation measurement readings. Such errors will be small, but account for inaccuracies in the compass-clinometer or unevenness of measured surfaces.

Differentiation of Equation 2.1 with respect to α' gives the gradient of change in γ with α':

$$\frac{\partial \gamma}{\partial \alpha'} = -\frac{1}{\sin^2 \alpha'} \tag{4.3}$$

The error in γ for an individual measurement of α' and a given angular error in observation or measurement, $\Delta\alpha'$, is therefore,

$$\Delta\gamma = \frac{\partial \gamma}{\partial \alpha'}.\Delta\alpha' \tag{4.4}$$

Plotting α' against $(\frac{\Delta\gamma}{\gamma}.100)$ hence shows the sensitivity of the shear strain as a percentage, over the range of orientations of shear fabric, α', from that in the country-rock gneiss ($\alpha' = \alpha$) to sub-parallelism with the shear zone ($\alpha' \rightarrow 0°$) (Figure 4.15).

For an assumed measurement inaccuracy of $\pm 4°$ in α' and a wall-rock planar fabric orientation such that $\alpha = 70°$ (see Table 2.1 for corresponding gneissic

std. dev. $\sigma(^\circ)$	lineation	$\alpha'(^\circ)$	$\alpha(^\circ)$	γ	% error in γ
+12	74/100	56	75	0.41	11.3
0	86/135	54	75	0.46	-
-12	78/255	49	72	0.54	18.5

Table 4.4: Estimating percentage error in strain due to potential inaccuracies in the observation and measurement of true lineation direction for Sample 3.

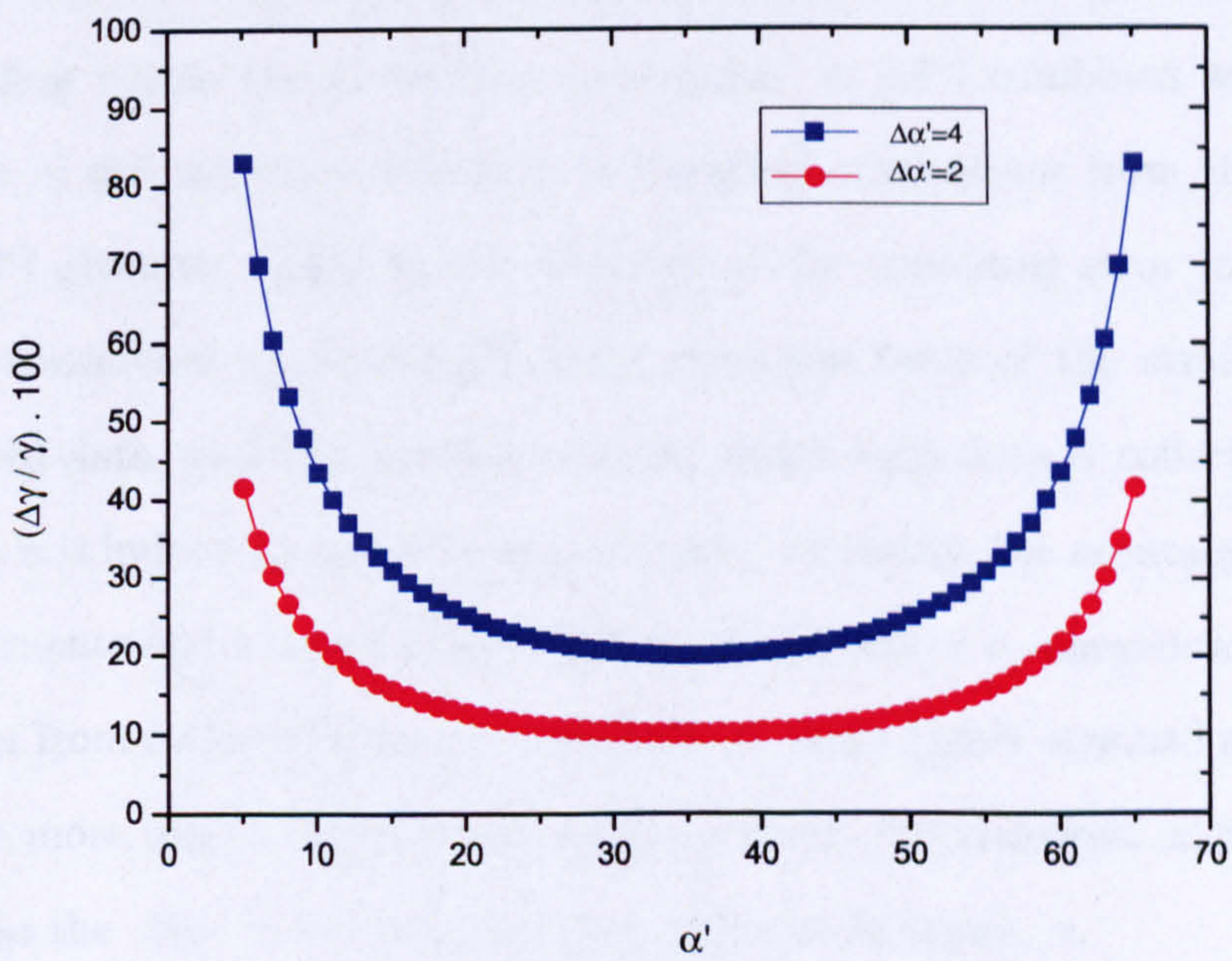

Figure 4.15: Sensitivity analysis of the potential error in the calculated shear strain, γ, expressed as a percent, with respect to α' shown for assumed angular errors in measurement, $\Delta\alpha'$, of 2° and 4°. α is constant at 70°. See text for definitions.

banding orientation), the relative error in γ is seen to be approximately 20% over the broad range of shear fabric orientations, $\alpha' = 20°\text{-}50°$. Relative percentage error is much greater at extreme values of α', as γ approaches 0 and ∞, and where fractional changes in the fabric orientation have disproportionately large effects on the calculated shear strain. Large error in these regions can be accepted however, given that the width of the highest strain zone tends to be narrow, minimising the potential effect of error on the overall inferred displacement, and low shear strain values are such that relatively large percentage error would have a negligible effect on the absolute value of shear strain, and one that would be very difficult to observe.

Combined error

An estimate of the potential error in observing and measuring the sheared gneissic banding within the shear zone (where $\Delta\alpha' < \pm 4°$) combined with an upper estimate of the standard deviation in lineation orientations from that measured ($< \pm 12°$) gives an upper bound estimate of the combined error in γ of $\pm 28\%$. This is considered an acceptable error given the basis of the strain calculation upon field data, and the conditions under which such data is collected. Furthermore, this is indeed an upper bound estimate. In reality, the accuracy of field data measurements and the observation and measurement of a representative lineation direction from collected samples, especially in more highly strained samples, were likely no more than a few degrees in angular error. Nevertheless, $\pm 28\%$ is adopted hereon as the error in the calculation of finite shear strain, γ.

4.3 The texture index, J

It is worth noting here the texture index, J, such that elements of the ensuing presentation of LPO and quantitative petrofabric data can be fully utilised and considered in context.

In order to quantify the sharpness of clustering of a petrofabric without consideration of the complexities of its distribution, Bunge (1969) described the texture index, J,

$$J = \int [f(g)]^2 dg \tag{4.5}$$

where $f(g)$ is the orientation distribution function (ODF),

$$\frac{\Delta V}{V} = \int f(g) dg \tag{4.6}$$

describing the volume fraction of data $\frac{\Delta V}{V}$ in Euler space with orientations in the interval $g + dg$ in a space containing all possible orientations.

The orientation distribution function $f(g)$ is evaluated via a spherical harmonic series expansion plus a smoothing function representing the distribution density. As more terms, L, of the series expansion are considered, the ODF is described with increasing perfection. In order to attain a compromise between reproducing the main features of the orientation distribution, whilst reducing computational time and allowing a sufficiently smoothed distribution density function, the series expansion must be truncated at an arbitrary finite degree, L_{max}, for which a value of 22 is commonly used and has been shown to give representative results (Mainprice & Silver, 1993; Skemer et al., 2005). This value is hence used here. Furthermore, a smoothing function Gaussian half-width of 10° was chosen to provide representative results with suitable smoothing of the ODF where the series expansion is truncated at $L = 22$ (Skemer et al., 2005).

Bunge (1969) further describes a measure of the LPO intensity associated with specific crystallographic poles, as may be required to quantify the strength of fabric in individual pole figures (see Section 4.4.1). Thus,

$$pfJ = J_{h_i} = \int [P_{h_i}(y)]^2 dy \tag{4.7}$$

where P_{h_i} is the distribution function giving the volume fraction of the sample for which a fixed crystallographic direction $h_i = (hkl)$ coincides with sample directions y, and integrated over the region dy. Note that, by definition $pfJ \leq J$ (Bunge, 1969).

J and pfJ are normalised in multiples of uniform distribution such that a random fabric has texture index $J = 1$, and as fabrics become increasingly clustered, approximating a single crystal scenario in monomineralic aggregates or for pole figures, $J \rightarrow \infty$ (Bunge, 1969).

The detailed derivation of J is shown to be dependent on crystal symmetry (Bunge, 1969, 1981). Furthermore, highly clustered fabrics for individual mineral phases in a polyphase aggregate may not necessarily share the same position in the aggregate orientation space, and may therefore act to weaken the sharpness of clustering, giving an underestimate of the fabric strength of the bulk aggregate. Hence, practical calculation of J is conducted separately for each constituent phase in an aggregate.

A convenient Fortran program, *SuperJ*, written by Prof. David Mainprice, exists for the efficient calculation of J from automated-EBSD orientation measurements in the form of a **.ctf* file database of phase-correlated Euler angle triplets (Section 3.4, Appendix C). In addition to the declaration of the crystal symmetry for the particular mineral phase, user-defined values are input for L_{max}, the smoothing function Gaussian half-width and a data binning option in the form of the integer size of weighted Euler angle cells, for which the values 22, 10 and 1, respectively, are used throughout. Calculation of pfJ is incorporated in the pole figure plotting program *PFch5* mentioned in Section 4.4.1.

4.4 Petrofabric

Section 3.4 introduced an automated method of quantifying LPO in a polycrystalline, polyphase aggregate in a SEM, using EBSD. Here, the results of analyses

of Samples 1-9 are presented and discussed in terms of petrofabric development and its relationship with finite strain.

4.4.1 LPO development

Crystal lattice orientation data are clearly and efficiently presented by means of crystallographic pole figures (Mainprice et al., 1986; Ji & Mainprice, 1988; Mainprice & Nicolas, 1989; Mainprice & Silver, 1993). Such stereographic plots present the orientation distribution, in a sample reference frame, of a single crystal lattice pole (hkl) or axis $[UVW]$ for a specified mineral throughout a rock aggregate. Given that samples are oriented parallel to the kinematic axes, pole figures are by default presented in a kinematic reference frame. A range of pole figures are commonly presented together, permitting the distribution, partitioning, and development of lattice-scale microstructure and deformation to be observed and characterised.

For undeformed and isotropic aggregates, pole figures tend to show a uniform orientation distribution of crystallographic poles and axes. With increasing ductile deformation by internal crystal-plasticity, such as dislocation slip mechanisms, crystal aggregates tends to create order and symmetry in their LPO distributions. Where one crystal slip system dominates, that is, slip parallel to a crystallographic direction on a crystallographic plane, pole and axis distributions tend to approach those of a single crystal of that mineral (Mainprice & Nicolas, 1989) (Figure 4.16). Slip planes tend to rotate into parallelism with the shear plane, XY, of the imposed macroscopic deformation field, and slip directions tend to form point maxima parallel with the shear direction, X (Mainprice & Nicolas, 1989).

Pole figures are plotted using the Fortran program *PFch5* developed by Prof. David Mainprice. This convenient program permits manifold user-defined plotting options, in addition to control over the specific crystallographic poles and axes to be generated from EBSD **.ctf* output data files (Appendix C).

Figures 4.17-4.21 present pole figures of representative crystallographic poles and axes for each of the constituent mineral phases indexed with EBSD for each of Samples 1-9. Figures 4.17 and 4.18 show lower hemisphere plots of non-polar EBSD-derived orientation data for hornblende and quartz respectively. Figure 4.19 presents polar data in both upper and lower hemisphere plots for plagioclase. The plane of projection represents the kinematic XZ plane for that sample, with XY parallel to the equator. All pole figures present orientation data that record a mean angular deviation (MAD) ≤ 1 (see Section 3.4), and are contoured with an Euler angle cell size of 1° and contour interval of 1 MUD (multiples of uniform distribution). Unfortunately the correlation of absolute values of MUD with the colour-scale of contouring cannot be user-defined, and so care must be taken in comparing plots based upon that colour-scale alone, and in its tendency to exaggerate maxima and minima in LPO distributions.

Hornblende

Figure 4.16 shows the relationship of crystallographic poles and axes for single crystal monoclinic hornblende.

Figure 4.17 shows crystallographic directions [100], [010] and [001]; and poles (100) and (001) for hornblende. Note that for the monoclinic symmetry of hornblende, the lattice direction [010] and pole (010) are parallel and therefore share an identical pole figure. The most striking observation from Figure 4.17 is the development of strong LPO in [001] and (100), parallel to the kinemtatic X-direction and XY-plane respectively. For Sample 9, for example, axes cluster with MUD's of 9.24 [001] and 7.86 (100) — roughly double those recorded for the other crystallographic axes, and more than three times that of the wall-rock protolith, Sample 1. This LPO pattern suggests that (100)[001] is the dominant slip system in hornblende in this deformation zone. Furthermore, it supports existing observations of (100)[001] as a dominant slip system in naturally deforming hornblende (Sieges-

mund et al., 1994; Berger & Stünitz, 1996; Azpiroz & Lloyd, in press).

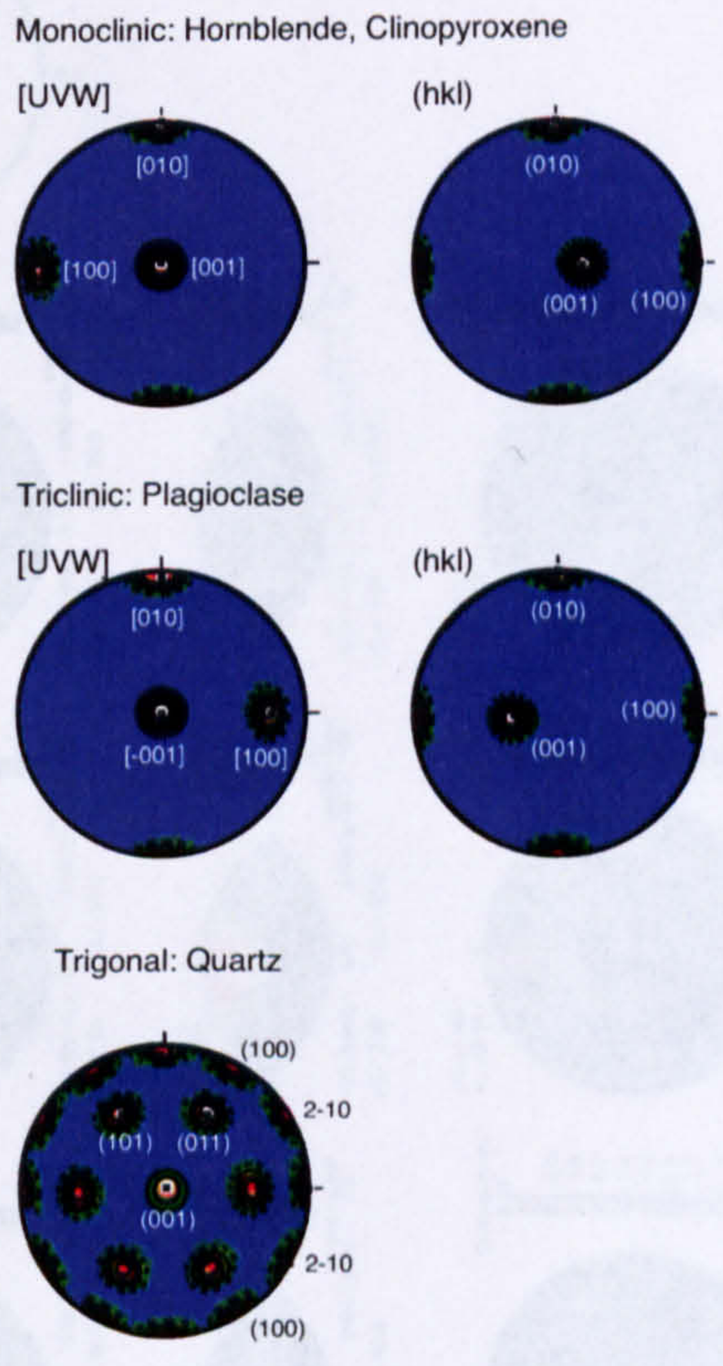

Figure 4.16: Representative single crystal pole figures for the crystal symmetries encountered in the hornblende, plagioclase, quartz (±clinopyroxene) doleritic aggregate in the Upper Badcall Scourie dyke. The three principle directions $[UVW]$ and poles to lattice planes (hkl) are shown for monoclinic and triclinic symmetries, and the commonly published c(001), a(2-10), m(100), r(101) and z(011) axes for the trigonal system. Red colours mark pole maxima, blue marks minima, with arbitrary contours. Lower hemisphere plots of non-polar data.

Section 4.3 introduces the parameter pfJ for describing the LPO intensity associated with specific crystallographic poles, or quantifying the strength of fabric in individual pole figures. Thus, in addition to the clear development of an ordered pattern in the LPO distribution in Figure 4.17, quantification of the fabric development with respect to individual crystallographic poles and axes is illustrated in Figure 4.22. An increase in pole figure clustering is clearly exhibited for all poles and axes, with particular order developed in [001] and (100).

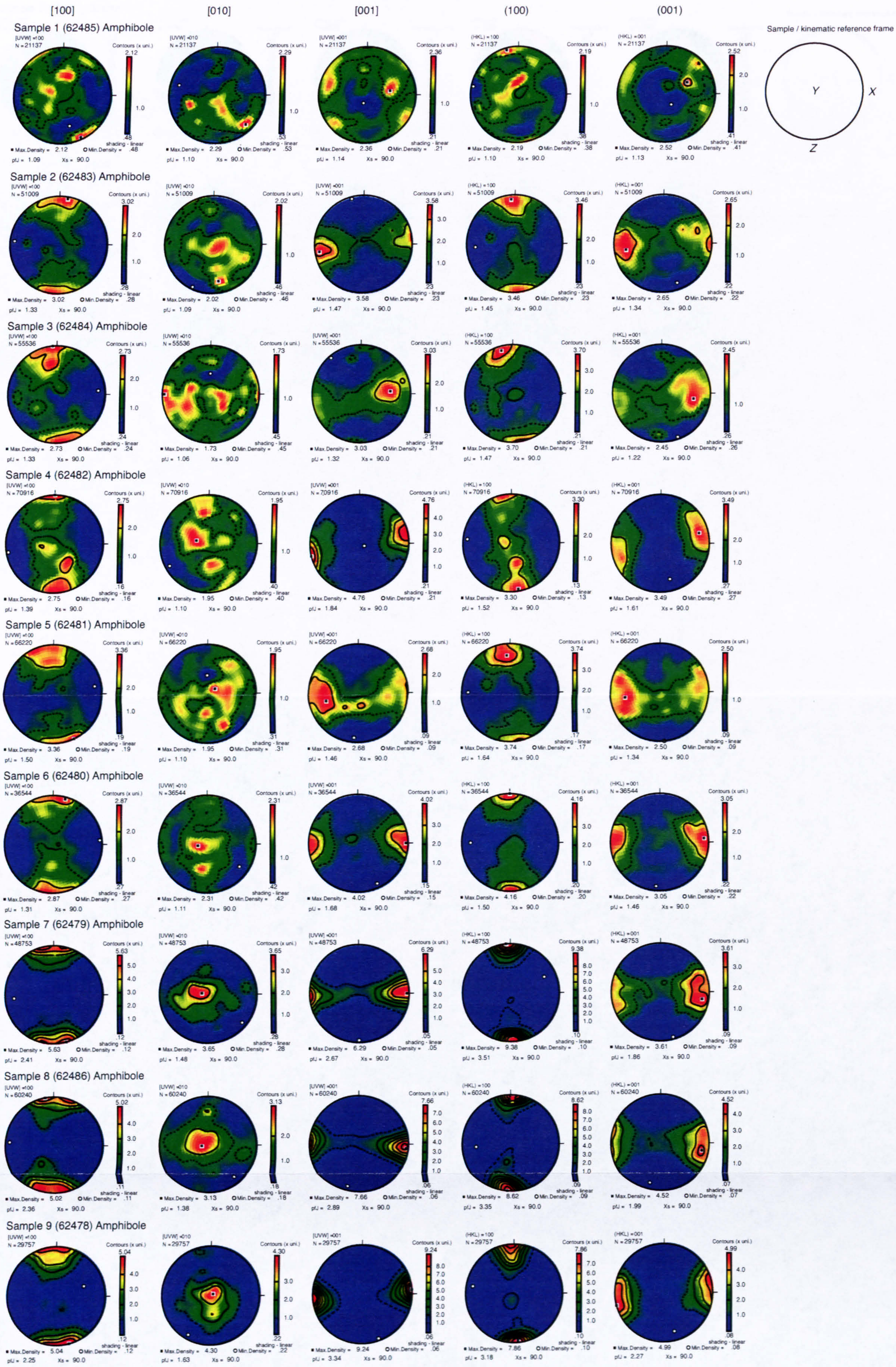

Figure 4.17: Hornblende phase $[UVW]$ and (hkl) pole figures. See text for details and discussion.

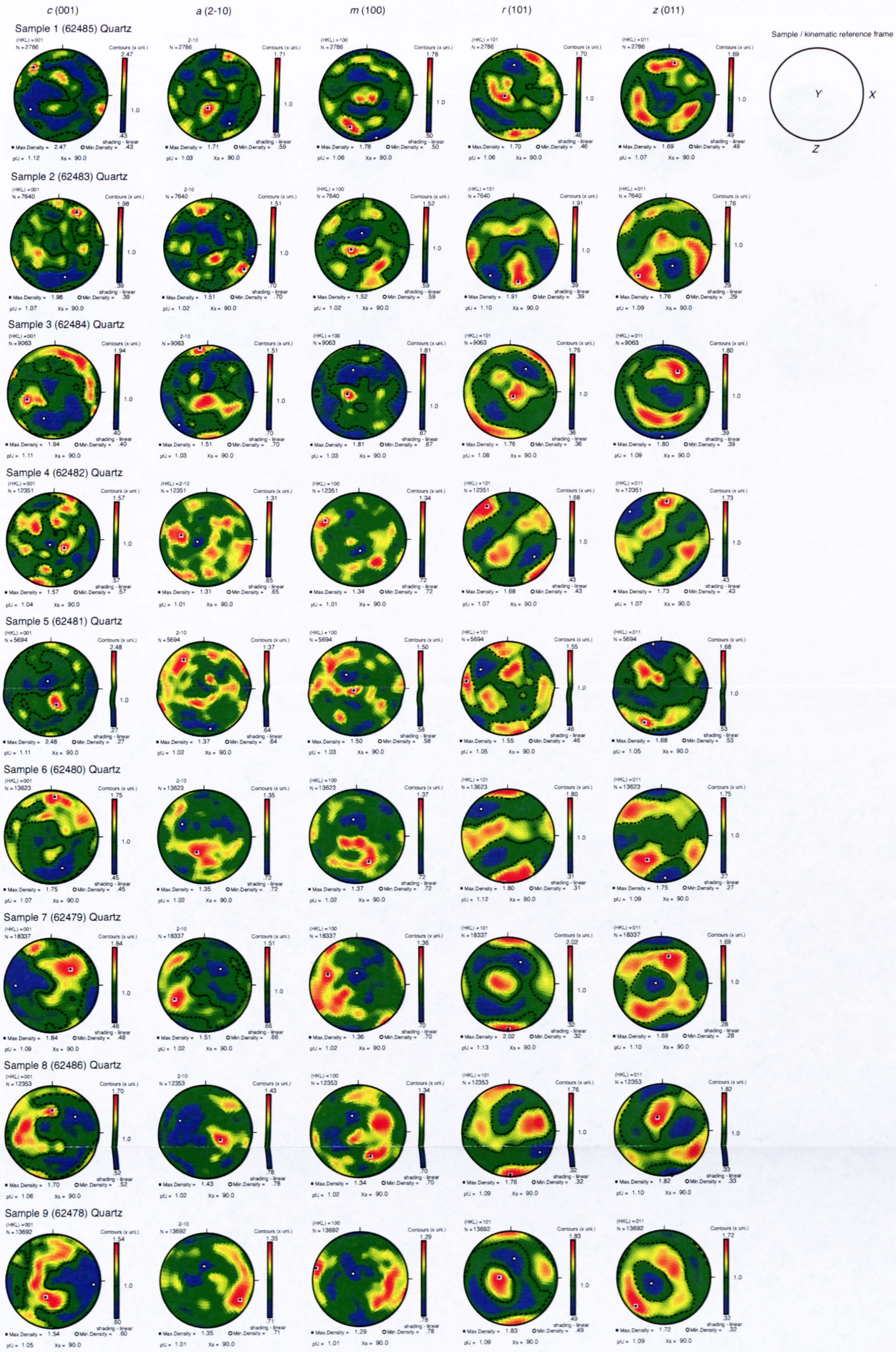

Figure 4.18: Quartz phase $[UVW]$ and (hkl) pole figures. See text for details and discussion.

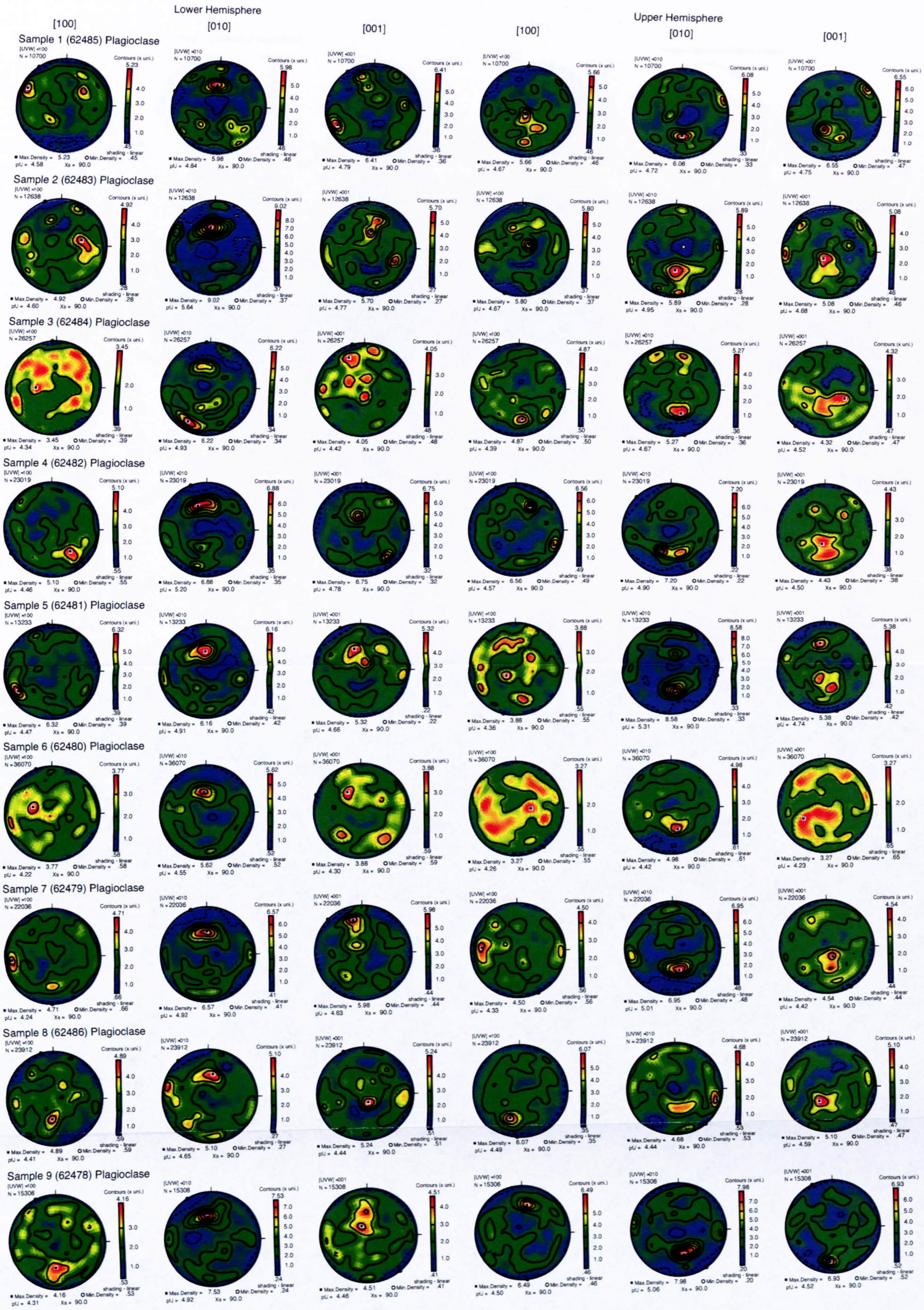

Figure 4.19: Plagioclase phase $[UVW]$ pole figures. Reference frame is as for Figure 4.20. See text for details and discussion.

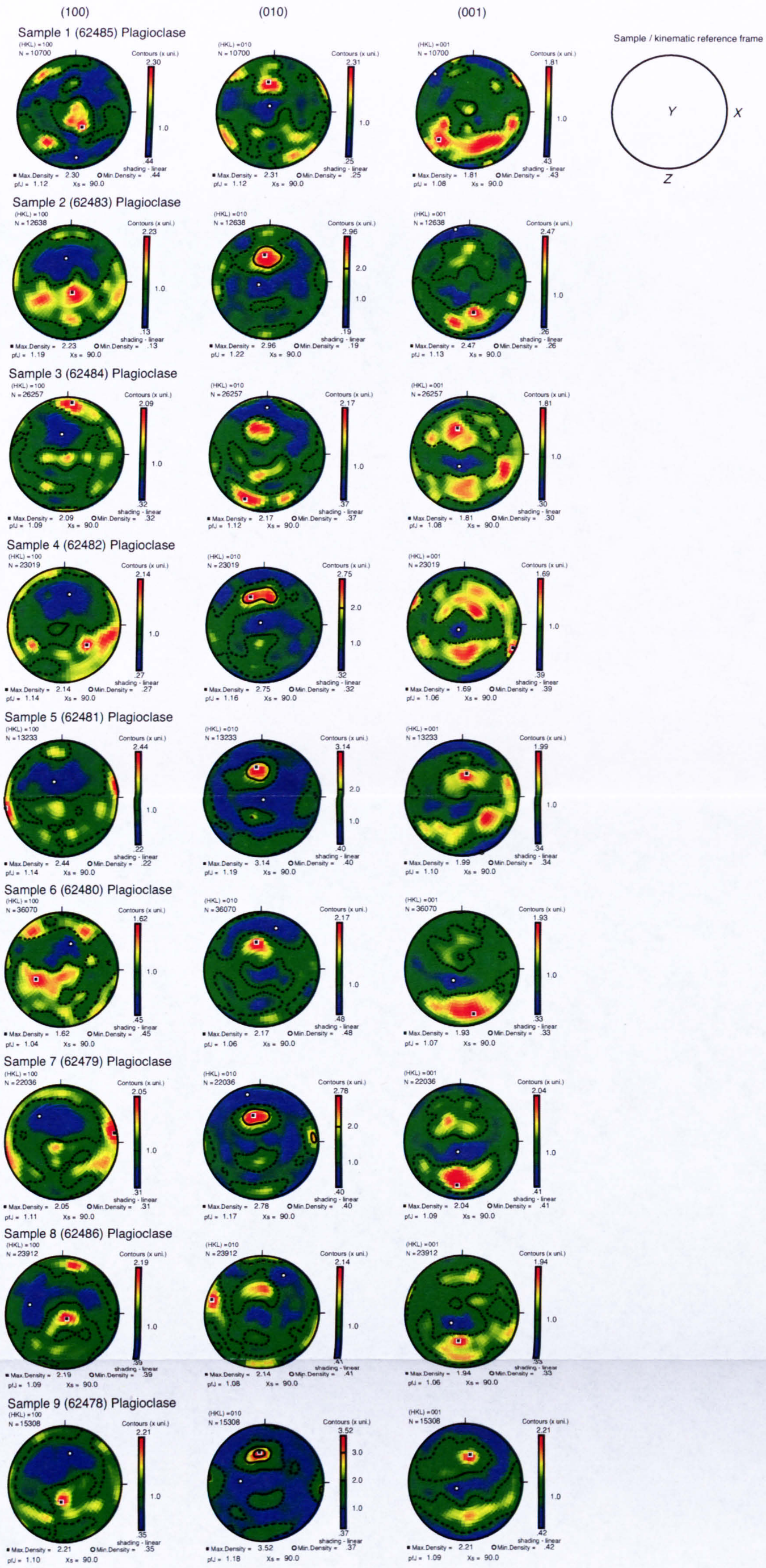

Figure 4.20: Plagioclase phase (hkl) pole figures. See text for details and discussion.

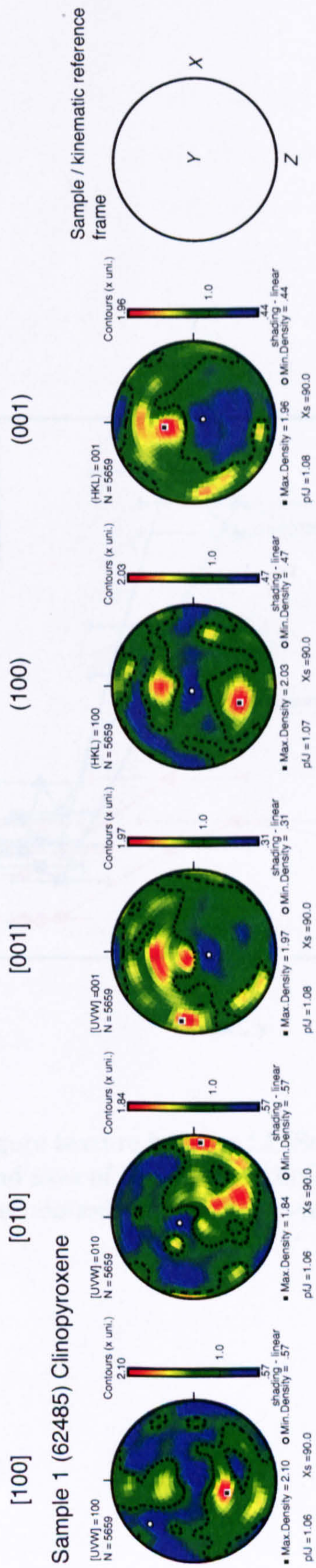

Figure 4.21: Clinopyroxene phase $[UVW]$ and (hkl) pole figures. See text for details and discussion.

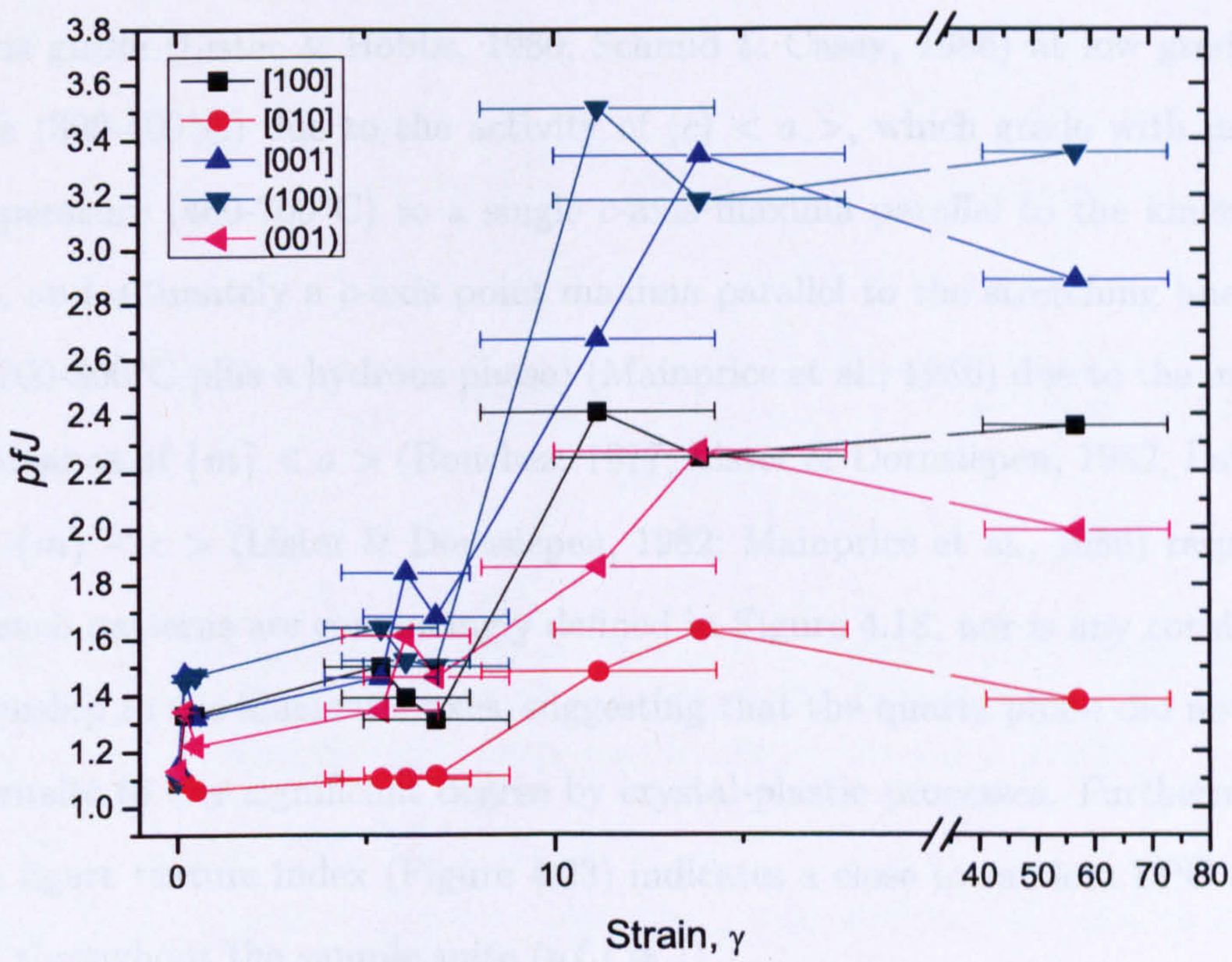

Figure 4.22: The pole figure texture index, pfJ (Section 4.3), versus strain for the crystallographic poles and axes of hornblende. 28% error bars are shown for strain values. Notice the split strain-axis to clarify low-value trends.

Quartz

Figure 4.16 shows the relationship of crystallographic poles and axes for single crystal trigonal quartz. Figure 4.18 displays the commonly presented crystallographic poles for quartz: c(001), a(2-10), m(100), r(101) and z(011) (Schmid et al., 1981; Law et al., 1986; Lloyd et al., 1992), although c and a are perhaps the most important in the interpretation of commonly observed and documented quartz LPO patterns and slip systems (e.g. Law et al., 1990). Examples include the crossed c-axis girdle (Lister & Hobbs, 1980; Schmid & Casey, 1986) at low grade conditions (300-400°C) due to the activity of $(c) < a_{,}>$, which grade with increasing temperature (400-700°C) to a single c-axis maxima parallel to the kinematic Y-axis, and ultimately a c-axis point maxima parallel to the stretching lineation X (at 700-800°C plus a hydrous phase) (Mainprice et al., 1986) due to the increasing dominance of $\{m\} < a >$ (Bouchez, 1977; Lister & Dornsiepen, 1982; Law, 1990) and $\{m\} < c >$ (Lister & Dornsiepen, 1982; Mainprice et al., 1986) respectively. No such patterns are convincingly defined in Figure 4.18, nor is any consistent relationship to the kinematic axes, suggesting that the quartz phase did not deform internally to any significant degree by crystal-plastic processes. Furthermore, the pole figure texture index (Figure 4.23) indicates a close to random LPO distribution throughout the sample suite ($pfJ \approx 1$).

Plagioclase

Figure 4.16 shows the relationship of crystallographic poles and axes for a single triclinic plagioclase crystal. As highlighted by Jiang et al. (2000) and Prior & Wheeler (1999), triclinic plagioclase orientation data is best represented as polar data in both lower and upper hemisphere pole figures. Figure 4.19 show both lower and upper hemisphere pole figure plots for polar crystallographic direction $[UVW]$ orientation data for the plagioclase phase throughout the sample suite, and Figure 4.20 shows lower hemisphere pole figure plots for non-polar plagioclase lattice

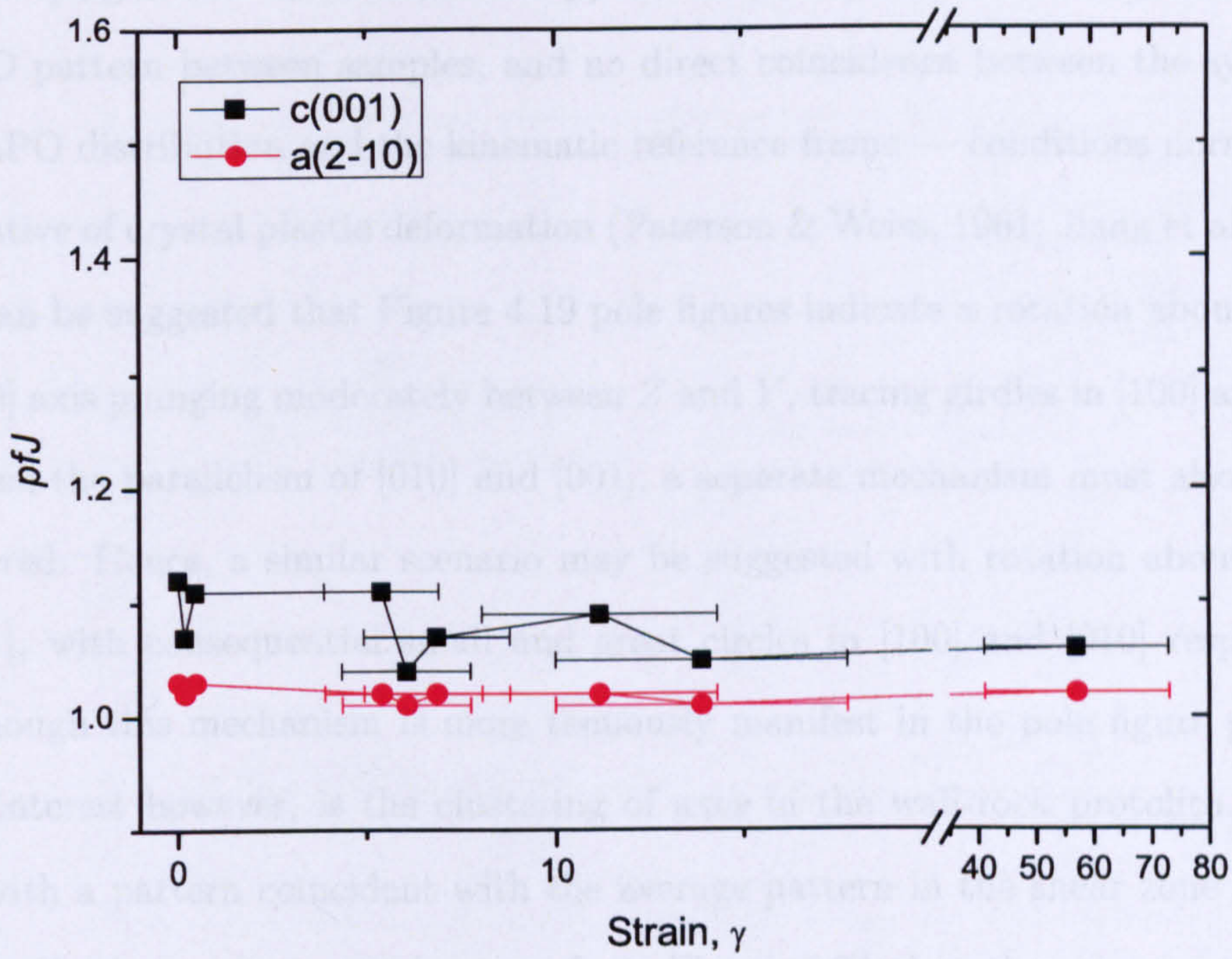

Figure 4.23: The pole figure texture index, pfJ (Section 4.3), versus strain for selected crystallographic poles and axes of quartz. 28% error bars are shown for strain values. Notice the split strain-axis to clarify low-value trends.

planes, (hkl). It can be seen that apparently non-random LPO distributions are prevalent in each sample from the shear zone, including wall-rock protolith Sample 1, characterised by a complex pattern of combined clusters and girdles. Dislocation slip in plagioclase on (010)[100] and (010)[001] is most commonly identified in the literature in ductile deformation of greenschist to amphibolite facies rocks (e.g. Olsen & Kohlstedt, 1985; Kruhl, 1987b; Ji & Mainprice, 1988), although Kruhl (1987b) and Siegesmund et al. (1994) also note the importance of (001) as a slip plane, perhaps at higher grade conditions. They show that their (hkl) align with the foliation plane, and $[UVW]$ cluster around the lineation, or shear direction. It can be seen from Figure 4.19 that maxima and girdles in [100], [010] and [001] can

be tenuously ascribed to a triclinic symmetry with angular relationships appropriate to plagioclase. However, there appears to be only very weak congruence of the LPO pattern between samples, and no direct coincidence between the symmetry of LPO distribution and the kinematic reference frame — conditions normally indicative of crystal plastic deformation (Paterson & Weiss, 1961; Jiang et al., 2000). It can be suggested that Figure 4.19 pole figures indicate a rotation about a fixed [010] axis plunging moderately between Z and Y, tracing girdles in [100] and [001]. Given the parallelism of [010] and [001], a separate mechanism must also be considered. Hence, a similar scenario may be suggested with rotation about a fixed [001], with consequential small and great circles in [100] and [010] respectively, although this mechanism is more tenuously manifest in the pole figure patterns. Of interest however, is the clustering of axes in the wall-rock protolith, Sample 1, with a pattern coincident with the average pattern in the shear zone samples, 2-9. Furthermore, it can be seen from Figure 4.24 that there is no significant change in the degree of clustering, in terms of pattern pfJ, between the protolith sample with $\gamma = 0$, and the deformed examples. The higher values of pfJ for crystallographic axes $[UVW]$ than poles (hkl) is a previously unappreciated artefact of the calculation of pfJ from polar data. Where axes are plotted in terms of non-polar data, pfJ values approach 1, as with those for (hkl). Such computational artefacts formed to impetus that drove Skemer et al. (2005) to develop an alternative measure of fabric strength, the M-index, although it remains for this method to recieve widespread application. What is important is that there is little variation in aggregate pfJ in plagioclase axes from protolith ($\gamma = 0$) to higher strains. Hence, under deformation of the whole rock aggregate, the plagioclase phase appears to deform such that the pattern and intensity of LPO, defined by axis clustering, does not develop beyond that observed in the protolith material, Sample 1. If the wall-rock protolith is considered to possess a random LPO, then the LPO distribution and pfJ indicate that this persists throughout the sample

suite and hence the deformation zone.

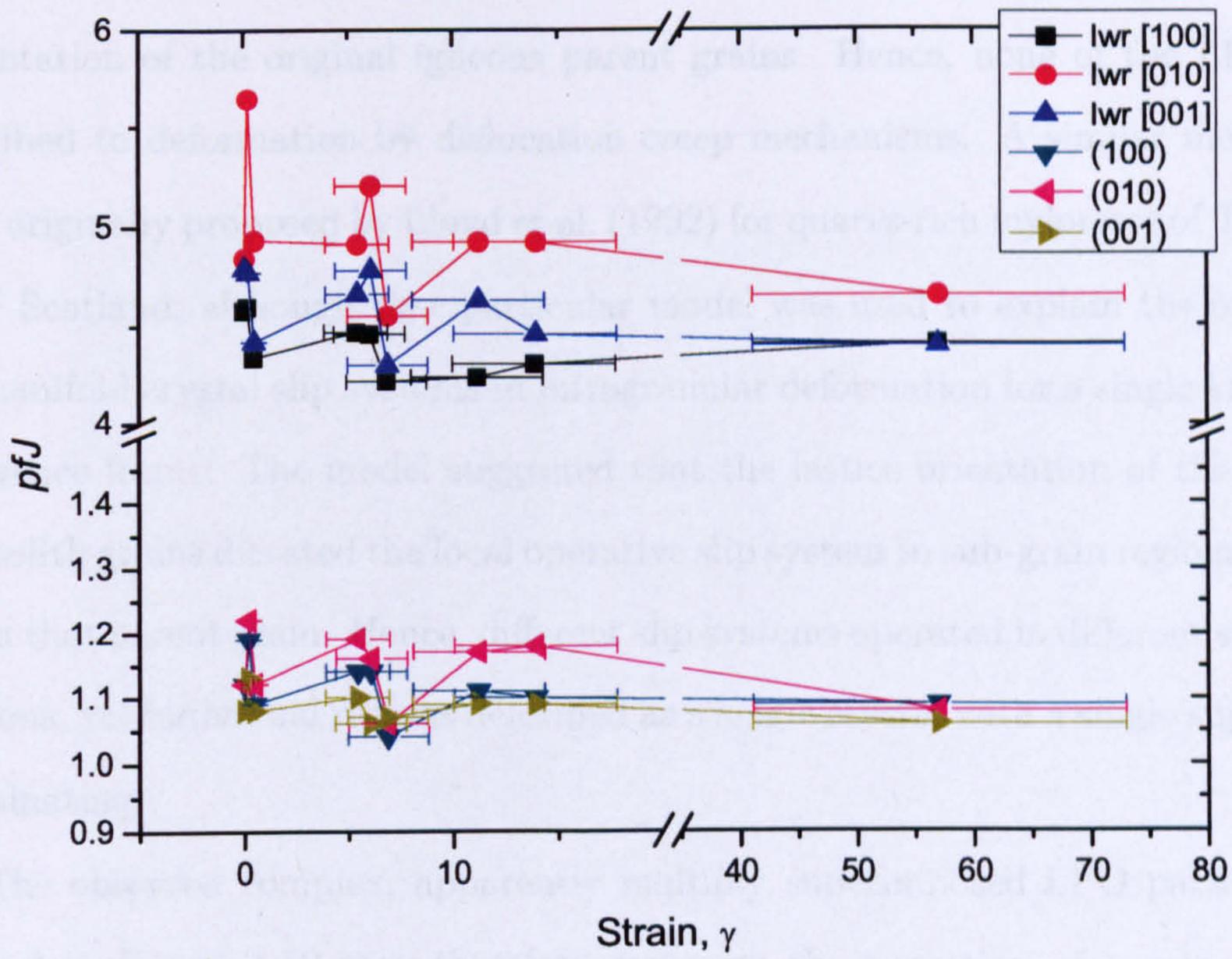

Figure 4.24: The pole figure texture index, pfJ (Section 4.3), versus strain for crystallographic poles and lower hemisphere polar axes of plagioclase. 28% error bars are shown for strain values. Notice the split strain-axis to clarify low-value trends.

A similar pattern of LPO fabric inheritance is was also observed in calcite for experimentally deformed calcite-anhydrite aggregates (Bruhn & Casey, 1997). Furthermore, Prior & Wheeler (1999) and Jiang et al. (2000) present a discussion of plagioclase pole figure patterns following EBSD LPO analysis of a greenschist facies sheared metagabbro from the Combin Zone of the Western Italian Alps. They describe domainal variation in non-random plagioclase pole figures with triclinic symmetry absent of a unique relationship between LPO patterns and the kinematic axes. It is highlighted from spatially subset data that domains of reduced grain size plagioclase which share a similar pole pattern reflect not the symmetry of

the deformation, but the symmetry of the original single parent grain, from which that domain was derived under reduced grain size granular flow. The variation in the LPO pattern across the analysed zone was a function of the differences in the orientation of the original igneous parent grains. Hence, none of the LPO were ascribed to deformation by dislocation creep mechanisms. A similar mechanism was originally proposed by Lloyd et al. (1992) for quartz-rich mylonites of Torridon, NW Scotland, although that particular model was used to explain the operation of manifold crystal slip systems in intragranular deformation for a single kinematic reference frame. The model suggested that the lattice orientation of the original protolith grains dictated the local operative slip system to sub-grain regions derived from that parent grain. Hence, different slip systems operated in different sub-grain regions, yet individual regions deformed as a single crystal with a single slip system dominating.

The observed complex, apparently multiply superimposed LPO patterns presented in Figure 4.19 may therefore represent the operation of a granular flow mechanism on distributed and initially random plagioclase grains in the doleritic aggregate, rather than a LPO formed under internal and homogeneous crystal-plastic deformation and one directly related to the symmetry of the kinematic system (e.g. Olsen & Kohlstedt, 1984; Ji & Mainprice, 1988; Terry & Heidelbach, 2006).

In order to test the theory of Jiang et al. (2000), three subsets of plagioclase orientation data were defined from each of Samples 1, 5 and 9 representing initial, intermediate and extreme positions in the strain gradient of the sample suite. Subsets were chosen based on a visual inspection of the sample and grain relationships. Each individual subset spatially isolates a single felsic clot. If the felsic clots are deforming by a granular flow mechanism of refined, uniformly distributed and randomly oriented original igneous plagioclase grains, then each subset should display a different and unique pole figure pattern that reflects some sort

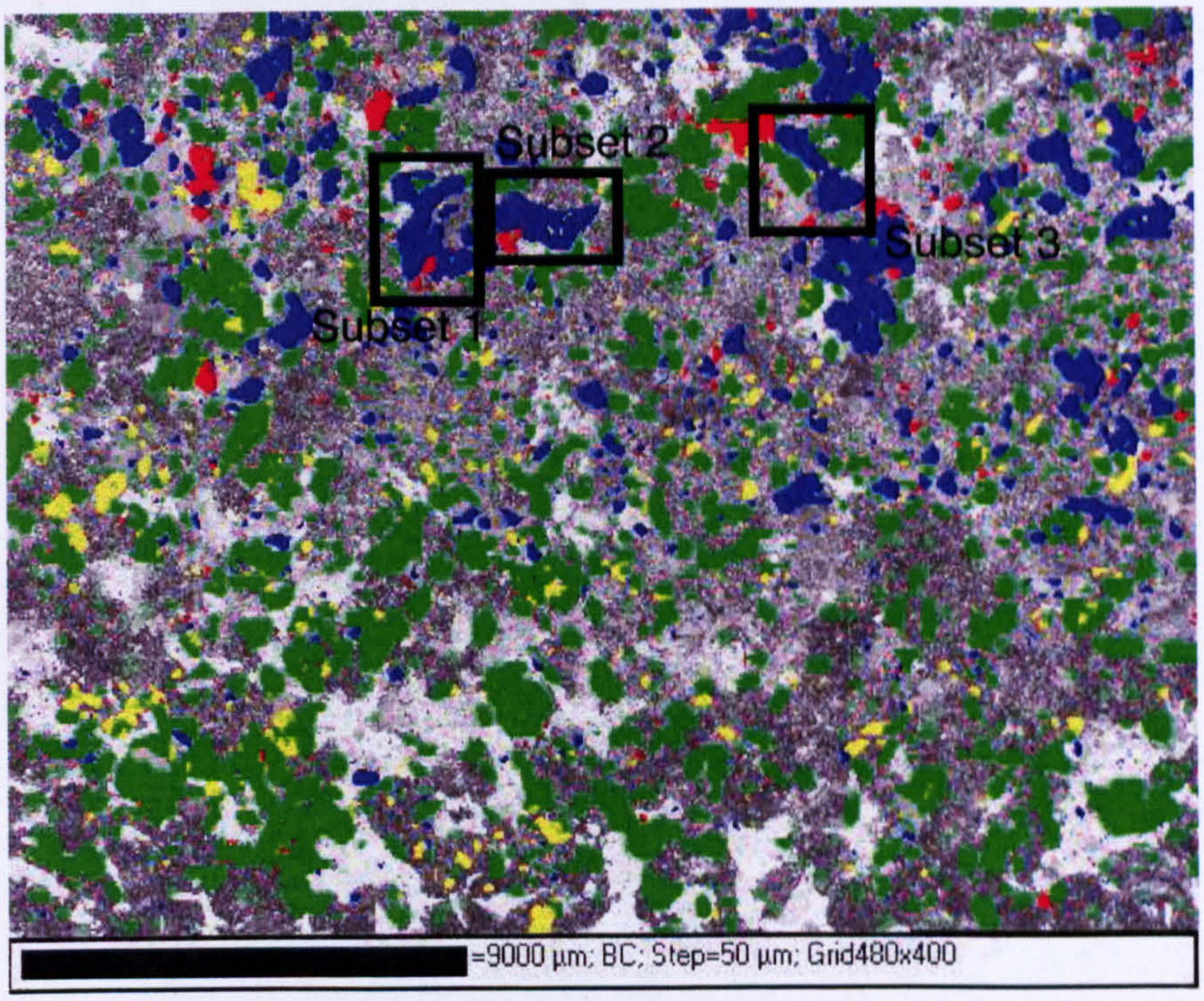

Figure 4.25: EBSD phase map of Sample 1, highlighting the three plagioclase subsets investigated. In this example, subsets represent single grains. Phase data is mounted on a band contrast image (see Section 3.4). Raw EBSD data is processed to remove wildspikes. Non-indexed points are marked by regions of no solid colour. Mis-indexed points are minimised by the different symmetries of the phases here (see Section 3.4), and are generally removed by processing of wildspikes. Green = hornblende, blue = plagioclase, red = quartz, and yellow = clinopyroxene.

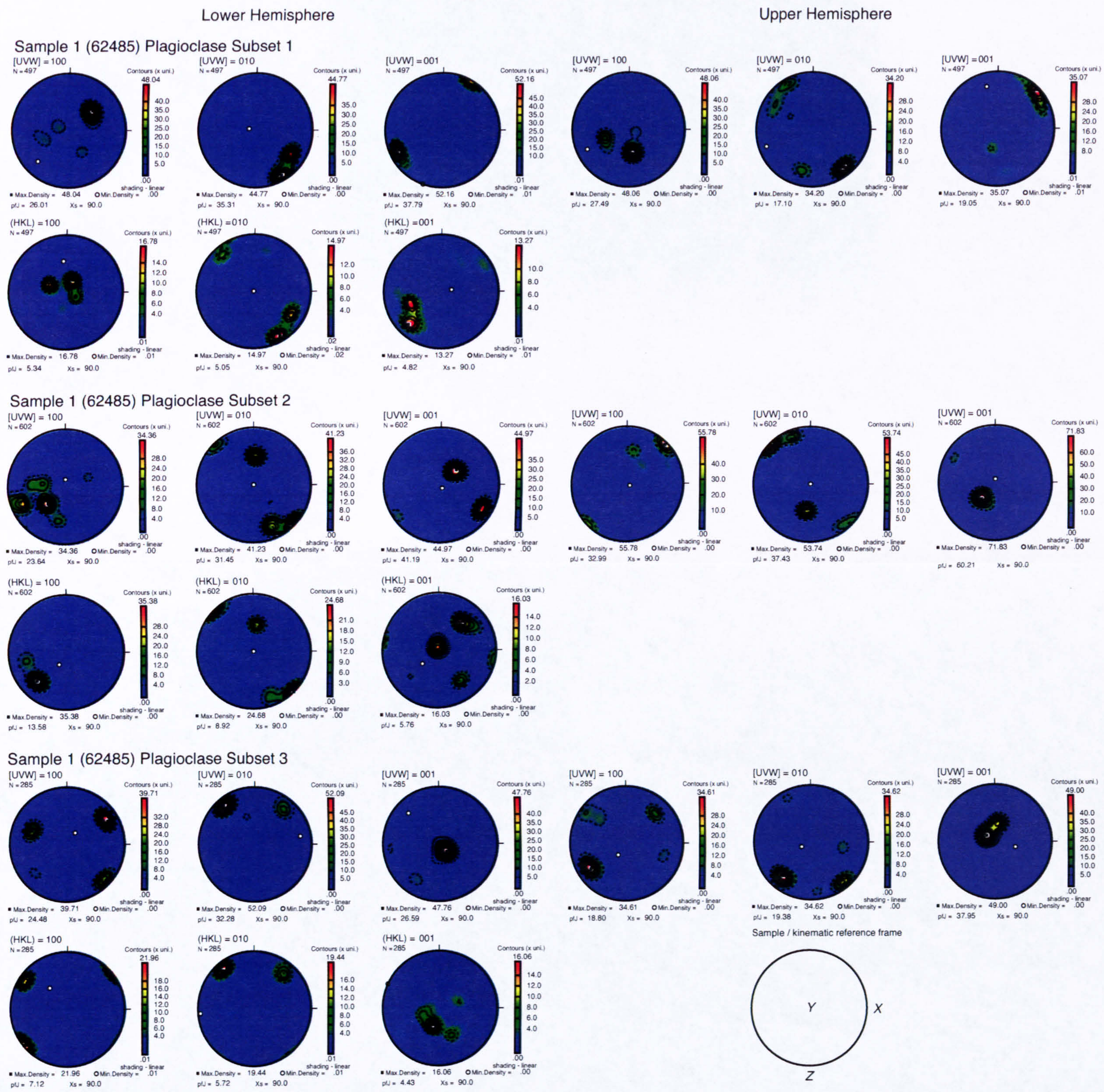

Figure 4.26: Plagioclase phase upper and lower hemisphere $[UVW]$ and (hkl) pole figures, Sample 1 subsets. See text for details and discussion.

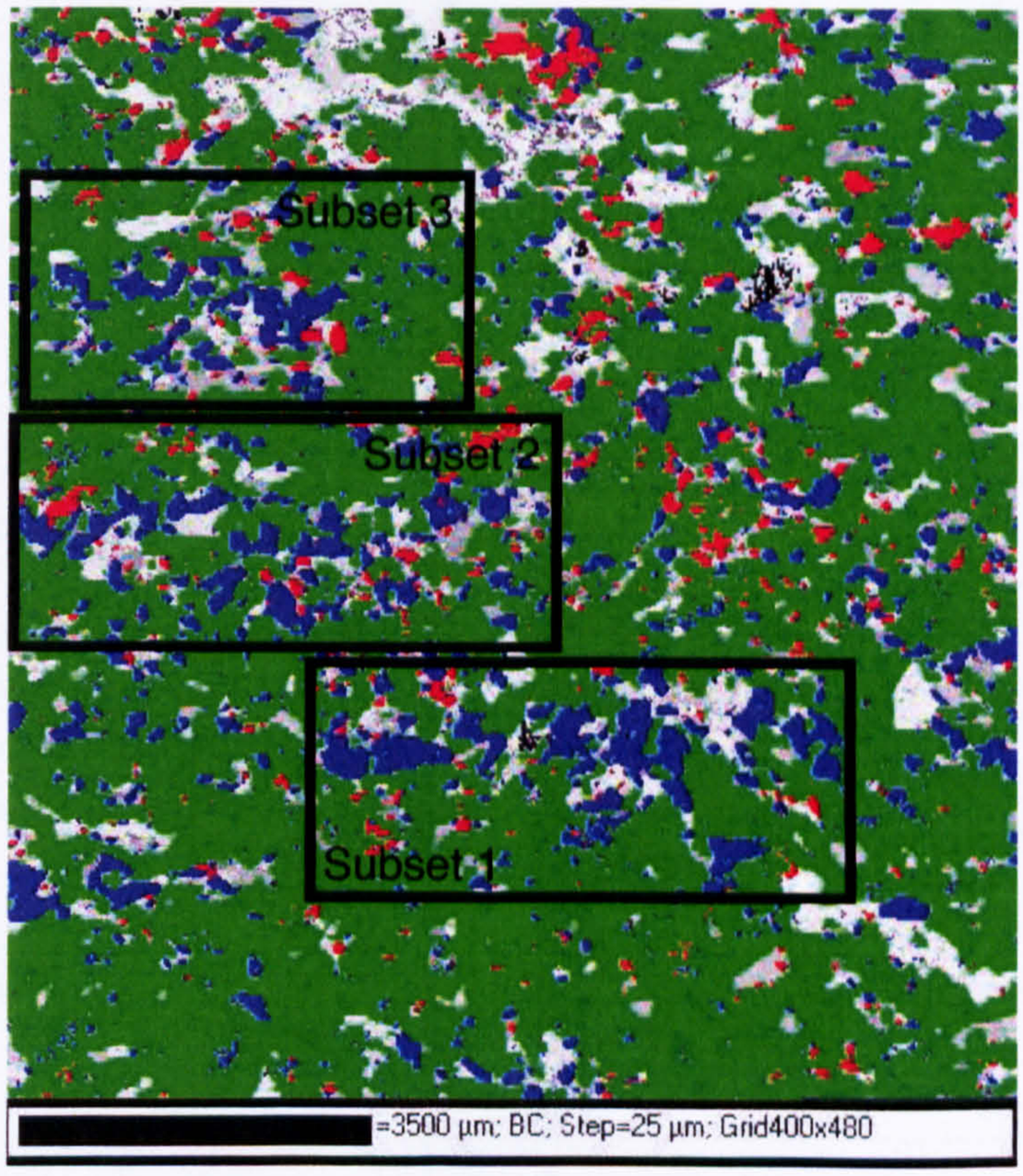

Figure 4.27: EBSD phase map of Sample 5, highlighting the three plagioclase subsets investigated. Subsets represent plagioclase aggregates of originally single grains. Phase data is mounted on a band contrast image (see Section 3.4). Raw EBSD data is processed to remove wildspikes. Non-indexed points are marked by regions of no solid colour. Mis-indexed points are minimised by the different symmetries of the phases here (see Section 3.4), and are generally removed by processing of wildspikes. Green = hornblende, blue = plagioclase, and red = quartz.

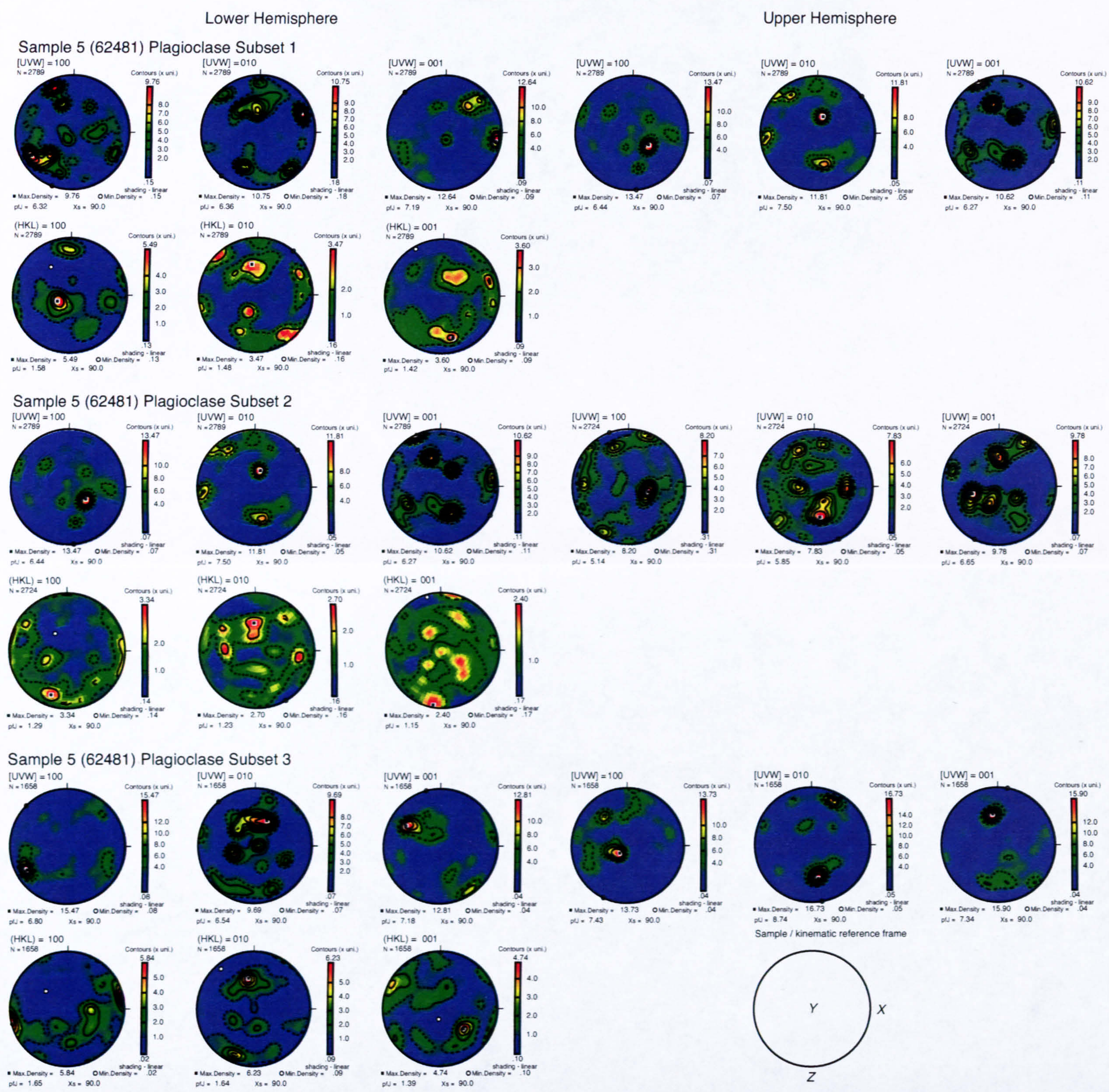

Figure 4.28: Plagioclase phase upper and lower hemisphere $[UVW]$ and (hkl) pole figures, Sample 5 subsets. See text for details and discussion.

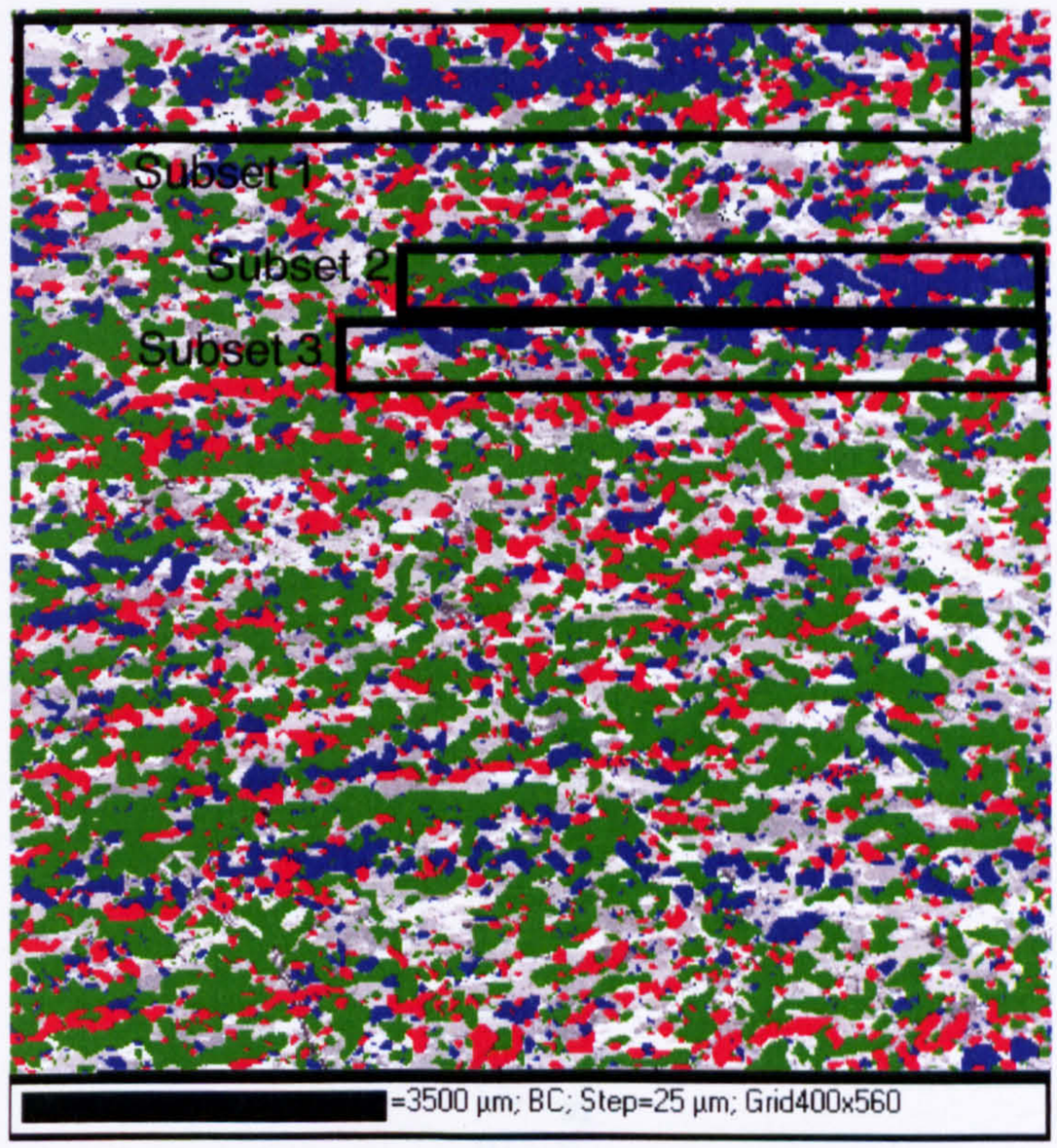

Figure 4.29: EBSD phase map of Sample 9, highlighting the three plagioclase subsets investigated. Subsets represent plagioclase aggregates of originally single grains. Phase data is mounted on a band contrast image (see Section 3.4). Raw EBSD data is processed to remove wildspikes. Non-indexed points are marked by regions of no solid colour. Mis-indexed points are minimised by the different symmetries of the phases here (see Section 3.4), and are generally removed by processing of wildspikes. Green = hornblende, blue = plagioclase, and red = quartz.

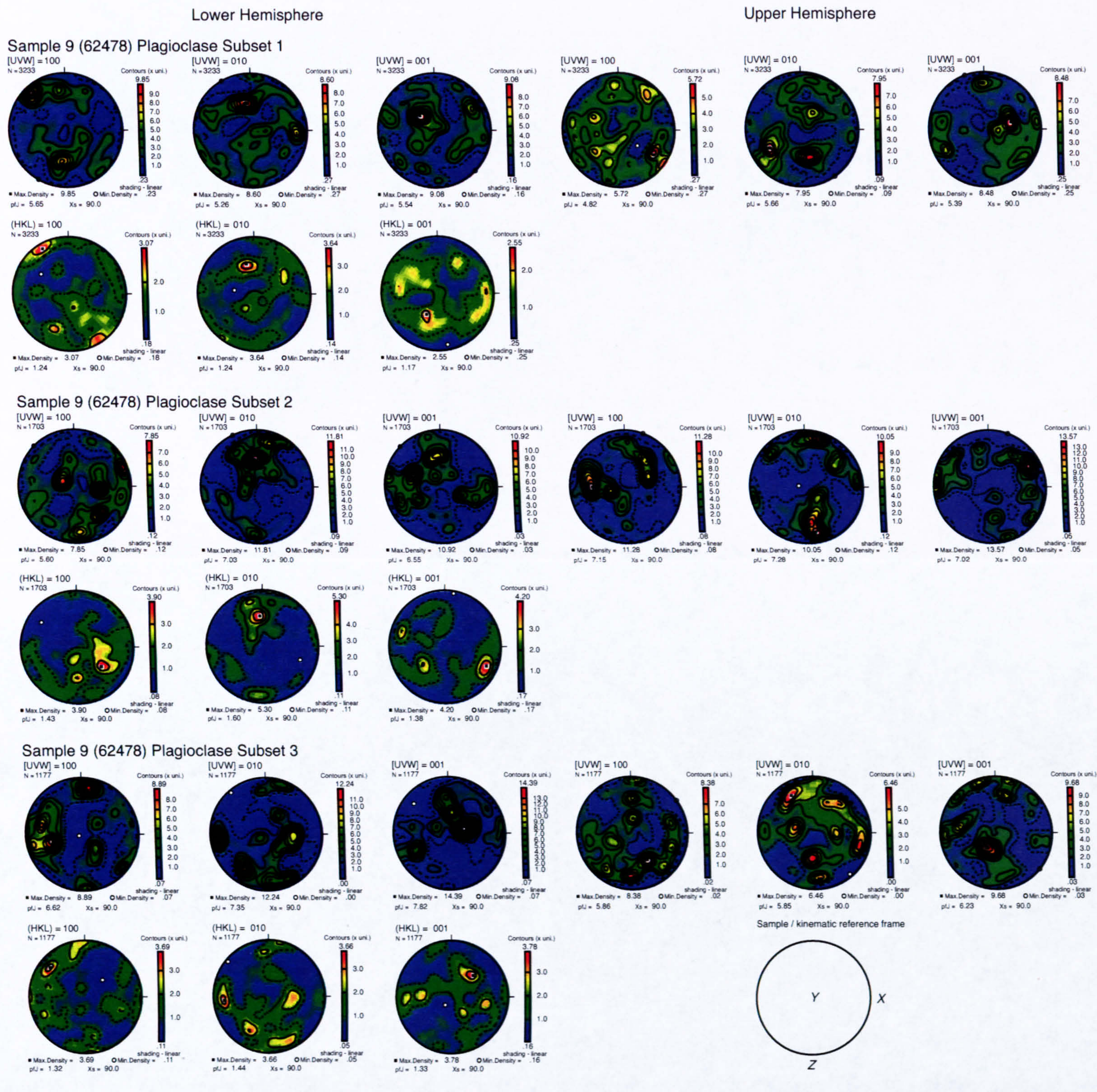

Figure 4.30: Plagioclase phase upper and lower hemisphere $[UVW]$ and (hkl) pole figures, Sample 9 subsets. See text for details and discussion.

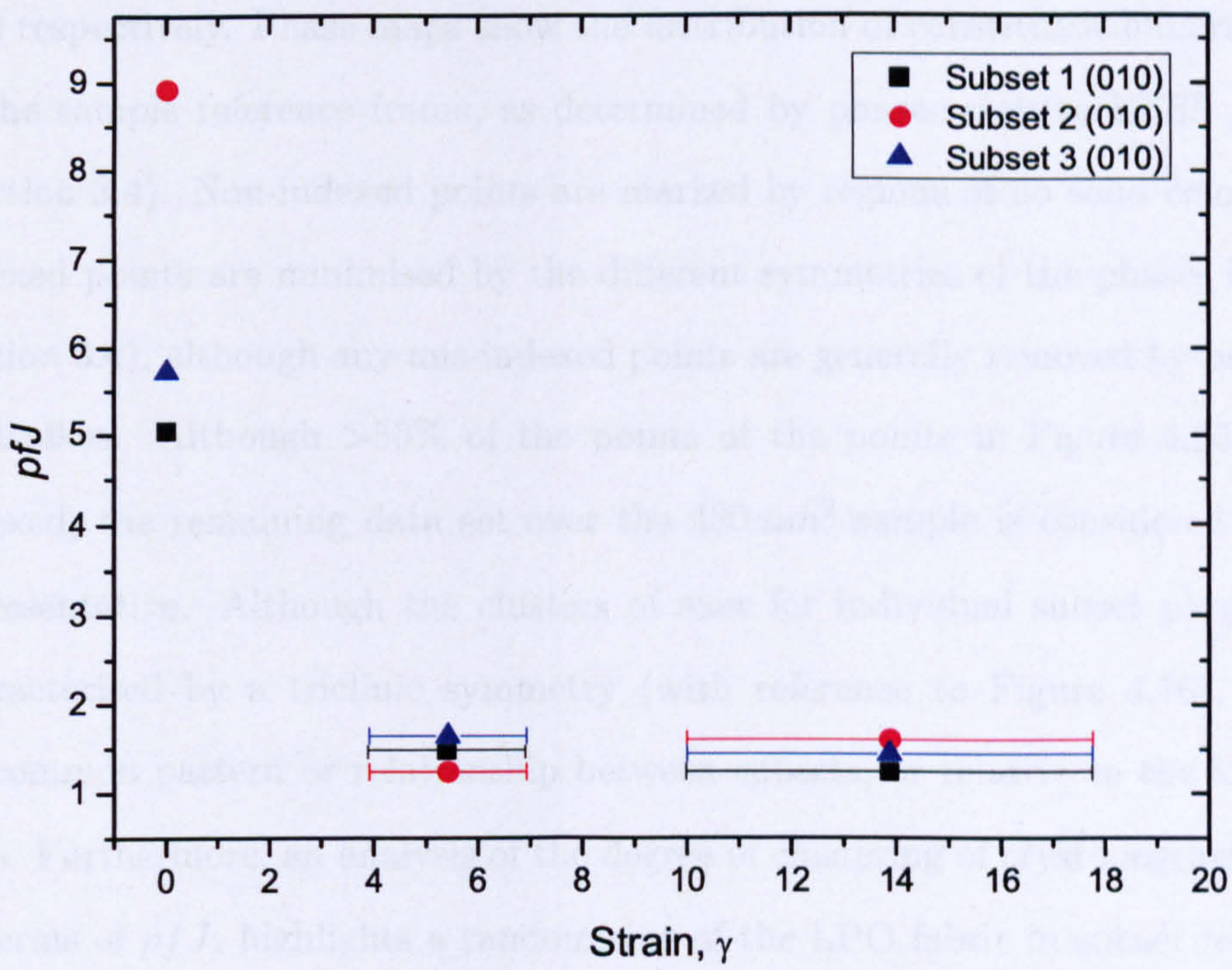

Figure 4.31: The pole figure texture index, pfJ (Section 4.3), versus strain for the crystallographic pole (010) of subset plagioclase. Subset areas are thought to represent originally single grains in the igneous protolith. Subsets 1-3 are non-correlatable between samples. Samples 1, 5 and 9 correspond to finite strains of 0, 5.40 and 13.88 respectively (Table 2.1). Originally single plagioclase grains (high pfJ, low γ) are seen to develop a random LPO with strain (low pfJ, high γ). 28% error bars are shown for strain values.

of crystallographic symmetry in each original parent grain, rather than a unifying LPO symmetry related to the kinematic axes. Moreover, LPO distributions should become increasingly random, from the single crystal symmetry, with increasing deformation.

EBSD-derived phase maps defining subset areas, and their associated pole figure plots are illustrated in Figures 4.25, 4.27 and 4.29, and Figures 4.26, 4.28 and 4.30 respectively. Phase maps show the distribution of constituent mineral phases in the sample reference frame, as determined by phase-sensitive EBSP indexing (Section 3.4). Non-indexed points are marked by regions of no solid colour. Mis-indexed points are minimised by the different symmetries of the phases here (see Section 3.4), although any mis-indexed points are generally removed by processing wildspikes. Although >50% of the points of the points in Figure 4.25 are not indexed, the remaining data set over the $480mm^2$ sample is considered suitably representative. Although the clusters of axes for individual subset plots can be characterised by a triclinic symmetry (with reference to Figure 4.16), there is no common pattern or relationship between subsets, or relative to the kinematic axes. Furthermore, an analysis of the degree of clustering of crystallographic poles in terms of pfJ, highlights a randomising of the LPO fabric in subset felsic clots from the wall-rock protolith, Sample 1 ($\gamma = 0$), through the increasingly deformed bulk material, Samples 5 ($\gamma = 5.40$) and 9 ($\gamma = 13.88$) (Figure 4.31). For simplicity, only (010) is shown in Figure 4.31, which is a commonly observed slip plane in plagioclase (references cites) and exhibits a relationship between finite strain and pfJ that is suitably representative of the other crystallographic poles and axes. Thus, as highlighted in Jiang et al. (2000) it appears that bulk internal crystal-plastic deformation (by e.g. dislocation slip) has not prevailed in the felsic clots of the doleritic material. Instead, LPO pattern symmetries for individual felsic clots reflect the randomised products of refined original single parent grains in an initially isotropic aggregate, rather than being related to and indicative of the

kinematic axes of the deformation system. Increasing strain thus tends to an increasingly diffuse LPO fabric in the reduced grain size felsic clots from that of the initial single parent crystal, as the clot deforms by granular flow.

Clinopyroxene

Figure 4.16 shows the relationship of crystallographic poles and axes for a single monoclinic clinopyroxene crystal. The LPO distribution for clinopyroxene in Sample 1 is close to random (Figure 4.21), supported by the values of $pfJ < 1.1$ for each of the crystallographic poles and axes (Figure 4.21). This is an intuitive result given its occurrence in the protolith material. The LPO pattern cannot be ascribed to commonly documented crystal slip systems, for example (100)[001] (Mainprice & Nicolas, 1989; Passchier & Trouw, 1998; Terry & Heidelbach, 2006). For monoclinic clinopyroxene, the pole figures for [010] and (010) are identical, and so only one is shown.

4.4.2 Texture index analysis

Section 4.3 introduced the texture index J as a means of quantifying the sharpness of clustering of a petrofabric without the complication of considering its orientation distribution. To supplement the results of the LPO analysis (Section 4.4), the texture index for constituent mineral phases of the sample suite are presented here.

Given that the development of LPO is a function of finite strain in rock aggregates, a positive correlation should be observed between the two (Pera et al., 2003; Skemer et al., 2005). Figure 4.32 shows the relationship between the shear strain γ and texture index J for each of the three major constituent mineral phases considered throughout the sample suite. Table 4.5 provides values of the texture index for the sample suite and includes the calculated finite strain for each sample for reference, and to facilitate easier reference with Figure 4.32. A positive rela-

tionship is exhibited in the hornblende phase, and can be approximated with a logarithmic function, whereby the LPO fabric development is very rapid to $J \leq 5$ with relatively low strain ($\gamma \leq 10$), at which point it saturates and continues to develop only fractionally (up to $J \approx 6$) with large increase in strain (in excess of $\gamma = 50$). Data remains too dispersed to fully substantiate this relationship, although a similar trend is observed in the relationship between pfJ and strain for hornblende (Figure 4.22). Clearly, more data from a larger sample base is required to better constrain the relationship. As predicted from observations of the patterns of LPO development, the texture index for the plagioclase and quartz phases appears independent of strain, maintaining a random or uniform distribution ($J \approx 1.5$) for all values of bulk strain. These results support the inference of strain partitioning into the hornblende phase suggested in Sections 4.2.1 and 4.4.1, and discussed further in Section 4.5.

Thus, a positive correlation does not always exists between increasing aggregate finite strain and the development of an LPO fabric. It depends on mineralogy and the mode of deformation exhibited by that phase, whether that be crystal-plastic or a non-crystal-plastic mechanism, such as granular flow. This is described quantitatively by J and pfJ, and illustrated graphically by the development of order and symmetry in pole figures.

4.5 Discussion of petrofabric results:

Deformation in a polyphase aggregate

The topic of deformation and rheology in polyphase aggregates is not a trivial one (Ramsay & Huber, 1983, p120), and the following discussion is by no means an exhaustive review of the subject, nor does it account for all of the chemical, physical and mechanical properties and forces that may affect it during deformation in a natural shear zone.

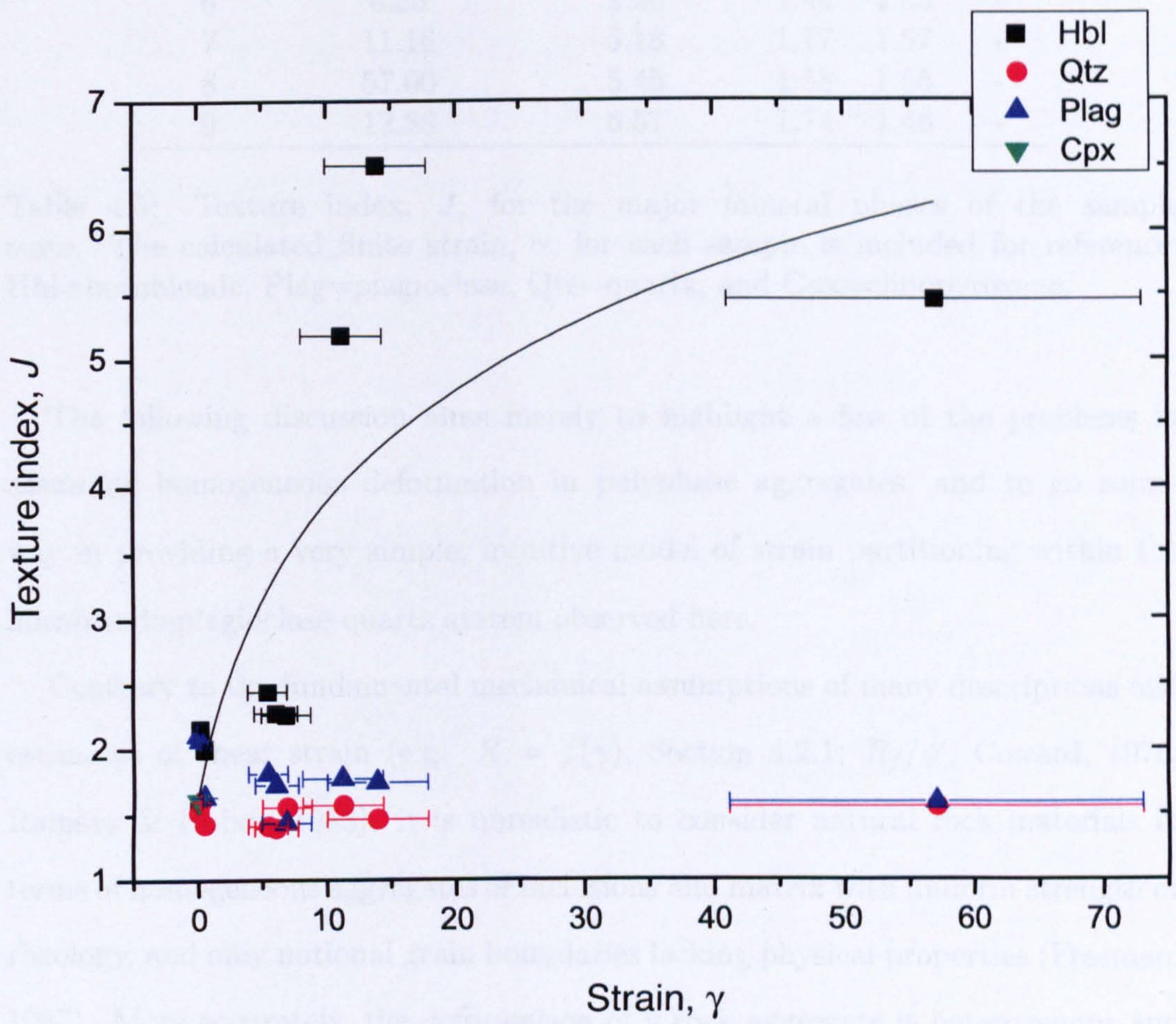

Figure 4.32: The relationship between the texture index, J and strain for constituent mineral phases of the sample suite. Hbl = hornblende, Qtz = quartz, Plag = plagioclase, and Cpx = clinopyroxene.

		Texture index			
Sample	Finite strain γ	J_{Hbl}	J_{Plag}	J_{Qtz}	J_{Cpx}
1	0.00	1.57	2.10	1.52	1.61
2	0.18	2.16	2.06	1.60	-
3	0.46	2.00	1.63	1.43	-
4	6.05	2.27	1.72	1.39	-
5	5.40	2.44	1.81	1.41	-
6	6.85	2.26	1.44	1.55	-
7	11.16	5.18	1.77	1.57	-
8	57.00	5.45	1.58	1.55	-
9	13.88	6.51	1.74	1.46	-

Table 4.5: Texture index, J, for the major mineral phases of the sample suite. The calculated finite strain, γ, for each sample is included for reference. Hbl=hornblende, Plag=plagioclase, Qtz=quartz, and Cpx=clinopyroxene.

The following discussion aims merely to highlight a few of the problems in assuming homogeneous deformation in polyphase aggregates, and to go someway in providing a very simple, intuitive model of strain partitioning within the hornblende-plagioclase-quartz system observed here.

Contrary to the fundamental mechanical assumptions of many descriptions and estimates of shear strain (e.g. $R = f(\gamma)$, Section 4.2.1; R_f/ϕ', Coward, 1976; Ramsay & Huber, 1983), it is unrealistic to consider natural rock materials in terms of homogeneous aggregates of inclusions and matrix with uniform strength or rheology, and only notional grain boundaries lacking physical properties (Freeman, 1987). More accurately, the deformation of a rock aggregate is heterogenous and is a function of a number of physical components including the relative modal fractions of component phases and the competency or viscosity contrast between those phases (Price, 1978; Ramsay & Huber, 1983; Bruhn & Casey, 1997; Kruse & Stünitz, 1999).

Initially postulated by Olsen & Kohlstedt (1984) to explain deformation partitioning in a quartz-feldspar aggregate as a function of relative modal fraction, Handy (1990, 1992) presents end-member microstructures for hypothetical two-phase aggregates with varying viscous strength contrasts between isolated, homo-

geneously distributed inclusions and an enveloping, interconnected matrix. End-member scenarios depend on on the relative volume proportion of the less competent phase. The aggregate can hence be considered in terms of a 'load-bearing framework' (LBF) of weak inclusions isolated in a strong matrix, or 'interconnected weak layers' (IWL) of strong inclusions in a weak matrix (Figure 4.33). Such models provide a mechanism for partitioning strain, and therefore microstructural deformation mechanisms and features, between different phases of a polyphase rock aggregate. Handy (1994) goes on to use this conceptual framework to derive flow laws for two-phase aggregates and to predict the partitioning of strain rate and stress between inclusions and matrix.

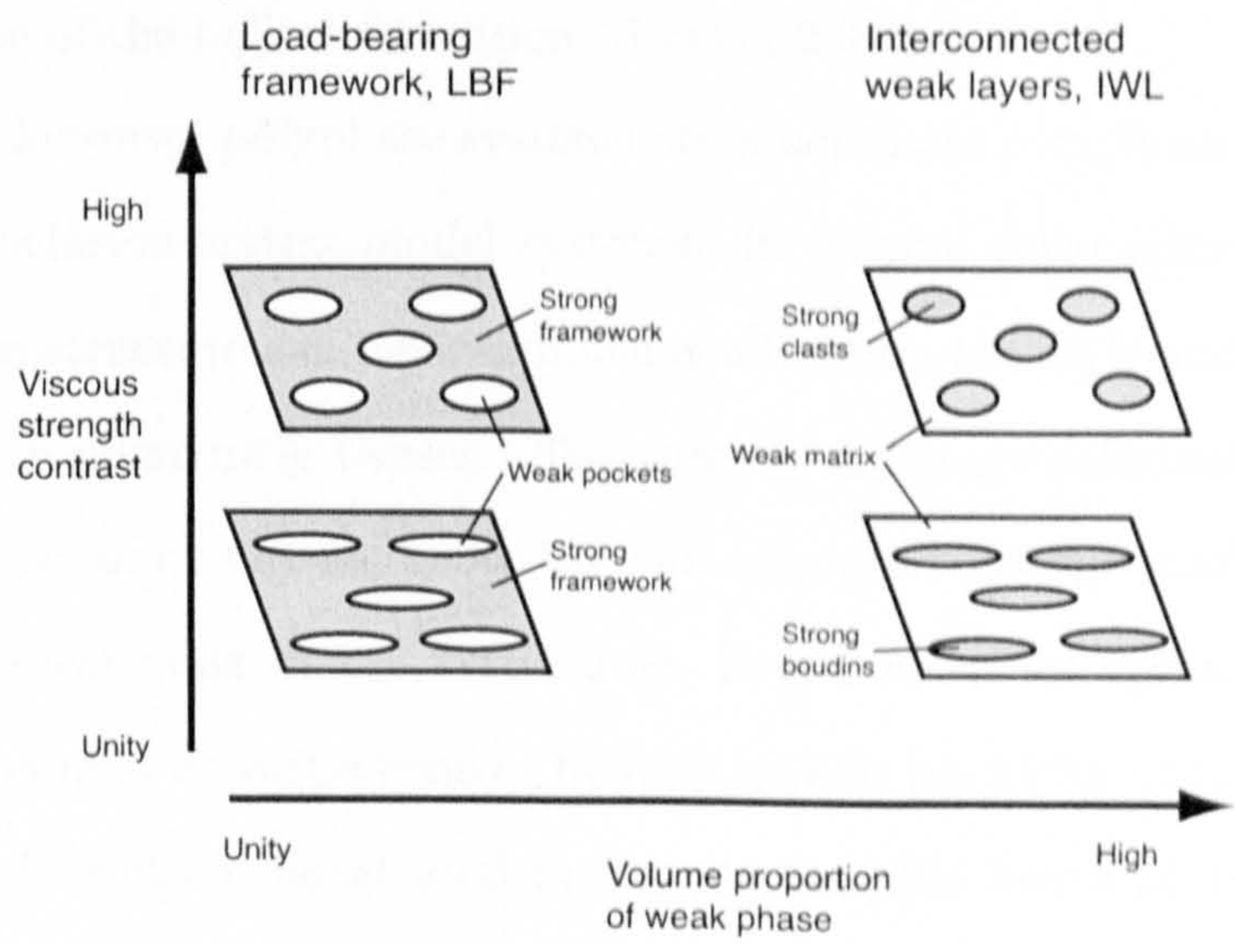

Figure 4.33: Microstructures in deformed two-phase viscous aggregates as a function of volume fraction of the weak phase and the viscous strength contrast between phases. Modified from Handy (1994).

Somewhat earlier, Gay (1968a) modelled Newtonian bodies in a Newtonian fluid matrix in two-dimensions to demonstrate how the viscosity contrast between an inclusion and its matrix is a key factor in controlling the change in particle shape during progressive pure and simple shear deformation. Noteworthy is the result that where the viscosity or competence contrast is > 1, that is, a more

competent inclusion phase with respect to the matrix, the particle changes shape more slowly than the strain ellipse representative of the bulk deformation. Hence, using the ellipticity, or aspect ratio, of more competent inclusions as a proxy for the finite strain ellipse with, for example, Equation 4.1, will give an underestimate of the total finite shear strain. By this logic the hornblende-plagioclase-quartz aggregate studied here, the isolated plagioclase-rich felsic clots must represent the more competent phase, where deformation may be preferentially accommodated in the network of hornblende. This result goes someway in explaining the erroneous underestimates of the finite shear strain calculated from shape fabric parameters in Section 4.2.1 with respect to those inferred from field data and perhaps more representative of the bulk deformation (Section 2.3.1).

In reality, however, polyphase systems are much more complicated than simple Newtonian inclusion-matrix model systems. In natural shear zones a constantly evolving microstructure can have significant affects on the style and expression of deformation. Kenkmann & Dresen (2002) present a 3-stage deformation process in the development of an ultramylonite from an amphibolite facies mafic (amphibole-plagioclase) shear zone in the Ivrea zone, Italy. From an essentially isotropic protolith, a banded mylonite evolves by bulk crystal plasticity at moderate strain where strain becomes concentrated into monomineralic layers of dynamically recrystallised plagioclase, although dynamic recrystallisation in amphibole layers continues also. Amphibole exhibits strong LPO indicating crystal plastic deformation. At larger strains, compositional banding is replaced by phase mixtures, with 10-30μm grains. In this condition, deformation proceeds via heterogeneous nucleation of phases and granular flow (a grain size sensitive process in aggregates with grains <30μm, Stünitz & FitzGerald, 1993), which dominates over contemporaneous crystal plasticity with dynamic recrystallisation (Kruse & Stünitz, 1999; Kenkmann & Dresen, 2002). Granular flow tends to destroy of randomise any original LPO, either from earlier crystal plastic plasticity or from an original single

crystal (Wenk & Christie, 1991). Small grain sizes are maintained in the mixed zones by non-similar phase boundaries (Kenkmann & Dresen, 2002). Thus, in this example, different phases and deformation mechanisms are important at different times in the evolution of the deforming aggregate. Support for the model of Kenkmann & Dresen (2002) is found in similar studies of high-grade mafic shear zones by Kruse & Stünitz (1999) and Baratoux et al. (2005).

The scheme of Kenkmann & Dresen (2002) can be tentatively related to the observations of the sample suite of this study. Although the most deformed samples, e.g. Sample 8 (Figure 4.10), do not show total phase mixing as described for the ultramylonite of Kenkmann & Dresen (2002), all the deformed rocks of the suite do show some degree of phase banding Figures 4.8-4.10). By this stage, Kenkmann & Dresen (2002) predicts that evidence of crystal plasticity by dynamic recrystallisation should be observed in the amphibole bands (especially if it initially formed an interconnected network, Brodie & Rutter, 1985; Kenkmann & Dresen, 2002; Baratoux et al., 2005), and strain should become concentrated in plagioclase bands, where crystal plasticity by dynamic recrystallisation and granular flow may compete depending of the amount of grain size refinement and development of nucleation processes. Although we observe random plagioclase LPO's with strong amphibole fabrics in the deformed samples from the Badcall suite (Figures 4.19-4.20) the post-deformation textural equilibration (with grain sizes 100-250μm) make it difficult to assess the original grain sizes prevalent during deformation. Nevertheless the scheme of Kenkmann & Dresen (2002) provides an interesting hypothesis for the strain accommodation history of Badcall shear zone.

Rigid-body rotation of grains has been proposed as a mechanism for developing LPO in amphibole under deformation, (e.g. Berger & Stünitz, 1996; Azpiroz & Lloyd, in press), where the grain long-axis and the crystallographic [001] axis are generally parallel. Berger & Stünitz (1996) stress that it is difficult to interpret amphibole LPO in terms of either crystal plasticity or passive rigid grain rotation

without e.g. TEM data. A number of observations from the sample suite, however, suggest that passive rotation is not an important mechanism here. (1) Initially equidimensional grains in the protolith do not appear to represent the precursor to rotated elongate grains in the deformed state, without invoking grain fracture (Berger & Stünitz, 1996). (2) Eradication of evidence of the disequilibrium texture characteristic of the protolith hornblende grains, and (3) compositional homogenisation suggests that intragranular processes, rather than, say, grain fracture and rotation, are important in this deformation zone. Furthermore, (4) compatibility issues are raised for rotating laths where hornblende forms the modally dominant phase in the aggregate, rather than being a relatively subordinate phase in a matrix of, say, plagioclase (Berger & Stünitz, 1996). Berger & Stünitz (1996) suggest that passive rotation may be a more important process in rocks with modally subordinate amphibole with respect to plagioclase, and where fluid activity is important.

The relative deformation mechanisms between amphibole and plagioclase is difficult to fully assess without additional analytical techniques, such as TEM (Berger & Stünitz, 1996; Kenkmann & Dresen, 2002), which are beyond the facilities available to this project and the objectives of this work. Furthermore, what appears to be significant textural equilibration has occurred post-deformation, such that original grain boundary geometries, phase relationships and grain size distributions cannot be accurately assessed with respect to deformation. What is clear is that both plagioclase and amphibole underwent grain size refinement related to deformation (Section 4.1). The strong LPO observed in amphibole also suggests that this phase accommodated strain by crystal plastic processes. Strain in the plagioclase fraction is further evident by LPO randomisation of original single crystal symmetries, which may indicate granular flow subsequent to sufficient grain refinement by dynamic recrystallisation such that grain size sensitive processes could prevail.

4.6 Conclusions

In order to provide a means of calculating the seismic properties of the sample suite, and to provide a reference frame relating their seismic properties and finite strain, it is necessary to characterise the petrofabric and petrophyisical properties of the rock aggregates.

1. In Section 4.1, optical microscopy and EMPA shows that the rock sample suite from Upper Badcall can be broadly regarded as an aggregate of hornblende, plagioclase and quartz (± clinopyroxene in the protolith material). Furthermore it illustrates the development of a strong tectonic fabric with increasing strain, with associated grain refinement.

2. Using the ellipticity of deformed felsic aggregates as a proxy for the finite strain ellipse, Section 4.2.1 presents an alternative method for calculating the finite strain profile for the deformation zone and sample suite. Values of strain are significantly underestimated with respect to those calculated from macro-scale structural data (Section 2.3). Restoration of displacements across the shear zone, calculated from the microstructurally-determined strain profile, does not provide a pre-deformation geometry of the Scourie dyke as observed in the wall-rock. Hence, this method of strain calculation is considered erroneous, in this example.

3. A sensitivity analysis of strain calculation to error in measuring linear and planar petrofabric elements suggests an error in presented strain values of ±28%.

4. Section 4.4 highlights electron backscatter diffraction (EBSD) as an efficient and accurate means of characterising the lattice preferred orientation (LPO) distribution in the constituent mineral phases of a rock aggregate. In the dominantly hornblende-plagioclase-quartz aggregate of the sample suite for

Upper Badcall, it is shown that a strong LPO fabric developed with increasing strain in the hornblende phase, whilst the plagioclase and quartz phases showed a consistently random LPO distribution across the strain gradient.

5. The symmetry of the LPO distribution in the hornblende phase is congruent with the kinematic axes, and suggests deformation accommodated by crystal-plasticity with a [100](001) slip system.

6. The random LPO fabrics of plagioclase and quartz cannot be correlated with the kinematic axes of the deformation. Analysis of refined clots of originally single plagioclase crystals from samples across the strain gradient exhibit a randomising of the LPO fabric with increasing strain, from an original single crystal configuration. This suggests deformation by a granular flow mechanism which acted to diffuse the original LPO of the protolith.

7. As quantified by the texture index, J (Section 4.3), LPO development in the hornblende phase becomes saturated by a finite shear strain of approximately $\gamma = 10$ (Section 4.4.2). This trend is reflected in a similar texture index for individual crystallographic poles or directions, pfJ, where the intensity of clustering of individual hornblende crystallographic axes and poles becomes saturated by $\gamma = 10$ (Section 4.4.1).

Chapter 5 continues the work-flow model with an additional step, describing how petrophysical properties, including the quantified aggregate LPO presented here, are used to calculate seismic properties for the sample suite.

Chapter 5

Seismic properties

This chapter presents a further step in the work-flow model to calculate strain-calibrated seismic properties in a representative lower crustal lithology from its petrofabric. Petrophysical and seismic properties are calculated from the quantified and strain-calibrated petrofabric data of Chapter 4, and an investigation is conducted into the relationship between seismic properties, finite strain and modal composition. Results presented herein comprise the foundations of a potentially valuable geophysical tool in remotely sensing finite strain and petrofabric intensity and orientation in the lower crust, as shown in Chapter 6.

5.1 Elastic and seismic anisotropy

Seismic anisotropy describes the azimuthal dependance of seismic wave velocity (P- and S-wave velocity anisotropy), and the differential velocity of orthogonally polarised waves during shear-wave birefringence (shear-wave splitting anisotropy) (Babuska & Cara, 1991; Kendall, 2000; Mainprice et al., 2000).

Sections 1.3- 1.4 describe the properties that have been shown to control or contribute to seismic velocity and anisotropy. As highlighted there, and in Section 1.5, it is the intrinsic material properties of a homogeneous aggregate, namely LPO, that are central in generating seismic anisotropy in the lower crust (e.g. Mainprice

& Nicolas, 1989), and hence in its calculation and prediction, and the competing effects of temperature and pressure on seismic properties are assumed to cancel (e.g. Holbrook et al., 1992; Christensen & Mooney, 1995). These assumptions form a platform upon which the following work-flow and calculations are based.

The seismic properties of a material are a function of the physical properties of that material. For example, it can be shown that the compressional and shear-wave velocities, V_p and V_s, are a function of the bulk (κ) and shear moduli (μ) of the host material, in addition to its bulk density (ρ) (Shearer, 1999; Sheriff & Geldart, 1999):

$$V_p = \sqrt{\frac{\kappa + \frac{4}{3}\mu}{\rho}} \tag{5.1}$$

$$V_s = \sqrt{\frac{\mu}{\rho}} \tag{5.2}$$

Such generalised equations hold true for homogeneous and elastically isotropic materials. However, most geological materials do not satisfy this condition. In nature, geological materials are polyphase and polycrystalline aggregates, where constitutive mineral phases themselves show an inherent elastic anisotropy as a function of their crystal structure and chemical composition. Hence, elastic anisotropy can exist in geological units on a micro- or crystal-scale, which is then manifest in meso- and macro-scales in, for example, aggregate LPO, compositional layering and hence tectonic structures (Mainprice & Nicolas, 1989; Mainprice, 2000).

Thus, for the determination of seismic properties, the bulk physical properties of geological materials are better described in terms of their elastic properties by the fourth-order elastic stiffness tensor, c_{ijkl}, relating the stress (σ) and infinitesimal strain (ε) tensors for that material or aggregate (Crampin, 1984b; Babuska & Cara,

1991; Kendall, 2000).

$$\sigma_{ij} = c_{ijkl}\varepsilon_{kl} \tag{5.3}$$

For infinitesimal strain,

$$\varepsilon_{kl} = \frac{1}{2}\left(\frac{\partial u_k}{\partial x_l} + \frac{\partial u_l}{\partial x_k}\right) \tag{5.4}$$

where u_n are material displacements and x_n refers to the defined Cartesian coordinate system (Crampin, 1984b; Babuska & Cara, 1991; Kendall, 2000).

For an arbitrary anisotropic medium, the elastic stiffness tensor possesses symmetry such that permutation of indices permits a reduction in the number of independent elastic coefficients. Thus 81 terms are reduced to 21 and represented in a 6×6 matrix, where only 21 independent terms are required to populate the 36 term matrix due to symmetry about the diagonal (Crampin, 1984b; Thomsen, 1986; Babuska & Cara, 1991; Kendall, 2000). The matrix C_{ij} thus forms a practical representation of the full c_{ijkl} tensor, and is more simply denoted according to Voigt (1928) where,

ij	kl	and	11	22	33	32=23	31=13	12=21
↓	↓		↓	↓	↓	↓	↓	↓
α	β		1	2	3	4	5	6

such that:

$$C_{\alpha\beta} = \begin{pmatrix} c_{11} & c_{12} & c_{13} & c_{14} & c_{15} & c_{16} \\ c_{12} & c_{22} & c_{23} & c_{24} & c_{25} & c_{26} \\ c_{13} & c_{23} & c_{33} & c_{34} & c_{35} & c_{36} \\ c_{14} & c_{24} & c_{34} & c_{44} & c_{45} & c_{46} \\ c_{15} & c_{25} & c_{35} & c_{45} & c_{55} & c_{56} \\ c_{16} & c_{26} & c_{36} & c_{46} & c_{56} & c_{66} \end{pmatrix} \tag{5.5}$$

The number of independent elastic coefficients required to characterise the elasticity matrix can be further reduced in materials with higher symmetry. For example, C_{ij} can be represented by 9 independent elastic coefficents for a material possessing orthorhomic symmetry, and 3 for a cubic one (Crampin, 1984b; Thomsen, 1986; Babuska & Cara, 1991).

Given a full description of the three-dimensional bulk elastic properties of a material, one can compute the phase velocity of a plane wave passing through that medium via a consideration of the equation of particle motion for elastic waves in terms of c_{ijkl}, with Equations 5.3 and 5.4 (Babuska & Cara, 1991; Shearer, 1999; Kendall, 2000),

$$\rho\frac{\partial^2 u_i}{\partial t^2} = \frac{\partial \sigma_{i,j}}{\partial x_j} = c_{ijkl}\frac{\partial^2 u_l}{\partial x_j \partial x_k} \tag{5.6}$$

where u_n refers to the displacement, ρ is density, t is time and x_n are the Cartesian coordinate components in a wave reference frame. Solution of this equation with the displacement field relationship (Babuska & Cara, 1991, p.15) gives the Christoffel equation (Babuska & Cara, 1991; Kendall, 2000),

$$\det \mid c_{ijkl}n_i n_j - \rho {v_n}^2 \delta_{il} \mid = 0 \tag{5.7}$$

relating the wave velocity v to the elasticity tensor c_{ijkl}, bulk material density ρ and the Kronecker delta δ_{il} ($\delta_{il} = 1$ for $i = l$, $\delta_{il} = 0$ for $i \neq l$) in a wave-front normal coordinate system with direction cosines $n_i n_j$. The Christoffel equation provides three solutions to the velocity for a given wave-front normal, n_i: one quasi-compressional wave and two orthogonally polarised quasi-shear waves — 'quasi' in recognition of the fact that in anisotropic materials, the seismic wave-front normal is not necessarily parallel to the wave path, nor are S-wave polarisations necessarily exactly orthogonal to it.

When velocities are calculated for all azimuths across a notional sphere repre-

senting the full three-dimensional distribution of velocities, the respective velocity anisotropies can be determined. Velocity anisotropies for V_p, and the relatively fast and slow orthogonally polarised shear-waves, V_{s1} and V_{s2} respectively, can be found by (Mainprice & Humbert, 1994),

$$AV_{p,s1,s2} = \left(\frac{V_{p,s1,s2}max - V_{p,s1,s2}min}{\overline{V_{p,s1,s2}}}\right) \times 100 \tag{5.8}$$

where $V_n max$ and $V_n min$ are not necessarily parallel. $\overline{V_n}$ is the average velocity, $\frac{1}{2}(V_n max + V_n min)$.

The shear-wave splitting anisotropy for a given azimuthal direction can be defined as the percentage velocity difference between V_{s1} and V_{s2} relative to the fast S-wave phase (Babuska & Cara, 1991; Mainprice & Silver, 1993):

$$AV_s = \left(\frac{V_{s1} - V_{s2}}{V_{s1}}\right) \times 100 \tag{5.9}$$

Alternatively, shear wave splitting anisotropy can be simply defined as the difference in fast and slow shear-wave velocities in any given azimuthal direction (Babuska & Cara, 1991; Mainprice & Silver, 1993),

$$\delta V_s = V_{s1} - V_{s2} \tag{5.10}$$

or the time lag, in seconds, between split shear waves propagating through an anisotropic medium over a distance d (Babuska & Cara, 1991; Mainprice & Silver, 1993):

$$\delta t_s = \frac{d}{\delta V_s} \tag{5.11}$$

The orientation of the fast polarised shear-wave, V_{s1}, is commonly presented with the aforementioned seismic attributes, and can be diagnostic in determining the spatial orientation of petrofabric in aggregate materials, where the polarisation

orientation is parallel to the plane of fastest V_{s1} (e.g. Babuska & Cara, 1991; Sapin & Hirn, 1997; Huang et al., 2000).

A more detailed and mathematically complete description of the elastic stiffness tensor and Christoffel's equation for phase velocity can be found in e.g. Babuska & Cara (1991); Kendall (2000); Mainprice et al. (2000).

A great deal of data is available in the literature defining the single crystal elastic constants for a plethora of rock-forming minerals and across their structurally and chemically defined bounds of variability and solid solution (e.g. Aleksandrov & Ryzhova, 1961*b*,*a*; Aleksandrov et al., 1974; Collins & Brown, 1998). Such data is generally experimentally derived, using resonance, ultrasonic pulse and X-ray scattering methods to name a few (see review in Aleksandrov & Ryzhova, 1961*a*). A data set of single crystal C_{ij}'s for rock-forming minerals thus allows us to calculate the the bulk C_{ij}'s for a polyphase and polycrystalline aggregate, given that the constituent phases, their relative modal fractions, densities and microstructural information, such as LPO, are known.

A number of averaging schemes for calculating the bulk or effective elastic properties of polyphase aggregates from single crystals have been proposed in the Earth and materials science literature. A far from exhaustive list of examples include Eshelby (1957); Hashin & Shtrikman (1962, 1963); Walpole (1969); Willis (1977); Hamilton & Kohn (1988); Castañeda & Willis (1995); Zheng & Du (2001), with reviews in Castañeda & Willis (1995); Mainprice (2000); Zheng & Du (2001); Wendt et al. (2003). Averaging principles vary in mathematical approach and complexity, and in terms of their fundamental assumptions and inclusion of microstructural elements such as grain size, grain shape, phase distribution, relative phase connectivity, and grain boundary conditions. Many of the more complex techniques are computationally intensive and impractical for everyday application.

One of the most popular and widely applied schemes however is the Voigt-Reuss-Hill average (Voigt, 1928; Reuss, 1929; Hill, 1952; Mainprice & Humbert,

1994; Mainprice, 2000; Mainprice et al., 2000), especially where LPO is the prime microstructure investigated. The VRH average is an arithmetic mean of the upper bound Voigt and lower bound Reuss estimates, which assume a macroscopically uniform material with no terms for grain shape, phase distribution, or grain-neighbour interactions. Although the VRH scheme is notably simplistic, and given that the Hill average lacks theoretical justification, it has consistently been shown to lie close to experimentally determined values and those of higher order averaging schemes (Hill, 1952; Mainprice & Humbert, 1994; Mainprice, 2000). The Voigt scheme is essentially an average of relationships expressing the stress in a single crystal in terms of a constant strain, and *vice versa*, the Reuss scheme averages relations expressing strains in terms of a given stress. That is, the Voigt and Reuss averages assume, respectively, that strain and stress across the sample is independent of position and is equal to the macroscopic value for the whole sample under a given stress and strain. The Voigt and Reuss elasticity bounds for a polyphase and polycrystalline aggregate of m mineral phases with volume fraction v are thus defined as (Mainprice & Humbert, 1994; Mainprice et al., 2000),

$$c_{ijkl}^{Voigt} = \Sigma \overline{c_{ijkl}^{m}} . v_m \tag{5.12}$$

$$c_{ijkl}^{Reuss} = \Sigma \overline{s_{ijkl}^{m}} . v_m \tag{5.13}$$

where s is the compliance which is related to the elastic stiffness according to $s = c^{-1}$, and the over-line refers to an aggregate average. $\overline{c_{ijkl}^{m}}$ is calculated from the orientation distribution of each phase by volume fraction weighted summation (Mainprice & Humbert, 1994; Mainprice et al., 2000),

$$\overline{c_{ijkl}^{m}} = \Sigma c_{ijkl}^{m}(g) . v(g) \tag{5.14}$$

where $v(g)$ is the volume fraction of grains of phase m in orientation g, and c^m_{ijkl} is the single crystal elastic stiffness tensor for that orientation of that phase. The Hill average is then the arithmetic mean of the Voigt upper bound and the Reuss lower bound (Hill, 1952):

$$c^{Hill}_{ijkl} = \frac{1}{2}(c^{Voigt}_{ijkl} + c^{Reuss}_{ijkl}) \tag{5.15}$$

Practically, the VRH elastic averaging algorithm is combined with the Christoffel equation (Babuska & Cara, 1991) for the calculation of seismic velocities and anisotropies across all possible azimuthal directions in the Fortran programs *ANISch5* and *VpG* — current generations of those presented in Mainprice (1990).

As described in Section 3.4, the output of petrofabric analysis via EBSD is a Channel text file, **.ctf* (Appendix C), containing a full description of the lattice orientation distibution, expressed as Euler angle triplets, for all user-defined mineral phases over the prescribed area of sample. The Mainprice (1990) programs are customised to accept **.ctf* files from automated-EBSD, and combine the LPO data, via its orientation distribution function, with relevant constitutive mineral phase data including density and single crystal C_{ij}'s according to Equations 5.7 to 5.15, to generate a bulk aggregate C_{ij} and a series of V_n and AV_n stereographic projections and data.

This method of calculating petrophysical and seismic properties from single crystal data and a description of the aggregate lattice orientation distribution is a well established one, and has been shown to provide representative results (e.g. Mainprice & Nicolas, 1989; Mainprice & Humbert, 1994; Kendall, 2000; Mainprice, 2000)

5.1.1 Single crystal seismic properties

As an example of the aforementioned procedure of seismic property calculation, and for reference in the subsequent sections, Figure 5.1 shows plots of V_p and AV_s for the single crystals of the major modal phases of Samples 1-9 (hornblende, plagioclase, quartz, ± clinopyroxene). Seismic properties for each mineral phase are presented in a reference frame such that the crystallographic axis of the commonly observed dominant crystal slip system in that phase (references cited, Section 4.4.1) is parallel to the kinematic X-direction, and the associated slip plane is normal to Z. This is only an approximation, and in some phases (e.g. quartz) the manifestation of crystal slip systems with respect to the kinematic axes is much more complex (see Section 4.4.1) (Passchier & Trouw, 1998).

It should be noted here that plots are contoured according to the inverse colour scheme typical in the presentation of seismic velocity and anisotropy data, whereby warm colours mark relatively slow values, or minima, and cold colours represent relatively fast values, or maxima.

For reference, the single crystal elastic stiffness matrices, C_{ij}, and their associated densities used in the calculation of seismic properties, here and in Section 5.2.1, are presented in Equations 5.16-5.19 below. Elastic matrices are presented in the reference frames as illustrated in Figure 5.1 and looking parallel to Y.

Hornblende, $\rho = 3.305 gcm^3$, Aleksandrov & Ryzhova (1961*b*):

$$C_{ij_{Hbl}} \begin{pmatrix} 1.1600 & 0.6140 & 0.4990 & 0.0000 & 0.0000 & -0.0430 \\ 0.6140 & 1.9160 & 0.6550 & 0.0000 & 0.0000 & -0.1000 \\ 0.4990 & 0.6550 & 1.5970 & 0.0000 & 0.0000 & 0.0250 \\ 0.0000 & 0.0000 & 0.0000 & 0.5740 & 0.0620 & 0.0000 \\ 0.0000 & 0.0000 & 0.0000 & 0.0620 & 0.3680 & 0.0000 \\ -0.0430 & -0.1000 & 0.0250 & 0.0000 & 0.0000 & 0.3180 \end{pmatrix} \quad (5.16)$$

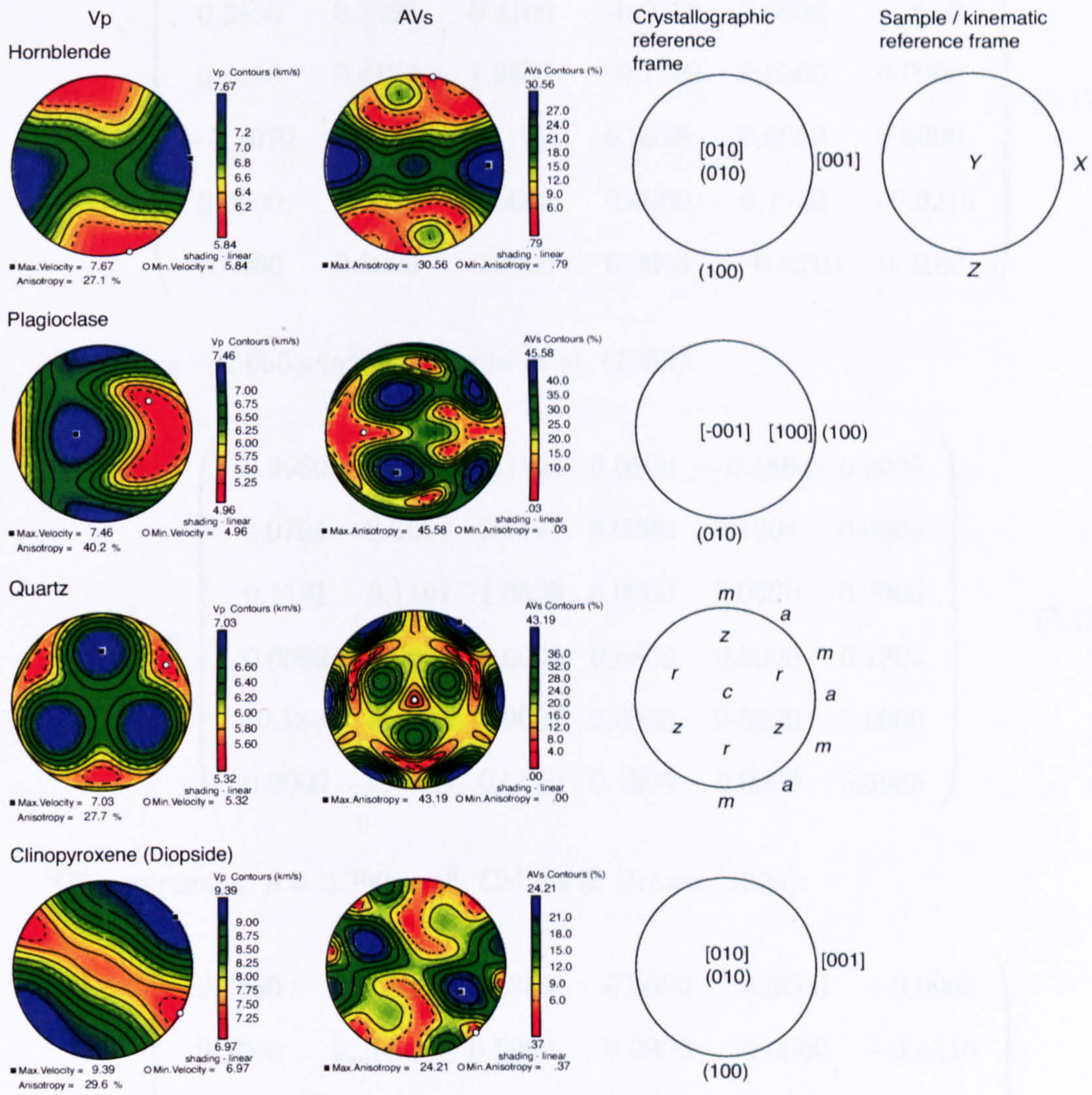

Figure 5.1: Lower hemisphere, equal area stereographic plots of V_p and AV_s for single crystals of the major constituent mineral phases of the sample suite. Also shown are the crystallographic reference frames in which the seismic properties are presented, and the kinematic reference frame to which such single crystal orientations are commonly correlated in deformed rocks. Note the inverse colour scheme for contouring, where cold colours represent maxima and warm colours mark minima.

Plagioclase, $\rho = 2.620 gcm^3$, Aleksandrov et al. (1974):

$$C_{ij_{Plag}} \begin{pmatrix} 1.3740 & 0.2890 & 0.2150 & -0.3070 & 0.0000 & 0.0000 \\ 0.2890 & 0.7480 & 0.4100 & -0.0910 & 0.0000 & 0.0000 \\ 0.2150 & 0.4100 & 1.2880 & -0.1920 & 0.0000 & 0.0000 \\ -0.3070 & -0.0910 & -0.1920 & 0.3020 & 0.0000 & 0.0000 \\ 0.0000 & 0.0000 & 0.0000 & 0.0000 & 0.1740 & -0.0210 \\ 0.0000 & 0.0000 & 0.0000 & 0.0000 & -0.0210 & 0.3180 \end{pmatrix} \quad (5.17)$$

Quartz, $\rho = 2.650 gcm^3$, McSkimin et al. (1965):

$$C_{ij_{Qtz}} \begin{pmatrix} 0.8680 & 0.0704 & 0.1191 & 0.0000 & -0.1804 & 0.0000 \\ 0.0704 & 0.8680 & 0.1191 & 0.0000 & 0.1804 & 0.0000 \\ 0.1191 & 0.1191 & 1.0575 & 0.0000 & 0.0000 & 0.0000 \\ 0.0000 & 0.0000 & 0.0000 & 0.5820 & 0.0000 & 0.1804 \\ -0.1804 & 0.1804 & 0.0000 & 0.0000 & 0.5820 & 0.0000 \\ 0.0000 & 0.0000 & 0.0000 & 0.1804 & 0.0000 & 0.3988 \end{pmatrix} \quad (5.18)$$

Clinopyroxene, $\rho = 3.390 gcm^3$, Collins & Brown (1998):

$$C_{ij_{Cpx}} \begin{pmatrix} 2.7380 & 0.8000 & 0.8350 & 0.0000 & 0.0000 & -0.0900 \\ 0.8000 & 2.2950 & 0.5990 & 0.0000 & 0.0000 & -0.4810 \\ 0.8350 & 0.5990 & 1.8360 & 0.0000 & 0.0000 & -0.0950 \\ 0.0000 & 0.0000 & 0.0000 & 0.7650 & -0.0840 & 0.0000 \\ 0.0000 & 0.0000 & 0.0000 & -0.0840 & 0.8160 & 0.0000 \\ -0.0900 & -0.4810 & -0.0950 & 0.0000 & 0.0000 & 0.7300 \end{pmatrix} \quad (5.19)$$

The seismic property distribution for hornblende exhibits an orthorhombic symmetry (Figure 5.1), with three orthogonal two-fold axes of symmetry (Winterstein, 1990). Both V_p and AV_s maxima ($7.67 kms^{-1}$ and 30.56% respectively) are sub-parallel to X and [001] with a 'crown' of velocity and anisotropy minima

($5.84kms^{-1}$ and 0.79% respectively) sub-parallel with Z and (100).

The plagioclase single crystal shows a much more complicated seismic distribution (Figure 5.1), with a single plane of symmetry in (010) (XY). V_p maxima ($7.46kms^{-1}$) exist close to both (010) (Z) and [001] (Y) with a minima ($4.96kms^{-1}$) around (100) (X). The AV_s distribution has minima (0.03%) broadly in a girdle parallel to the plane (010) (XY) and maxima (45.58%) between the pole (010) and [001].

The trigonal symmetry (one three-fold axis) of the seismic distribution for the quartz single crystal is directly related to that of its crystallographic symmetry (Figure 5.1). V_p minima ($5.32kms^{-1}$) occur between m and r, with maxima ($7.03kms^{-1}$) parallel to z. A similar distribution of minima is observed in AV_s although with a c-parallel minima also (as low as 0%). AV_s maxima are a-parallel (43.19%).

In the crystallographic orientation depicted in (Figure 5.1), the seismic distribution of the clinopyroxene single crystal lacks symmetry with respect to the kinematic axes. Nevertheless, with respect to arbitrary axes, an orthorhombic symmetry can be seen in V_p with a minima ($6.97kms^{-1}$) between [001] and the pole (100) and a maxima ($9.39kms^{-1}$) again between [001] and the pole (100), in the adjacent quadrant. AV_s maxima (24.21%) lies off the girdle containing [010] and [001].

The seismic properties of constituent single crystals, described by their petrophysical parameters (e.g. C_{ij}, ρ) are hence combined according to the procedure outlined above (Equations 5.7 to 5.15, incorporated into the Mainprice programs) to investigate the seismic properties of the rock aggregates of the sample suite, 1-9 (Section 5.2.1).

5.2 Seismic property results

5.2.1 Seismic properties of samples and correlation to strain

Figure 5.2 shows lower hemisphere, equal area stereographic plots of the V_p and AV_s distribution for Samples 1-9. Plots of V_p and AV_s are shown as these constitute the most informative and applied velocity and anisotropy attributes in seismic experiments of lithospheric characterisation (Blackman et al., 1993; Owens & Zandt, 1997; Huang et al., 2000; Kendall, 2000; Schulte-Pelkum et al., 2005). Single crystal elastic constants and petrophysical properties for use in the VRH average to determine the bulk aggregate C_{ij} are given in Equations 5.16-5.19, Section 5.1. Raw EBSD data is only processed to exclude lattice orientations indexed by *Channel* with an EBSP MAD>1 (see Section 3.4). Plots are contoured according to the inverse colour scheme, where warm colours mark minima, and cold colours represent maxima. A complete account of seismic velocity and anisotropy data for the sample suite is listed in Tables 5.1 and 5.2.

The most striking trend seen in Figure 5.2 is the development of a strong and ordered pattern of orthorhombic symmetry (Winterstein, 1990) from Sample 2, through to Samples 7 to 9. Sample 1 exhibits an essentially isotropic case for velocities and anisotropies, where maxima and minima lie within tight and negligible

Sample	Strain, γ	$V_p max$	$V_p min$	$\%AV_p$
1	0.00	6.55	6.43	1.90
2	0.18	6.55	6.16	6.00
3	0.46	6.42	6.13	4.50
4	6.05	6.56	6.16	6.30
5	5.40	6.62	6.17	7.10
6	6.85	6.27	6.00	4.40
7	11.16	6.45	5.97	7.80
8	57.00	6.63	5.97	10.50
9	13.88	6.47	5.97	8.00

Table 5.1: The complete description of P-wave seismic properties for the sample suite.

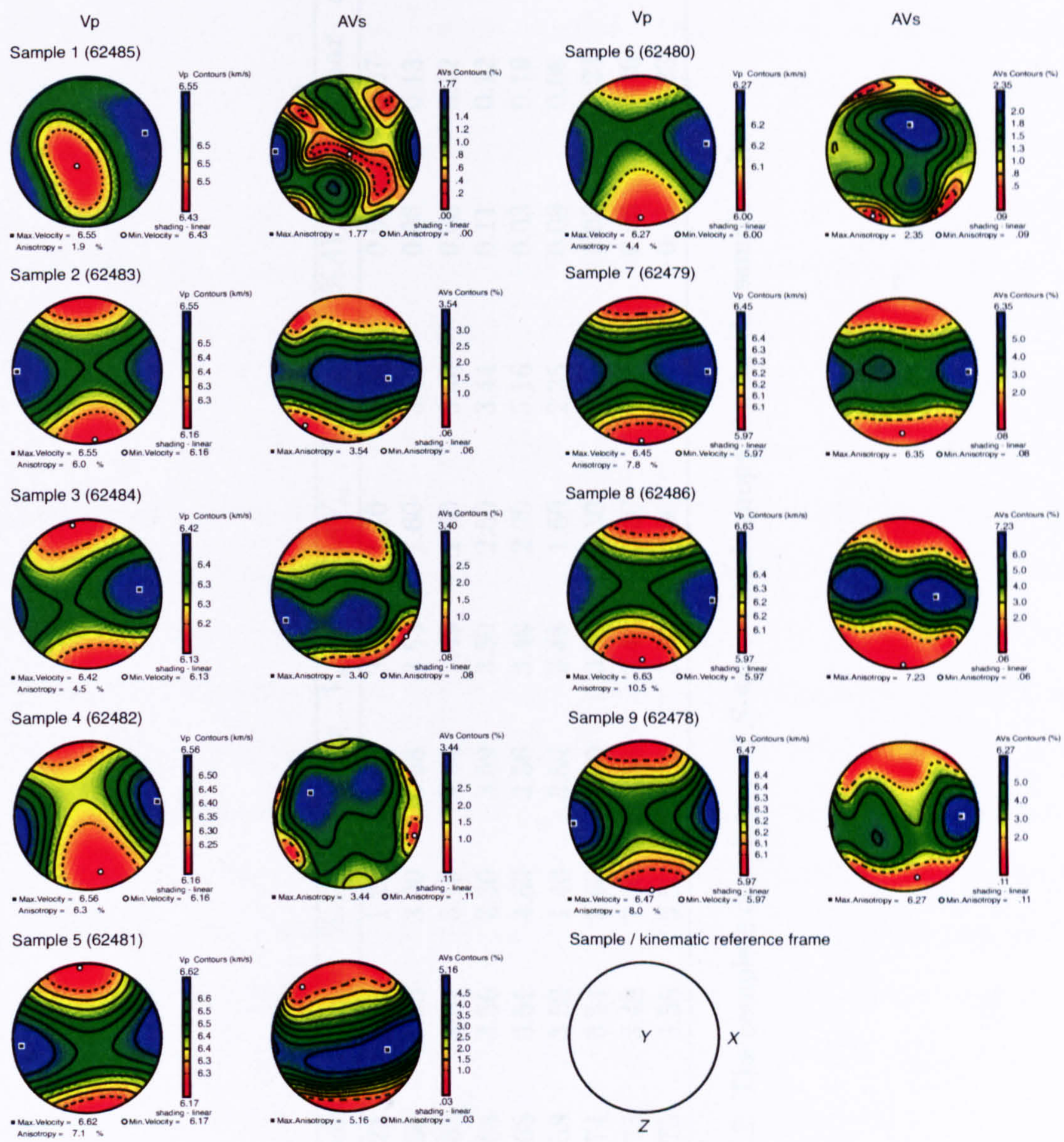

Figure 5.2: Lower hemisphere, equal area stereographic plots of V_p and AV_s for the sample suite. Also shown is the sample/kinematic reference frame in which the plots are oriented. Note the inverse colour scheme. Cold colours mark maxima, and warm colours represent minima.

Sample	Strain, γ	$V_{s_1}max$	$V_{s_1}min$	$\%AV_{s_1}$	$V_{s_2}max$	$V_{s_2}min$	$\%AV_{s_2}$	$\%AV_s max$	$\%AV_s min$	$dV_s max$	$dV_s min$
1	0.00	3.71	3.67	1.20	3.68	3.64	1.10	1.77	0.00	0.07	0.00
2	0.18	3.66	3.55	3.00	3.58	3.53	1.60	3.54	0.06	0.13	0.00
3	0.46	3.62	3.51	3.10	3.54	3.49	1.60	3.40	0.08	0.12	0.00
4	6.05	3.64	3.56	2.30	3.59	3.50	2.50	3.44	0.11	0.12	0.00
5	5.40	3.68	3.51	4.60	3.56	3.49	2.20	5.16	0.03	0.19	0.00
6	6.85	3.58	3.52	1.40	3.54	3.48	1.60	2.35	0.09	0.08	0.00
7	11.16	3.74	3.54	5.60	3.59	3.51	2.30	6.35	0.08	0.23	0.00
8	57.00	3.73	3.48	7.00	3.58	3.46	3.30	7.23	0.06	0.26	0.00
9	13.57	3.75	3.55	5.50	3.62	3.51	3.00	6.27	0.11	0.23	0.00

Table 5.2: The complete description of S-wave seismic properties for the sample suite.

bounds of $0.12kms^{-1}$ in V_p (1.9% AV_p), and 1.77% in AV_s. In contrast, Sample 8, correlated with the highest strain part of the shear zone (Section 2.3.1; Table 2.1), is characterised by clearly defined orthorhombic symmetry in its seismic properties, with a strong V_p maxima ($6.63kms^{-1}$) parallel to the kinematic X-direction, and a minima parallel to the foliation-normal, or kinematic Z-direction ($5.97kms^{-1}$, 10.5% AV_p). Similarly, the AV_s pattern is characterised by a foliation-parallel (XY) band of relatively high anisotropy, with the AV_s maxima (7.23%) approximately bisecting X-Y, and a foliation-normal 'crown' of relatively lower anisotropy, with a Z-parallel minima of 0.06%. Velocity and anisotropy plots for Samples 2-7, and 9, track the intermediate steps in the development of this order.

Juxtaposition of Figure 5.2 with Figure 5.1 highlights the dominance of hornblende in controlling the magnitude and distribution of seismic velocity and anisotropy in the aggregates of the sample suite. The orthorhombic symmetry in both V_p and AV_s of the hornblende single crystal is well represented in the aggregate, as is the X-parallel V_p maxima and the low velocity, low anisotropy Z-parallel 'crown'. This is particularly well developed in samples of a higher finite strain state, although the characteristic orthorhombic symmetry in hornblende seismic attributes can be identified very early in the stain gradient, in Sample 2 for example where $\gamma = 0.18$. This suggests that hornblende petrofabric, and particularly LPO becomes sufficiently ordered by $\gamma \leq 0.2$ as to establish a gross control on the seismic properties of the aggregate. The reduced velocity and anisotropy maxima of highly strained samples (e.g. Sample 8, $AV_s = 7.23\%$) compared to the single crystal values (e.g. hornblende, $AV_s = 30.56\%$) is likely due to dilution and weakening of the strong hornblende fabric by randomly oriented plagioclase and quartz. The characteristic orthorhombic symmetry remains, however.

Despite the development of order and symmetry in the spatial distributions of seismic velocity and anisotropy with increasing finite strain (as indicated by Samples 1-9, Figure 5.2), the absolute values of P- and S-wave velocities are no-

ticeably insensitive to strain (Figure 5.3). Fractional divergence of velocity maxima and minima however, necessitates the development of significant anisotropy with increasing finite strain. Figure 5.4 shows the relationship of P- and S-wave anisotropy with finite strain. Both show a relationship such that anisotropy increases rapidly with strain up to $\gamma \approx 10$ (correlating to $AV_p \approx 8\%$ and $AV_s max \approx 6\%$), past which point further increase in strain leads to increasingly smaller changes in AV_n. Given the assumption here that seismic anisotropy is a function of LPO only (Section 1.5), this relationship suggests that aggregate petrofabric, or at least that of the phase most influencing the observed velocity and anisotropy distribution, must also show a steep positive relationship with strain, saturating at $\gamma \approx 10$. Figures 4.22 and 4.32 substantiate this claim for LPO fabric development in hornblende, shown above to be the major influence on seismic velocity and anisotropy distributions. In an attempt to relate trends in both seismic and petrofabric properties, Figure 5.4 depicts the relationship of seismic anisotropy with petrofabric, parameterised by the texture index for hornblende, J_{Hbl} (Section 4.3). Predicably, in view of the positive correlation between finite strain and J_{Hbl} (Figure 4.32), an increasingly ordered petrofabric is correlated with an increase in anisotropy (Figure 5.5). A logarithmic function can be tenuously ascribed to the relationship, whereby anisotropy tends to saturate by $J_{Hbl} \leq$ 3-4 ($\gamma \leq$ 5-10) as petrofabric development itself saturates (Figure 4.32). The relationship of J with anisotropy is probably more linear at lower values of J (Skemer et al., 2005).

Many early seismic velocity measurements were based on the assumption that deep crustal materials are isotropic (Christensen, 1965; Christensen & Fountain, 1975; Holbrook et al., 1992; Weiss et al., 1999). Although the consideration of seismic anisotropy in lower crustal materials that exhibit textural ordering will have the apparent scatter effect on 'isotropic' velocities (Weiss et al., 1999), measurements based on isotropic assumptions can still give useful support to seismic velocities determined from microstructure (LPO). Data compiled from multiple

sources (refer to Weiss et al., 1999, for a full description) show V_p between 6.5-7.2kms^{-1} and V_s between 3.8-4.2kms^{-1} for amphibolite and granulite facies mafic gneiss. These figures are in close correlation to those presented above for the Badcall sample suite (Tables 5.1-5.2).

Weiss et al. (1999) also present velocity and anisotropy measurements for an amphibolite sample from the Spessart Mountains, Germany, comprising 58% hornblende, 40% plagioclase and 2% accessories, similar to Table 4.1 in terms of mafic:felsic components. Although they do not quantify the sample strain, Weiss et al. (1999) note a macroscopic shear fabric and LPO development in hornblende ((100) pole normal to foliation, [001] parallel to lineation, as observed in Section 4.4), and plagioclase ((100) poles normal to foliation). Laboratory-derived ultrasonic pulse transmission velocities at 400MPa (such that crack and grain boundary effects are minimised) are presented with those calculated from textural data (as outlined in Section 5.1) give complementary results. Each show V_pmax parallel to the tectonic lineation X between 7.3-7.38kms^{-1}, with the same V_p distribution as observed in Samples 2-9 (Figure 5.2). P-wave velocities are higher than those of Samples 2-9 (6.42-6.63kms^{-1}, Table 5.1) although are still in relatively close agreement. Weiss et al. (1999) do not calculate anisotropy for this sample, but from their data it can be approximated to 10%AV_p, similar to Sample 10 (Table 5.1). Weiss et al. (1999) do, however, compare this data with previously published laboratory-derived and calculated velocities of a range of high-grade materials (see Weiss et al., 1999, for references). These are incorporated in a structural reference frame into layered models of the Ivrea crustal section, Italy (see Section 1.3), and the Calabria crustal section, Italy (Weiss et al., 1999). Average P-wave velocities across the sections of 6.8-7.0kms^{-1} (where V_pmax is parallel to lineation X and V_pmin is normal to foliation) and P-wave anisotropy <7.3% are correlatable with those of the Badcall suite, particularly higher strained samples, Samples 4-9 ($\gamma > 6$, AV_p 6.3-10.5%, Table 5.1). Weiss et al. (1999) also calculate

maximum δV_s of $0.2kms^{-1}$ and AV_s 5% from their crustal models. Again, this supports velocity and anisotropy calculations from the Badcall suite of samples (Table 5.2) δV_s 0.19-0.26kms^{-1} for deformed Samples 5-9 ($\gamma > 5.4$). This close agreement between average velocity and anisotropy for a multi-lithology layered crustal model and those derived from the variably deformed dolerite studied here lends support to the approximation of the deep crust with the single homogeneous mafic composition (see Section 1.5).

Siegesmund et al. (1989) present a combined study of laboratory-derived velocity measurements at pressure and temperature, and those calculated from textural data (as outlined in Section 5.1), for a deformed amphibolite from the Ivrea section, Italy (41% hornblende, 36% plagioclase, 11% pyroxene, + accessories). The rock has strong linear and planar tectonic fabrics defined by felsic and mafic bands, and aligned hornblende prisms. Hornblende shows a strong LPO (poles to (100) normal to the foliation and [001] parallel to X). Plagioclase shows weak LPO. Direct velocity experiments at 600°C and $600MPa$ show a V_pmax parallel to X (7.18kms^{-1}) and V_smax in the XY plane (4.09kms^{-1}) (Siegesmund et al., 1989). Calculated velocities were marginally different to those measured directly, and is attributed to the fact that accessory phases were not considered in the calculations (Siegesmund et al., 1989). Calculated V_pmax 7.23kms^{-1} parallel to X (AV_p 6.56%) and V_smax 3.95kms^{-1} in the XY plane (AV_s 6.56%, δV_s 0.2kms^{-1}). A comparison with the velocity distribution of component phase aggregates indicated that the velocity distribution was dominantly affected by the hornblende fraction. Again, the values and distribution of velocity and anisotropy presented by Siegesmund et al. (1989) are broadly consistent with those exhibited by the Badcall sample suite (Tables 5.1-5.2, Figure 5.2). Any inconsistencies are likely due to difference modal fractions of component minerals between the two studies.

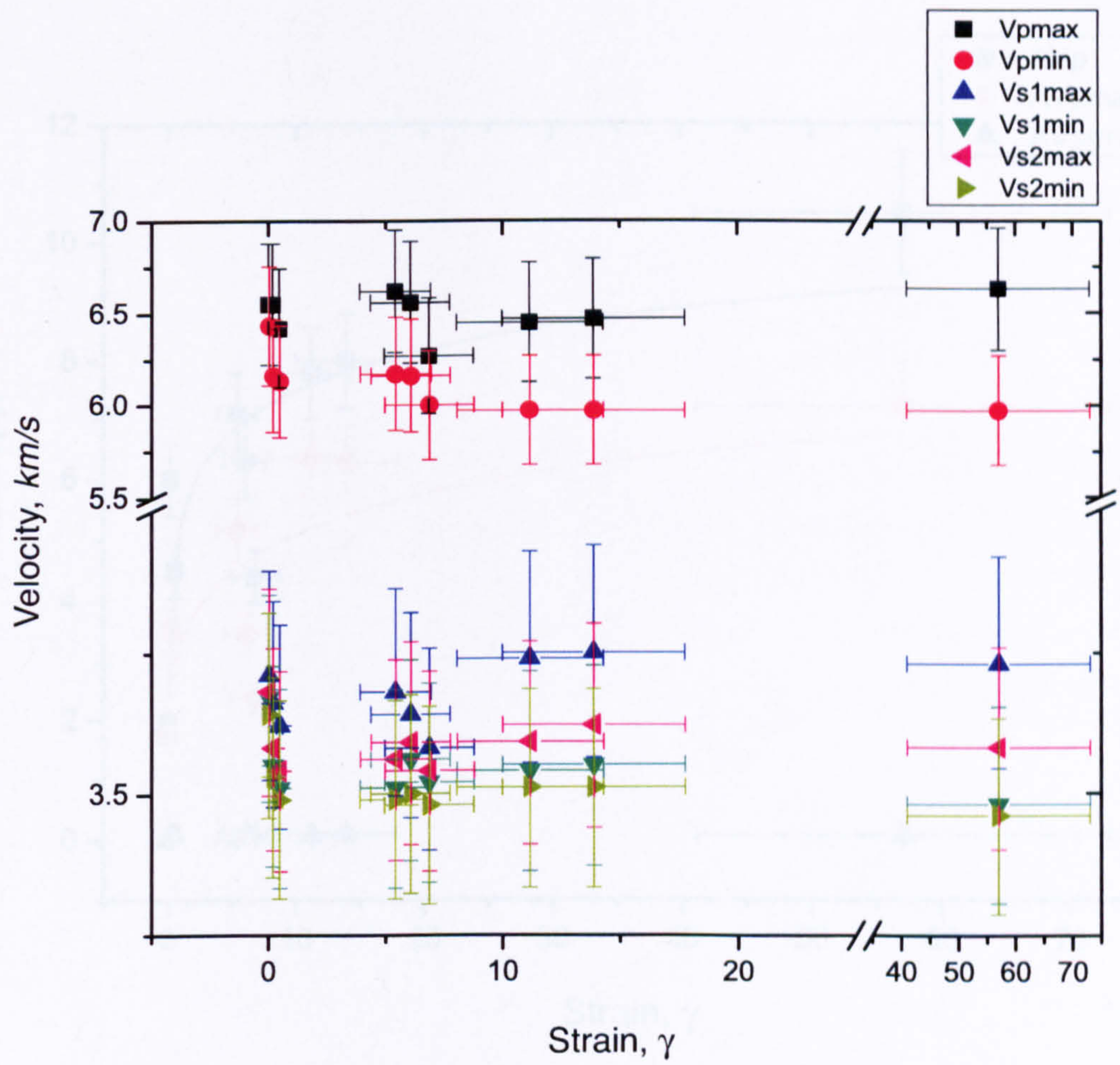

Figure 5.3: The relationship between P- and S-wave velocities and finite strain exhibited by the sample suite. Error in seismic velocity is calculated from Voigt and Reuss bounds (see Section 5.1). ±28% error bars are shown for finite strain. Notice the split axes to clarify low-value trends.

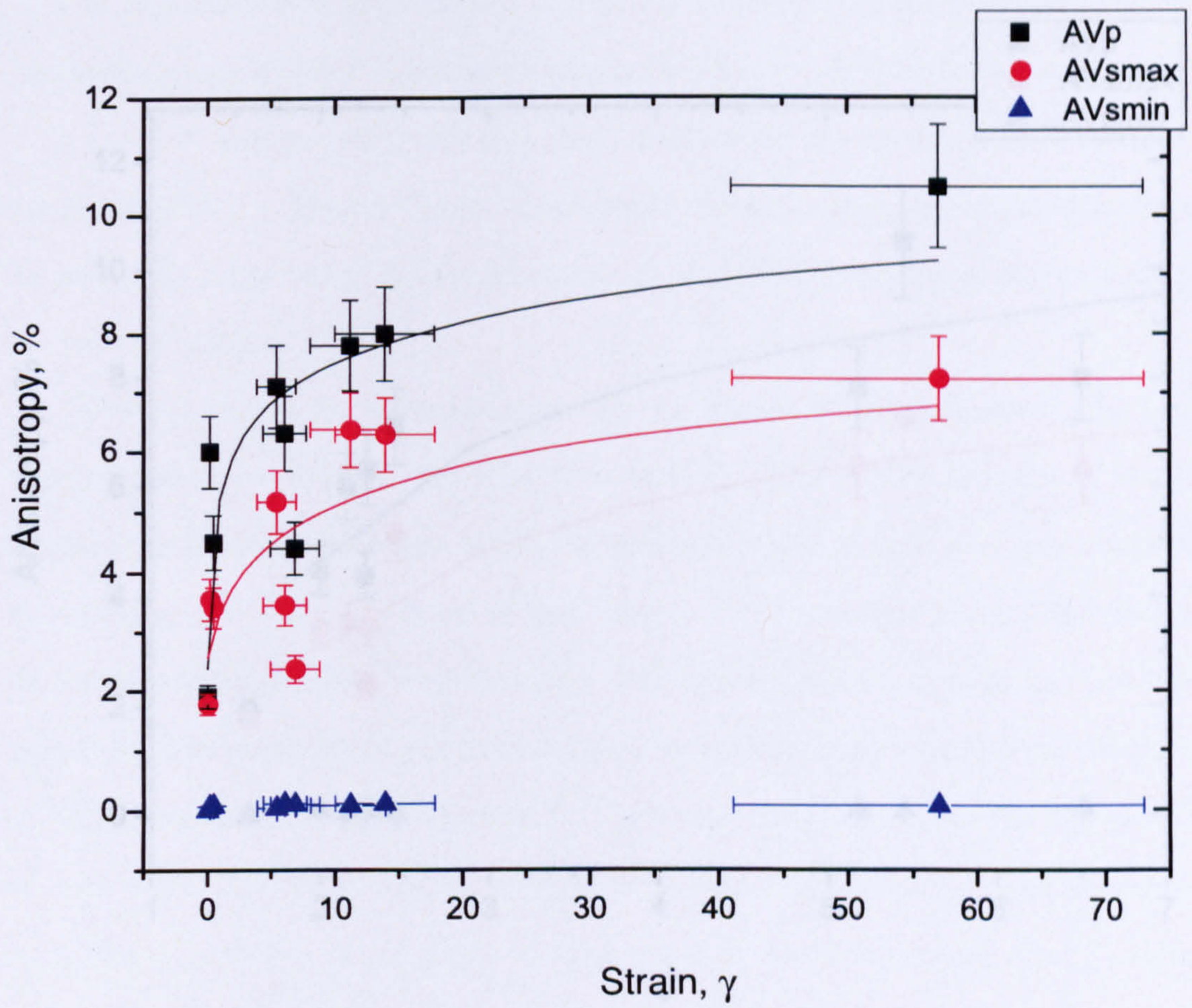

Figure 5.4: The relationship between P- and S-wave anisotropies and finite strain exhibited by the sample suite. Error in seismic anisotropy is calculated from Voigt and Reuss bounds (see Section 5.1). ±28% error bars are shown for finite strain. Best-fit curves are logarithmic functions.

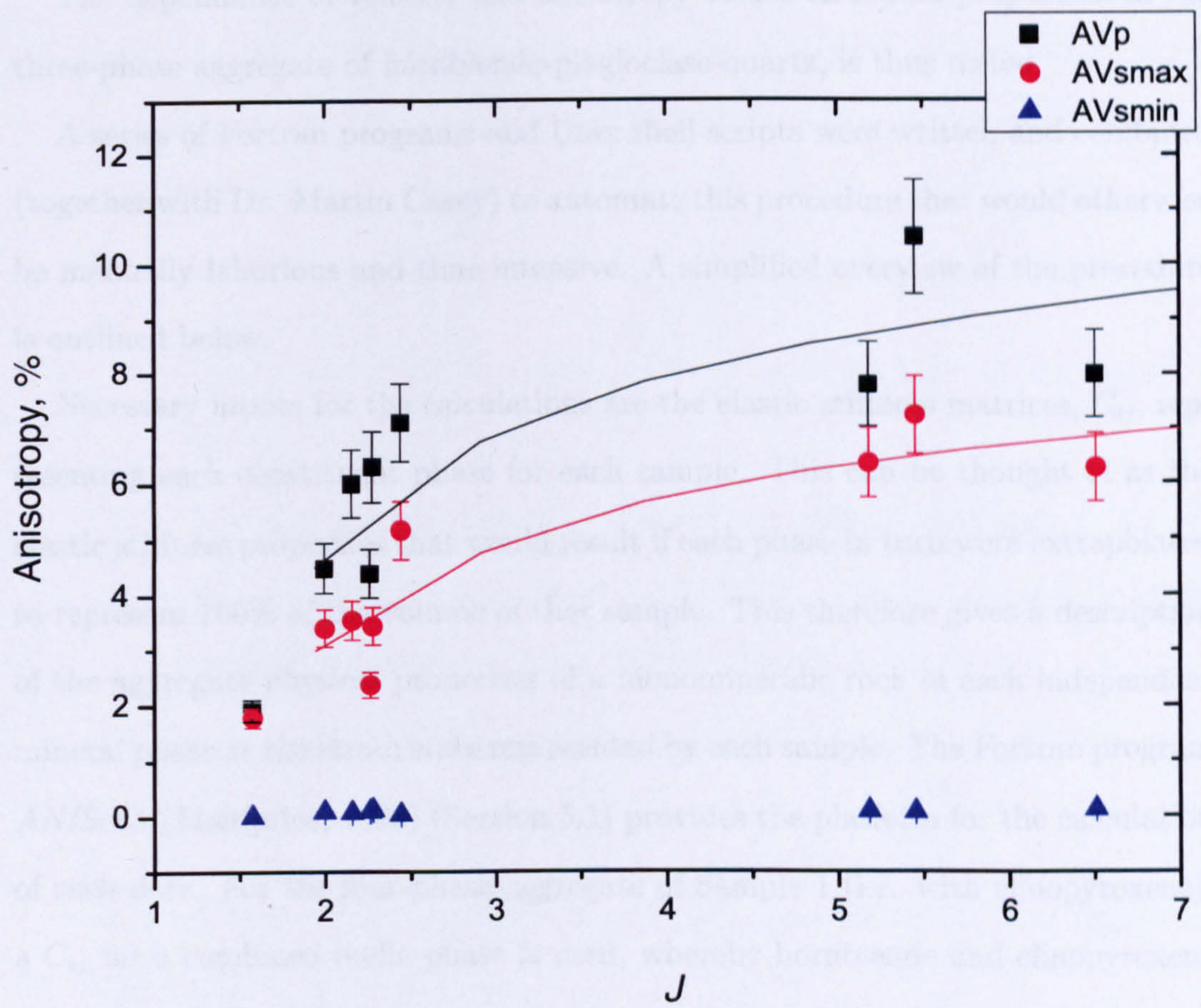

Figure 5.5: The relationship between P- and S-wave anisotropies and the texture index, J, exhibited by the sample suite. Error in seismic anisotropy is calculated from Voigt and Reuss bounds (see Section 5.1). Best-fit curves are logarithmic functions.

5.2.2 The effect of varying modal composition

It is clear from Figures 4.32, 5.1 and 5.2 that the increase in strength and the development of symmetry in the patterns of anisotropy can be correlated with the development of LPO in the hornblende phase.

The dependance of velocity and anisotropy values on modal proportion in the three-phase aggregate of hornblende-plagioclase-quartz, is thus tested.

A series of Fortran programs and Unix shell scripts were written and combined (together with Dr. Martin Casey) to automate this procedure that would otherwise be manually laborious and time-intensive. A simplified overview of the procedure is outlined below.

Necessary inputs for the calculations are the elastic stiffness matrices, C_{ij}, representing each constituent phase for each sample. This can be thought of as the elastic stiffness properties that would result if each phase in turn were extrapolated to represent 100% of the volume of that sample. This therefore gives a description of the aggregate physical properties of a monomineralic rock in each independent mineral phase at the strain state represented by each sample. The Fortran program *ANISch5* (Mainprice, 1990) (Section 5.1) provides the platform for the calculation of such data. For the four-phase aggregate of Sample 1 (i.e. with clinopyroxene), a C_{ij} for a combined mafic phase is used, whereby hornblende and clinopyroxene orientation data for Sample 1 are mixed according to their relative modal fraction with respect to each other, that is 4:1 hornblende:clinopyroxene.

Two controlling Unix shell scripts, *Tern* and **pl*, were written for the purpose of collating seismic velocity and anisotropy data, and presenting that data, respectively. Programs were run for each sample in turn. The pertinent steps in each sample-wise run are described here.

1. Firsly, *Tern* outlines all the possible permutations of hornblende, quartz and plagioclase relative modal fractions at intervals of 0.1, and together summing to 1.

(a) For each run, or combination of the volume fractions, the Fortran program *Ematrix5* inputs the monomineralic aggregate elastic constants for that sample (derived as above) and combines them in the *Tern*-defined volume fractions to generate, via a VRH average (see Section 5.1), a bulk elastic tensor.

(b) This tensor forms the input for *Velcalc*, calculating seismic velocity and anisotropy data (similar to *ANISch5*, but from aggregate C_{ij} rather than **.ctf*).

(c) The procedure is repeated for all modal fraction permutations

2. (a) Velocity and anisotropy data is serially captured from the output file of *Velcalc* via the script **pl.*

(b) This also has the function of arranging seismic data into a ternary plot coordinate system pertaining to the relative modal fractions of the hornblende-plagioclase-quartz system defined in Step (1).

(c) Data is plotted and contoured via *GMT* (Generic Mapping Tools, Wessel & Smith, 1998).

Ternary plots showing the sensitivity of V_p, AV_p and AV_s to modal composition are illustrated in Figures 5.6 to 5.8.

Besides showing a general trend towards higher maximum P-wave velocities with increased sample strain, Figure 5.6 illustrates the strong dependence of seismic properties on the volume fraction of hornblende in this three-phase system. For example, up to $1kms^{-1}$ increase in V_p can result between end-member aggregates of monomineralic plagioclase and hornblende.

This sensitivity of seismic properties to the modal fraction of hornblende is further highlighted in Figures 5.7 and 5.8 for AV_p and AV_s respectively. These plots show, especially for the more highly strained samples (Figures 5.7 and 5.8, plots 7-9), that the greatest rate of change in anisotropy with respect to modal composition

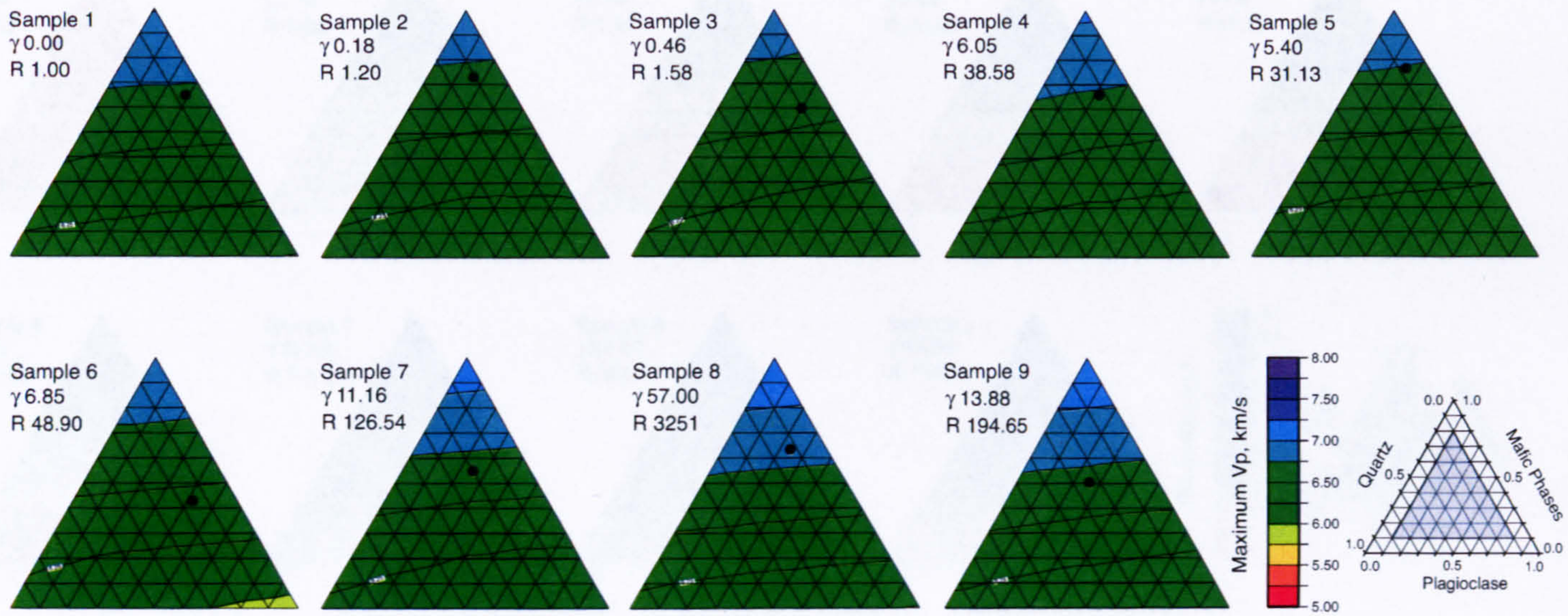

Figure 5.6: Ternary plots for Samples 1-9 showing the sensitivity of $V_p max$ to relative modal composition in the three-phase aggregate of hornblende-feldspar-quartz. The value of γ ($\pm 28\%$) and corresponding ellipticity of the finite strain ellipse, R, are shown for each sample (see Section 2.3.1) The shaded area of the legend ternary plot indicates the region of confident extrapolation of data. Dots indicate the original modal composition of each sample.

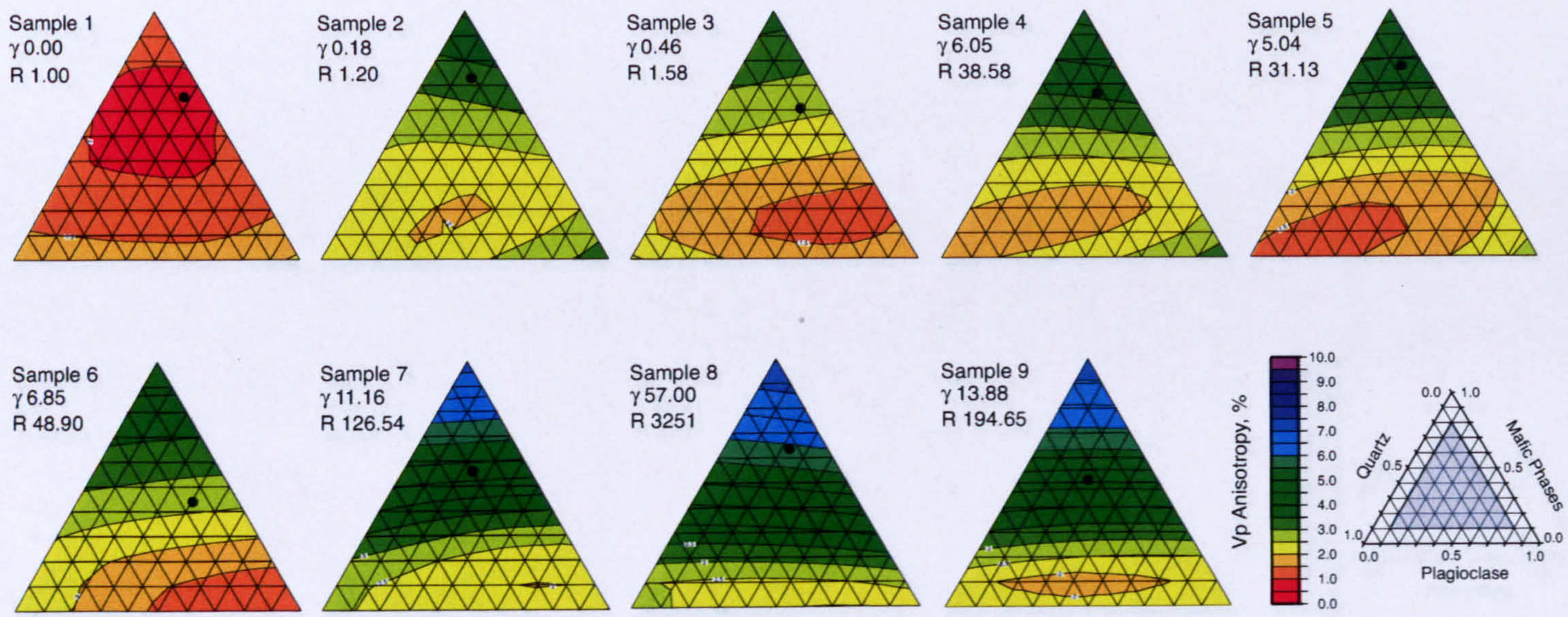

Figure 5.7: Ternary plots for Samples 1-9 showing the sensitivity of AV_p to relative modal composition in the three-phase aggregate of hornblende-feldspar-quartz. The value of γ ($\pm 28\%$) and corresponding ellipticity of the finite strain ellipse, R, are shown for each sample (see Section 2.3.1). The shaded area of the legend ternary plot indicates the region of confident extrapolation of data. Dots indicate the original modal composition of each sample.

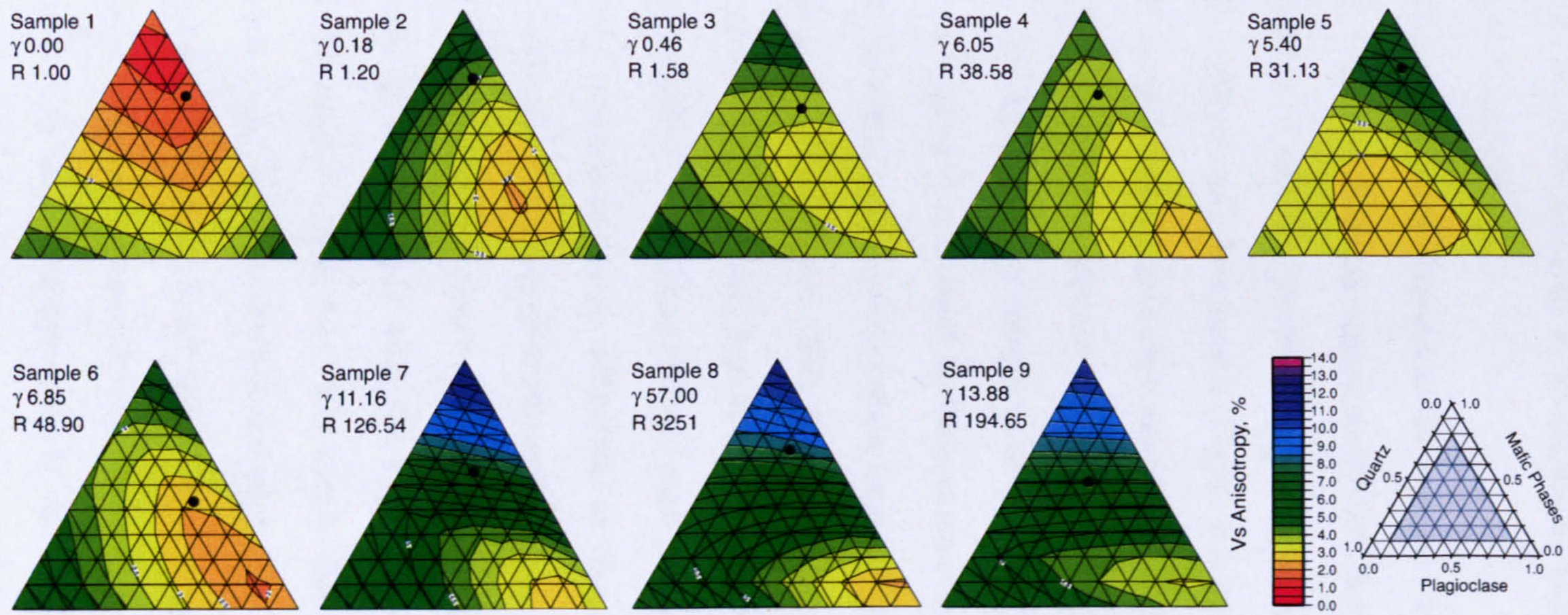

Figure 5.8: Ternary plots for Samples 1-9 showing the sensitivity of AV_s to relative modal composition in the three-phase aggregate of amphibole-feldspar-quartz. The value of γ ($\pm 28\%$) and corresponding ellipticity of the finite strain ellipse, R, are shown for each sample (see Section 2.3.1). The shaded area of the legend ternary plot indicates the region of confident extrapolation of data. Dots indicate the original modal composition of each sample.

occurs with changes in the hornblende fraction, where changes in composition move approximately perpendicular to contours in anisotropy. At its most extreme, compositional variation between 100% plagioclase and 100% hornblende can be equated with up to 5% increase in maximum V_p anisotropy and up to 8% increase in maximum V_s anisotropy.

In general, the effect of changes in the volume fraction of the quartz component are minimal. From a starting aggregate of 50% hornblende and 50% plagioclase, the contribution of a quartz fraction up to 100% yields only a 2% increase in AV_p in the most highly strained Sample 8 (Figure 5.7, plot 8), and an increase of 2% in AV_s at 50% quartz returning to zero change at 100% quartz (Figure 5.8, plot 8).

Previous investigations into the relative effects of component phases on seismic properties also highlight the dominant role of mafic components (e.g. pyroxene, amphibole and garnet) compared to felsic components (plagioclase and quartz) in influencing the seismic properties of mafic aggregates (e.g. Christensen & Fountain, 1975; Fountain & Christensen, 1989; Tatham et al., 2008).

Note that the range of relative modal fractions for which these plots can be applied is likely limited. As outlined above, each plot is based on the interpolation of monomineralic aggregate elastic properties in that sample, over all permutations of modal fractions, including monomineralic in each mineral phase. The elastic properties of each mineral phase are, however, representative of their deformation in a polyphase aggregate with the specific relative modal volume fractions of the original sample (Table 4.1). The strain distribution in the original sample and its partitioning into specific mineral phases is likely to be such that the microstructure and petrofabric (and hence elastic properties) of constituent mineral phase fractions are not representative of how that phase would behave in, say, a monomineralic rock of that composition at the strain observed in the bulk sample. For example, deformation of an aggregate of 60% hornblende, 30% plagioclase, and 10% quartz (similar to that of Samples 1-9) seems to preferentially partition

strain into the hornblende phase, leaving the plagioclase and quartz phases with poorly developed LPO (see Section 4.4). Deformation of a monomineralic aggregate of quartz or plagioclase to the same bulk strain, however, would probably see the development of a strong LPO (Marshall & McLaren, 1977a,b; Lister & Dornsiepen, 1982; Olsen & Kohlstedt, 1984, 1985; Mainprice et al., 1986; Kruhl, 1987b). Hence, Figures 5.6-5.8 should be used only for obviously polymineralic assemblages. From results of flow-law calculations in a selection of two-phase aggregates, Handy (1994) postulates that the presence of $\geq$10% of a weak phase is necessary for that phase to govern the bulk strength of the aggregate, although this depends upon a number of factors including temperature, strain rate and the strength contrast between phases. Thus, it is suggested that the results of Figures 5.6-5.8 are accurate between 10% and 90% in each phase for each possible two-phase system of the three-phase aggregate. That is, a central triangle of each ternary plot holds true, bordered by a potentially erroneous border of 0-10% volume fraction in each phase.

5.3 Conclusions

This chapter describes a key stage in the work-flow model in combining quantitative petrofabric (LPO) data from Chapter 4 with the petrophysical properties of single crystals of constituent mineral phases to calculate seismic properties of the sample suite.

1. The Voigt-Reuss-Hill average is used herein for the calculation of bulk aggregate elastic properties from those representative of single crystals of the constituent mineral phases. This elastic property averaging scheme is considered appropriate for scenarios where aggregate properties are largely controlled by the intrinsic material properties of the constituent mineral phases and their LPO. This relatively simple calculation forms the bridge in relating quantified

petrofabric information (LPO) to their petrophysical properties (aggregate elasticity), of which seismic properties are a direct function.

2. The Christoffel equation is introduced as a means of deriving seismic properties from petrophysical information described by the aggregate elastic stiffness tensor.

3. Given that petrofabric and petrophysical properties of each rock sample are directly correlated with the finite strain calculated for that sample, seismic attributes calculated from those parameters can also be calibrated to finite strain. Moreover, given that petrofabric properties are described and quantified in a known kinematic reference frame (based upon the linear and planar fabrics of the original rock samples), the directional dependence of seismic attributes can be correlated also to the geometry of petrofabrics or kinematics.

4. *P*- and *S*-wave seismic velocity maxima and minima show little variation with strain, although their anisotropies exhibit a strong positive relationship, approximated by a logarithmic function. That is, the gradient in change of AV_p and AV_s with strain is most rapid up to a finite strain of $\gamma \approx 10$, with values attaining 8% and 6% respectively, beyond which the change in anisotropy with continued increase in strain is reduced. This saturation of anisotropy by $\gamma \leq 10$ is compatible with the relationship of the texture index of hornblende petrofabric with strain. Indeed, the symmetry of the distribution of seismic attributes is congruent with those of single crystal hornblende, although the absolute values are somewhat reduced due to 'dilution' from randomly oriented plagioclase and quartz fractions.

5. The dominance of the hornblende phase in controlling seismic properties is further illustrated in an investigation into the sensitivity of seismic properties to the modal composition of a three phase hornblende-plagioclase-quartz-(±

clinopyroxene) aggregate, for each rock sample of the suite. Petrophysical properties of monomineralic compositions are representative of the monomineralic aggregate petrofabric for that sample, rather than single crystal properties. For the sample suite studied here, where plagioclase and quartz LPO remains random from the protolith material through the strain gradient (Section 4.4), a relationship showing a strong dependance of seismic properties to the relative modal fraction of hornblende is illustrated.

This chapter thus provides a sample-wise description of the relationship between seismic properties and finite strain, correlated with a known petrofabric and kinematic reference frame. It therefore represents an important framework for further study and application. Chapter 6 builds upon this framework, and presents continuum relationships between seismic properties, finite strain and petrofabric orientation. Furthermore, it provides examples of the application of these relationships in geodynamic models.

Chapter 6

Seismo-structural modelling

In this chapter, the relationship between petrofabric and seismic properties will be addressed, towards satisfying the objectives of interpreting ductile deformation in a mafic lower crustal assemblage using seismic anisotropy. Sample-wise seismic attributes of Chapter 5 are normalised to consistent modal compositions, representing the average of the sample suite, and combined to present the continuum relationship between strain, petrofabric orientation (XYZ) and seismic velocity and anisotropy. Furthermore, a series of case studies are presented in order to provide an example of the final stage in the work-flow model described in this project, and how its results can be used to provide increased resolution, or make first order predictions, in the interpretation of crustal strain and structure. Moreover, their aid in the discrimination between competing theories of strain localisation within the ductile lower crust is illustrated.

6.1 Reaffirmation of some physical assumptions

The physical assumptions and simplified crustal model described in Section 1.5 are of particular relevance and application in the ensuing models. Most noteworthy is the approximation of the entire lower crust as a homogeneous mafic lithology that is free from fractures, and the seismic anisotropy of which is a function of

its intrinsic properties alone. For this study, that lithology is represented by the hornblende-plagioclase-quartz aggregate of Samples 1-9 described in Chapter 4, from the quartz-dolerite Scourie dyke at Upper Badcall, NW Scotland. The sample area analysed with EBSD, from which subsequent calculations and inferences are based, is considered suitably large with respect to grain size and the phase distribution that its material properties are representative of the bulk rock sample and are hence scale-insensitive. This assumption permits simple up-scaling of physical properties from sample- to crustal-scales.

Section 5.2.2 showed how seismic properties are dependant upon aggregate composition. In order to apply each of Samples 1-9 as a single lithology, varying only in its petrofabric and petrophysical properties, sample compositions are normalised in terms of their modal composition. That is, slight and natural variation in modal fractions between samples, amounting to only a few percent (see Table 4.1), are removed by applying a constant modal distribution. A composition of 60% hornblende, 30% plagioclase and 10% quartz, close to the average of the sample suite, is considered appropriate and realistic. This is supported by observations from published compositions of deep-crustal lithologies (e.g. Christensen & Fountain, 1975; Siegesmund & Kern, 1990; Percival et al., 1992; Khazanehdari et al., 2000; Arbaret & Burg, 2003; Azpiroz & Lloyd, in press).

Normalisation of modal compositions is practically achieved using the Fortran programs *ANISch5* and *Ematrix5* to characterise the elastic stiffness matrix of the monomineralic aggregate components of each sample, and to combine them in the desired quantities to calculate the bulk aggregate elastic properties, respectively. This is the procedure outlined in Section 5.2.2 up to and including Step 1(a). The suite of aggregate C_{ij}'s output from *Emaitrix*5 for each sample, normalised to the given modal composition, and calibrated against sample finite strain (e.g. Table 5.1), form the basis for the ensuing seismic modelling, and indeed, the crux of the work-flow model described by this thesis.

6.2 Seismic signature of strain intensity & petrofabric orientation

In order to make valid predictions on the state of strain and crustal structure in areas of ductilely deforming mafic lower crust, seismic and petrofabric attributes must be considered together in a co-related continuum. Relevant seismic velocity and anisotropy results must therefore be presented with respect to quantitative and qualitative petrofabric elements such that data can be easily referenced and transferred into seismo-structural models.

Figures 6.1-6.4 depict the variation in V_p with respect to strain intensity and petrofabric orientation for a vertically propagating seismic ray-path travelling through a notional $10km$ thick section of material. Figures 6.5-6.8 and Figures 6.9-6.12 show the relationship of δt_s and the fast shear-wave polarisation orientation (see Section 5 for definitions), respectively, to the same variables and for the same physical scenario. A vertical seismic ray-path is envisaged to approximate a tele-seismic signal received at a surface seismometer array, shown schematically in Figure 6.13. A $10km$ thick section is used to provide practical values of δt_s. Most simplistically, plots can be envisaged as looking down onto a surface above $10km$ of lower crustal material of the aforementioned modal composition. Beneath that surface, material properties vary in both finite strain and petrofabric orientation. At each point on the plot with respect to the variables of the coordinate axes, the values of seismic properties shown are those of a seismic ray travelling vertically through that material and out of the surface (or page). This is illustrated schematically in Figure 6.14.

In each plot, fabric orientation is considered in the range $-90° \leq \theta \leq +90°$, where θ refers to the angle that the planar petrofabric (the sample and kinematic XY-plane, or the foliation) makes with horizontal. Positive rotations are clockwise when looking from a positive position towards the origin along the axis of rotation.

Rotations of the planar fabric are considered about two axes (Figure 6.15(a)-(c)). Figure 6.15(b) shows the planar fabric rotated about the X-axis, or a horizontal lineation, such that the lineation itself remains spatially unchanged. In contrast, the planar fabric in Figure 6.15(c) is rotated about the Y-axis, or the axis orthogonal to the lineation, X, and in the foliation plane, XY. In the latter scenario the lineation orientation varies between horizontal ($\theta = 0°$) and vertical ($\theta = \pm 90°$) with the planar fabric.

For each axial rotation of the deformation petrofabric, strain is parameterised as both the finite shear strain, γ, and the length of the major axis of the plane strain ellipse, S_1 pertaining to that shear strain (equivalent to $\sqrt{\lambda_1}$, Equation 4.1) where the unity value of S_1 represents an undeformed marker circle. Portraying the variation of seismic properties with respect to both γ and S_1 maintains the utility of the plots where strain data may be described for a simple shear zone, or by the manifold parameters pertaining to bulk pure shear. For example, the β-factor for extension directly correlates to S_1 (where $\beta = S_1$), or alternatively, the ellipticity of the strain ellipse, either measured directly from micro- or meso-structural proxies, or inferred from crustal thickness changes, can be used where $S_1 = \sqrt{R}$ (from Equation 4.2).

The processes and calculations involved in the generation of Figures 6.1-6.12 can be summarised according to the following steps. Computational elements of the modelling are the product of collaborative research with Dr. James Wookey, University of Bristol.

1. Sample-wise bulk elastic stiffness matrices, C_{ij}, are interpolated between their predetermined finite shear strains (γ) or the associated strain ellipse long axis (S_1) to describe the variation of elastic stiffness with strain. The interpolated grid is discrete but of high resolution, with interpolations at increments of 0.1 for both γ and S_1.

2. All figures of sample petrofabric and seismic attributes are hitherto presented

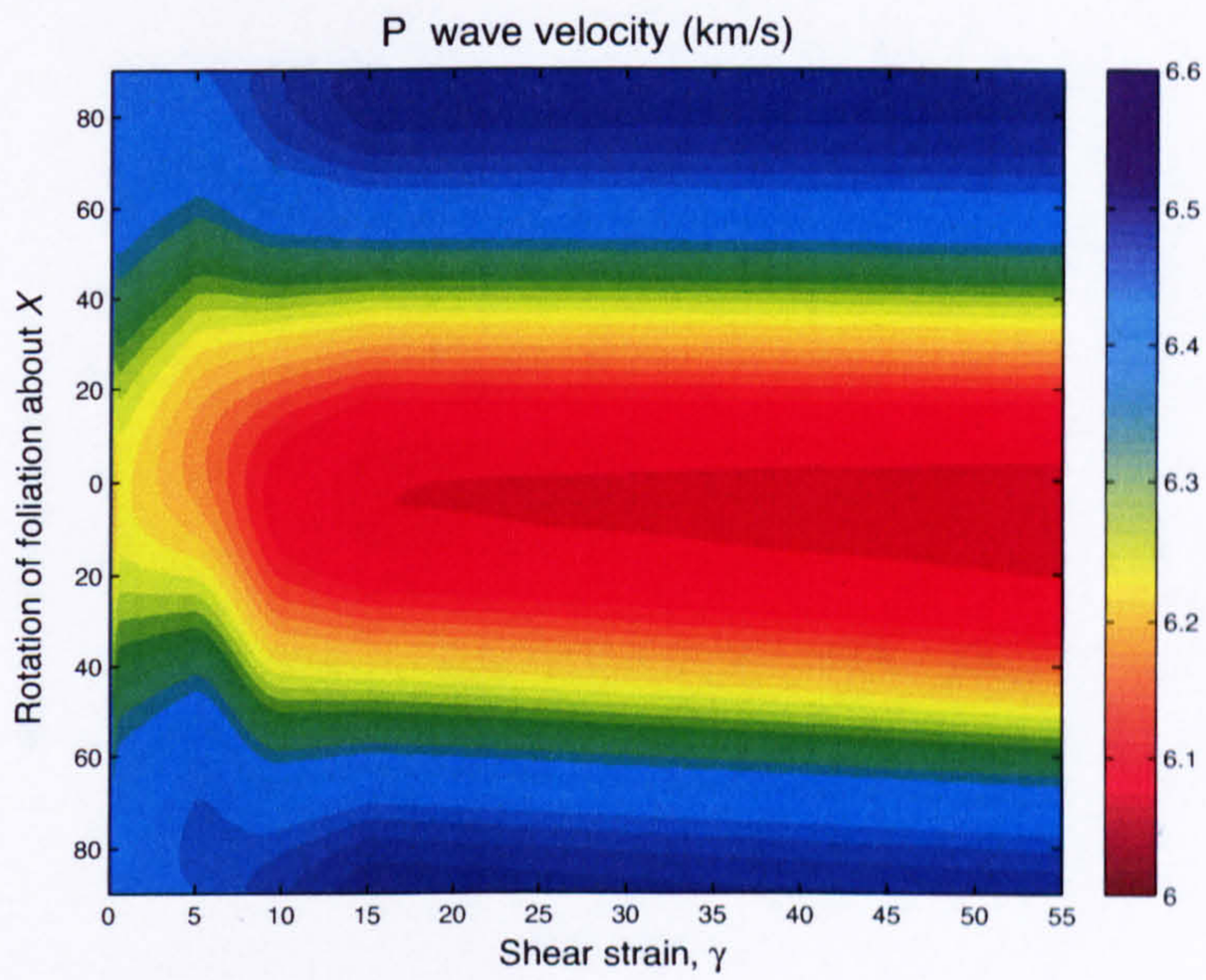

Figure 6.1: Continuum relationship between P-wave velocity, finite strain, γ, and petrofabric orientation, rotated about the kinematic X-axis. Data is that of a vertical seismic ray passing through a $10km$ thick section of material.

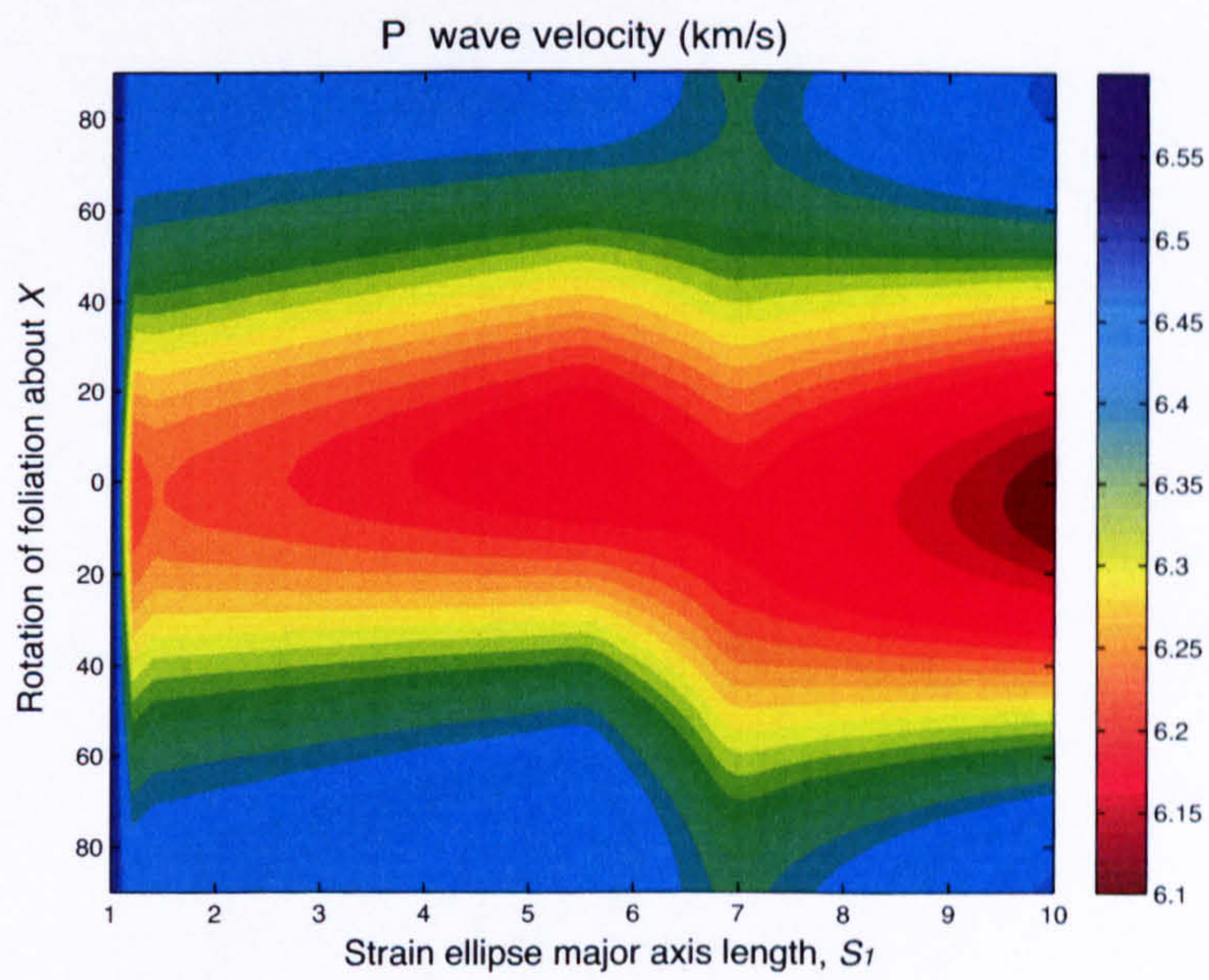

Figure 6.2: Continuum relationship between P-wave velocity, strain ellipse major axis length, S_1, and petrofabric orientation, rotated about the kinematic X-axis. Data is that of a vertical seismic ray passing through a $10km$ thick section of material.

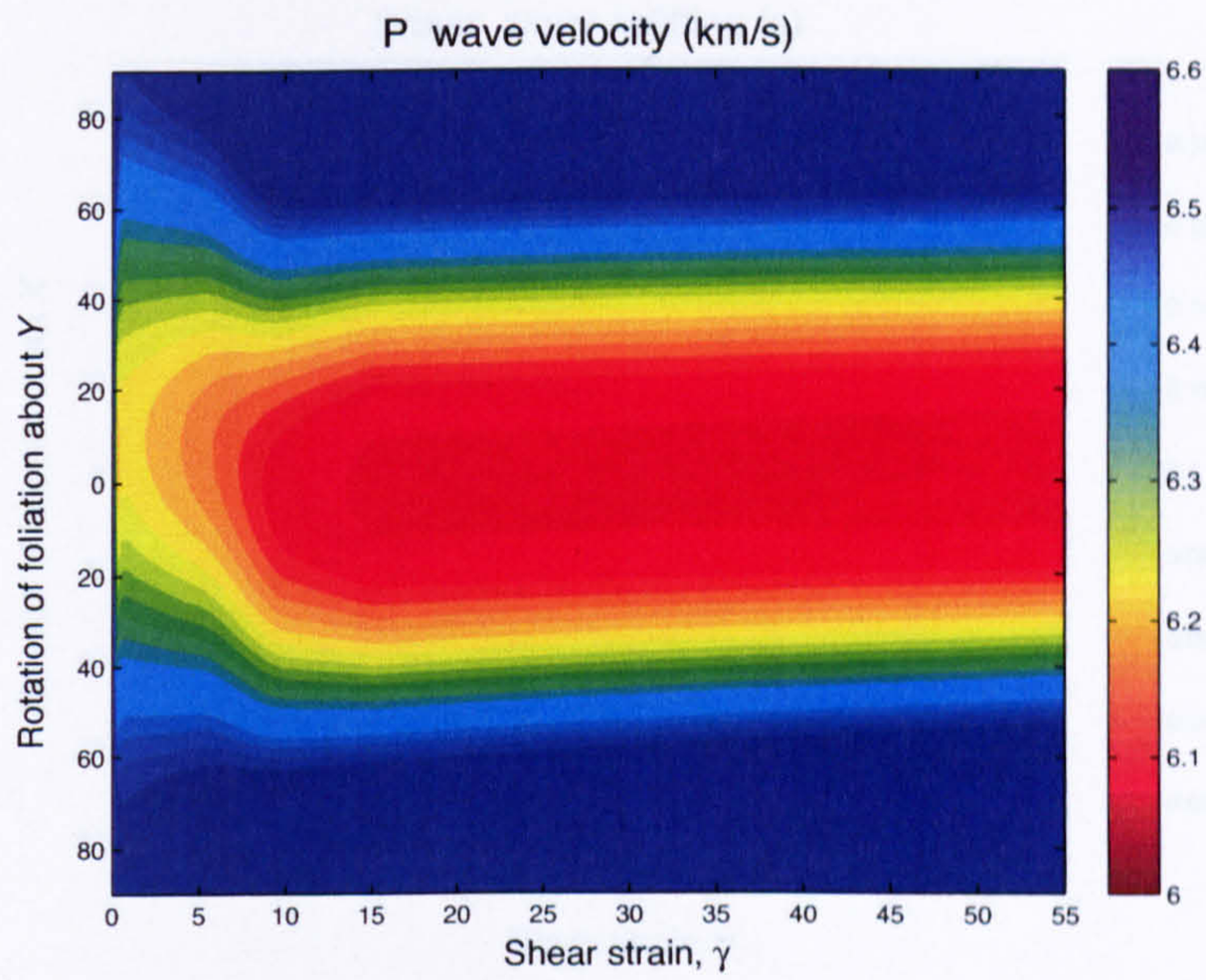

Figure 6.3: Continuum relationship between P-wave velocity, finite strain, γ, and petrofabric orientation, rotated about the kinematic Y-axis. Data is that of a vertical seismic ray passing through a $10km$ thick section of material.

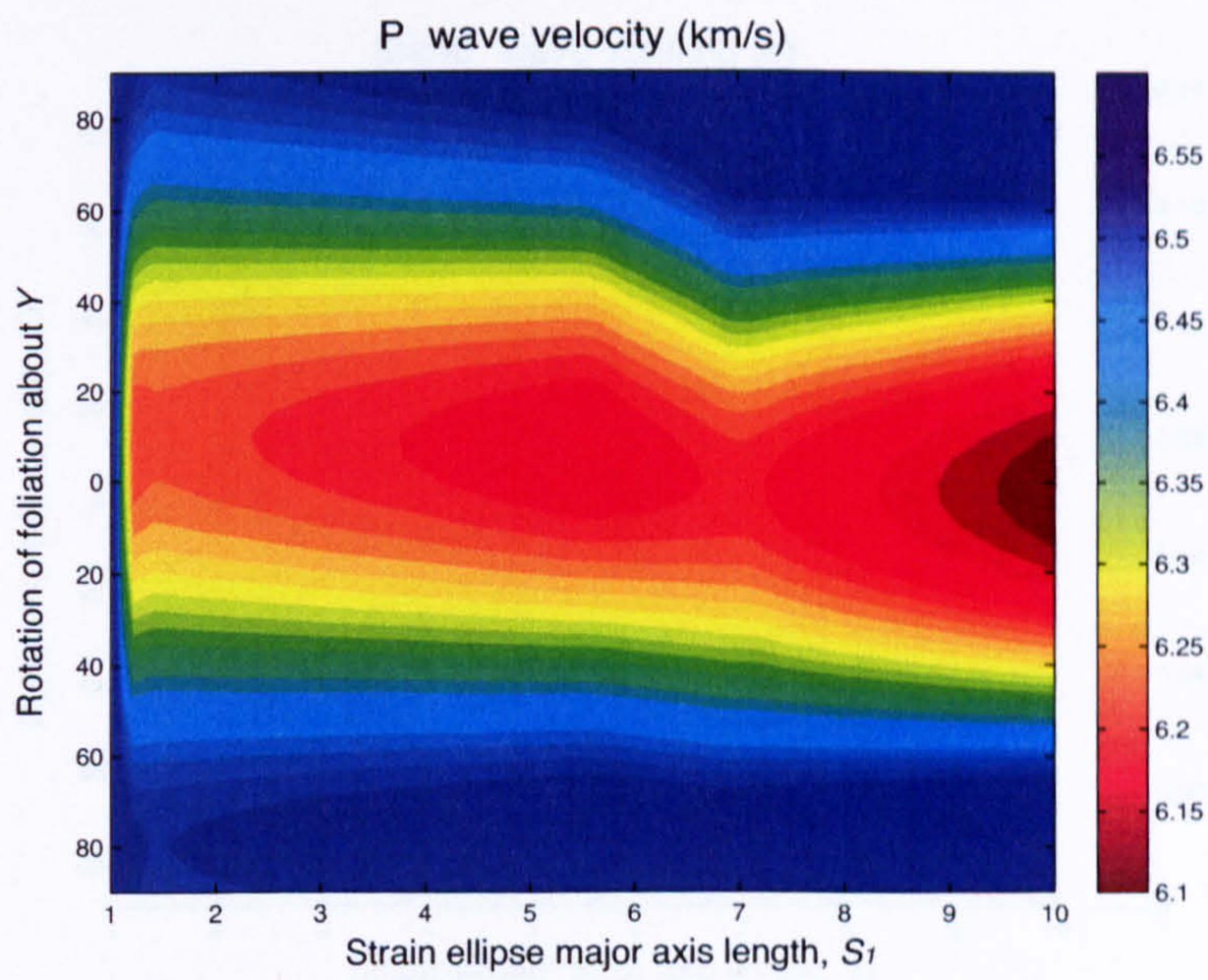

Figure 6.4: Continuum relationship between P-wave velocity, strain ellipse major axis length, S_1, and petrofabric orientation, rotated about the kinematic Y-axis. Data is that of a vertical seismic ray passing through a $10km$ thick section of material.

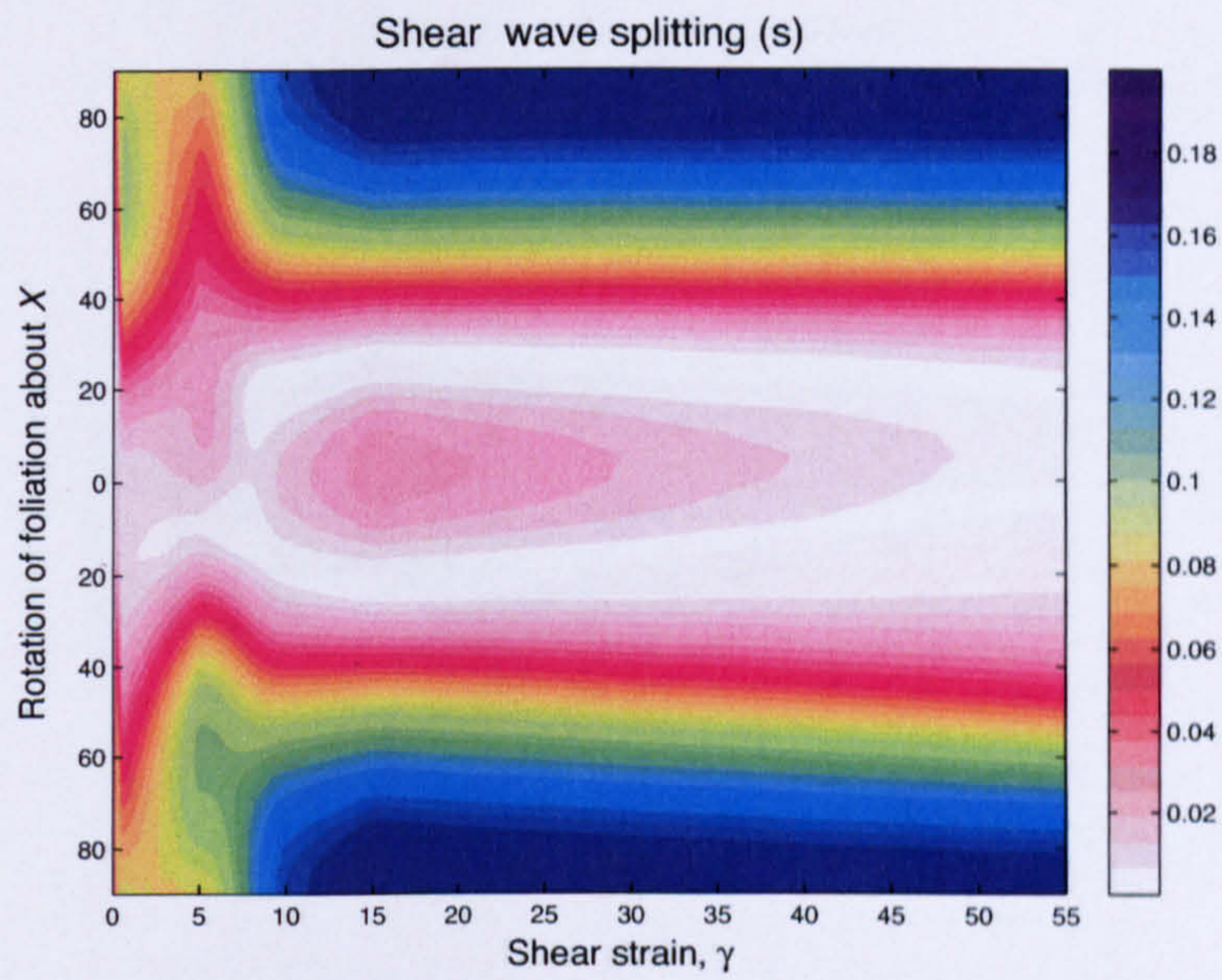

Figure 6.5: Continuum relationship between shear-wave splitting time delay, δt_s, finite strain, γ, and petrofabric orientation, rotated about the kinematic X-axis. Data is that of a vertical seismic ray passing through a $10km$ thick section of material.

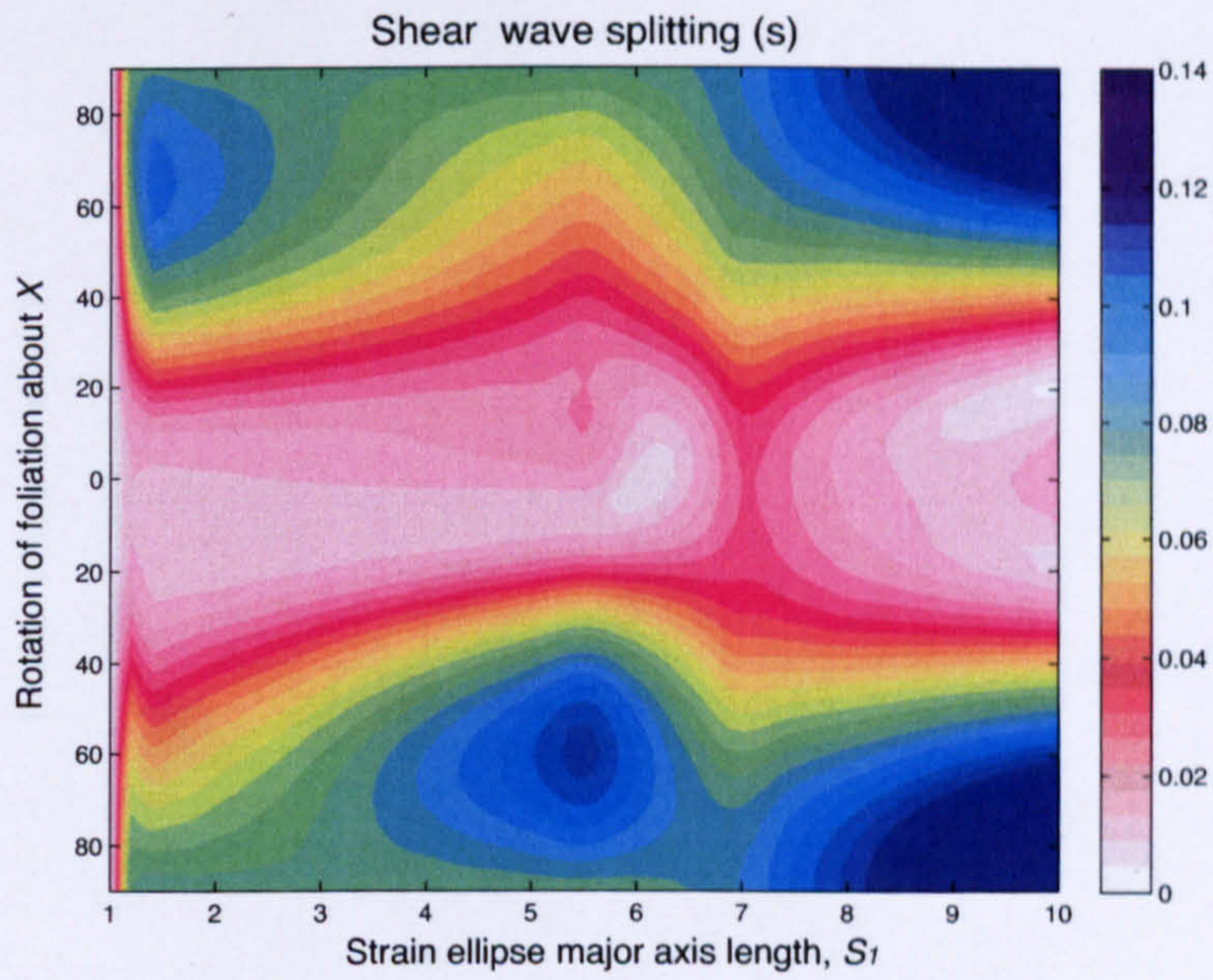

Figure 6.6: Continuum relationship between shear-wave splitting time delay, δt_s, strain ellipse major axis length, S_1, and petrofabric orientation, rotated about the kinematic X-axis. Data is that of a vertical seismic ray passing through a $10km$ thick section of material.

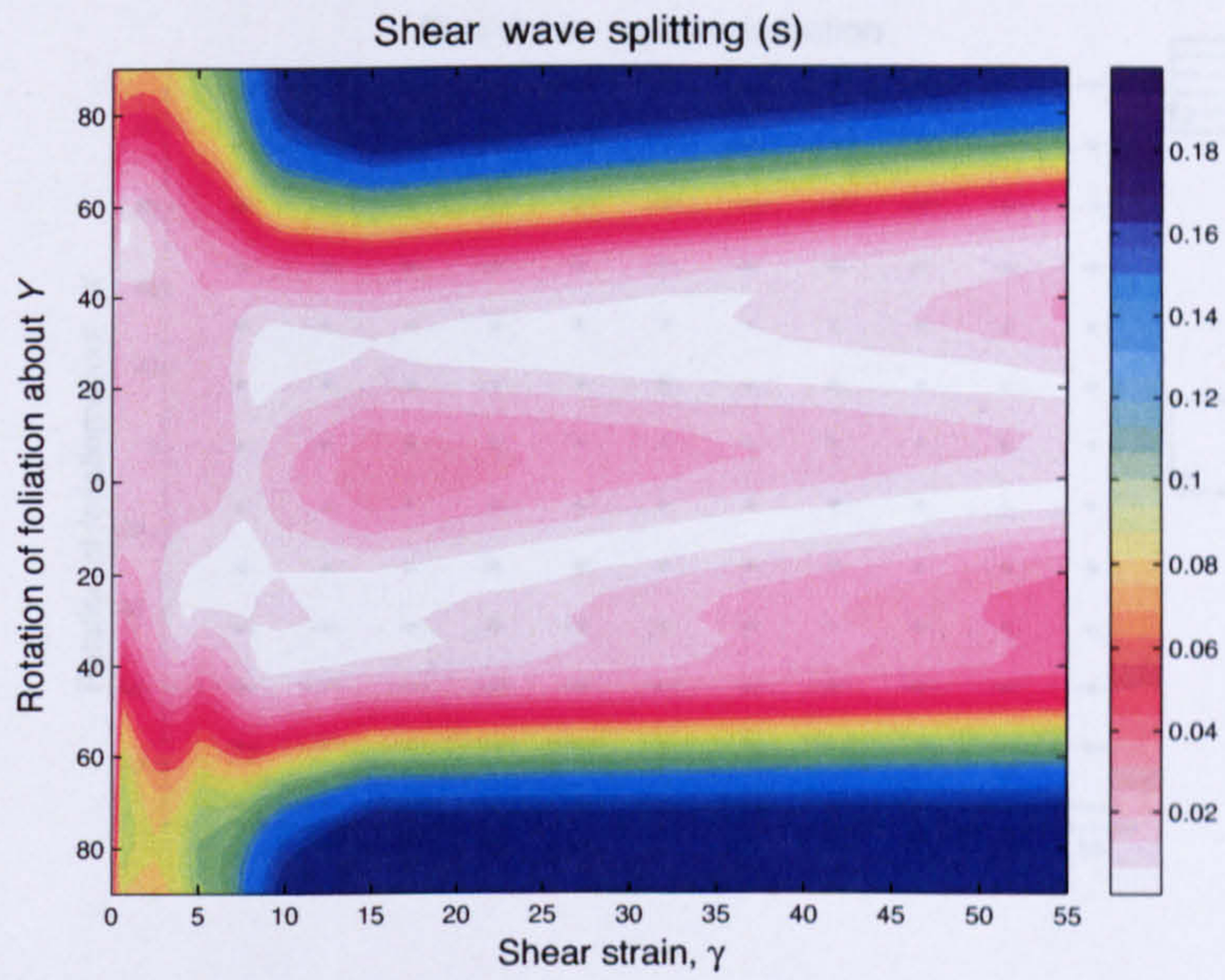

Figure 6.7: Continuum relationship between shear-wave splitting time delay, δt_s, finite strain, γ, and petrofabric orientation, rotated about the kinematic Y-axis. Data is that of a vertical seismic ray passing through a $10km$ thick section of material.

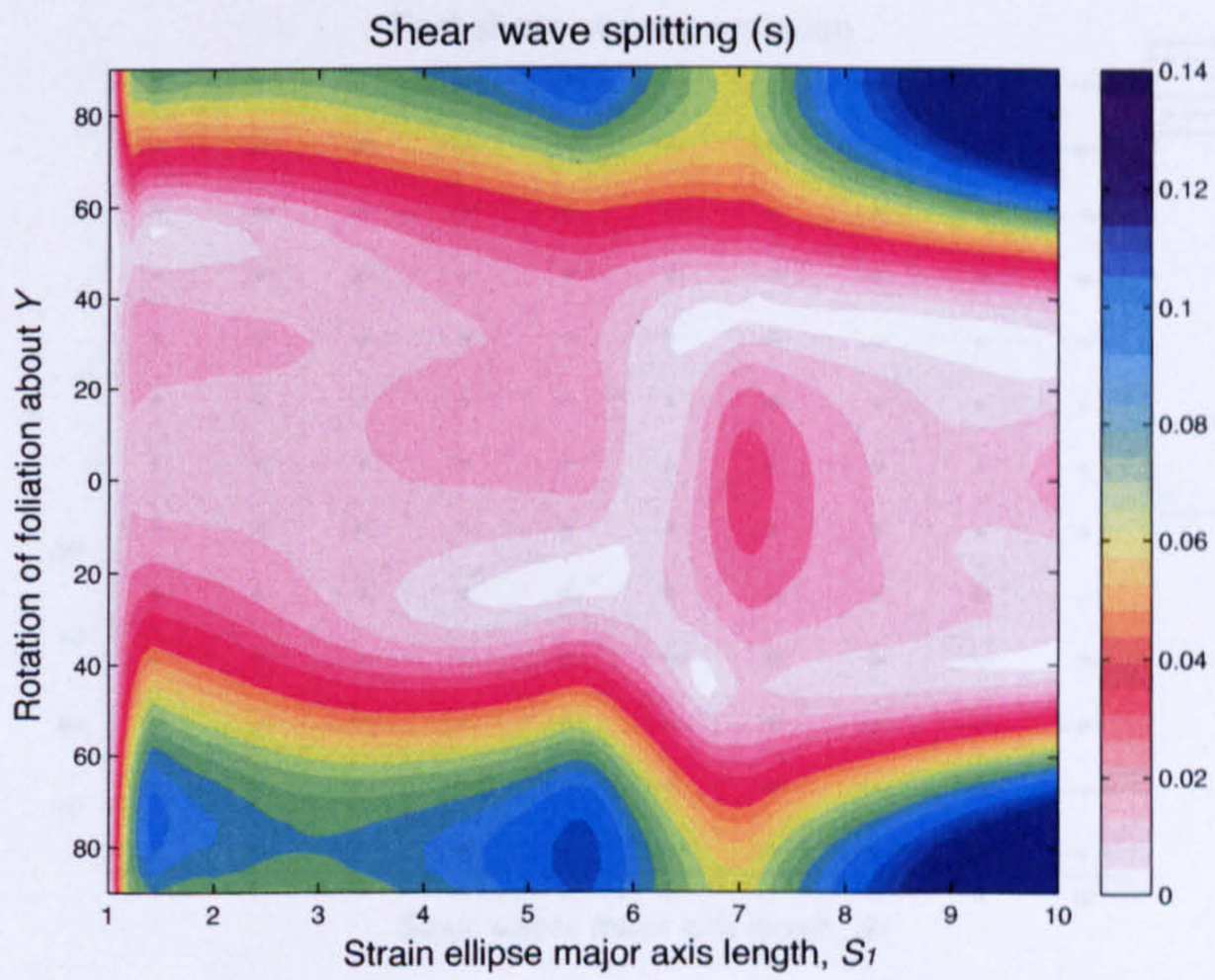

Figure 6.8: Continuum relationship between shear-wave splitting time delay, δt_s, strain ellipse major axis length, S_1, and petrofabric orientation, rotated about the kinematic Y-axis. Data is that of a vertical seismic ray passing through a $10km$ thick section of material.

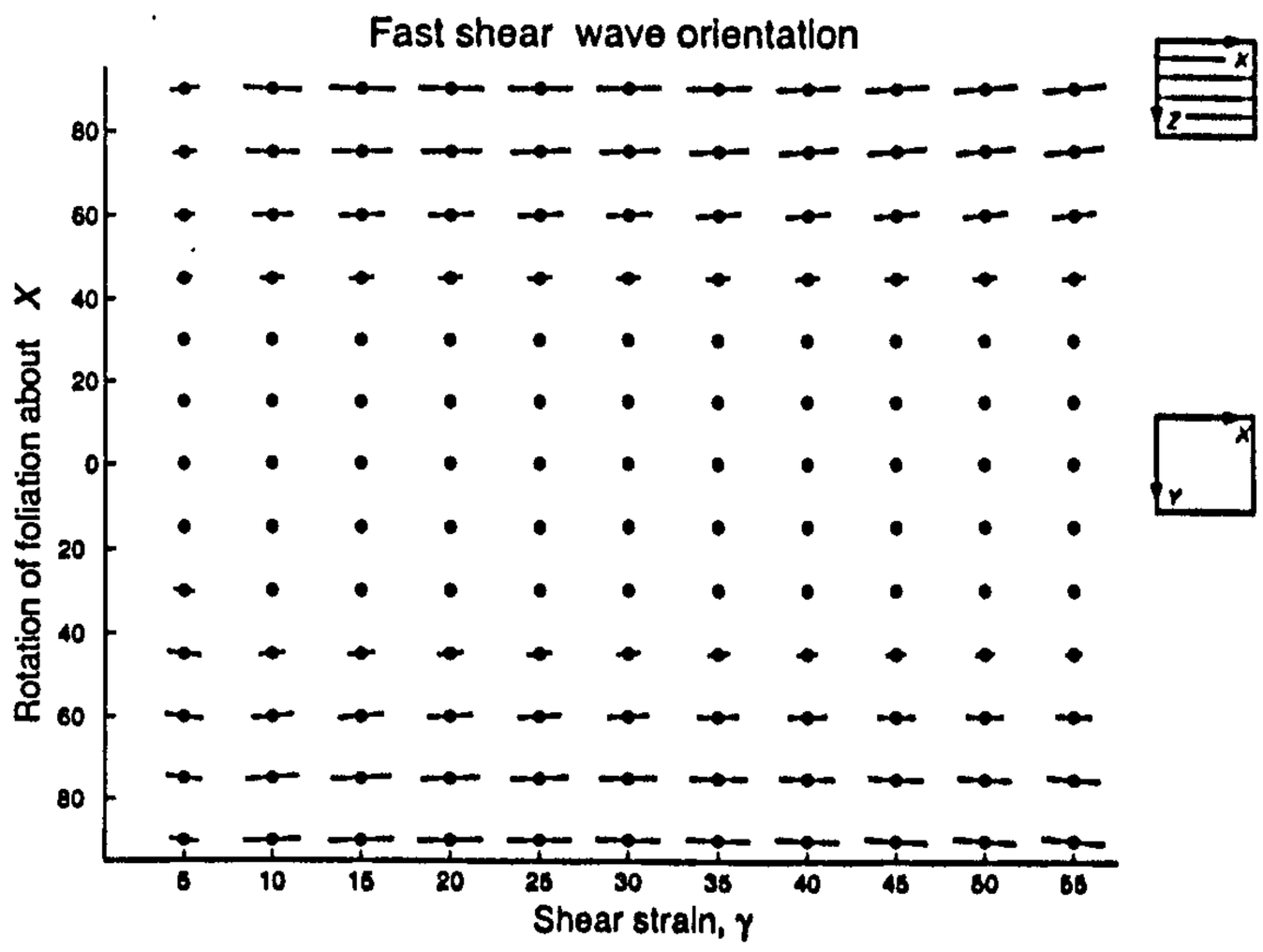

Figure 6.9: Relationship between the fast shear-wave orientation, V_{s1}, finite strain, γ, and petrofabric orientation, rotated about the kinematic X-axis. Inserts illustrate petrofabric orientation. Node points with no ticks are where no surface expression of shear-wave polarisation is observed. Data is that of a vertical seismic ray passing through a $10km$ thick section of material.

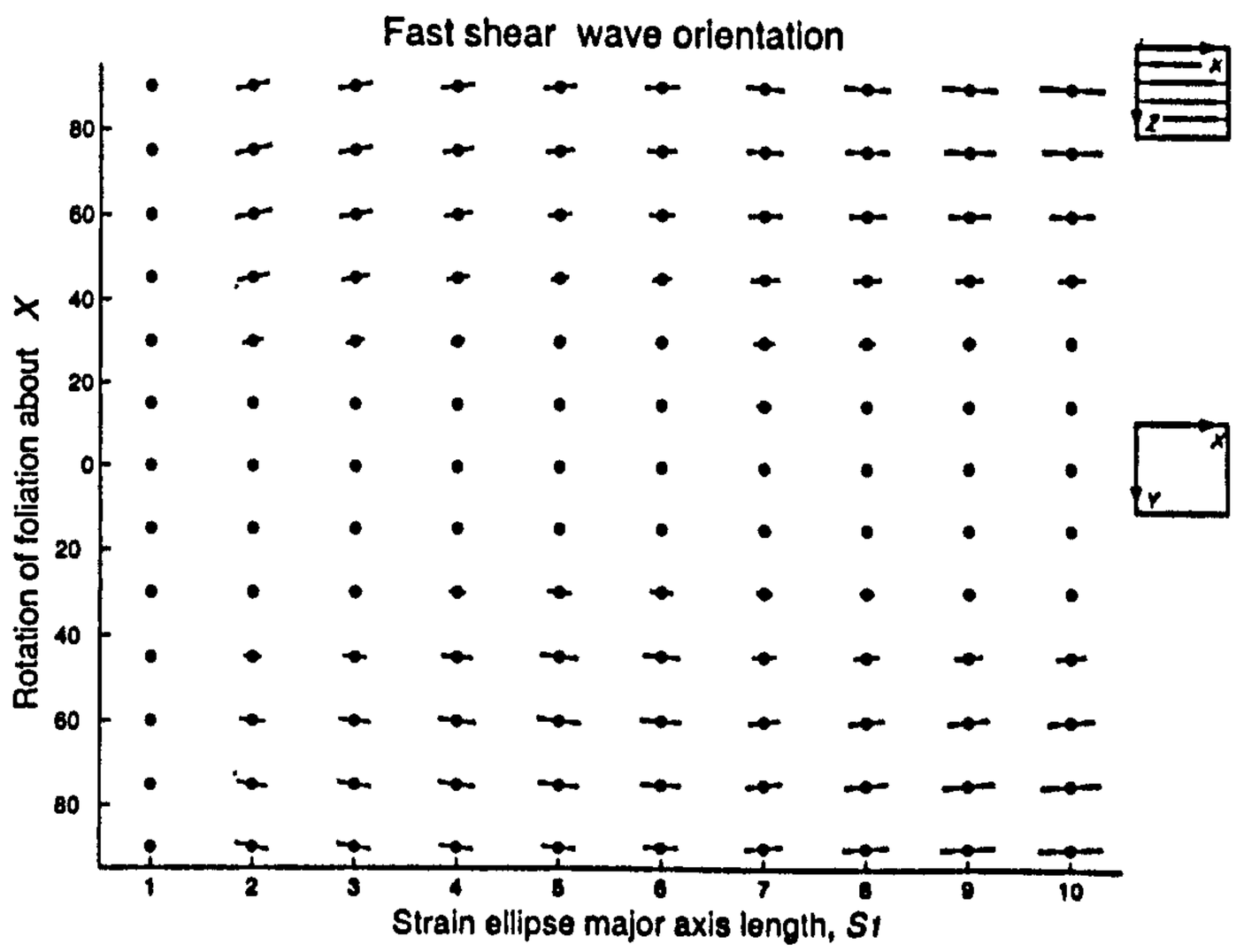

Figure 6.10: Relationship between the fast shear-wave orientation, V_{s1}, the strain ellipse major axis length, S_1, and petrofabric orientation, rotated about the kinematic X-axis. Inserts illustrate petrofabric orientation. Node points with no ticks are where no surface expression of shear-wave polarisation is observed. Data is that of a vertical seismic ray passing through a $10km$ thick section of material.

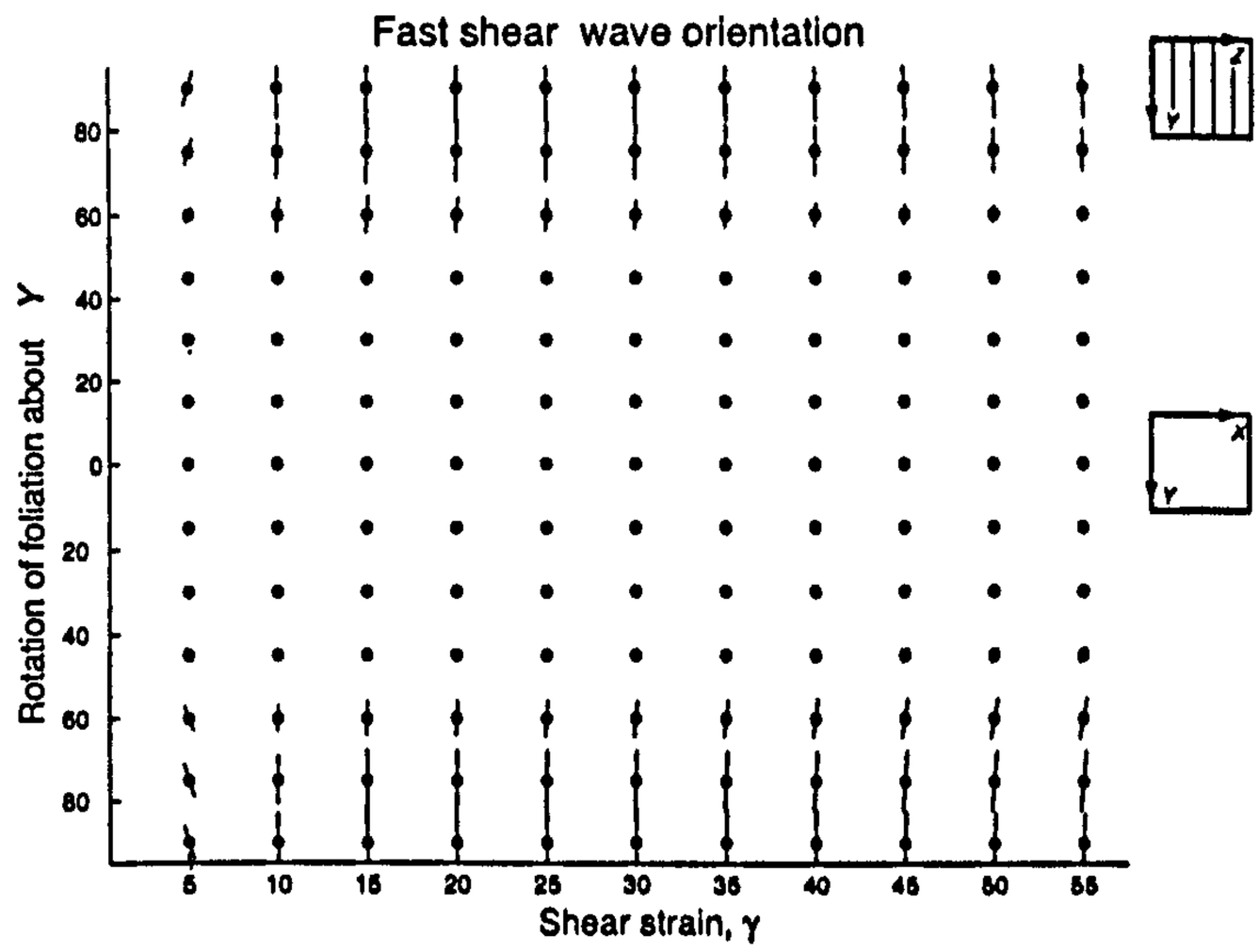

Figure 6.11: Relationship between the fast shear-wave orientation, V_{s1}, finite strain, γ, and petrofabric orientation, rotated about the kinematic Y-axis. Inserts illustrate petrofabric orientation. Node points with no ticks are where no surface expression of shear-wave polarisation is observed. Data is that of a vertical seismic ray passing through a $10km$ thick section of material.

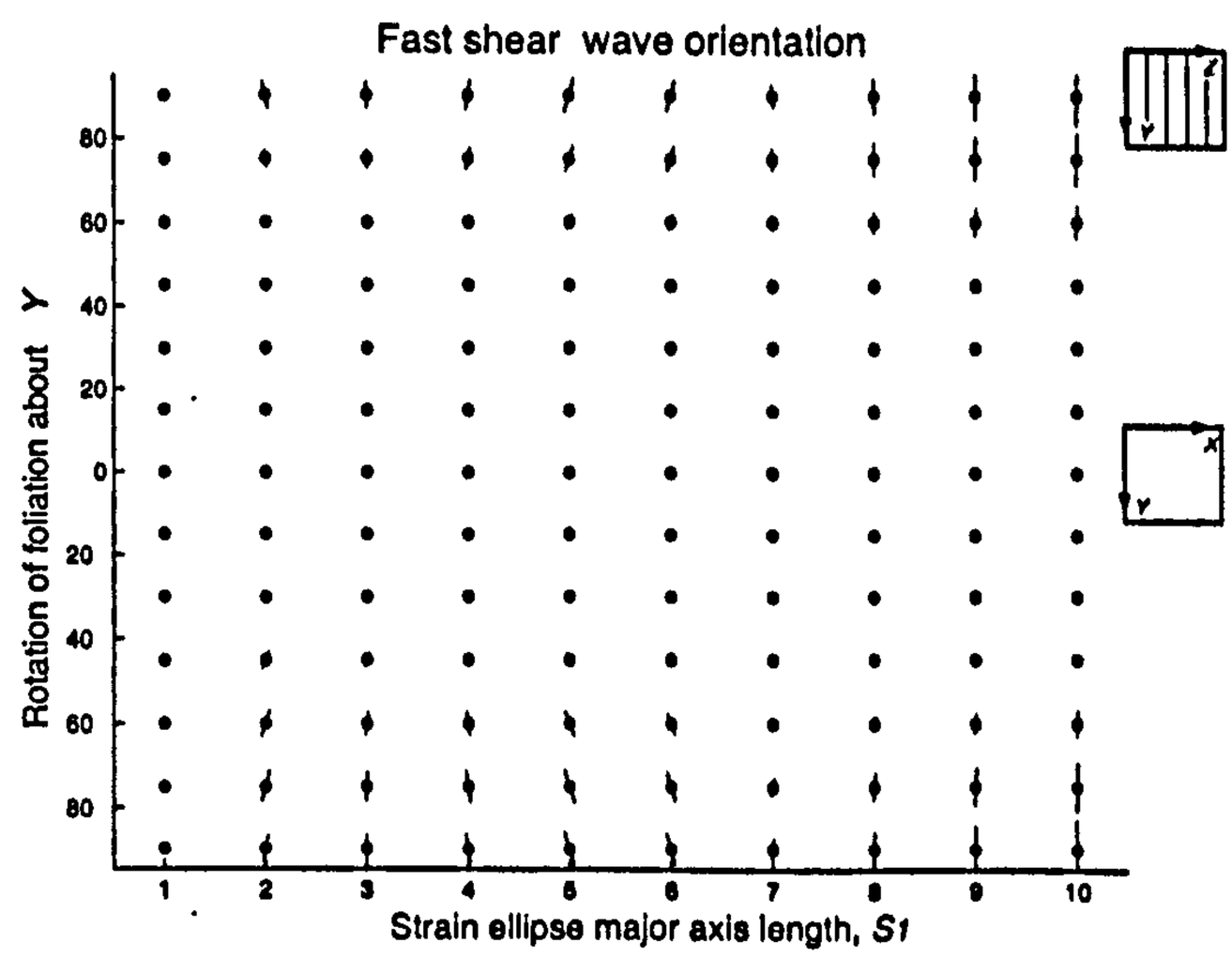

Figure 6.12: Relationship between the fast shear-wave orientation, V_{s1}, the strain ellipse major axis length, S_1, and petrofabric orientation, rotated about the kinematic Y-axis. Inserts illustrate petrofabric orientation. Node points with no ticks are where no surface expression of shear-wave polarisation is observed. Data is that of a vertical seismic ray passing through a $10km$ thick section of material.

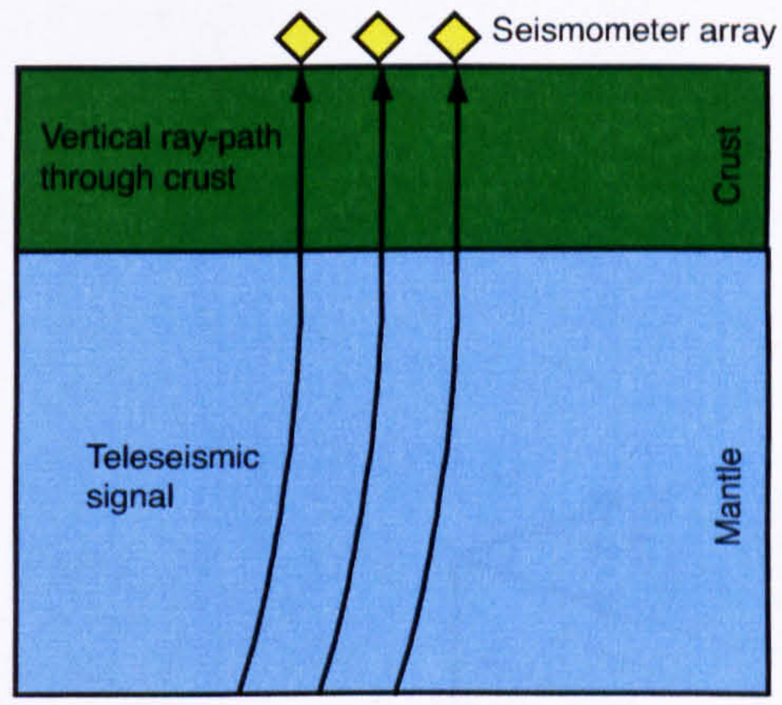

Figure 6.13: Schematic representation of a vertical teleseismic ray-path passing through the crust.

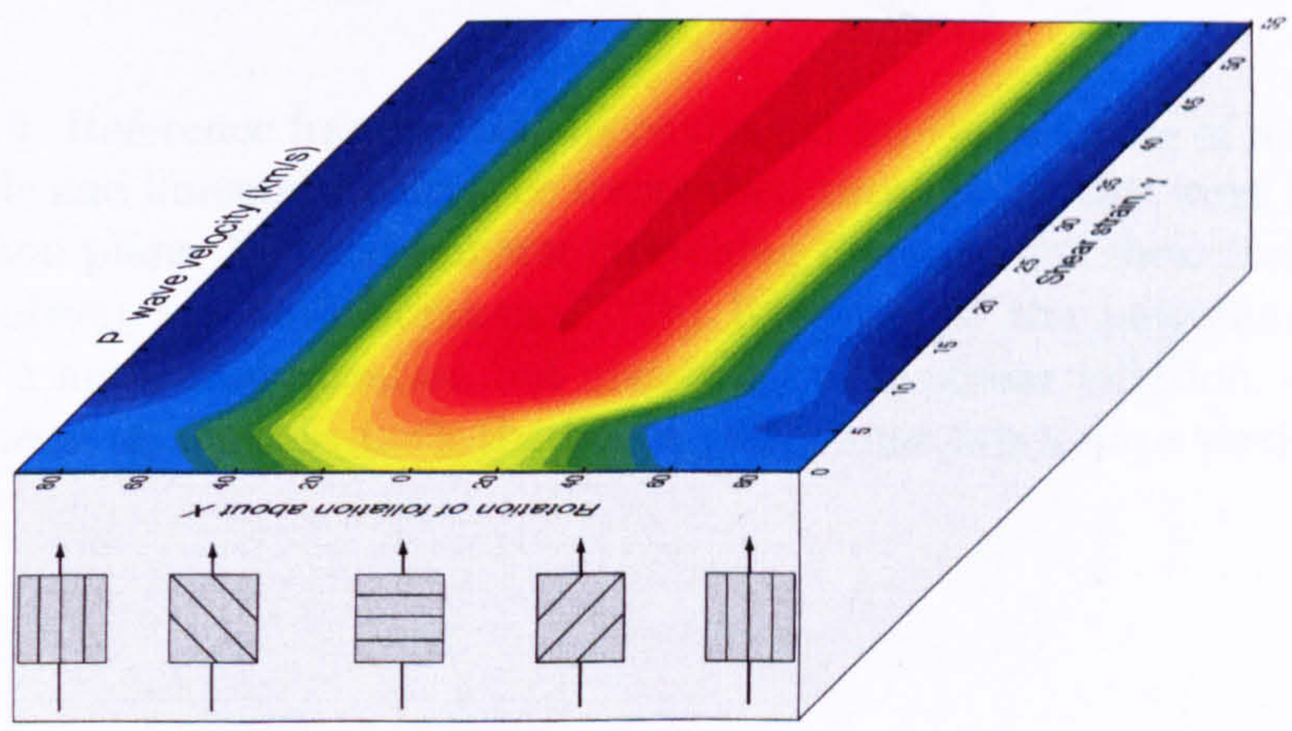

Figure 6.14: Schematic representation to aid in the visualisation and interpretation of continuum relationship models of seismic properties, Figures 6.1-6.12.

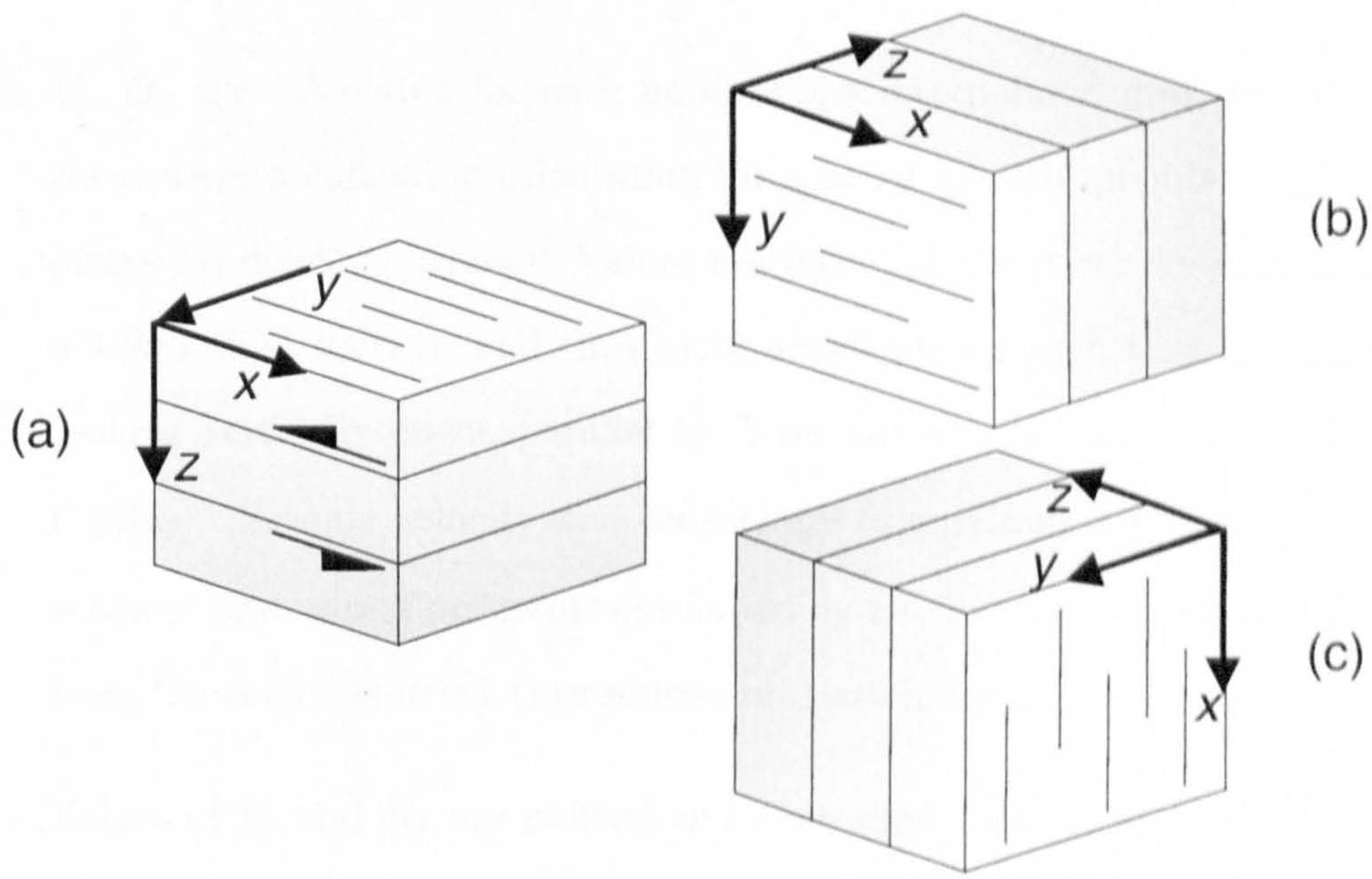

Figure 6.15: Reference frame rotations envisaged for the purpose of modelling. (a) The sample and kinematic reference frame used throughout this work (Figure 3.1). The foliation plane XY and mineral stretching lineation (or shear/tectonic movement direction) are both horizontal. (b) Rotation of the petrofabric about X maintains a horizontal lineation but gives a vertical planar foliation. (c) Rotation about Y necessitates that both the linear and planar fabrics are vertical.

as viewed parallel to the kinematic Y-axis onto the XZ-plane, where X and XY are envisaged to have a horizontal attitude spatially (as in Figure 3.1(a) and Figure 6.15(a)). Consequently, in order to highlight the variation of seismic properties with fabric orientation, the interpolated strain scale of C_{ij} is incrementally rotated with respect to either X or Y. Again, the interpolated scale of petrofabric rotation is discrete but of high resolution, with increments of 5°.

3. V_p, δt_s are calculated for each node of the interpolated grid, and the fast shear-wave polarisation orientation for a more sparsely populated grid necessary for display purposes. Values are those for a vertical ray-path through a $10km$ thick section, and thus plots are displayed such that the reader is looking vertically down, parallel to Z for the unrotated case (Figure 6.14, 6.15(a)). Seismic velocity and anisotropy calculations are processed via a series of customised programs developed by Dr. James Wookey, and derived from the code *Ematrix5* (introduced in Section 5.2.2).

4. Values of V_p and δt_s are plotted and contoured with an appropriate colour scale in *GMT*.

Each of Figures 6.1-6.12 are crudely symmetric about the line of zero rotation, where deviation from a perfect symmetry is due to slight non-orthorhombicity of the aggregate C_{ij}. This may reflect the complex interaction between constituent phases with different seismic attribute symmetries (as illustrated graphically in Figure 5.1), natural variation in the microstructure from ideal and symmetric about the kinematic axes, error in cutting specimens in the kinematic reference frame (see Section 4.2.2), or some combination of each. This suggests that in an ideal case, at least, the direction of fabric rotation, whether positive or negative about the kinematic X- or Y-axis, does not affect the pattern or magnitude of seismic velocity or anisotropy to any significant degree.

Apparently anomalous steps or jumps in the distribution of seismic properties are an amplified effect of sample variation. Discontinuities in the smoothly varying distribution (e.g. between S_1 = 6-8, Figure 6.6) mark points of sample control, and smoothly varying regions (e.g. between S_1 = 2-6, Figure 6.6) are regions of interpolation of physical properties between samples. Likewise, the complex pattern of peaks and cusps within the central band of low shear-wave splitting time lag in Figures 6.5-6.8 are due to local effects around sample control points. Such peaks and cusps are comparatively low in relief having very little value, and are considered anomalous to the overall trends outlined below. Clearly, this point highlights the need for the repetition of experimental procedures as outlined in this thesis for a plethora of natural shear zones exhibiting a strain gradient in rocks of similar lithology such that sample control in the data can be maximised, and the range over which interpolation is necessary can be reduced. This is a long-term goal however, and one beyond the scope of this project, that will ultimately provide a better characterised relationship between seismic properties and strain.

Despite the aforementioned potential anomalies that may be introduced into modelling from the results of analyses of a suite of natural samples, a number of important trends and relationships can be observed in Figures 6.1-6.8. Most noteworthy is the similarity in both the velocity and anisotropy distributions between those models in which the fabric is rotated about the X-axis, and those with a rotation about Y. This is exemplified in plots of V_p distribution (Figures 6.1-6.4) where the pattern of the distribution between those plots with a rotation about X and those with a rotation about Y are closely congruent, and the main difference is the magnitude of values. This similarity in seismic property distribution between plots with rotations about X and Y is also seen in the shear-wave splitting analysis (Figures 6.5-6.8).

A key trend exhibited in the plots is a general decrease in the magnitude of seismic velocity and anisotropy with increasing strain for sub-horizontal petrofabric

orientations. This contrasts with a trend of velocity and anisotropy values increasing with strain at high, sub-vertical, fabric orientations. The greatest rate of change is observed between $0 \leq \gamma \leq 10$ equating to $1 \leq S_1 \leq 10$, beyond which further increases in strain result in negligible change in velocity or anisotropy. This supports the suggestion of a logarithmic relationship between seismic attributes and strain presented in Section 5.2.1 and illustrated in Figures 5.4 and 5.5 whereby petrofabric and hence petrophysical properties become saturated by $\gamma \approx 10$. Note that the P-wave velocities of Figures 6.1-6.4 refer specifically to vertically propagating waves. Thus, their relationship with strain is different to that inferred from Figure 5.3 which plots the maximum P-wave velocity calculated across the entire three-dimensional distribution, irrespective of its azimuthal direction.

A somewhat steeper gradient in the change in V_p and δt_s with strain can be observed in detail between $1 \leq S_1 \leq 1.2$ or $0 \leq \gamma \leq 0.4$ (e.g. Figures 6.1 and 6.2). For example, for sub-horizontal petrofabrics, this corresponds to a drop in V_p from $6.60 kms^{-1}$ typical of the isotropic petrofabric of the undeformed protolith to $6.25 kms^{-1}$ at $\gamma = 0.4$ or $S_1 = 1.2$ (shown most clearly in Figure 6.2). Similar large changes with fractional increase in strain are seen in plots of δt_s (e.g. Figure 6.5), and suggests that a very small amount of initial strain imposed upon an initially isotropic protolith can have dramatic effects upon its seismic response. This inference is again supported by the observation of a symmetry developed in the seismic velocity and anisotropy distribution of Sample 2 at its low strain ($\gamma = 0.18$) (Figure 5.2) that is congruent with those representative of very high finite shear strain (e.g. Sample 8, $\gamma = 57$); and the steep initial gradient in the relationship between anisotropy and strain (Figure 5.4).

The change from a dominantly decreasing trend to one of increasing values of seismic attributes with strain occurs around fabric a orientation of 20°-40° for V_p and δt_s with fabric rotation about X (e.g. Figures 6.1 and 6.5). This switch occurs closer to 60° for δt_s with fabric rotation about Y (Figures 6.7 and 6.8), and

is a reflection of the details of the distribution in the AV_s pole figure (Figure 5.2). That is, the 'crown' of low anisotropy in Figure 5.2 (e.g. Sample 7, AV_s) occupies a greater portion of the XZ-plane (the pole figure circumference) than the YZ-plane (the plane vertically 'north-south' through the pole figure). This leads to a comparatively wider central band of low δt_s values about sub-horizontal petrofabrics in Figures 6.7-6.8 than Figures 6.5-6.6.

It follows that for a given strain, a move from sub-horizontal to sub-vertical petrofabrics is associated with an increase in values of V_p and δt_s.

Analysis of V_{s1} polarisation orientations (Figures 6.9-6.12) shows a distribution similar to those of V_p and δt_s whereby the vertical expression of shear-wave polarisation becomes more acute with increasing strain and an increasingly vertical tectonic foliation, XY. This is an intuitive result and reflects the development of an increasingly defined planar fabric with strain, and the increasing parallelism of that petrofabric with the seismic ray-path. The V_{s1} polarisation plane is consistently parallel to the plane of petrofabric foliation (Figures 6.9-6.12 inserts), which is in turn parallel with the girdle of greatest shear-wave anisotropy (Figure 5.2).

Interpolation of the petrophysical properties of a discrete, strain calibrated, microstructurally characterised and compositionally normalised sample suite thus permits the evaluation of seismic properties against finite strain and petrofabric orientation in that material, across a continuum. The proceeding sections show how such generic results can be utilised and incorporated into structural models of continental deformation.

6.3 Application in crustal modelling

Results presented hitherto describing the dependance of seismic properties on aggregate modal composition, petrofabric orientation, and bulk strain, together comprise a useful tool for manifold geological and geophysical applications. For example, strain-calibrated seismic velocities and anisotropy could prove invaluable

in increasing the accuracy and authenticity in both forward and reverse modelling between lower crustal anisotropy and strain in regions of recent or contemporary continental deformation, and in making inferences on the mechanical communication between the upper and lower crust with respect to strain distribution.

In order to provide an example of the application of strain-calibrated physical and seismic properties in structural models, three case studies are presented.

6.3.1 Model assembly

The models presented here are simplified and length-averaged block models for regions of crustal extension and compression where two or more competing theories have been proposed in order to explain their spatially and temporally complex structure and histories. They are, therefore, not a unifying model of the crustal structure in each of the regions discussed, nor are they intended to account for the spatially and temporally finer scale complexities and heterogeneities. Their purpose is to show how the use of simple, broadly representative crustal models that incorporate logical and intuitive predictions of tectonic strain state, and hence the petrofabric and seismic attribute development and orientation, can be used to highlight structure within an iso-compositional lower crust. This approach may therefore help to differentiate, to a first approximation, between end-member modes of crustal deformation. These simplistic but representative models provide a foundation for augmentation in further studies with spatially and temporally more complex structures and petrophysical profiles.

Each model can be considered in terms of an assemblage of seismo-structural building blocks or domains (e.g. Figure 6.18). Each domain is associated with a material property that is representative of the finite strain and petrofabric orientation for that position in the structural framework. This dictates that each domain is associated with specific seismic properties, of which the P-wave velocity of a vertically propagating ray is of interest here (as presented in Figures 6.1

to 6.8). Seismo-structural domains are colour-coded according to their vertical P-wave velocity. Velocity contrasts between domains are often subtle.

For the purpose of generating realistic crustal cross-sections, an approximation of the seismic properties of upper crustal and lithospheric mantle material is necessary. For the upper crust, this is realised by a synthetic isotropic aggregate of 50% quartz, 25% plagioclase, and 25% orthoclase to approximate granitic composition. The aggregate material properties are generated from randomised single crystal elastic stiffness matrices, C_{ij}'s, via *Ematrix5* (see Section 5.2.2), mixed to the appropriate ratio. Its isotropy means that is has velocity but no anisotropy, and therefore should not mask the effect of anisotropy in the lower crust. For those models necessitating the incorporation of a sediment package (North Sea example), the same procedure is followed for an aggregate of 50% quartz, 15% plagioclase, 15% orthoclase, 10% calcite and 10% muscovite — one thought to be representative of the bulk composition of a North Sea sediment package (J.S. Maddock, pers. comm. 2006). Mantle properties are approximated from material and seismic parameters incorporated in the global velocity model *ak135* (Kennett et al., 1995). Also shown are the synthetic zero-offset reflection profiles for each model. Such profiles approximate a series of reflection seismograms from collocated seismic source and receivers in an array, where a vertically downward propagating seismic ray is reflected upwards to the surface/receiver by consecutive interfaces, or discrete seismic impedance contrasts (Shearer, 1999). Synthetic zero-offset profiles are considered a suitable analogue, at much reduced computational expense, for wide-angle reflection profiles commonly employed in deep crustal seismic studies (e.g. Allmendinger et al., 1983; Klemperer, 1988; Meissner et al., 2004, ; J.Wookey, pers. comm. 2006).

The pertinent steps in the calculation of synthetic zero-offset reflection profiles are summarised as follows:

1. From the seismo-structural block models (e.g. Figure 6.18), a series of vertical

depth profiles of elastic properties (C_{ij}) are compiled at a range of 'stations' across the model.

2. Depth profiles of elastic constants are converted to two-way travel time profiles using vertical P-wave velocities calculated from elastic constants using Equation 5.7, or approximated by (Babuska & Cara, 1991, ; J. Wookey, pers. comm. 2006):

$$V_p vert \approx \sqrt{\frac{c_{33}}{\rho}} \tag{6.1}$$

3. Across each velocity interface in the model, the reflectivity of a vertically propagating reflected P-wave is calculated from the impedance contrast across that boundary, according to the reflection coefficient, R_c (Sheriff & Geldart, 1999; Shearer, 1999):

$$R_c = \frac{V_{p_2}\rho_2 - V_{p_1}\rho_1}{V_{p_2}\rho_2 + V_{p_1}\rho_1} = \frac{Z_2 - Z_1}{Z_2 + Z_1} = \frac{A_1}{A_0} \tag{6.2}$$

where the product $V_{p_n}.\rho$ between vertical P-wave velocity and density is the impedance, Z_n. Note that R_c is related to the amplitude of the reflected ray, A_1, relative to that of the incident ray, A_0. Reflection amplitude, being related to the reflection coefficient, can therefore be used as a proxy for lateral changes in material properties along a reflector, such as variations in material finite strain state.

Practically, this step is computed using the program *RMatrix* for modelling the reflection response of a stack of generally anisotropic layers (Martin & Thomson, 1997).

4. The reflectivity profile or trace of Step 3, being a function of reflection strength with travel time, is convoluted with a simple source wavelet (a 2 second dominant period Kuepper wavelet).

5. Finally, white noise is added with a signal to noise ration of 20:1 to make the seismograms appear more realistic. The resulting trace is broadly comparable with a processed deep seismic reflection survey (J. Wookey, pers. comm. 2006).

This simple method of producing synthetic seismograms is chosen because more detailed modelling would require much more input as in the type of survey trying to be reproduced, such as wide-angle or receiver function. Those synthetic seismograms would require processing like real data, and the conclusions that might be drawn would be dependant on that processing. This level of modelling is beyond the scope of this research. It does, however, present avenues for subsequent research projects, where, for example, wide-angle reflection profiles, may prove to be more adept in highlighting and distinguishing contrasts in deformation in deep crustal materials with sub-horizontal petrofabrics.

Three case studies are presented: the eastern Basin and Range Province, the northern North Sea, and the Tibetan Plateau. The reasons for choosing these examples are manifold. Primarily, they collectively span a range of important examples of continental deformation including continental rifting, observed both subaerially and submarine, and continental collision. Of equal importance, each area is represented in the literature by at least two competing models regarding their crustal structure and strain localisation. Furthermore, each area is particularly well studied, both geologically and by geophysical techniques, and so key structural information, such as depth to Moho, fault offsets and the base of seismicity (marking the brittle-ductile transition), are relatively well constrained.

6.3.2 Eastern Basin and Range Province

The eastern Basin and Range Province of the southwestern United States provides a classic example of a region of complex continental extensional deformation to which two broad end-member models have been applied.

Structural models of the Basin and Range Province must satisfy a number of key geological and geophysical observations. These include:

1. A uniform, relatively shallow Moho depth of approximately $30km$, estimated from seismic reflection profiling (Gans, 1987; Brady et al., 2000). Pre-extensional crustal thickness is predicted from observations of the neighbouring and relatively undeformed Colorado Plateau region, where the Moho depth is estimated around $45km$ (Gans, 1987; Brady et al., 2000).

2. A depth to the brittle-ductile transition of approximately $10km$ is based on compatible estimates of the base of seismicity (Smith & Bruhn, 1984) and projections from structural and petrological observations in exhumed sections exhibiting the interface between distributed brittle faulting in the hanging-wall and pervasive ductile deformation of the footwall (Rehrig & Reynolds, 1980; Snoke, 1980; Miller et al., 1983).

3. Surface observations of widespread extensional deformation. These include zones of low-angle normal faulting, fragmented extensional allochthons and metamorphic core complexes (Wernicke, 1985). Such structures expose mid- to lower crustal rocks exhibiting pervasive ductile deformation, beneath, or at least in a zone at the brittle-ductile transition (Rehrig & Reynolds, 1980; Snoke, 1980; Miller et al., 1983).

Wernicke (1981, 1985) proposed a model of uniform-sense normal simple shear of the lithosphere to explain the observed spatial discrepancy between areas of maximum surface extension and the position of maximum crustal thinning inferred from unmigrated seismic profiles (Figure 6.16). His model shows a distributed zone of upper crustal faulting detaching at the brittle-ductile transition in the mid-crust onto single zone of ductile simple shear, which continues through the lower crust and beyond as a discrete zone, offsetting both the Moho and the base of the lithosphere.

In contrast, a number of workers have contended the concept of a crustal-penetrating shear zone, suggesting that evidence better fits a model of pervasive pure shear throughout the lower crust (Miller et al., 1983; Smith & Bruhn, 1984; Gans, 1987) (Figure 6.17). Such models cite the lack of Moho relief observed on migrated seismic reflection profiles as evidence for uniform ductile stretching in the lower crust, acting to smooth out spatially heterogeneous strain in the upper crust (Smith & Bruhn, 1984; Gans, 1987).

Furthermore, evidence for through-crustal reflectors in seismic reflection profiles from the Basin and Range Province, representing discrete shear zones, is sparse, with continuous dipping reflectors rarely penetrating deeper than $10km$ (Smith & Bruhn, 1984; Allmendinger et al., 1987; Brady et al., 2000). This suggests that normal faults detaching at mid-crustal levels beneath which ductile pure shear prevails is the dominant deformation style.

Two crustal structure models are presented, together with their associated synthetic zero-offset reflection profiles, corresponding to each of the Wernicke (1985) and Smith & Bruhn (1984) type scenarios (Figures 6.18 and 6.19). Lower crustal domains are annotated with reference to their strain state by either S_1 or γ depending of whether the zone is modelled by pure or simple shear respectively. The finite strain ellipse is also shown where possible.

The lower crust of Figure 6.18 is dominated by undeformed material, with the model being dissected by a gently dipping shear zone. Based on constraints from field and seismic observations, a 10° dip (Allmendinger et al., 1983; Wernicke, 1985) is imposed on the $2km$ wide shear zone (Miller et al., 1983; Davis, 1987), with a total dip-slip displacement of $86km$ (in accord with estimates of extension in e.g. Allmendinger et al., 1983; Wernicke, 1985; Gans, 1987), necessitating a shear strain in the deformation zone of $\gamma = 43$. This geometry thins a $45km$ crustal section to $30km$. Based on evidence of rapid increase in strain over a narrow distance relative to the width of the shear zone (Section 2.3), it is considered unnecessary

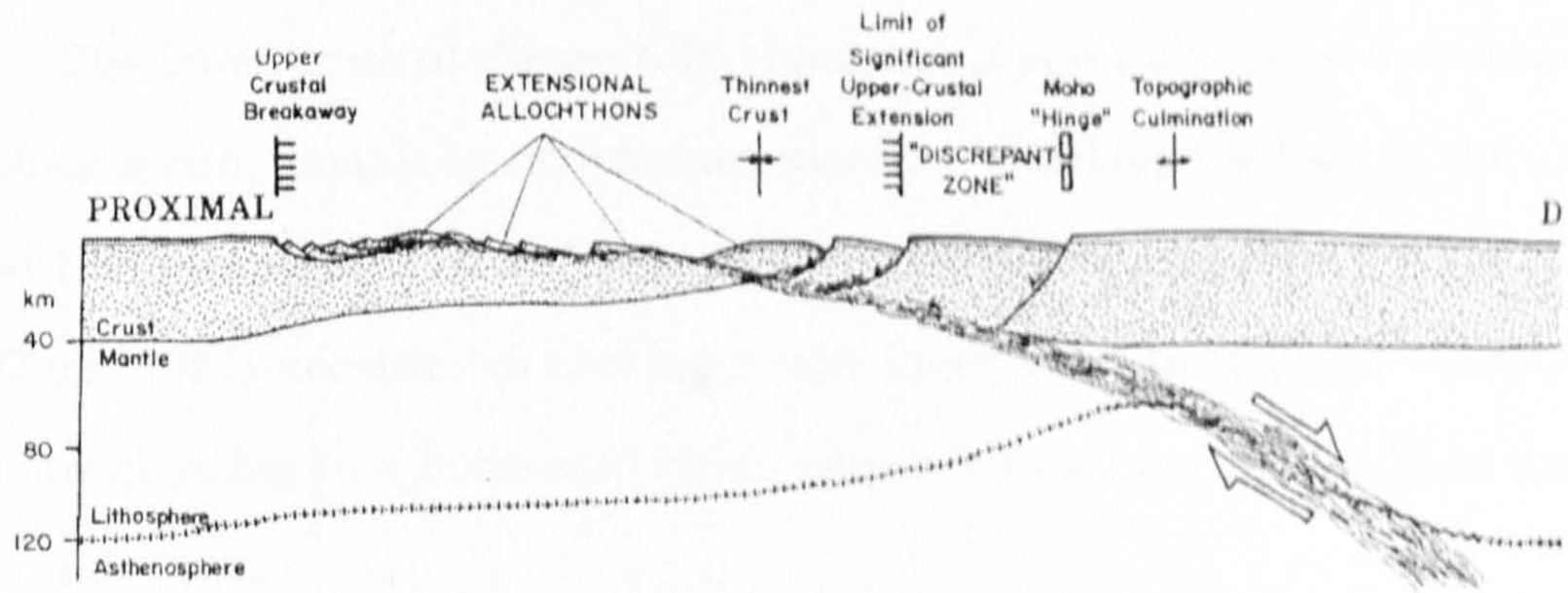

Figure 6.16: Hypothetical model of normal simple shear of the entire continental lithosphere, from Wernicke (1985). His model is based around the observation of a 'discrepant zone' where inferred crustal thinning is not matched by observations of an equal extensional deformation in the upper crust.

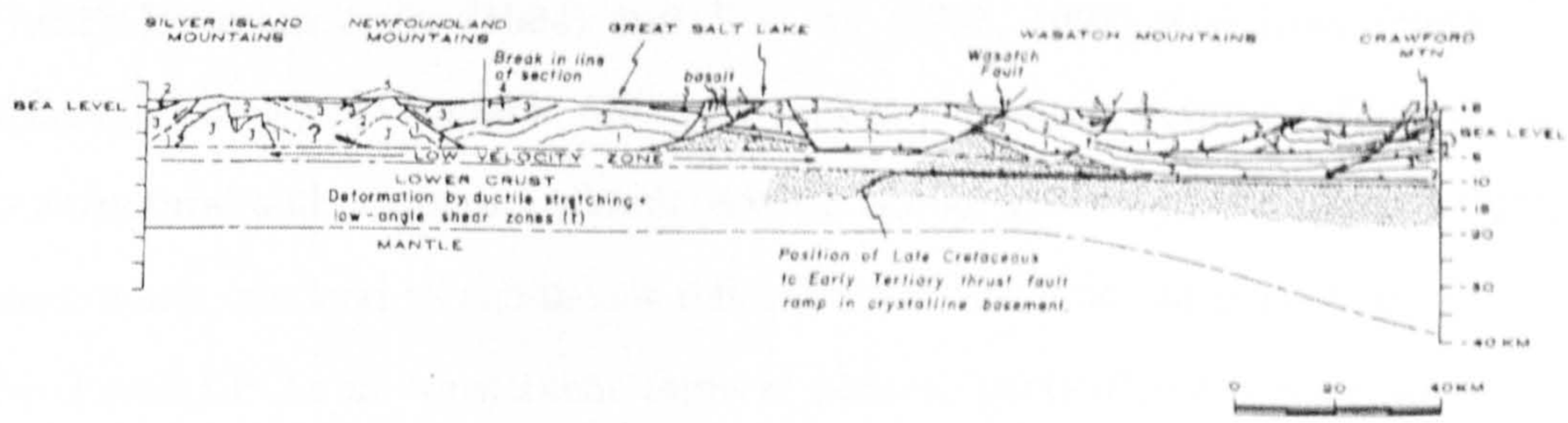

Figure 6.17: Model of uniform lower crustal stretch beneath the northern Utah east-west section of the Basin and Range Province, from Smith & Bruhn (1984). Numbers refer to locally-named sedimentary units, and are unimportant here.

and an over-complication to include a strain gradient bordering the high strain simple shear zone of Figure 6.18. The internal structure of the upper crust and mantle are not considered.

The lower crust of Figure 6.19 comprises a central zone of homogeneous pure shear strain, flanked by undeformed material. Marking the base of the upper crust at $10km$ throughout, the aforementioned crustal thinning from $45km$ to $30km$ (e.g. Gans, 1987) necessitates necking in the lower crust from $35km$ to $20km$. Strain corresponding to a horizontal strain ellipse long axis of $S_1 = 1.75$ is thus applied to this zone.

Initial observation of Figures 6.18 and 6.19 synthetic seismograms shows only subtle differences between them. For example, the reflectivity of the interface between the upper crust and undeformed lower crustal material (Figure 6.18) is indistinguishable from that with strained material (Figure 6.19).

Perhaps the most important feature is the dipping reflector through the lower crust representing a shallow dipping crustal-penetrating shear zone (Figure 6.18). This suggests at least partial success of the models such that resolvable lower crustal reflectivity can result from zones of strain contrast, without the necessity for a change in bulk composition. This lends support to work by Jones & Nur (1982); Fountain et al. (1984) and Ji et al. (1993, 1997) who have shown that although lithological contacts are important in generating seismic reflectivity, microstructural and petrofabric characteristics of high-grade and retrogressed ductile shear zones can lead to significant reflectivity of the zone. In particular, strongly developed LPO's in constituent mineral phases, particularly phyllosilicates and hornblende (which show a significant velocity low parallel to Y in their ordered states compared to their isotropic velocities), can give low to moderate reflection coefficients against an isotropic protolith of the same composition. This effect is enhanced when it coincides with a lithological interface. Geometrical characteristics of the shear zones can have the effect of increasing their reflectivity due to

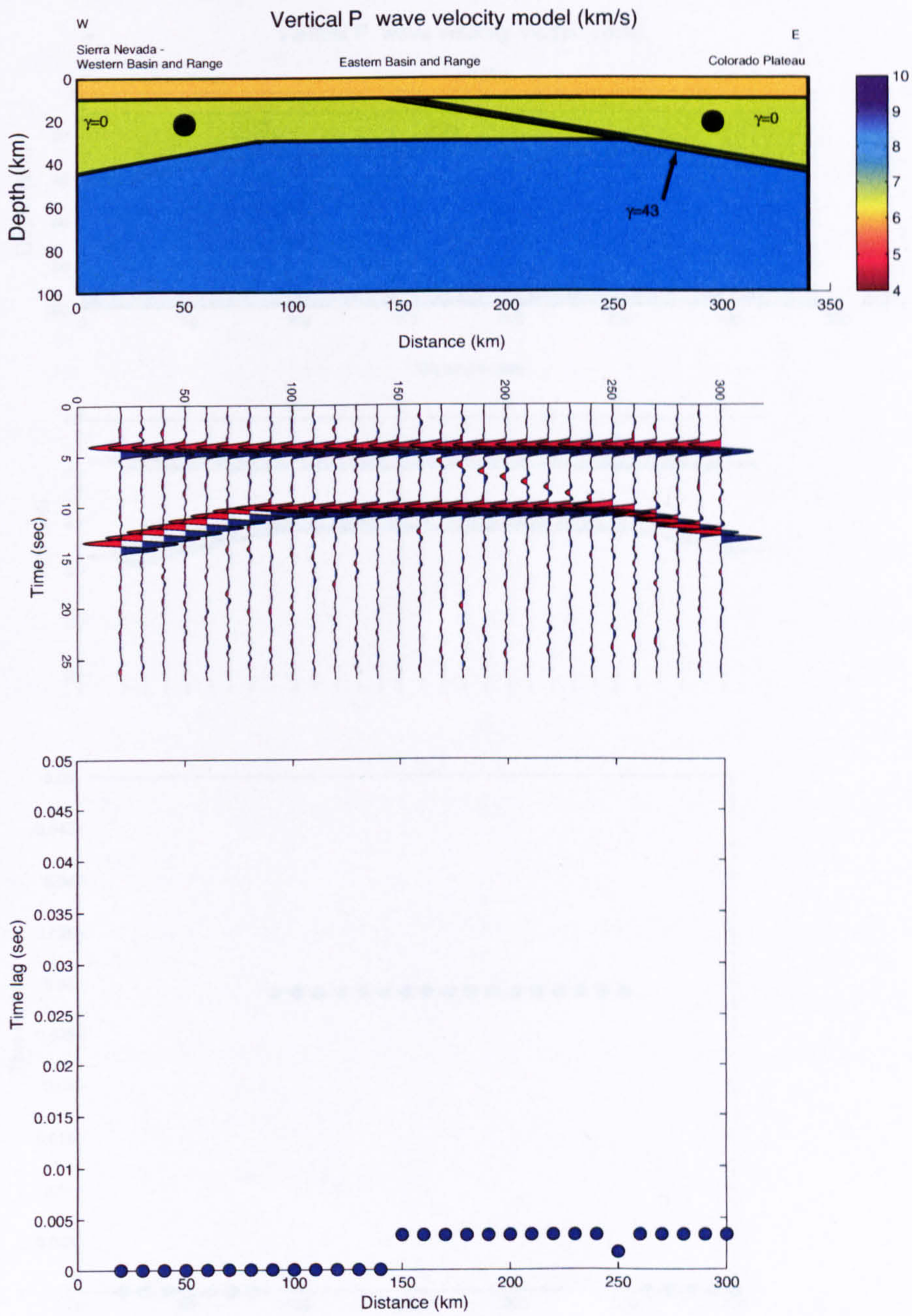

Figure 6.18: (Top) Crustal P-wave velocity model of the eastern Basin and Range Province, based on the normal simple shear model of Wernicke (1985). (Middle) Associated zero-offset seismic reflection profile. Notice the dipping reflector between $150km$-$250km$ and 5-10 seconds two-way time. (Bottom) Time lag (δt_s) between split shear-waves propagating vertically through the model.

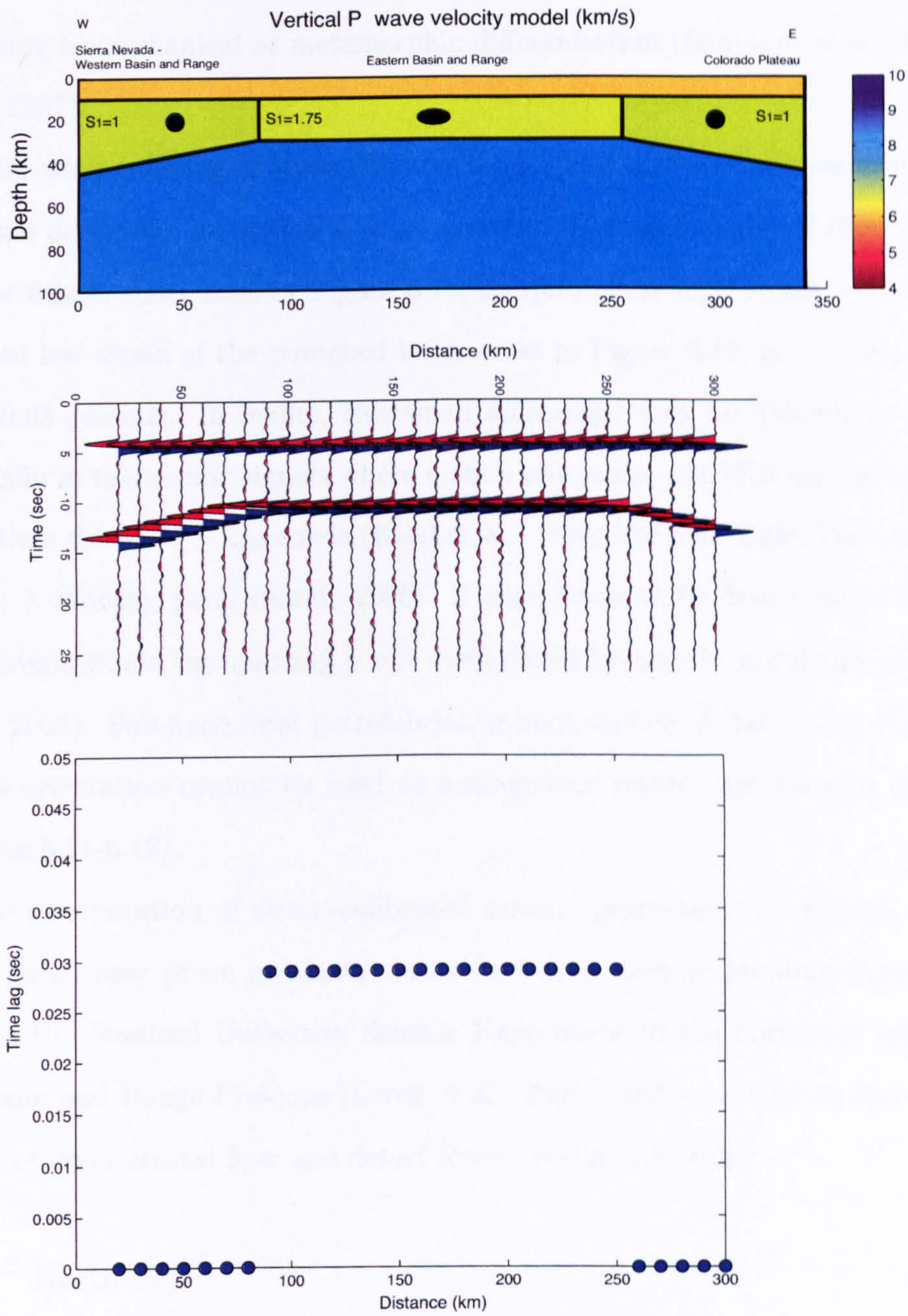

Figure 6.19: (Top) Crustal P-wave velocity model of the eastern Basin and Range Province, based on the uniform, ductile pure shear stretching model of Smith & Bruhn (1984). (Middle) Associated zero-offset seismic reflection profile. (Bottom) Time lag (δt_s) between split shear-waves propagating vertically through the model.

complex constructive interference of multiple reflections across a narrow, finely layered or anastomosing network of shears or compositional layering within the shear due to mechanical or metamorphic differentiation (Fountain et al., 1984; Ji et al., 1997).

Shear wave splitting analysis (Figures 6.6-6.7 and 6.18-6.19) indicates only minor time delay, δt_s, in vertical S-wave arrivals. The shallow dip of the relatively narrow simple shear zone of Figure 6.18, in spite of its high strain, and the distributed low strain of the stretched lower crust in Figure 6.19, predict δt_s around 0.003-0.03 seconds. In reality, this small anisotropy may be difficult to resolve, especially in teleseismic signals where mantle anisotropy for SKS signals may generate time delays of ≤ 2 seconds (Kind et al., 1985; Kendall, 2000; Park & Levin, 2002, ; J. Wookey, pers. comm., 2006). It may, however, be detectable in shallow, local events where the splitting is not overprinted by mantle anisotropy (e.g. Keir et al., 2005). Sub-horizontal petrofabrics in both models dictates that V_{s1} polarisation orientation cannot be used as a diagnostic seismic attribute in this case (Figures 6.11-6.12).

The incorporation of strain-calibrated seismic properties into crustal models, as outlined, may prove invaluable in current deep seismic profiling experiments such as the Stanford University Seismic Experiment in the northwest margin of the Basin and Range Province (Lerch et al., 2005), and especially in their efforts to image lower crustal flow and detect lower crustal anisotropy.

6.3.3 North Sea

Like the Basin and Range Province, the northern North Sea is a region of extended continental crust to which end-member pure and simple shear models have been applied.

McKenzie (1978) proposed a uniform stretching model of extensional basins whereby an initial and rapid uniform stretching and thinning of the crust is followed

by a slow thermal subsidence with associated sediment accumulation. McKenzie (1978) used estimates of the thickness of the Tertiary sedimentary pile in the North Sea Rift to infer stretch by a factor of 1.5 ($\beta = 1.5$) there.

McKenzie's mathematical model has since received consistent support (Christie & Sclater, 1980; Klemperer, 1988; Badley et al., 1988; Fichler & Hospers, 1990). Klemperer (1988) presents a series of depth-migrated deep reflection profiles from which a number of key features can be observed (Figure 6.20):

1. Discrete and continuous dipping reflectors through the lower crust linking extensional structures in the upper crust to isolated dipping reflectors in the upper mantle, are notably lacking.

2. Extensional structures in the upper crust typically have an asymmetric expression.

3. The Moho depth shallows from approximately $30km$ beneath the Shetland and Norwegian margins (considered to be representative of the pre-rift crustal thickness for northwest Europe, Meissner et al., 1986, 1987) to roughly $20km$ beneath the centre of the Viking Graben. A crustal thickness of $25km$ is, however, more typical of the bulk of the rifted zone, flanking the axial Viking Graben.

4. The variation in thickness of the syn- and post-rift sediment packages reflects the patten of crustal thickness change. That is, the thickest sediment package of approximately $8km$ is observed in the Viking Graben with a $5km$ veneer being more typical of the flanking areas within the bounds of the rift.

5. The northern North Sea rift is thus characterised by an axis of crustal thinning that is spatially coincident with the axes of syn- and post-rift sedimentation, representative of the rift- and thermal subsidence phases of its tectonic evolution.

Figure 6.20: Annotated seismic reflection profile of the northern North Sea, from Brun & Tron (1993). The profile highlights the interpretations of both Pinet (1989) (1) and Klemperer (1988) (2) on Moho depth. The shaded region is the inferred lower crust. (3) marks mantle reflections, and BCU refers to the base Cretaceous unconformity, taken as the interface between pre-rift basement and syn- and post-rift sediment packages.

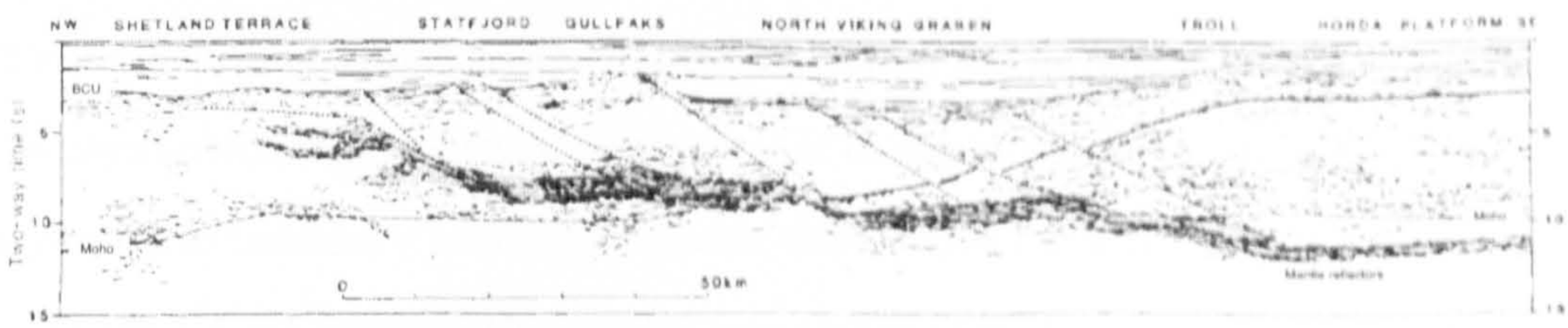

Figure 6.21: Annotated, unmigrated seismic reflection profile of the northern North Sea, from Beach (1986). The profile highlights a broad zone of lower crustal reflectors (shaded) interpreted to represents a simple shear zone. Base Cretaceous unconformity (BCU) marks the interface between pre-rift basement and syn- and post-rift sediment packages.

Crustal thinning associated with extension is here considered in terms of changes in the pre-rift basement. That is, not inclusive of the syn- and post-rift sedimentary pile. The symmetry of basement thickness is concordant with that of crustal and sediment thickness however, amounting to approximately $15km$ beneath the Viking Graben, and $20km$ across the remaining rifted zone.

Klemperer (1988) incorporated these observations and relationships to propose a model of decoupled symmetric stretching with asymmetric brittle faulting in the upper crust passing to pervasive ductile pure shear extension in the lower crust (Figure 6.20).

As highlighted by Brun & Tron (1993), although Klemperer's model incorporates pervasive ductile thinning in the lower crust, it does not necessitate that it is uniform. Indeed, his model indicates proportionally greater ductile thinning beneath the Viking Graben than it does beneath the adjoining rifted portions (Figure 6.20). Brun & Tron (1993) propose a further model of northern North Sea rifting from the results of Pinet (1989), whereby ductile pure shear in the lower crust is uniform (Figure 6.20). This model is supported by their picking of Moho reflectors beneath the Viking Graben somewhat deeper than Klemperer (1988), such that the Moho is uniformly flat at approximately $25km$ within the rift (Figure 6.20). In addition, they apply results of analogue modelling to attribute the asymmetric upper crustal expression of extension in the norther North Sea to asymmetric boundary conditions during the incipient stages of its development.

Beach (1986) adopted the crustal-penetrating simple shear zone model of Wernicke (1985) in order to explain observations from non-migrated reflection profiles (Figure 6.21). In particular, he highlights a broad and tenuous zone of concentrated lower crustal reflectors in addition to a generally asymmetric disposition of inferred structural features and dipping upper mantle reflectors coincident with the down-dip continuation of his shear zone (Figure 6.21). Upon depth-migration however, the concentrated zone of lower crustal reflectors disappear. Furthermore,

the age and origin of upper mantle reflectors remain enigmatic (Klemperer, 1988).

Three crustal models are presented, based on those of Klemperer (1988); Brun & Tron (1993) and Beach (1986), with their associated synthetic zero-offset seismic reflection profiles (Figures 6.22-6.24). Lower crustal domains are annotated with reference to their strain state by either S_1 or γ depending of whether the zone is modelled by pure or simple shear, respectively. The finite strain ellipse is also shown where possible. For the purpose of completeness and to add realism to the synthetic reflection profiles, a supra-crustal sediment layer of appropriate thickness is included in each model to represent the syn- and post-rift package.

Figure 6.22 approximates the model and observations of Klemperer (1988). A uniform base to the upper crust is set at $15km$ as indicated by the lower cut-off of brittle faulting on reflection profiles (e.g. Klemperer, 1988) and the upper limit to the lower crustal simple shear zone envisaged by Beach (1986). Strain values for each domain, and hence the material and seismic properties there, are determined from lower crustal thickness estimates relative to that of the original, pre-rift crust (Meissner et al., 1986, 1987; Klemperer, 1988). Domain widths are determined directly from reflection profiles of Klemperer (1988).

Figure 6.23 corresponds to the model of Brun & Tron (1993). Both the sediment and basement thickness satisfy observations from reflection profiles documented by Brun & Tron (1993), in addition to being in cross-sectional area balance with the model of Figure 6.22 for Klemperer (1988). In this model, the stretched lower crust is represented by a single domain, whose strain state ($S_1 = 1.6$) is again a reflection of the lower crustal thickness relative to that of the original, pre-rift crust (Meissner et al., 1986, 1987; Klemperer, 1988; Brun & Tron, 1993).

Beach's simple shear model is realised in that of Figure 6.24. Crustal thickness and domain widths are determined directly from the reflection profiles and data of e.g. Beach (1986); Meissner et al. (1986); Klemperer (1988). In order to thin originally $30km$ crust to $20km$ (basement thickness) via a shallow dipping (<

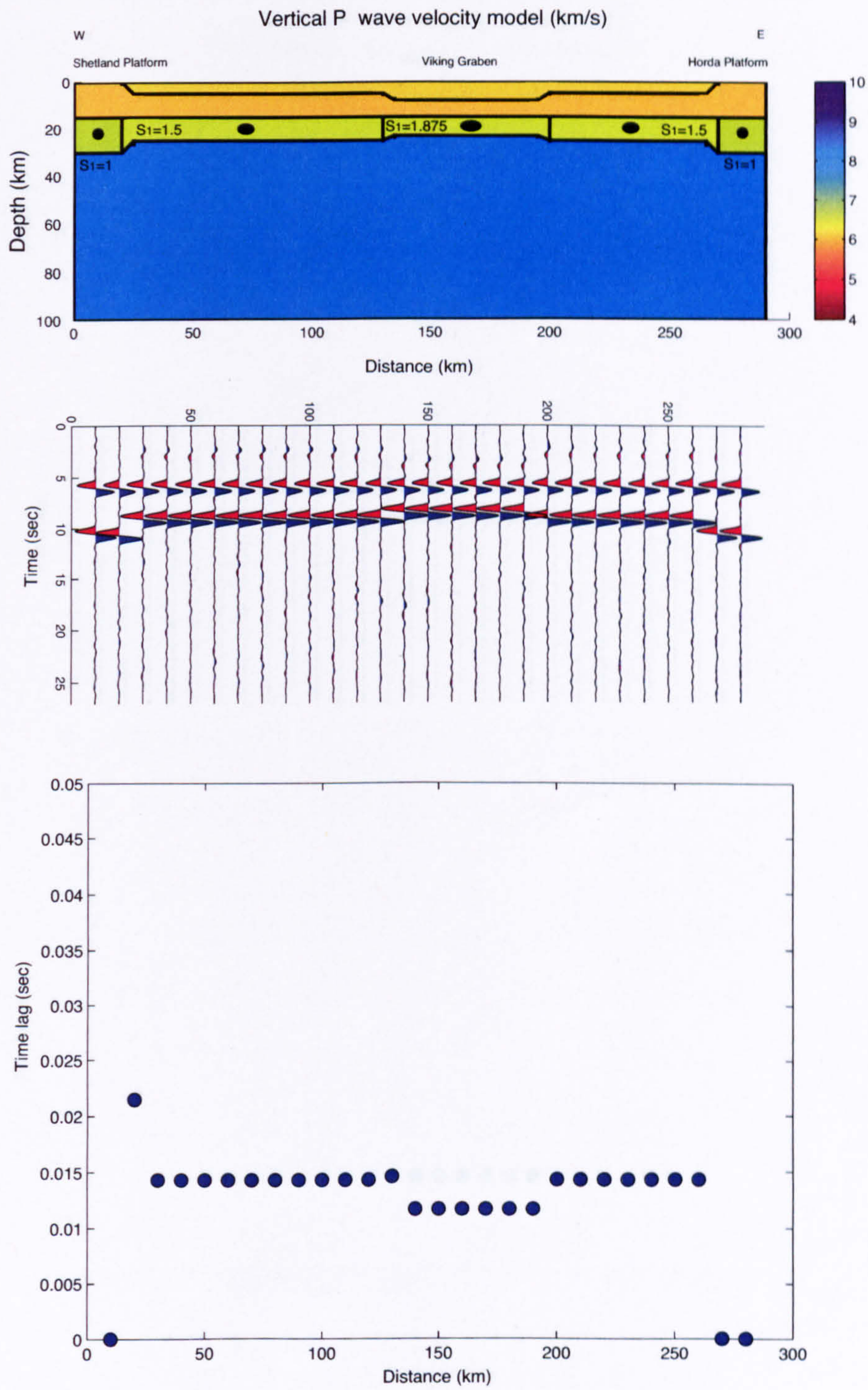

Figure 6.22: (Top) Crustal P-wave velocity model of the northern North Sea basin, based on the non-uniform, ductile pure shear stretching model of Klemperer (1988). (Middle) Associated zero-offset seismic reflection profile. (Bottom) Time lag (δt_s) between split shear-waves propagating vertically through the model.

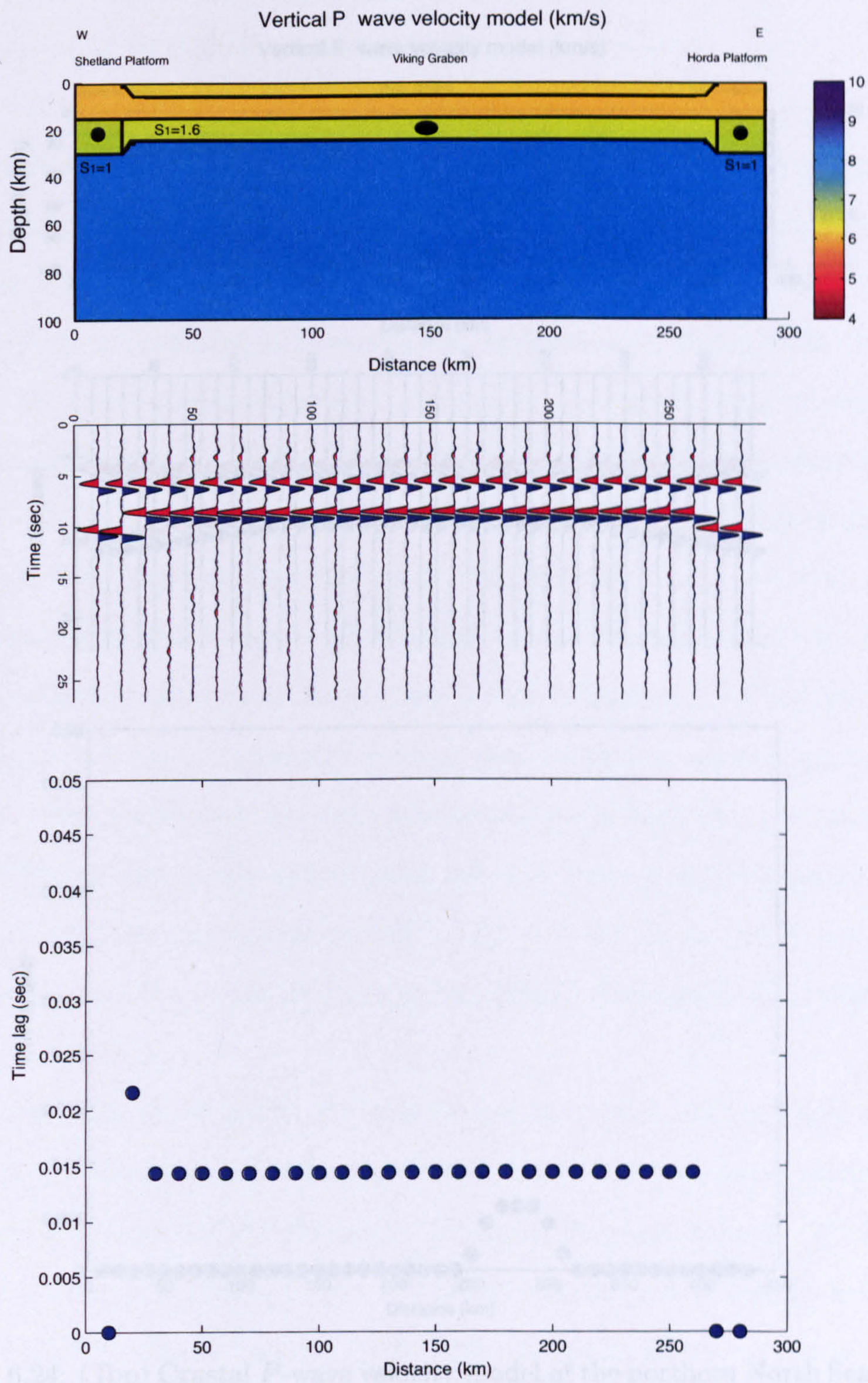

Figure 6.23: (Top) Crustal P-wave velocity model of the northern North Sea basin, based on the uniform, ductile pure shear stretching model of Pinet (1989); Brun & Tron (1993). (Middle) Associated zero-offset seismic reflection profile. (Bottom) Time lag (δt_s) between split shear-waves propagating vertically through the model.

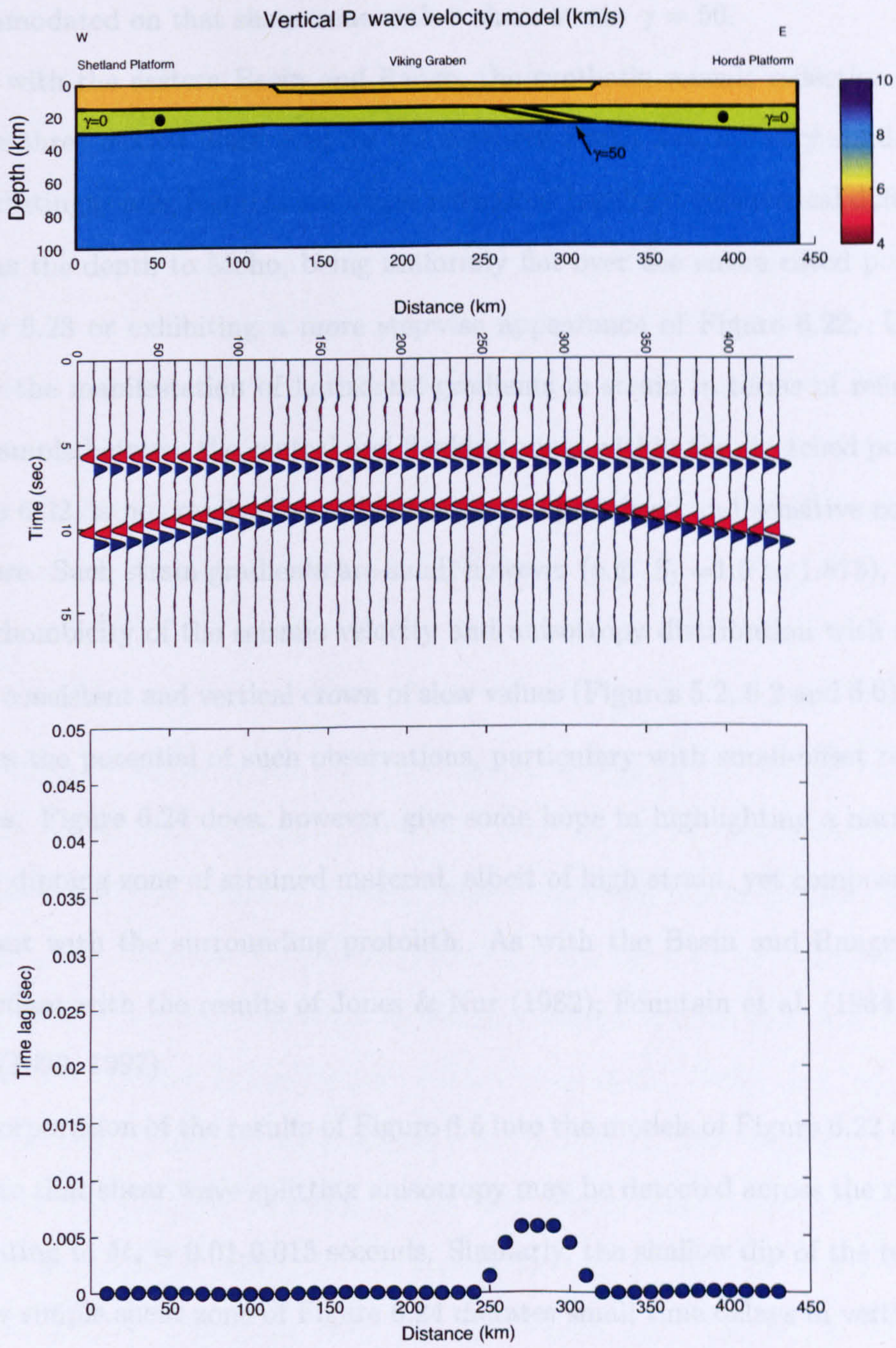

Figure 6.24: (Top) Crustal P-wave velocity model of the northern North Sea basin, based on the crustal penetrating simple shear zone model of Beach (1986). (Middle) Associated zero-offset seismic reflection profile. Notice the weak dipping reflector between $250km$-$300km$ and 6-8 seconds two-way time. (Bottom) Time lag (δt_s) between split shear-waves propagating vertically through the model.

10°), $2km$ wide crustal-penetrating shear zone, $100km$ of displacement must be accommodated on that shear zone with a shear strain $\gamma = 50$.

As with the eastern Basin and Range, the synthetic seismic reflection profiles for the three models illustrated for the northern North Sea, are very similar. The main distinguishing features are where reflections highlight geometrical differences, such as the depth to Moho, being uniformly flat over the entire rifted portion in Figure 6.23 or exhibiting a more stepwise appearance of Figure 6.22. Unfortunately the manifestation of horizontal gradients in strain in terms of reflectivity, for example between the central and flanking zones within the stretched portion of Figure 6.22, is not resolvable, at least without specialised and sensitive computer software. Such strain gradients are small however (e.g. S_1 =1.5 to 1.875), and the orthorhombicity of the seismic velocity and anisotropy distribution with its relatively consistent and vertical crown of slow values (Figures 5.2, 6.2 and 6.6) greatly hinders the potential of such observations, particulary with small-offset reflection profiles. Figure 6.24 does, however, give some hope in highlighting a narrow and gently dipping zone of strained material, albeit of high strain, yet compositionally constant with the surrounding protolith. As with the Basin and Range, this is concordant with the results of Jones & Nur (1982); Fountain et al. (1984) and Ji et al. (1993, 1997).

Incorporation of the results of Figure 6.6 into the models of Figure 6.22 and 6.23 indicate that shear wave splitting anisotropy may be detected across the rift zone, amounting to δt_s = 0.01-0.015 seconds. Similarly, the shallow dip of the relatively narrow simple shear zone of Figure 6.24 dictates small time delays in vertical rays around <0.006 seconds (Figure 6.7). As with the eastern Basin and Range models, such small values of δt_s may be difficult to resolve in nature, especially where masked by mantle anisotropy in teleseismic signals. Again, shallow, local events may be necessary to detect shear-wave splitting (Keir et al., 2005). The fast shear-wave polarisation orientation would not be manifest at surface seismic stations in

any of the three models, due to their sub-horizontal petrofabrics (Figures 6.11-6.12).

The dispute between pure and simple shear models is generally considered to be resolved for the North Sea in favour of the pure shear model and on the basis of axially symmetric and vertically stacked zones of basement thinning, and syn- and post-rift subsidence (reviews in White, 1990; Klemperer & White, 1989). Nevertheless, this procedure provides a neat and useful test. For example, the lack of a continuous reflector representing a through-going ductile shear zone (Klemperer, 1988) as predicted by Figure 6.24, lends support to a pure shear model. However, noise from natural lower crustal heterogeneities may, unfortunately, mask this low-amplitude signal in real data.

6.3.4 Tibet

The Tibetan Plateau is one the most expansive regions of elevated continental crust on Earth, covering some $7 \times 10^5 km^2$ and with an average elevation of $5km$ (Dewey et al., 1988; Clark & Royden, 2000). Although topographically high, the Plateau surface is notably low-relief (Fielding et al., 1994; Clark & Royden, 2000). A product of the collision between the Indian continental crust and that of Eurasia since $45Ma$ (Molnar & Tapponnier, 1975; Dewey et al., 1988), and indeed their continued convergence (Wang et al., 2001; Jouanne et al., 2004; Zhang et al., 2004), the apparently paradoxical geological and geophysical observations of the Tibetan Plateau have made it subject to the application of a plethora of crustal structure models (Powell & Conaghan, 1975; Zhao & Morgan, 1987; England & Houseman, 1986).

Constrained by seismic studies, the unusually thick crust beneath the Tibetan Plateau, around $70km$, is well documented (Dewey et al., 1988; Zhao et al., 2001; Meissner et al., 2004). Assuming an original crustal thickness of $35km$, typical of the shield areas globally (Mooney et al., 1998), this suggests a doubling of the

crustal thickness. This would intuitively lead to the inference that the region has undergone horizontal shortening by a factor of two. Palaeomagnetic data does indicate significant shortening across the Plateau, with quotes typically close to 2000km (Molnar & Chen, 1978; Achache et al., 1984). The paradox arises however, in the observation of relatively little surface strain across Tibet. Restoration of folds and thrusts across the Tibetan Plateau give integrated shortening on the order of a few hundred kilometres — a value significantly less than that expected from palaeomagnetic estimates of convergence (Tapponnier et al., 1981; Coward et al., 1988).

Three major models have been important in the development of our understanding of Tibet (Figure 6.25). (1) Underplating of the Tibetan crust by flat northward subduction of buoyant Indian lithosphere, progressively doubling the crustal thickness behind its leading edge (Figure 6.25(b)). This model was first proposed by Argand (1924) and later advocated by Powell & Conaghan (1973, 1975). (2) A model of diffuse crustal thickening, or vertical stretching pure shear, was speculated by Dewey & Burke (1973) and significantly developed in the numerical models of England & Houseman (1985); Houseman & England (1986); England & Houseman (1986); England & Searle (1986) (Figure 6.25(c)). Such models approximate the Tibetan crust to behave as a thin viscous sheet deforming under the influence of a northward moving, non-subducting rigid indentor (the Indian crust) and have been extremely successful in recreating the observed bulk geometries of the Tibetan Plateau and its spatial distribution of deformation. (3) Zhao & Morgan (1985, 1987) and Zhao & Yuen (1987), and more recently supported by Westaway (1995) and Kola-Ojo & Meissner (2001), developed a model that appears somewhat of an intermediate between the prior two end-member configurations. Their model, dubbed the 'hydraulic pump', describes underplating Indian crust injecting into weak Tibetan lower crust, and advancing northward to a point at which it becomes assimilated into the Tibetan lower crust (Figure 6.25(d)). The action of

the injecting 'ram' of Indian crust in conjunction with its assimilation (and hence volumetrically increasing ductile Tibetan lower crust) acts to raise the 'hydraulic' pressure within the lower crustal layer, generating uniform and contemporaneous uplift over the Plateau.

Models (1) and (2) are inconsistent with a number of observations however. For example, whole crustal pure shear thickening of (2) would require 2000km of shortening to be accommodated in upper crustal structures, while a northward migrating 'double-thickness front' and 1000km of post-collisional northward migration of India relative to southern Tibet (with no convergence within Tibet) are inherent to model (1). Rather, upper crustal structures tend to fall short in accounting for the total convergence within Tibet since collision (Coward et al., 1988). In addition, uplift tends to be spatially and temporally uniform (Harrison et al., 1992; Lal et al., 2003), and the post-collisional northward movement of India relative to southern Tibet is small, on the order of a few hundred kilometres (Molnar & Tapponnier, 1975; Besse et al., 1984; Dewey et al., 1988; Johnson, 2002) with approximately 2000km of convergence taken up within the Eurasian plate, north of the suture (Molnar & Tapponnier, 1975; Achache et al., 1984; Dewey et al., 1988). Thus, none of the requisites for models (1) and (2) are observed, and hence invalidating those models, at least in their simplest forms.

Dewey et al. (1988), however, claim to be able to account for the shortening across Tibet in their observations and restoration of near-surface structures. In view of this, and the fact that a thin viscous sheet model is still widely used as an approximation for Tibetan crust in numerical simulations of Tibetan deformation (Royden et al., 1997; Shen et al., 2001), a pervasive, vertical stretch pure shear model, in addition to the hydraulic pump of Zhao & Morgan (1987) will be modelled and investigated here.

Figures 6.26 and 6.27 show crustal models and their associated zero-offset synthetic seismic reflection profiles for uniform pure shear thickening (e.g. Dewey &

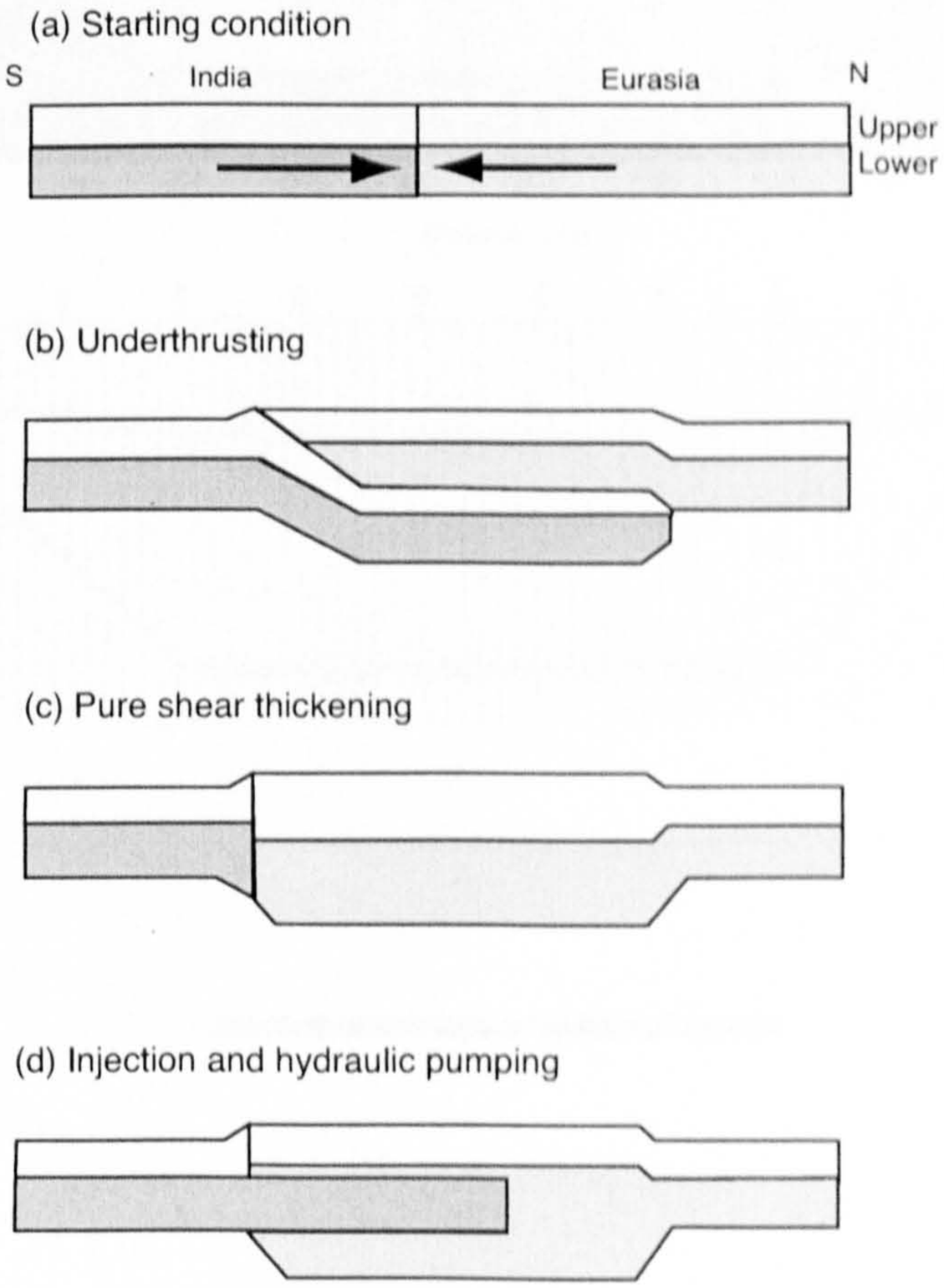

Figure 6.25: Schematic representation of the starting condition (a) and three models of continental deformation for the Tibetan Plateau region (b)-(d). (b) The model of e.g. Powell & Conaghan (1973, 1975) with wholesale underthrust of Indian crust beneath Eurasia, progressively doubling crustal thickness with northward subduction. (c) Pure shear thickening of the Tibetan crust under the force of an Indian indentor (e.g. Dewey & Burke, 1973; England & Houseman, 1985, 1986; Houseman & England, 1986). (d) The 'hydraulic pump' model of Zhao & Morgan (1985, 1987) whereby Indian lower crust injects into, and thickens Tibetan lower crust. Modified from Haines et al. (2003).

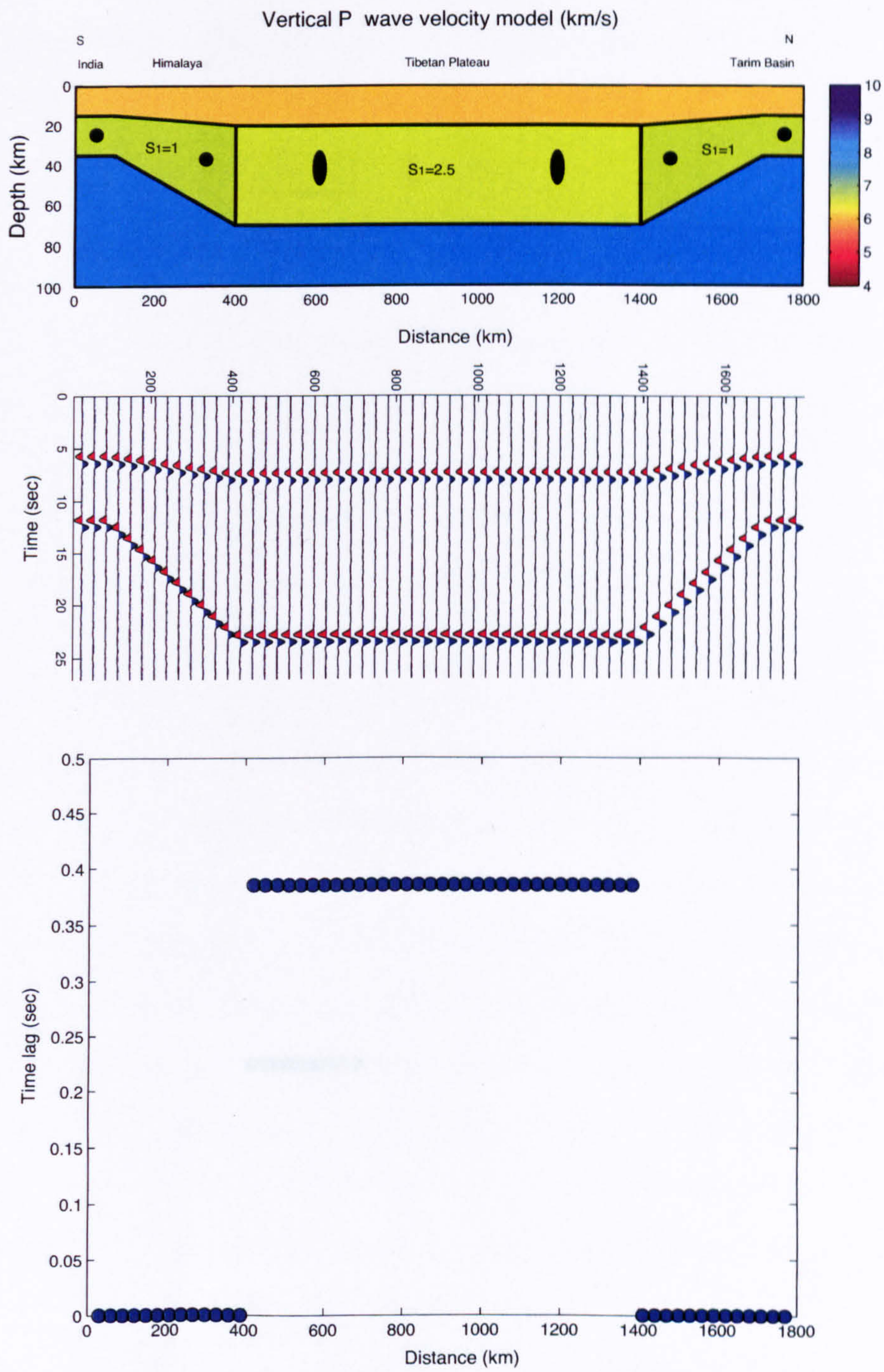

Figure 6.26: (Top) Crustal P-wave velocity model of the Tibetan Plateau, based on the uniform pure shear vertical stretching model of e.g. Dewey & Burke (1973); England & Houseman (1985, 1986). (Middle) Associated zero-offset seismic reflection profile. (Bottom) Time lag (δt_s) between split shear-waves propagating vertically through the model.

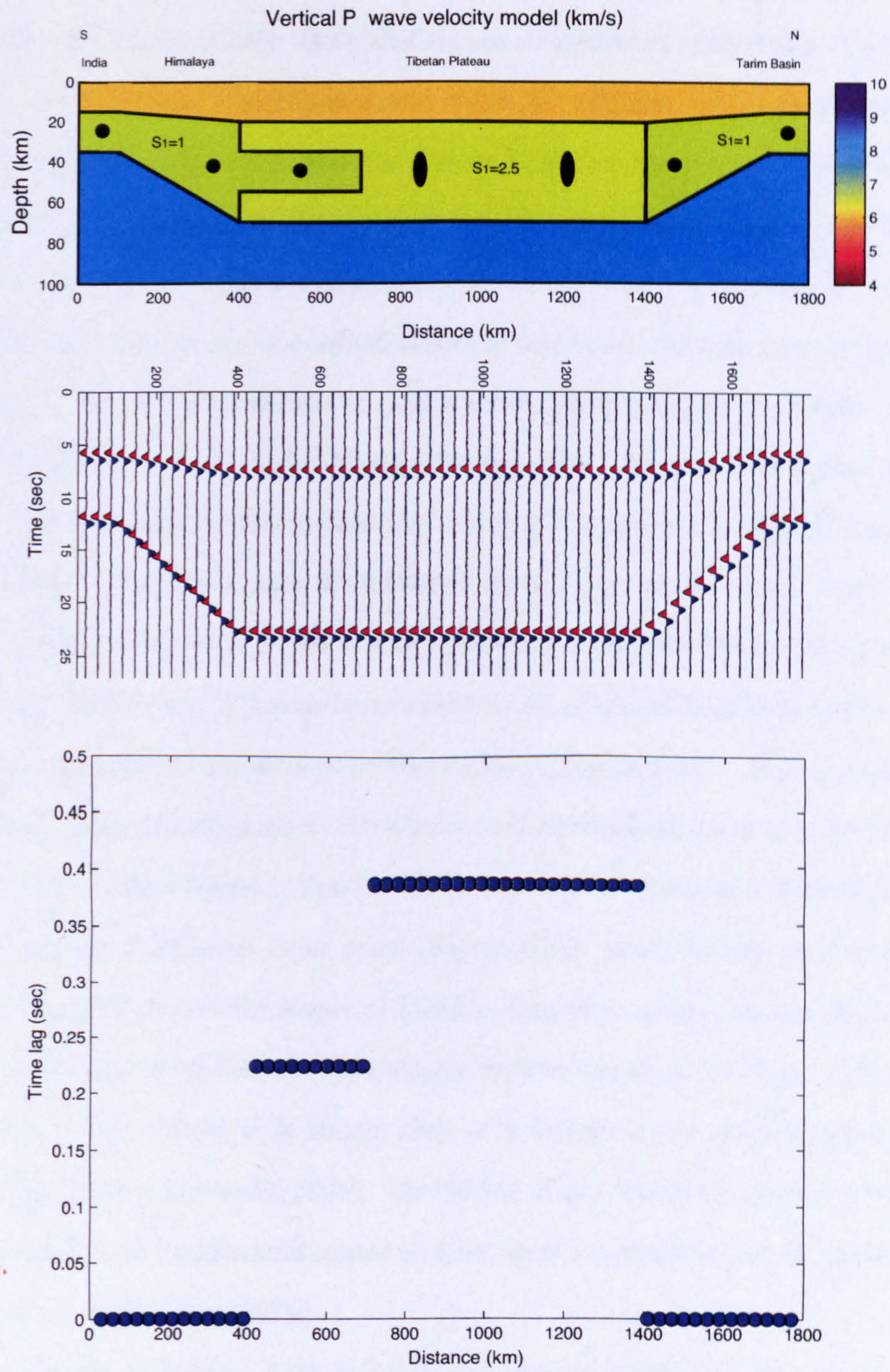

Figure 6.27: (Top) Crustal P-wave velocity model of the Tibetan Plateau, based on the 'hydraulic pump' model of e.g. Zhao & Morgan (1987). (Middle) Associated zero-offset seismic reflection profile. Notice the weak reflectors near 12 and 18 seconds two-way time and between $400km$ and $700km$. (Bottom) Time lag (δt_s) between split shear-waves propagating vertically through the model.

Burke, 1973; England & Houseman, 1986) and hydraulic pumping (e.g. Zhao & Morgan, 1987) respectively. Both models are consistent in their crustal thicknesses, that is $70km$ beneath the Plateau, and $35km$ for original, undeformed crust of the Indian craton to the south and the Tarim Basin to the north. The base of the upper crust is marked at $15km$ depth for the undeformed crust, and $20km$ for the Plateau region. This is consistent with observations of the base of seismicity and from interpretations of controlled source and local, shallow event seismic data (Molnar & Chen, 1983; Seeber & Armbruster, 1984; Kind et al., 1996; Nelson et al., 1996; Chen & Yang, 2004; Klemperer, in press). Tibetan upper crust is thickened relative to that of the undeformed crust in the models in view of some upper crustal shortening structures documented there (Tapponnier et al., 1981; Coward et al., 1988; Dewey et al., 1988). The injector or ram of Indian crust is envisaged to extend $300km$ into Tibetan lower crust north of the India-Tibet suture (Indus-Tsangpo suture) at the $400km$ profile marker (Figure 6.27). This is based on a variety of mutually supportive teleseismic and controlled source seismic data (e.g. Zhao et al., 1993; Owens & Zandt, 1997). A reduced thickness of Indian crust is shown intruding Tibetan lower crust (Figure 6.27) based on estimates that a few tens of percent of the thickness of Indian crust is removed during underthrusting and incorporated into the Himalayan system (Zhao & Morgan, 1987; Owens & Zandt, 1997). Here, it is shown that only Indian lower crust survives underthrusting (Owens & Zandt, 1997). The width of the transition between thickened crust and that of undeformed craton is fixed as the average width of the Himalaya (Molnar & Tapponnier, 1975).

The models of Figures 6.26 and 6.27 are broadly similar in their lower crustal strain distribution. They vary only in the presence of an injector of Indian crust. The central domain of lower crust, thickened by vertical stretch pure shear is represented by the material and seismic properties calibrated to a strain where $S_1 = 2.5$, or a vertical stretch in the lower crust to 2.5 times its original thickness

($50km/20km$). The petrofabric there is modelled such that the planar fabric, XY, is vertical, with the lineation, X, vertical and Y in-and-out of the plane of viewing. This geometry is consistent with rotation of the planar petrofabric about Y as in Figure 6.15(c).

Contrary to many examples in the literature that show lower crustal flow in collisional settings generating horizontal lamination due to shear stresses in channel flow (Clark & Royden, 2000; Shen et al., 2001; Klemperer, in press), convergence is here intuitively modelled to result in vertical planar petrofabrics normal to the direction of maximum compression (σ_1 horizontal, north-south) with a vertical lineation (parallel to the direction on maximum extension, σ_3) (Royden et al., 1997; Cagnard et al., 2006).

Although there is increasing evidence of east-west extensional collapse of the orogen accommodated by lower crustal flow into the flanking regions east of the Plateau (e.g. Clark & Royden, 2000; Wang et al., 2001; Meissner et al., 2004, 2006; Klemperer, in press) it is as yet difficult to quantify the finite amount of this spreading in terms of resetting the original vertical stretching petrofabric from purely north-south compression, not to mention it being beyond the scope of this exercise. Moreover, strain calculations and petrofabric geometries are here considered for plane strain. Hence, vertical thinning or thickening cannot be accommodated for a vertical planar fabric where the lineation is horizontal (as in Figure 6.15(c)). Thus, only the strain and petrofabric associated with north-south compression is considered (vertical planar fabric, vertical lineation), and is assumed to be directly related to the change in crustal thickness. This may be representative of longitudinal transects that are central to the the plateau, say 85°E, where the effects of eastward extrusion of material are expected to be minimised (Wang et al., 2001).

As with models incorporating pervasive and uniform pure shear in the lower crust for the Basin and Range Province and the northern North Sea, the effect of domains of strained lower crust on reflection coefficients across an interface are

unresolvable, at least by eye. This fractional effect of relatively small contrasts in the magnitude of material finite strain across an interface is exhibited in Figure 6.27 by the tenuous reflectors near 12 and 18 seconds two-way time and between the $400km$ and $700km$ markers across the profile, demarcating the upper and lower boundaries, respectively, of the injecting Indian crust.

The vertical petrofabric inherent to these models may make the shear-wave splitting time delay, δt_s, and V_{s1} polarisation orientation more useful indicators of lower crustal strain. As shown in Figure 6.8, the effect of a vertical foliation with a vertical lineation can give shear-wave time delays that are an order of magnitude greater than those for settings with horizontally foliated petrofabrics (e.g. Basin and Range Province). For $S_1 = 2.5$ beneath the Plateau, Figures 6.8 and 6.26-6.27 indicate $\delta t_s = 0.4$ seconds for a $50km$ thick lower crust compared to $\delta t_s = 0.24$-0.4 seconds for rays that have travelled vertically through that part of the Plateau into which the Indian crust has penetrated. This would be associated with an east-west fast shear-wave polarisation orientation (Figure 6.12).

Shear-wave splitting anisotropies have been observed on a small number of teleseismic arrays across Tibet. Hirn et al. (1995) document up to 1 second shear-wave splitting in SKS phases across $400km$ of southernmost Tibet, with the fast phase polarised roughly east-west. They attribute this splitting to partial melt pockets in the crust and upper mantle, and to eastward flow of mantle material. In a reappraisal of this data however, Sapin & Hirn (1997) stress that although the shear-wave splitting anisotropy is characteristic of east-flowing mantle, the exact radial level in the Earth at which the splitting is generated is not known. Moreover, they cite a lack of decisive evidence of the magnitude of shear-wave splitting anisotropy due to crustal deformation as a reason for their preference to attribute the observed shear-wave time delays to oriented mantle olivine. It is shown here however, that up to half of their observed 1 second δt_s can be accounted for solely by pervasive crustal deformation, or up to one third where injecting, isotropic

Indian crust is present in the Tibetan lower crust.

This is supported by Huang et al. (2000) who report between 1 and 2 seconds shear-wave splitting anisotropy with east-west polarisation in stations of a teleseismic array covering southern and central Tibet. They also note that zero splitting is recorded at seismometer stations south of the Banggong-Nujiang Suture in Tibet — approximately the northern limit to which Indian crust penetrates Tibetan lower crust, and close to the $700km$ horizontal marker of Figure 6.27. Indeed, they attribute the lack of observed anisotropy there to the presence of seismically isotropic injecting Indian crust, although their observations are limited to splitting delays of $\delta t_s \geq 0.8$ seconds, and hence don't necessarily invalidate the results of Hirn et al. (1995) and Sapin & Hirn (1997). Using a novel technique based on the analysis of overlapping Fresnel zones for observations at adjacent seismometer stations within the array, Huang et al. (2000) estimate the depth of the anisotropic layer beneath south-central Tibet, where over 2 seconds δt_s is observed, to less than $80km$. This suggests that the bulk of the observed splitting there occurs within the crust, although they maintain that due to the inaccuracy in their limited splitting measurements, a mantle component of up to 1 second cannot be excluded. Nevertheless, up to 1 second of shear-wave splitting time delay can be assigned to crustal anisotropy, for which Huang et al. (2000) propose a model of a thick lower crust exhibiting a vertical and east-west trending foliation north of the penetration front of Indian crust. The remaining time delay is explained by east-west oriented mantle LPO. Their model remains qualitative however, and the suggested crustal fabric responsible for the reported splitting data is not strain-calibrated.

A more quantitative understanding of how the mantle anisotropy develops as a function of strain, and how it can be can be calibrated against that finite strain, may allow the mantle and crustal contributions of such observed shear-wave splitting time delays to be deconvoluted.

6.4 Conclusions

The main product of Chapter 5 was a quantitative description of the petrophysical and seismic properties of the sample suite from Upper Badcall. These properties were inherently correlated to sample finite strain and petrofabric elements (e.g. lineation, foliation). In addition, it highlighted the sensitivity of seismic properties to modal composition..

This chapter built upon the framework of discrete data of Chapter 5 by illustrating how, subsequent to normalisation to a constant composition, sample-wise data can be interpolated to illustrate the continuum relationship between seismic attributes, finite strain and petrofabric orientation. A series of such relationships were illustrated graphically for P-wave velocity, V_p, shear-wave splitting time delay, δt_s, and the fast shear wave (V_{s1}) polarisation orientation. For horizontal petrofabric elements, V_p shows a trend of decreasing velocity with increasing strain, whereas for vertical fabric elements, the overall trend is one of increasing velocity with finite strain (although an initial decrease in velocity is observed between isotropic protolith and very low strain material). A similar relationship is observed for δt_s, except for horizontal petrofabrics where little bulk variation in values is observed with respect to finite strain. The greatest change in the values of seismic properties with strain tends to occur where $0 \leq \gamma \leq 10$, beyond which values vary only fractionally with further increase in finite strain.

The latter part of the chapter provides a set of simplified case-study examples of how generic petrofabric- and strain-calibrated seismic data can be incorporated into structural models in regions of continental deformation. Preliminary models are promising in their ability to resolve, in seismic reflection profiles and shear-wave splitting analyses, strain contrasts in an iso-compositional mafic lower crust. Synthetic seismic reflection profiles show that high-strain crustal through-going shear zones can exhibit sufficient seismic anisotropy due to petrofabric development such that the reflection coefficient with respect to its isotropic protolith is

resolvable by vertical incidence reflection surveys (e.g. Figure 6.18). Strain variations superimposed on lithological contacts are, however, masked by the high reflectance associated with the compositional interface (e.g. Figure 6.19). Strain variations are impossible to resolve in such cases. These observations support those of Jones & Nur (1982); Fountain et al. (1984) and Ji et al. (1993, 1997). Shear-wave splitting analysis is successful in differentiating between the simplistic models tested here (e.g. Figure 6.18-6.19), whereby measured time lags are a function of the thickness of anisotropic crust in addition to the magnitude and orientation of the anisotropy. Detecting small shear-wave splitting time delays in more heterogeneous and complex natural examples may be more testing, however. These models indicate that supplementary analyses that can detect anisotropic properties parallel to the horizontal plane of the models, such as wide angle reflection/refraction surveys, would be necessary to fully resolve the structure and strain state (e.g. Rabbel & Lüschen, 1996; Rabbel & Mooney, 1996).

Such models are potentially useful in both forward and reverse modelling in regions of continental deformation. That is, in predicting the seismic expression of a region, where its crustal structure and deformation is well characterised, and in the interpretation of seismic data with respect to lower crustal strain and structure in comparatively less well studied areas. It also presents a useful resource for testing and subsequent feedback into geodynamic models of continental deformation.

Chapter 7

Conclusions

The principal aim of this study was to develop and prove an efficient and reproducible work-flow model for the calibration of seismic attributes of a representative lower crustal lithology in terms of finite strain.

Major steps in the work-flow, and specific objectives included:

1. Identify and sample a strain gradient in a representative high-grade mafic lithology.

2. Characterise the collected sample suite in terms of its finite strain and petrofabric.

3. Illustrate the dependence of seismic velocity and anisotropy with strain intensity and petrofabric orientation.

4. Show examples of how such strain-calibrated seismic properties can be included into geodynamic models.

This chapter summarises the principal results and conclusions of this study, and indicates areas for the continuation and diversification of the study.

7.1 Approximations in studying the lower continental crust

Chapter 1 set the scene for this study and summarised the bulk rheological and compositional models of the lower crust. Numerous observations from wide-angle seismic profiles, deep-sources xenoliths and exposed high-grade sections point to a compositionally and rheologically heterogeneous lower crust, on both a local and global scale (Fountain & Salisbury, 1981; Blundell, 1990; Holbrook et al., 1992; Percival et al., 1992; Rudnick, 1992; Weiss et al., 1999; Rutter et al., 2003; Waters et al., 2003). It was shown, however, that over geological time-scales, the physical properties of the lower crust can be approximated as a uniform ductile zone of mafic composition, between relatively more competent upper crust above and upper mantle beneath (Holbrook et al., 1992; Rudnick & Fountain, 1995; Burov & Watts, 2006). A simplified model was proposed therefore, for application throughout the rest of this study whereby the lower crust is defined as that region below the brittle-ductile transition and above the Moho, characterised by ductile processes and represented by a macroscopically homogeneous mafic composition. In studies of the lower crust, and where a homogeneous composition is assumed, extrinsic rock properties such as cracks, fractures and compositional layering can largely be ignored in contributing to the bulk physical, and hence seismic properties of the material. Thus, under these circumstances seismic properties are here studied as being a function of intrinsic properties alone, namely the properties of constituent mineral phases and their orientation distribution (e.g. Mainprice & Nicolas, 1989).

7.2 Strain gradient in a mafic lower crustal analogue

The Lewisian gneiss complex was introduced in Chapter 2 as a currently exposed high-grade terrane. Although the Lewisian terrane in itself is compositionally heterogeneous and shows evidence of a protracted period of complex polyphase deformation, one unit in particular is useful in providing a representative analogue

material for this study. Being intruded prior to the final major tectonothermal event interpreted in the Lewisian complex, the Scourie dyke suite is present as both an undeformed igneous protolith of doleritic composition, equilibrated to amphibolite facies conditions, and also in strain gradients where dykes are cross-cut by discrete, ductile, amphibolite-facies shear zones of Laxfordian age.

The deformation zone at Upper Badcall was shown to provide an accessible and useful example of where a Scourie dyke is deformed by a Laxfordian shear zone, and permitted the collection of a suite of nine rock samples across a strain gradient from undeformed protolith ($\gamma = 0$) to highly strained material ($\gamma \leq 57$). Detailed structural mapping was shown to be an important resource in establishing a structural reference frame, in characterising a deformation history, and in providing a means of calculating a quantitative strain profile of the deformation zone and sample suite. Analysis of field data showed that the deformation zone at Upper Badcall is complex, and is best described as an overall simple shear zone, with a transversely varying shear direction. Nevertheless, calculation of a strain profile for the deformation zone shows a relatively simple, positive strain gradient from undeformed wall-rock to a high strain shear zone core.

7.3 Characterising petrofabric

In order to provide a means of calculating the seismic properties of the sample suite, and to provide a reference frame relating their seismic properties and finite strain, it is necessary to characterise the petrofabric and petrophysical properties of the rock aggregates. In Chapter 4, optical microscopy and electron microprobe analysis (EMPA) showed that the rock sample suite from Upper Badcall could be broadly regarded as an aggregate of hornblende, plagioclase and quartz ($\pm$ clinopyroxene in the protolith material). Furthermore it illustrated the development of a strong tectonic fabric with increasing strain through the sample suite, with associated grain refinement.

Chapter 4 continued by highlighting electron backscatter diffraction (EBSD) techniques as providing an efficient and accurate means of characterising the lattice preferred orientation (LPO) distribution in the constituent mineral phases of a rock aggregate. In the dominantly hornblende-plagioclase-quartz aggregate of the sample suite for Upper Badcall, it was shown that a strong LPO fabric developed with increasing strain in the hornblende phase, whilst the plagioclase and quartz phases showed a consistently random LPO distribution across the strain gradient. The symmetry of the LPO distribution in the hornblende phase is congruent with the kinematic axes, and suggests deformation accommodated by crystal-plasticity with a [100](001) slip system. The random fabrics of plagioclase and quartz cannot be correlated with the kinematic axes of the deformation. Analysis of refined clots of originally single plagioclase crystals from samples across the strain gradient exhibit a randomising of the LPO fabric with increasing strain, from an original single crystal configuration. This suggests deformation by a granular flow mechanism which acted to diffuse the original LPO of the protolith. The rock material of the sample suite from Upper Badcall was considered therefore as a three-phase aggregate consisting of an interconnected weak phase of hornblende, with more competent inclusions of plagioclase with quartz. Deformation was partitioned into the relatively weak hornblende network, which deformed by homogeneous internal crystal-plasticity to develop a strong LPO with increasing strain. Felsic phases formed relatively more competent inclusions that deformed by granular flow. The shape fabric of these felsic aggregates was shown to provide an underestimate of the finite strain ellipse compared to that inferred from macroscopic field data.

As quantified by the texture index, J, LPO development in the hornblende phase becomes saturated by a finite shear strain of approximately $\gamma = 10$. This trend is reflected in a similar texture index for individual crystallographic poles or directions, pfJ, where the intensity of clustering of individual hornblende crystallographic axes and poles becomes saturated by $\gamma = 10$.

7.4 Calibration of seismic attributes with strain

Chapter 5 outlined a procedure by which quantified LPO data from EBSD analysis of rock aggregates (Chapters 3 and 4) can be combined with the single crystal physical properties of their constituent mineral phases to give an estimate of the bulk physical properties of the rock aggregate, quantified in terms of the elastic stiffness tensor. The averaging technique highlighted herein as being suitable for aggregates whose properties are largely controlled by intrinsic material properties, is the Voigt-Reuss-Hill scheme. This relatively simple calculation forms the bridge in relating quantified petrofabric information, such as LPO, to their petrophysical properties, namely aggregate elasticity, of which seismic properties are a direct function. Hence, via the Christoffel equation, seismic velocities and anisotropies were calculated from the petrophysical properties of each component of the sample suite. Given that petrofrabric and petrophysical properties of each rock sample are a function of finite strain, seismic attributes calculated from those parameters can also be calibrated to finite strain. Moreover, given that petrofabric properties are quantified in a known kinematic reference frame based upon the linear and planar fabrics of the original rock samples, the directional dependence of seismic attributes can be correlated also to the geometry of petrofabrics or kinematics.

P- and *S*-wave seismic velocity maxima and minima showed little variation with strain, although their anisotropies exhibited a strong positive relationship, approximated by a logarithmic function. That is, the gradient in change of AV_p and AV_s with strain is most rapid up to a finite strain of $\gamma = 10$, with values attaining 8% and 6% respectively, beyond which the change in anisotropy with continued increase in strain reduced. This saturation of anisotropy by $\gamma \leq 10$ is compatible with the relationship of the texture index of hornblende petrofabric with strain. Indeed, the orthorhombic symmetry of the distribution of seismic properties is congruent with those of single crystal hornblende, although the absolute values are somewhat reduced due to 'dilution' from randomly oriented plagioclase and

quartz fractions.

7.5 Seismic and structural modelling

Chapter 6 presented the final stage of the work-flow model by in terms of the manipulation and application of results.

Interpolation of petrophysical, petrofabric and seismic properties between the discrete, sample-wise data of the sample suite (Chapter 5) permited the relationship between seismic properties, finite strain and petrofabric orientation to be considered in a continuum. Velocity and anisotropy modelling of a vertically propagating seismic ray through a $10km$ block of material, approximating a teleseismic signal, show strong relationships with both finite strain and the orientation of petrofabric or kinematic elements. For a horizontally oriented lineation, X, and foliation, XY, increasing strain was correlated with a reduction in vertical P-wave velocity from $6.6kms^{-1}$ in undeformed material to $6.0kms^{-1}$ where $\gamma > 15$. The gradient of change levels around $\gamma = 10$. At steeper petrofabirc orientations, that is, vertical foliation, XY, a trend of increasing V_p with strain was observed. P-wave velocities of 6.35-6.40kms^{-1} at low strains ($\gamma < 5$) increased to velocities of 6.50-6.60kms^{-1} with increasing strain and fabric intensity. This trend occurred irrespective of whether the tectonic lineation, X, is vertical or horizontally oriented in that foliation. Shear-wave splitting anisotropy, parameterised in terms of the time delay between fast and slow split shear-waves, δt_s, showed little change with strain for horizontal petrofabric elements, with values remaining low around $\delta t_s < 0.02$ seconds. Where petrofabric elements assumed a vertical orientation, shear-wave splitting of a vertical ray showed a clear trend of increasing values with finite strain. Low to zero shear-wave splitting at low strain ($\gamma < 1$) increased to $\delta t_s > 0.18$ seconds where $\gamma > 10$.

The latter part of Chapter 6 presented the application of strain-calibrated seismic properties by incorporation into a series of crustal models. Three case studies

were presented, representing regions of contemporary or recent continental deformation: the eastern Basin and Range Province, northern North Sea Basin, and the Tibetan Plateau. These models were promising in their ability to differentiate between regions of lower crust characterised by a uniform mafic composition, but different finite strain state and/or petrofabric geometry, using a combination of seismic velocity and anisotropy attributes.

7.6 Work-flow model

The major steps in the work-flow model described and tested by this thesis are outlined in Figure 7.1.

A reproducible work-flow model has therefore been developed and proven as an efficient means of calibrating the petrofabric-derived seismic properties of a representative lower crustal lithology in terms of finite strain.

This project has thus satisfied the aims outlined in Chapter 1 and above.

7.7 The contribution of this research to science

Previous research into the seismic properties of the lower crust has been somewhat dominated by analyses of discrete, representative samples of the range of lithologies observed in exposed lower crustal terranes and sections, or in exhumed xenoliths (e.g. Rudnick, 1992; Weiss et al., 1999; Rutter et al., 2003). Less of an emphasis has been on the relationship between the seismic properties of representative lower crustal lithologies with strain. A study into the seismic properties of a single, typical lower crustal lithology calibrated against a strain gradient typical of a high-grade deformation zone has thus been presented. In describing and testing a productive, efficient and reproducible work-flow model for the calculation of seismic attributes from petrofabric data, and their calibration against finite strain state in the representative lower crustal material from which they are derived, this thesis

Work-flow model:
Strain-calibrated seismic properties in lower crustal material

Major Steps	Main objectives	Additional investigations
(1) Establish assumptions and simplifications. [Chapter 1]	Depending upon the nature and detail of the study, a series of physical assumption may need to be set. These should be presented at the onset.	Physical assumptions may include: (a) Homogeneous or heterogenous lower crustal composition. (b) The nature of that composition. (c) Homogeneous/uniform or spatially heterogenous lower crustal structure. (d) Material properties upon which seismic properties are considered dependant e.g. LPO, cracks/fractures, compositional layering.
(2) Identify, characterise and sample a strain gradient in a representative lower crustal lithology across a high-grade deformation zone. [Chapter 2]	(i) Identify a high-grade terrane. (ii) Identify a high-grade lithology representative of lower crustal material within that terrane. (iii) Identify a high-grade deforamtion zone across which the representative lithology is deformed in a strain gradient. (iv) Map and characterise that deformation zone in terms of its deformation style (simple/pure shear) and strain history. (v) Collect a sample suite across that strain gradient, with sufficient resolution as to characterise the major features or trends in the deformation zone. (vi) Calculate a finite strain profile across that deformation zone from, say, field data and test, where possible. (vii) Calibrate that sample suite against the strain profile.	
(3) Characterise the sample suite in terms of petrofabric. [Chapter 3 & 4]	*[At this stage, a finite strain-calibrated sample suite exists.]* Combining analytical techniques including optical microscopy, electron microprobe analysis (EMPA) and electron backscatter diffraction (EBSD): **Note:** Samples must be described and analysed in a kinematic reference frame, i.e. with respect to lineation *X* and foliation *XY*, which is directly related to the kinematics of the deformation zone from which they are collected. (i) Describe and characterise the sample suite in terms of its petrography, microstructure and petrofabric. (ii) Quantify the petrofabric development in the sample suite in terms of the bulk aggregate lattice preferred orientation (LPO). [Note that microstructural analysis may permit the detrmination of an additional finite strain profile for the deformation zone (mentioned in Step (1.vi)) from e.g. petrofabric or microstructural parameters. Again, this should be tested.]	(a) Consider strain partitioning in polyphase aggregates and its effect on bulk deformation and petrophysical properties. (b) Where strain partitioning in a polyphase aggregate is inferred, test the validity strain profiles deduced from microstructural observations.
(4) Calculation of seismic properties and calibration against strain [Chapter 5]	*[At this stage, a database of strain-calibrated petrofabric properties exists.]* (i) Calculate material/petrophysical properties for samples, from their quantified petrofabric data (Step (2)), in terms of their bulk aggregate elastic propeties (Cij). Sample-wise data remains inherently calibrated against finite strain (Step (2.vii)). (ii) Calculate sample-wise seismic properties from their petrophysical properties (using e.g. Christoffel's equation). Again, these seismic preoperties remain inherently calibrated against sample finite strain. *[At this point, a discrete, sample-wise set of seismic data exists that is directly corelated to sample finite strain and petrofabric orientation in the kinematic reference frame.]*	
(5) Modelling [Chapter 6]	(i) Petrofabric- and strain-calibrated seismic data (Step (4)) can be interpolated between sample control points to illustrate the continuum relationship between seismic properties, material finite strain, and petrofabric orientation. (ii) Such generic data can hence be incorporated into various geodynamic, structural and seismic models where a tight constraint on the relationship between seismic properties, finite strain and petrofabric may increase model resolution or provide tests for feedback in both forward and reverse modelling.	

Figure 7.1: Conclusive work-flow model for the calibration of seismic properties against finite strain and petrofabric orientation.

therefore provides an original and significant contribution to science.

7.8 Future work

This project has been multidisciplinary in its approach, combining previously disparate techniques. Furthermore, it is the first study of its type, and so continued and focussed research in individual techniques and in the integration of techniques according to the outlined work-flow model will provide an increasingly large and better constrained database of results.

The application of seismic properties that are calibrated against petrofabric and petrophysical properties is exciting and potentially vast. A number of specific areas have, however, been highlighted as potential for further study.

1. This project concentrated on a specific mafic lithology thought to be representative of the bulk composition of the lower continental crust, namely a quartz-dolerite equilibrated to amphibolite facies conditions. However, field studies of exposed lower crustal sections, and indeed high-grade xenoliths, often show very different compositions, from quartzo-feldspathic to ultramafic. Thus in order to fully characterise the strain-calibrated seismic properties of lower crust globally, this work-flow model should be repeated for strain gradients in the plethora of other lower crustal materials observed. With this, more complex seismo-structural models can be used that include both compositional and strain heterogeneities.

2. The steep strain gradient in the deformation zone at Upper Badcall meant that the sample suite was relatively under-represented with respect to high finite strains. The effect of this sampling became evident with the contouring of interpolated properties in Chapter 6. Repetitions of this work-flow with lithologies of similar modal composition (modal fractions can be normalised within certain bounds, Chapter 6) and over a broad range of finite strain

states will better characterise the relationship between seismic attributes and strain, presented herein.

3. Further experimental rock deformation research is necessary to support data. Specifically, *in situ* seismic experiments on natural high-grade rock samples at realistic strains and *P-T* conditions, and under a range of different deformation styles will provide rigorous tests to both petrofabric-derived seismic properties, and natural seismic data.

4. Most importantly, collaborative and multi-disciplinary research between structural geologists and seismologists is required to provide more natural seismic data to compare results against and to mutually refine both seismic and geological models. Furthermore, collaborative research is necessary to ensure that seismic attributes recorded and computed from field experiments are useful and pertinent to applications in structural geology.

Appendix A

Publications

See integral folder.

Tatham, D.J. & Casey, M. (2007), Inferences from shear zone geometry: An example from the Laxfordian shear zone at Upper Badcall, Lewisian Complex, NW Scotland, *in* A. Reis and R.W.H. Butler and R. Graham, eds, 'Deformation of the Continental Crust', Geological Society of London, Special Publication, 272, pp.47-57.

Tatham, D.J., Lloyd, G.E., Butler, R.W.H. & Casey, M. (2008), 'Amphibole and lower crustal seismic properties', *Earth and Planetary Science Letters* **267**, 118-128.

Appendix B

Detailed fair copy map, Upper Badcall

See integral folder.

Appendix C

Data

The attached CD contains the following supporting data:

1. Field data.
2. EMPA data.
3. LPO data (in *.ctf format).

Appendix D

Sample Numbers

The sample numbers used in this thesis relate to those of the Department of Earth Science, University of Leeds, sample catalogue as follows.

Sample	Leeds University Catalogue Number
1	62485
2	62483
3	62484
4	62482
5	62481
6	62480
7	62479
8	62486
9	62478

Bibliography

Achache, J., Courtillot, V. & Zhou, Y. (1984), 'Paleogeographic and tectonic evolution of southern Tibet since middle Cretaceous time: New paleomagnetic data and synthesis', *Journal of Geophysical Research* **89**, 10311–10339.

Afonso, J. & Ranalli, G. (2004), 'Crust and mantle strengths in continental lithosphere: is the jelly sandwich model obsolete?', *Tectonophysics* **394**, 221–232.

Aleksandrov, K. & Ryzhova, T. (1961*a*), 'The elastic properties of crystals', *Soviet Physics, Crystallography* **6**, 228–252.

Aleksandrov, K. & Ryzhova, T. (1961*b*), 'The elastic properties of rock-forming minerals: Pyroxenes and amphiboles', *Izvestiya Akademii Nauk SSSR, Seriya Geologicheskaya* **8**, 1339–1344.

Aleksandrov, K., Alchikov, U., Belikov, B., Zalavskii, B. & Krupnyi, A. (1974), 'Velocities of elastic waves in minerals at atmospheric pressure and increasing precision of elastic constants by means of EVM', *Izvestiya Akademii Nauk SSSR, Seriya Geologicheskaya* **10**, 15–24.

Allmendinger, R., Hauge, T., Hauser, E., Potter, C. & Oliver, J. (1987), Tectonic heredity and the layered lower crust in the Basin and Range Province, western United States, *in* M. Coward, J. Dewey & P. Hancock, eds, 'Continental Extensional Tectonics', Geological Society of London, Special Publication, 28, pp. 223–246.

Allmendinger, R., Sharp, J., Tish, D. V., Serpa, L., Brown, L., Kaufman, S. & Oliver, J. (1983), 'Cenozoic and Mesozoic structure of the eastern Basin and Range province, Utah, from COCORP seismic-reflection data', *Geology* **11**, 532–536.

Arbaret, L. & Burg, J. (2003), 'Complex flow in lowest crustal, anastamosing mylonites: Strain gradients in a Kohistan gabbro, northern Pakistan', *Journal of Geophysical Research* **108**, 2467–2485.

Argand, E. (1924), 'La tectonique de l'Asie', *Proceedings of the 13th International Geology Congress, Brussels* **7**, 170–372.

Attfield, P. (1987), The structural history of the Canisp Shear Zone, *in* R. Park & J. Tarney, eds, 'Evolution of the Lewisian and Comparable Precambrian High Grade Terrains', Geological Society of London, Special Publication, 27, pp. 165–173.

Azpiroz, M. D. & Lloyd, G. (in press), 'Development of lattice preferred orientation in clinoamphiboles deformed under low pressure metamorphic conditions. a SEM/EBSD study of metabasites from the Aracena metaorphic belt, S.W. Spain'.

Babuska, V. & Cara, M. (1991), *Seismic anisotropy in the Earth*, Kluwer Academic Publishers.

Backus, G. (1962), 'Long-wave elastic anisotropy producted by horizontal layering', *Journal of Geophysical Research* **67**, 4427–4440.

Badley, M., Price, J., Dahl, C. R. & Agdestein, T. (1988), 'The structural evolution of the northern Viking Graben and its bearing upon extensional modes of basin formation', *Journal of the Geological Society of London* **145**, 455–472.

Baratoux, L., Schulmann, K., Ulrich, S. & Lexa, O. (2005), Contrasting microstructures and deformation mechanisms in metagabbro mylonites contemporaneously

deformed under different temperatures (c.650°c and c.750°c), *in* D. Gapais, J. Brun & P. Cobbold, eds, 'Deformation Mechanisms, Rheology and Tectonics: from minerals to the lithosphere', Geological Society of London, Special Publication, 243, pp. 97–125.

Barber, A., Beach, A., Park, R., Tarney, J. & Stewart, A. (1978), *The Lewisian and Torridonian rocks of NW Scotland*, Geologists Association Guides, 21.

Barruol, G. & Kern, H. (1996), 'Seismic anisotropy and shear-wave splitting in lower-crustal and upper-mantle roks from the Ivrea Zone — experimental and calculated data', *Physics of the Earth and Planetary Interiors* **95**, 175–194.

Beach, A. (1974), 'The measurement and significance of displacements on Laxford shear zones, north-west Scotland', *Proceedings of the Geologists Association* **85**, 13–21.

Beach, A. (1986), 'A deep seismic reflection profile across the northern North Sea', *Nature* **323**, 53–55.

Beach, A., Bird, T. & Gibbs, A. (1987), Extensional tectonics and crustal structure: deep seismic reflection data from the northern North Sea Viking graben, *in* M. Coward, J. Dewey & P. Hancock, eds, 'Continental Extensional Tectonics', Geological Society of London, Special Publication, 28, pp. 467–476.

Beach, A., Coward, M. & Graham, R. (1974), 'An interpretation of the structural evolution of the Laxford Front, north-west Scotland', *Scottish Journal of Geology* **9**, 297–308.

Berger, A. & Stünitz, H. (1996), 'Deformation mechanisms and reaction of hornblende: examples from the Bergell tonalite (Central Alps)', *Tectonophysics* **257**, 149–174.

Besse, J., Courtillot, V., Pozzi, J., Westphal, M. & Zhou, Y. (1984), 'Palaeomagnetic estimates of crustal shortening in the Himalayan thrusts an Zangbo suture', *Nature* **311**, 621–626.

Birch, F. (1961), 'The velocity of compressional waves in rocks to 10 kilobars, part 2', *Journal of Geophysical Research* **66**, 2199–2224.

Blackman, D., Orcutt, J., Forsyth, D. & Kendall, J. (1993), 'Seismic anisotropy in the mantle beneath an oceanic spreading centre', *Nature* **366**, 675–677.

Blundell, D. (1990), 'Seismic images of the continental lithosphere', *Journal of the Geological Society of London* **147**, 895–913.

Blundy, J. & Holland, T. (1990), 'Calcic amphibole equilibria and a new amphibole-plagioclase geothermometer', *Contributions to Mineralogy and Petrology* **104**, 208–224.

Bohlen, S. & Mezger, K. (1989), 'Origin of granulite terranes and the formation of the lowermost continental crust', *Science* **244**, 326–329.

Boriani, A., Giobbi-Origoni, E., Borghi, A. & Caironi, V. (1990), 'The evolution of the Serie dei Laghi (Strona-Ceneri and Scisti dei Laghi): the upper component of the Ivrea-Verbano crustal section, southern Alps, north Italy and Ticino, Switzerland', *Tectonophysics* **182**, 103–118.

Bouchez, J. (1977), 'Plastic deformation of quartzites at low temperature in an area of natural strain gradient', *Tectonophysics* **39**, 25–50.

Brace, W. & Kohlstedt, D. (1980), 'Limits on lithospheric stress imposed by laboratory experiments', *Journal of Geophysical Research* **85**, 6248–6252.

Brady, R., Wernicke, B., McNutt, M., Mutter, J. & Correa, G. (2000), 'Results of the Basin and Range Geoscientific Experiment (BARGE): A marine-style

seismic reflection survey across the eastern boundary of the central Basin and Range Province', *Geochemistry Geophysics Geosystems* **1**, 1–9.

Brodie, K. & Rutter, E. (1985), On the relationship between deformation and metamorphism, with special reference to the behaviour of basic rocks, *in* A. Thompson & D. Rubie, eds, 'Metamorphic reactions: kinetics, textures and deformation', Springer, pp. 138–179.

Bruhn, D. & Casey, M. (1997), 'Texture development in experimentally deformed two-phase aggregates of calcite and anhydrite', *Journal of Structural Geology* **5**, 909–925.

Brun, J. & Tron, V. (1993), 'Development of the North Viking Graben: Inferences from laboratory modelling', *Sedimentary Geology* **86**, 31–51.

Bunge, H. (1969), *Mathematische Methoden der Texturanalyse*, Akademie-Verlag.

Bunge, H. (1981), 'Fabric analysis by orientation distribution functions', *Tectonophysics* **78**, 1–21.

Bunge, H. (1982), *Texture Analysis in Materails Science*, Butterworths.

Burov, E. & Diament, M. (1995), 'The effective elastic thickness of continental lithosphere: What does it really mean?', *Journal of Geophysical Research* **100**, 3905–3927.

Burov, E. & Watts, A. (2006), 'The long-term strength of the lithosphere: "jelly sandwich" or "crème brûlée?', *GSA Today* **16**, 4–10.

Byerlee, J. (1978), 'Friction of rocks', *Pure and Applied Geophysics* **116**, 615–626.

Cagnard, F., Brun, J. & Gapais, D. (2006), 'Modes of thickening of analogue weak lithospheres', *Tectonophysics* **421**, 145–160.

Carter, N. & Tsenn, M. (1987), 'Flow properties of continental lithosphere', *Tectonophysics* **136**, 27–63.

Cartwright, I. & Barnicoat, A. (1989), Evolution of the Scourian complex, *in* J. Daly, R. Cliff & B. Yardley, eds, 'Evolution of Metamorphic Belts', Geological Society of London, Special Publication, 43, pp. 297–301.

Cartwright, I., Fitches, W., O'Hara, M., Barnicoat, A. & O'Hara, S. (1985), 'Archaean supracrustal rocks from the Lewisian near Stoer, Sutherland', *Scottish Journal of Geology* **21**, 187–196.

Castañeda, P. P. & Willis, J. (1995), 'The effect of spatial distribution on the effective behavior of composite materials and cracked media', *Journal of the Mechanics and Physics of Solids* **43**, 1919–1951.

Chapman, H. (1979), '2390Myr Rb-Sr whole rock age of the Scourie dykes of north-west Scotland', *Nature* **277**, 642–643.

Chapman, H. & Moorbath, S. (1977), 'Lead isotope measurements from the oldest recognised Lewisian gneisses of north-west Scotland', *Nature* **268**, 41–42.

Cheadle, M., McGeary, S., Warner, M. & Matthews, D. (1987), Extensional structures of the westers UK continental shelf: a review of evidence from deep seismic profiling, *in* M. Coward, J. Dewey & P. Hancock, eds, 'Continental Extensional Tectonics', Geological Society of London, Special Publication, 28, pp. 445–465.

Chen, W. & Molnar, P. (1983), 'Focal depths of intracontinental and intraplate Earthquakes and their implications for the thermal and mechanical properties of the lithosphere', *Journal of Geophysical Research* **88**, 4183–4214.

Chen, W. & Yang, Z. (2004), 'Earthquakes beneath the Himalayas and Tibet: Evidence for strong lithospheric mantle', *Science* **304**, 1949–1952.

Christensen, N. (1965), 'Compressional wave velocities in metamorphic rocks are pressures to 10 kilobars', *Journal of Geophysical Research* **70**, 6147–6164.

Christensen, N. (1979), 'Compressional wave velocities in rocks at high temperatures and pressures, critical thermal gradients, and crustal low-velocity zones', *Journal of Geophysical Research* **84**, 6849–6857.

Christensen, N. (1984), 'The magnitude, symmetry and origin of upper mantle anisotropy based on fabric analyses of ultramafic tectonites', *Geophysical Journal of the Royal Astronomical Society* **76**, 89–111.

Christensen, N. & Fountain, D. (1975), 'Constitution of the lower continental crust based on experimental studies of seismic velocities in granulite', *Geological Society of America Bulletin* **86**, 227–236.

Christensen, N. & Mooney, W. (1995), 'Seismic velocity structure and omposition of the continental crust: A global view', *Journal of Geophysical Research* **100**, 9761–9788.

Christensen, N. & Wepfer, W. (1989), Laboratory techniques for determining seismic velocities and attenuations, with applications to the continental lithosphere, *in* L. Pakiser & W. Mooney, eds, 'Geophysical framework of the continental United States', Geological Society of America Memoir 172, pp. 91–102.

Christie, P. & Sclater, J. (1980), 'An extensional origin for the Buchan and Witchground Graben in the North Sea', *Nature* **283**, 729–732.

Clark, M. & Royden, L. (2000), 'Topographic ooze: Building the eastern margin of Tibet by lower crustal flow', *Geology* **28**, 703–706.

Cloetingh, S. & Burov, E. (1996), 'Thermomechanical structure of european continental lithosphere: constraints from rheological profiles and EET estimates', *Geophysical Journal International* **124**, 695–723.

Cohen, A., O'Nions, R. & O'Hara, M. (1991), 'Chronology and mechanism of depletion in Lewisian granulites', *Contributions to Mineralogy and Petrology* **106**, 142–153.

Collins, M. & Brown, J. (1998), 'Elasticity of an upper mantle clinopyroxene', *Physics and Chemistry of Minerals* **26**, 7–13.

Corfu, F., Crane, A., Moser, D. & Rogers, G. (1998), 'U-pb zircon systematics at Gruinard Bay, northwest Scotland: Implications for the early orogenic evolution of the Lewisian complex', *Contributions to Mineralogy and Petrology* **133**, 329–345.

Corfu, F., Heaman, L. & Rogers, G. (1994), 'Polymetamorphic evolution of the Lewisian complex, NW Scotland, as recorded by U-Pb isotopic compositions of zircon, titanite and rutile', *Contributions to Mineralogy and Petrology* **117**, 215–228.

Coward, M. (1976), 'Strain within ductile shear zones', *Tectonophysics* **34**, 181–197.

Coward, M. (1990), 'Shear zones at the Laxford front, NW Scotland and their significance in the interpretation of lower crustal structure', *Journal of the Geological Society of London* **147**, 279–286.

Coward, M. & Park, R. (1987), The role of mid-crustal shear zones in the Early Proterozoic evolution of the Lewisian, *in* R. Park & J. Tarney, eds, 'Evolution of the Lewisian and Comparable Precambrian High Grade Terrains', Geological Society of London, Special Publication, 27, pp. 127–138.

Coward, M. & Potts, G. (1983), 'Complex strain patterns developed at the frontal and lateral tips to shear zones and thrust zones', *Journal of Structural Geology* **5**, 383–399.

Coward, M., Kidd, W., Yun, P., Shackleton, R. & Hu, Z. (1988), 'The structure of the 1985 Tibet Geotraverse, Lhasa to Golmud', *Philosophical Transactions of the Royal Society of London* **327**, 307–333.

Crampin, S. (1978), 'Seismic wave propagation through a cracked solid: polarisation as a possible dilatancy diagnostic', *Geophysical Journal of the Royal Astronomical Society* **53**, 467–496.

Crampin, S. (1984*a*), 'Apparent anisotropy in inhomogeneous media', *Geophysical Journal of the Royal Astronomical Society* **76**, 65–69.

Crampin, S. (1984*b*), 'Effective anisotropic elastic constants for wave propagation through cracked solids', *Geophysical Journal of the Royal Astronomical Society* **76**, 135–145.

Crampin, S. (1984b), 'An introduction to wave propagation in anisotropic media', *Geophysical Journal of the Royal Astronomical Society* **76**, 17–28.

Crampin, S., Booth, D., Evans, R., Peakock, S. & Fletcher, J. (1990), 'Changes in shear wave splitting at Anza near the time of the North Palm Springs Earthquake', *Journal of Geophysical Research* **95**, 11197–11212.

Crampin, S., Chesnokov, E. & Hipkin, R. (1984), 'Seismic anisotropy — the state of the art: II', *Geophysical Journal of the Royal Astronomical Society* **76**, 1–16.

Davies, F. (1978), 'Progressive simple shear deformation on the Laxford shear zone', *Proceedings of the Geologists Association* **89**, 177–196.

Davis, G. (1987), A shear-zone model for the structural evolution of metamorphic core complexes in southeastern Arizona, *in* M. Coward, J. Dewey & P. Hancock, eds, 'Continental Extensional Tectonics', Geological Society of London, Special Publication, 28, pp. 247–266.

Day, A. (1993), *Developments in the EBSD technique and their application to grain imaging*, PhD thesis, University of Bristol.

Dewey, J. & Burke, K. (1973), 'Tibetan, Variscan and Precambrian basement reactivation: Products of a continental collision', *Journal of Geology* **81**, 683–692.

Dewey, J., Shackleton, R., Chengfa, C. & Yiyin, S. (1988), 'The tectonic evolution of the Tibetan Plateau', *Philosophical Transactions of the Royal Society of London* **327**, 379–413.

Downes, H. & Leyreloup, A. (1986), Granulitic xenoliths from the French Massif Central — petrology, Sr and Nd isotope systematics and model age estimates, *in* J. Dawson, D. Carswell, J. Hall & K. Wedepohl, eds, 'The nature of the lower continental crust', Geological Society of London, Special Publication, 24, pp. 319–330.

Droop, G., Fernandes, L. & Shaw, S. (1999), 'Laxfordian metamorphic conditions of the Palaeoproterozoic Loch Maree Group, Lewisian Complex, NW Scotland', *Scottish Journal of Geology* **35**, 31–50.

England, P. & Houseman, G. (1985), 'Role of lithospheric strength heterogeneities in the tectonics of Tibet and neighbouring regions', *Nature* **315**, 297–301.

England, P. & Houseman, G. (1986), 'Finite strain calculations of continental deformation 2: Comparison with the India-Asia collision zone', *Journal of Geophysical Research* **91**, 3664–3676.

England, P. & Searle, M. (1986), 'The Cretaceous-Tertiary deformation of the Lhasa block and its implications for crustal thickening in Tibet', *Tectonics* **5**, 1–14.

Escher, A., Escher, J. & Watterson, J. (1975), 'The reorientation of the Kangamiut dyke swarm, west Greenland', *Canadian Journal of Earth Science* **12**, 158–173.

Eshelby, J. (1957), 'The determination of the elastic field of an ellipoidal inclusion, and related problems', *Proceedings of the Royal Society of London, Series A* **241**, 376–396.

Evans, C. & Lambert, R. (1974), 'The Lewisian of Lochinver, Sutherland; the type area for the Iinverian metamorphism', *Journal of the Geological Society of London* **130**, 125–150.

Fettes, D., Mendum, J., Smith, D. & Watson, J. (1992), *Geology of the Outer Hebrides*, HMSO.

Fichler, C. & Hospers, J. (1990), 'Deep crustal structure of the northern North Sea Viking Graben: Results from deep reflection seismic and gravity data', *Tectonophysics* **178**, 241–254.

Fielding, E., Isacks, B., Barazangi, M. & Duncan, C. (1994), 'How flat is Tibet?', *Geology* **22**, 163–167.

Fountain, D. (1976), 'The Ivrea-Verbano and Strona-Ceneri zones, northern Italy: a cross-section of the continental crust – new evidence from seismic velocities of rock samples', *Tectonophysics* **33**, 145–165.

Fountain, D. & Christensen, N. (1989), Composition of the continental crust and upper mantle; a review, *in* L. Pakiser & W. Mooney, eds, 'Geophysical framework of the continental United States', Geological Society of America Memoir **172**, pp. 711–742.

Fountain, D. & Salisbury, M. (1981), 'Exposed cross-sections through the continental crust: implications for crustal structure, petrology and evolution', *Earth and Planetay Science Letters* **56**, 263–277.

Fountain, D., Huruch, C. & Smithson, S. (1984), 'Seismic reflectivity of mylonite zones in the crust', *Geology* **12**, 195–198.

Freeman, B. (1987), 'The behaviour of deformable ellipsoidal particles in three-dimentional slow flows: implications for geological strain analysis', *Tectonophysics* **132**, 297–309.

Frey, F. & Prinz, M. (1978), 'Ultramafic inclusions from San Carlos, Arizona: petrologic and geochemical data bearing on their petrogenesis', *Earth and Planetary Science Letters* **38**, 129–176.

Friend, C. & Kinny, P. (1995), 'New evidence for protolith ages of Lewisian granulites, northwest Scotland', *Geology* **23**, 1027–1030.

Friend, C. & Kinny, P. (2001), 'A reappraisal of the Lewisian Gneiss Complex: Geochronological evidence for its tectonic assembly from disparate terranes in the Proterozoic', *Contributions to Mineralogy and Petrology* **142**, 198–218.

Frost, B., Fyfe, W., Tazaki, K. & Chan, T. (1989), 'Grain-boundary graphite in rocks and implications for high electrical conductivity in the lower crust', *Nature* **340**, 134–136.

Gans, P. (1987), 'An open-system, two-layer crustal stretching model for the eastern Great Basin', *Tectonics* **6**, 1–12.

Gay, N. (1968a), 'Pure shear and simple shear deformation of inhomogeneous viscous fluids, 1: theory', *Tectonophysics* **5**, 211–234.

Geis, W., Cook, F., Green, A., Milkereit, B., Percival, J. & West, G. (1990), 'Thin thrust sheet formation of the Kapuskasing zone revealed by the Lithoprobe seismic reflection data', *Geology* **18**, 513–516.

Giletti, B., Moorbath, S. & Lambert, R. (1961), 'A geochronological study of the metamorphic complexes of the Scottish Highlands', *Quarterly Journal of the Geological Society of London* **117**, 233–264.

Goetze, C. (1978), 'The mechanisms of creep in olivine', *Philosophical Transactions of the Royal Society of London* **1978**, 99–119.

Goldstein, J., Newbury, D., Joy, D., Lyman, C., Echlin, P., Lifshin, E., Sawyer, L. & Michael, J. (2003), *Scanning electron microscopy and X-ray microanalysis*, Klewer Academic/Plenum Publishers.

Graham, C. & Powell, R. (1984), 'A granet-hornblende geothermometer: calibration, testing and application to the Pelona Schist, southern California', *Journal of Metamorphic Geology* **2**, 13–31.

Haines, S., Klemperer, S., Brown, L., Jingru, G., Mechie, J., Meissner, R., Ross, A. & Wenjin, Z. (2003), 'INDEPTH III seismic data: From surface observations to deep crustal processes in Tibet', *Tectonics* **22**, 1–18.

Hamilton, G. & Kohn, R. (1988), 'Variational bounds on the effective moduli of anisotropic composites', *Journal of the Mechanics and Physics of Solids* **36**, 597–629.

Hamilton, P., Evensen, N., O'Nions, R. & Tarney, J. (1979), 'Sm-Nd systematics of Lewisian gneisses: Implications for the origin of granulites', *Nature* **277**, 25–28.

Hamilton, W. (1987), Crustal extension in the Basin and Range Province, southwestern United States, *in* M. Coward, J. Dewey & P. Hancock, eds, 'Continental Extensional Tectonics', Geological Society of London, Special Publication, 28, pp. 155–176.

Hammarstrom, J. & Zen, E. (1986), 'Aluminium in hornblende: an empirical igneous geobarometer', *American Mineralogist* **71**, 1297–1313.

Handy, M. (1990), 'The solid state folw of polymineralic rocks', *Journal of Geophysical Research* **95**, 8647–8661.

Handy, M. (1992), 'Corection and addition to "The solid state folw of polymineralic rocks"', *Journal of Geophysical Research* **97**, 1897–1899.

Handy, M. (1994), 'Flow laws for rocks containing two non-linear viscous phases: a phenomenological approach', *Journal of Structural Geology* **16**, 287–301.

Handy, M., Braun, J., Brown, M., Kukowski, N., Paterson, M., Schmid, S., Stöckhert, B., Stüwe, K., Thompson, A. & Wosnitza, E. (2001), 'Rheology and geodynamic modelling: the next step forward', *International Journal of Earth Sciences* **90**, 149–156.

Handy, M., Franz, L., Heller, F., Janott, B. & Zurbriggen, R. (1999), 'Multistage accretion and exhumation of the continental crust, Ivrea crustal section, Italy and Switzerland', *Tectonics* **18**, 1154–1177.

Harrison, T., Copeland, P., Kidd, W. & Yin, A. (1992), 'Raising Tibet', *Science* **255**, 1663–1670.

Hashin, Z. & Shtrikman, S. (1962), 'On the variational principles in anisotropic and nonhomogeneous elasticity', *Journal of the Mechanics and Physics of Solids* **10**, 335–342.

Hashin, Z. & Shtrikman, S. (1963), 'A variational approach to the theory of the elastic behaviour of multiphase materials', *Journal of the Mechanics and Physics of Solids* **11**, 127–140.

Heaman, L. & Tarney, J. (1989), 'U-Pb baddeleyite ages for the Scourie dyke swarm, Scotland: Evidence for two distinct intrusion events', *Nature* **340**, 705–708.

Heier, K. (1973), 'Geochemistry of granulite facies rocks and problems of their origin', *Philosophical Transactions of the Royal Society of London* **A273**, 429–442.

Hess, H. (1964), 'Seismic anisotropy of the uppermost mantle under oceans', *Nature* **203**, 629–631.

Hill, R. (1952), 'The elastic behaviour of a crystalline aggregate', *Proceedings of the Physical Society of London, Section A* **65**, 349–354.

Hirn, A., Jiang, M., Sapin, M., Diaz, J., Nercessian, A., Lu, Q., Lépine, J., Shi, D., Sachpazi, M., Pandey, M., Ma, K. & Gallart, J. (1995), 'Seismic anisotropy as an indicator of mantle flow beneath the Himalayas and Tibet', *Nature* **375**, 571–574.

Holbrook, W., Gajewski, D., Krammer, A. & Prodehl, C. (1988), 'An interpretation of wide-angle compressional and shear wave data in southwest Germany: Poisson's ratio and petrological implications', *Journal of geophysical research* **93**, 12081–12106.

Holbrook, W., Mooney, W. & Christensen, N. (1992), The seismic velocity structure of the deep continental crust, *in* D. Fountain, R. Arculus & R. Kay, eds, 'Continental Lower Crust', Elsevier, pp. 1–43.

Holland, J. & Lambert, R. (1975), 'The chemistry and origin of the Lewisian gneisses of the Scottish mainland: The Scourie and Inver assemblages and subcrustal accretion', *Precambrian Research* **2**, 161–174.

Houseman, G. & England, P. (1986), 'Finite strain calculations of continental deformation 1: Method and general results for convergent zones', *Journal of Geophysical Research* **91**, 3651–3663.

Huang, W., Ni, J., Tilmann, F., Nelson, D., Guo, J., Zhao, W., Mechie, J., Kind, R., Saul, J., Rapine, R. & Hearn, T. (2000), 'Seismic polarization anisotropy beneath the central Tibetan Plateau', *Journal of Geophysical Research* **105**, 27979–27989.

Humphries, F. & Cliff, R. (1982), 'Sm-Nd dating and cooling history of Scourian granulites, Sutherland', *Nature* **295**, 515–517.

Hyndman, R. & Shearer, P. (1989), 'Water in the continental lower crust: modelling magnetotelluric and seismic reflection results', *Geophysical Journal International* **98**, 343–365.

Jackson, I. & Arculus, R. (1984), 'Laboratory wave velocity measurements on lower crustal xenoliths from Calcutteroo, South Australia', *Tectonophysics* **101**, 185–197.

Jackson, I., Rudnick, R., O'Reilly, S. & Bezant, C. (1990), 'Measured and calculated elastic wave velocities for xenoliths from the lower crust and upper mantle', *Tectonophysics* **173**, 207–210.

Jackson, J. (2002), 'Strength of the continental lithosphere: time to abandon the jelly sandwich?', *GSA Today* **12**, 4–10.

Ji, S. & Mainprice, D. (1988), 'Natural deformation fabrics of plagioclase; implications for slip systems and seismic anisotropy', *Tectonophysics* **147**, 145–163.

Ji, S. & Xia, B. (2002), *Rheology of polyphase Earth material*, Polytechnic International Press.

Ji, S., Long, C., Martignole, J. & Salisbury, M. (1997), 'Seismic reflectivity of a finely layered, granulite-facies ductile shear zone in the southern Grenville Province, Quebec', *Tectonophysics* **279**, 113–133.

Ji, S., Salisbury, M. & Hanmer, S. (1993), 'Petrofabric, P-wave anisotropy and seismic reflectivity of high-grade tectonites', *Tectonophysics* **222**, 195–226.

Jiang, Z., Prior, D. & Wheeler, J. (2000), 'Albite crystallographic preferred orientation and grain misorientation distribution in a low-grade mylonite: implications for granular flow', *Journal of Structural Geology* **22**, 1663–1674.

Johnson, M. (2002), 'Shortening budgets and the role of continental subduction during the India-Asia collision', *Earth Science Reviews* **59**, 101–123.

Jones, A. (1992), Electrical conductivity of the continental lower crust, *in* D. Fountain, R. Arculus & R. Kay, eds, 'Continental lower crust', Elsevier, Developments in Geotectonics, 23, pp. 81–143.

Jones, T. & Nur, A. (1982), 'Seismic velocity and anisotropy in mylonites and the reflectivity of deep crustal fault zones', *Geology* **10**, 260–263.

Jouanne, F., Mugnier, J., Gamind, J., Fort, P. L., Pandey, M., Bollinger, L., Flouzat, M. & Avouac, J. (2004), 'Current shortening across the Himalayas of Nepal', *Geophysical Journal International* **157**, 1–14.

Keir, D., Kendall, J., Ebinger, C. & Stuart, G. (2005), 'Variations in late syn-rift melt alignment inferred from shear-wave splitting in crustal earthquakes beneath the Ethiopian rift', *Geophysical Research Letters* **32**, 1–4.

Kendall, J.-M. (2000), Seismic anisotropy in the boundary layers of the mantle, *in* S. Karato, A. Forte, R. Liebermann, G. Masters & L. Stixrude, eds, 'Earth's deep interior: mineral physics and tomography from the atomic to the global scale', AGU, pp. 133–159.

Kenkmann, T. & Dresen, G. (2002), 'Dislocation microstructure and phase distribution in a lower crustal shear zone — an example from the Ivrea Zone, Italy', *International Journal of Earth Science* **91**, 445–458.

Kennett, B., Engdahl, E. & Buland, R. (1995), 'Constraints on seismic velocities in the Earth from traveltimes', *Geophysical Journal International* **122**, 108–124.

Kern, H. (1978), 'The effect of high temperature and high confining pressure on compressional wave velocities in quartz-bearing and quartz-free igneous and metamorphic rocks', *Tectonophysics* **44**, 185–203.

Khazanehdari, J., Rutter, E. & Brodie, K. (2000), 'High-pressure–high-temperature seismic velocity structure of the mid-rustal and lower crustal rocks of the Ivrea-Verbano zone and Serie dei Laghi, NW Italy', *Journal of Geophysical Research* **105**, 13843–13858.

Khazanehdari, J., Rutter, E., Casey, M. & Burlini, L. (1998), 'The role of crystallographic fabric in the generation of seismic anisotropy and reflectivity of high strain zones in calcite rocks', *Journal of Structural Geology* **20**, 293–299.

Kind, R., Kosarev, G., Makeyeva, L. & Vinnik, L. (1985), 'Observations of laterally inhomogeneous anisotropy in the continental lithosphere', *Nature* **318**, 358–361.

Kind, R., Ni, J., Zhao, W., Wu, J., Yuan, X., Zhao, L., Sandvol, E., Reese, C., Nabelek, J. & Hearn, T. (1996), 'Evidence from Earthquake data for a partially molten crustal layer in southern Tibet', *Science* **274**, 1692–1994.

Kinny, P. & Friend, C. (1997), 'U-Pb isotopic evidence for the accretion of different crustal blocks to form the Lewisian Complex of northwest Scotland', *Contributions to Mineralogy and Petrology* **129**, 326–340.

Kirby, S. (1985), 'Rock mechanics observations pertinent to the rheology of the continental lithosphere and the localisation of strain along shear zones', *Tectonophysics* **119**, 1–27.

Kitamura, K. (2006), 'Constraint of lattice preferred orientation (LPO) on Vp anisotropy of amphibole-rich rocks', *Geophysical Journal International* **165**, 1058–1065.

Klemperer, S. (1988), 'Crustal thinning and nature of extension in the northern north sea from deep seismic reflection profiling', *Tectonics* **7**, 803–821.

Klemperer, S. (in press), Crustal flow in Tibet: Geophysical evidence for the physical state of the Tibetan lithosphere, and inferred patterns of active flow, *in*

R. Law, M. Searle & L. Godin, eds, 'Channel flow, ductile extrusion and exhumation in continental collision zones', Geological Society of London, Special Publication, p. pp39.

Klemperer, S. & White, N. (1989), Coaxial stretching or lithospheric simple shear in the North Sea? Evidence from deep seismic profiling and subsidence, *in* A. Tankard & H. Balkwill, eds, 'AAPG Memoir, Extensional Tectonics and Stratigraphy of the North Atlantic Margins, 46', American Association of Petroleum Geologists, pp. 511–522.

Knight, R. & Nolen-Hoeksema, R. (1990), 'A laboratory study of the dependence of elastic wave velocities on pore scale fluid distribution', *Geophysical Research Letters* **17**, 1529–1532.

Kohn, M. & Spear, F. (1990), 'Two new geobarometers for garnet amphibolites, with applications to southeasters Vermont', *American Mineralogist* **75**, 89–96.

Kola-Ojo, O. & Meissner, R. (2001), 'Southern Tibet: Its deep seismic structure and some tectonic implications', *Journal of Asian Earth Sciences* **19**, 249–256.

Kruhl, J. (1987b), 'Preferred lattice orientations of plagioclase from amphibolite and greenschist facies rocks near the Insubric Line (Western Alps)', *Tectonophysics* **135**, 233–242.

Kruse, R. & Stünitz, H. (1999), 'Deformation mechanisms and phase distribution in mafic high-temperature mylonites from the Jotun Nappe, southern Norway', *Tectonophysics* **303**, 223–249.

Lal, D., Harris, N., Sharma, K., Gu, Z., Ding, L., Liu, T., Dong, W., Caffee, M. & Jull, A. (2003), 'Erosion histroy of the Tibetan Plateau cince the last interglacial: Constraints from the first studies of cosmogenic ^{10} Be from Tibetan bedrock', *Earth and Planetary Science Letters* **217**, 33–42.

Law, R. (1990), Crystallographic fabrics: A selective review of their applications to research in structural geology, *in* R. Knipe & E. Rutter, eds, 'Deformation mechanisms, rheology and tectonics', Geological Society of London, Special Publication, 54, pp. 335–352.

Law, R., Casey, M. & Knipe, R. (1986), 'Kinematic and tectonic significance of microstructures and crystallographic fabrics within quartz mylonites from the Assynt and Eriboll regions of the Moine thrust zone, NW Scotland', *Transactions of the Royal Society of Edinburgh: Earth Sciences* **77**, 99–125.

Law, R., Schmid, S. & Wheeler, J. (1990), 'Simple shear deformation and quartz crystallographic fabrics: A possible natural example from the torridon area of NW Scotland', *Journal of Structural Geology* **12**, 29–45.

Leake, B., Woolley, A., Arps, C., Birch, W., Gilbert, M., Grice, J., Hawthorne, F., Kato, A., Kisch, H., Krivovichev, V., Linthout, K., Laird, J., Mandarino, J., Maresch, W., Nickel, E., Rock, N., Schumacher, J., Smith, D., Stephenson, N., Ungaretti, L., Whittaker, E. & Youzhi, G. (1997), 'Nomenclature of amphiboles; report of the subcommittee on amphiboles of the international mineralogical association commission on new minerals and mineral names', *Mineralogical Magazine* **61**, 295–321.

Leary, P., Crampin, S. & McEvilly, T. (1990), 'Seismic fracture anisotropy in the Earth's crust: An overview', *Journal of Geophysical Research* **95**, 11105–11114.

Lerch, D., Gashawbeza, E., Klemperer, S., Miller, E., Colgan, J. & Wilson, C. (2005), 'Preliminary results from the 2004 Stanford University seismic experiment; a 260km refraction/reflection/teleseismic experiment in the northwestern Basin and Range', *Geological Society of America Abstracts with Programs* **37**, 65–66.

Lister, G. & Dornsiepen, U. (1982), 'Fabric transitions in the Saxony granulite terrane', *Journal of Structural Geology* 4, 81–92.

Lister, G. & Hobbs, B. (1980), 'The simulation of fabric development during plastic deformation and its application to quartzite: the influence of deformation history', *Journal of Structural Geology* **2**, 355–371.

Lister, G. & Paterson, M. (1979), 'The simulation of fabric development during plastic deformation and its application to quartzite: fabric transitions', *Journal of Structural Geology* **1**, 99–115.

Lister, G. & Price, G. (1978), 'Fabric development in a quartz-feldspar mylonite', *Tectonophysics* **49**, 37–78.

Lloyd, G. (1985), Review of instrumentation, techniques and applications of SEM in mineralogy, *in* J. White, ed., 'Applications of Electron Microscopy in the Earth Sciences', Mineralogical Association of Canada, Short Course, 11, pp. 75–94.

Lloyd, G. (1987), 'Atomic number and crystallographic contrast images with the SEM: A review of backscattered electron techniques', *Mineralogical Magazine* **51**, 3–19.

Lloyd, G. (2000), 'Grain boundary contact effects during faulting of quartzite: An SEM/EBSD analysis', *Journal of Structural Geology* **22**, 1675–1693.

Lloyd, G. & Kendall, J. (2005), Petrofabric derived seismic properties of a mylonitic quartz simple shear zone: Implications for seismic reflection profiling, *in* P. Harvey, T. Brewer, P. Pezard & V. Petrov, eds, 'Petrophysical Properties of Crystalline Rocks', Geological Society of London, Special Publication, 240, pp. 75–94.

Lloyd, G., Law, R., Mainprice, D. & Wheeler, J. (1992), 'Microstructural and crystal fabric evolution during shear zone formation', *Journal of Structural Geology* **14**, 1079–1100.

Love, G., Kinny, P. & Friend, C. (2004), 'Timing of magmatism and metamorphism in the Gruinard Bay area of the Lewisian Gneiss Complex: Comparisons with the Assynt Terrane and implications for terrane accretion', *Contributions to Mineralogy and Petrology* **146**, 620–636.

Maggi, A., Jackson, J., McKenzie, D. & Priestley, K. (2000), 'Earthquake focal depths, effective elastic thickness, and the strength of the continental lithosphere', *Geology* **28**, 495–498.

Mainprice, D. (1990), 'A Fortran program to calculate seismic anisotropy from the lattice preferred orientation of minerals', *Computers and Geosciences* **16**, 385–393.

Mainprice, D. (2000), 'The estimation of seismic properties of rocks with heterogeneous microstructures using a local cluster model - preliminary results', *Physics and Chemistry of the Earth* **25**, 155–161.

Mainprice, D. & Humbert, M. (1994), 'Methods of calculating petrophysical properties from lattice preferred orientation data', *Surveys in Geophysics* **15**, 575–592.

Mainprice, D. & Nicolas, A. (1989), 'Development of shape and lattice preferred orienations: Application to the seismic anisotropy of the lower crust', *Journal of Structural Geology* **11**, 175–189.

Mainprice, D. & Silver, P. (1993), 'Interpretation of SKS-waves using samples from the subcontinental lithosphere', *Physicas of the Earth and Planetary Interiors* **78**, 257–280.

Mainprice, D., Barruol, G. & Ismaïl, W. B. (2000), The seismic anisotropy of the Earth's mantle: from single crystal to polycrystal, *in* S. Karato, A. Forte, R. Liebermann, G. Masters & L. Stixrude, eds, 'Earth's deep interior: mineral physics and tomography from the atomic to the global scale', AGU, pp. 237–264.

Mainprice, D., Bouchez, J., Blumenfeld, P. & Tubia, J. (1986), 'Dominant c slip in naturally deformed quartz: implications for dramatic plastic softening at high temperature', *Geology* **14**, 819–822.

Manghnani, M., Romananantoandro, R. & Clark, S. (1974), 'Compressional and shear wave velcities in granulite facies rocks and eclogites to 10 kilobars', *Journal of Geophysical Research* **79**, 5427–5446.

Marshall, D. & McLaren, A. (1977a), 'The direct observation and analysis of dislocations in experimentally deformed plagioclase feldspars', *Journal of Materials Science* **12**, 893–903.

Marshall, D. & McLaren, A. (1977b), 'Deformation mechanisms in experimentally deformed plagioclase feldspars', *Physics and Chemistry of Minerals* **1**, 351–370.

Martin, B. & Thomson, C. (1997), 'Modelling surface waves in anisotropic structures II: Examples', *Physics of the Earth and Planetary Interiors* **103**, 253–279.

Matthews, D. (1986), Seismic reflections from the lower crust around Britain, *in* J. Dawson, D. Carswell, J. Hall & K. Wedepohl, eds, 'The nature of the lower continental crust', Geological Society of London, Special Publication, 24, pp. 11–22.

Mazzoli, C., Sassi, R. & Burlini, L. (2002), 'Experimental study of the seismic properties of the Eastern Alps (Italy) along the Aurina-Tures-Badia Valleys transect', *Tectonophysics* **354**, 179–194.

McKenzie, D. (1978), 'Some remarks on the development of sedimentary basins', *Earth and Planetary Science Letters* **40**, 25–32.

McKenzie, D. & Jackson, J. (2002), 'Conditions for flow in the continental crust', *Tectonics* **21**, 5.1–5.7.

McSkimin, H., Andreatch, P. & Thurston, R. (1965), 'Elastic moduli of quartz versus hydrostatic pressure at 25 degrees and -195.8 degrees C', *Journal of Applied Physics* **36**, 1624–1632.

Meissner, R. & Kuznir, N. (1987), 'Crustal viscosity and th reflectivity of the lower crust', *Annales Geophysicae* **5B**, 365–374.

Meissner, R. & Rabbel, W. (1999), 'Nature of crustal reflectivity along the DEKORP profiles in Germany in comparison with reflection patterns from difference tectonic units worldwide: a review', *Pure and applied geophysics* **156**, 7–28.

Meissner, R., Matthews, D. & Wever, T. (1986), 'The Moho in and around Great Britain', *Annales Geophysicae* **4B**, 659–664.

Meissner, R., Rabbel, W. & Kern, H. (2006), 'Seismic lamination and anisotropy of the lower continental crust', *Tectonophysics* **416**, 81–99.

Meissner, R., Tilmann, F. & Haines, S. (2004), 'About the lithospheric structure of central Tibet, based on seismic data from the INDEPTH III profile', *Tectonophysics* **380**, 1–25.

Meissner, R., Wever, T. & Flüh, E. (1987), 'The Moho in Europe – implications for crustal development', *Annales Geophysicae* **5B**, 357–364.

Miller, E., Gans, P. & Garing, J. (1983), 'The Snake Range décollement: An exhumed mid-Tertiary ductile-brittle transition', *Tectonics* **3**, 239–263.

Molnar, P. (1988), 'Continental tectonics in the aftermath of plate tectonics', *Nature* **335**, 131–137.

Molnar, P. & Chen, W. (1978), 'Evidence for large Cainozoic crustal shortening of Asia', *Nature* **273**, 218–220.

Molnar, P. & Chen, W. (1983), 'Focal depths and fault plane solutions of earthquakes under the Tibetan plateau', *Journal of Geophysical Research* **88**, 1180–1196.

Molnar, P. & Tapponnier, P. (1975), 'Cenozoic tectonics of Asia: Effects of a continental collision', *Science* **189**, 419–426.

Mooney, W. & Meissner, R. (1992), Multi-genetic origin of crustal reflectivity: a review of seismic reflection profiling of the continental lower crust and Moho, *in* D. Fountain, R. Arculus & R. Kay, eds, 'Continental lower crust', Elsevier, Developments in Geotectonics, 23, pp. 45–79.

Mooney, W., Laske, G. & Masters, G. (1998), 'Crust 5.1: A global crustal model at 5°x5°seismic polarisation anisotropy beneath the central Tibetan Plateau', *Journal of Geophysical Research* **103**, 727–747.

Moorbath, S., Welke, H. & Gale, N. (1969), 'The significance od lead isotope studies in ancient, high-grade metamorphic basement complexes, as exemplified by the Lewisian rocks of northwest Scotland', *Earth and Planetary Science Letters* **6**, 245–256.

Nelson, K., Zhao, W., Brown, L., Kuo, J., Che, J., Liu, X., Klemperer, S., Makovsky, Y., Meissner, R., Mechie, J., Kind, R., Wenzel, F., Ni, J., Nabelek, J., Leshou, C., Tan, H., Wei, W., Jones, A., Booker, J., Unsworth, M., Kidd, W., Hauck, M., Alsdorf, D., Ross, A., Cogan, M., Wu, C., Sandvol, E. & Edwards, M. (1996), 'Partially molten middle crust beneath southern Tibet: Synthesis of project INDEPTH results', *Science* **274**, 1684–1688.

Newton, R. & Hansen, E. (1986), The South Iindia-Sri Lanka high-grade terrain as a possible deep-crust section, *in* J. Dawson, D. Carswell, J. Hall & K. Wedepohl, eds, 'The nature of the lower continental crust', Geological Society of London, Special Publication, 24, pp. 297–307.

Nicolas, A. & Poirier, J. (1976), *Crystalline plasticity and solid state flow in metamorphic rocks*, John Wiley & Sons.

Oberti, R., Ungareti, L., Cannillo, E. & Hawthorne, F. (1993), 'The mechanism of Cl incorporation in amphibole', *American Mineralogist* **78**, 746–752.

O'Hara, M. (1961), 'Petrology of the Scourie dyke, Sutherland', *Mineralogical Magazine* **32**, 848–865.

Okrusch, M., Schöder, B. & Schnütgen, A. (1979), 'Granulite facies metabasite ejecta in the Laacher See area, Eifel, West Germany', *Lithos* **12**, 251–270.

Olsen, T. & Kohlstedt, D. (1984), 'Analysis of dislocations in some naturally deformed plagioclase feldspars', *Physics and Chemistry of Minerals* **11**, 153–160.

Olsen, T. & Kohlstedt, D. (1985), 'Natural deformation and recrystallisation of some intermediate plagioclase feldspars', *Tectonophysics* **111**, 107–131.

O'Nions, R., Hamilton, P. & Hooker, P. (1983), 'A Nd isotope investigation of sediments related to crustal development in the British Ilses', *Earth and Planetary Science Letters* **63**, 229–240.

Owens, T. & Zandt, G. (1997), 'Implications of crustal property variations for models of Tibetan plateau evolution', *Nature* **387**, 37–43.

Park, J. & Levin, V. (2002), 'Seismic anisotropy: Tracing plate dynamics in the mantle', *Science* **296**, 485–489.

Park, R. (1970), 'Observations on Lewisian chonology', *Scottish Journal of Geology* **6**, 379–399.

Park, R. & Cresswell, D. (1973), The dykes of the Laxfordian belts, *in* R. Park & J. Tarney, eds, 'The Early Precambrian of Scotland and related rocks of Greenland', University of Keele, pp. 119–130.

Park, R. & Tarney, J. (1987), The Lewisian complex: A typical Precambrian high-grade terrane?, *in* R. Park & J. Tarney, eds, 'Evolution of the Lewisian and Comparable Precambrian High Grade Terrains', Geological Society of London, Special Publication, 27, pp. 13–25.

Park, R., Crane, A. & Niamatullah, M. (1987), Early Proterozoic structure and kinematic evolution of the southern mainland Lewisian, *in* R. Park & J. Tarney, eds, 'Evolution of the Lewisian and Comparable Precambrian High Grade Terrains', Geological Society of London, Special Publication, 27, pp. 139–151.

Passchier, C. & Trouw, R. (1998), *Micotectonics*, Springer.

Paterson, M. & Weiss, L. (1961), 'Symmetry concepts in the structural analysis of deformed rocks', *Bulletin of the Geological Society of America* **72**, 841–882.

Peach, B., Horne, J., Gunn, W., Clough, C., Hinxman, L. & Teall, J. (1892), *Lochinver Sheet, 107, 1 inch to a mile*, Geological Survey of Scotland.

Peach, B., Horne, J., Gunn, W., Clough, C., Hinxman, L. & Teall, J. (1907), *The geological structure of the north-west Highlands of Scotland*, Memoir of the Geological Survey of Great Britain.

Pera, E., Mainprice, D. & Burlini, L. (2003), 'Anisotropic seismic properties of the upper mantle beneath the Torre Alfina area (Northern Apennines, Central Italy', *Tectonophysics* **370**, 11–30.

Percival, J. & Card, K. (1983), 'Archaean crust as revealed in the Kapuskasing uplift, Superior province, Canada', *Geology* **11**, 323–326.

Percival, J. & McGrath, P. (1986), 'Deep crustal structure and tectonic history of the northern Kapuskasing uplift of Ontario: an integrated petrological-geophysical study', *Tectonics* **5**, 553–572.

Percival, J., Fountain, D. & Salisbury, M. (1992), Exposed crustal cross sections as windows on the lower crust, *in* D. Fountain, R. Arculus & R. Kay, eds, 'Continental Lower Crust', Elsevier, pp. 317–362.

Phillips, M., Colville, A. & Ribbe, P. (1971), 'The crystal structures of two oligoclases: A comparison with low and high albite', *Zeitschrift fuer Kristallographie* **133**, 43–65.

Pidgeon, R. & Bowes, D. (1972), 'Zircon U-Pb ages of granulites from the central region of the Lewisian, northwestern Scotland', *Geological Magazine* **109**, 247–258.

Pinet, B. (1989), 'Deep seismic profiling and sedimentary basins', *Bulletin de la Societé Géologique de France* **5**, 749–766.

Pohl, M., Wenzel, F., Weiss, T., Siegesmund, S., Bohlen, T. & Rabbel, W. (1999), 'Realistic models of anisotropic laminated lower crust', *Pure and applied geophysics* **156**, 139–155.

Powell, C. & Conaghan, P. (1973), 'Plate tectonics and the Himalayas', *Earth and Planetary Science Letters* **20**, 1–12.

Powell, C. & Conaghan, P. (1975), 'Tectonic models of the Tibetan plateau', *Geology* **3**, 727–731.

Price, G. (1978), 'Study of heterogeneous fabric and texture within a quartz-feldspar mylonite using the photometric method', *Geological Society of America Bulletin* **89**, 1359–1372.

Prior, D. & Wheeler, J. (1999), 'Feldspar fabrics in a greenschist facies albite-rich mylonite from electron backscatter diffraction', *Tectonophysics* **303**, 29–49.

Prior, D., Boyle, A., Brenker, F., Cheadle, M., Day, A., Lopez, G., Peruzzo, L., Potts, G., Reddy, S., Speiss, R., Timms, N., Trimby, P., Wheeler, J. & Zetter-

ström, L. (1999), 'The application of electron backscatter diffraction and orientation contrast imaging in the SEM to textural problems in rocks', *American Mineralogist* **84**, 1741–1759.

Pros, Z., Lokajíček, T., Přikryl, R. & Klíma, K. (2003), 'Direct measurement of 3D elastic anisotropy on rocks from the Ivrea zone (Southern Alps, NW Italy)', *Tectonophysics* **370**, 31–47.

Rabbel, W. & Lüschen, E. (1996), 'Shear wave anisotropy of laminated lower crust at the Urach geothermal anomaly', *Tectonophysics* **264**, 219–233.

Rabbel, W. & Mooney, W. (1996), 'Seismic anisotropy of the crystalline crust: what does it tell us?', *Terra Nova* **8**, 16–21.

Ramberg, H. & Ghosh, S. (1977), 'Rotation and strain or linear and planar structures in three-dimensional progressive deformation', *Tectonophysics* **40**, 309–337.

Ramsay, J. (1967), *Folding and fracturing of rocks*, McGraw Hill.

Ramsay, J. (1980), 'Shear zone geometry: a review', *Journal of Structural Geology* **2**, 83–99.

Ramsay, J. & Graham, R. (1970), 'Strain variation in shear belts', *Canadian Journal of Earth Sciences* **7**, 786–813.

Ramsay, J. & Huber, M. (1983), *The techniques of modern structural geology. Volume 1: Strain analysis*, Academic Press.

Ranalli, G. (2000), 'Rheology of the crust and its role in tectonic reactivation', *Journal of Geodynamics* **30**, 3–15.

Ranalli, G. & Murphy, D. (1987), 'Rheological stratification of the lithosphere', *Tectonophysics* **132**, 281–295.

Randle, V. (2003), *Microstructure Determination and its Applications*, Maney Publishing.

Reed, S. J. B. (1996), *Electron microprobe analysis and scanning electron microscopy in geology*, Cambridge University Press.

Rehrig, W. & Reynolds, S. (1980), Geologic and geochronologic reconnaissance of a northwest-trending zone of metamorphic core complexes in southern and western Arizona, *in* M. Crittenden, P. Coney & G. Davis, eds, 'Cordilleran Metamorphic Core Complexes', Geological Society of America Memoir 153, pp. 131–157.

Reuss, A. (1929), 'Berechnung der fließgrenze von mischkristallen auf grund der plastizitätsbedingung für einkristalle', *Zeitschrift für Angewandte Mathematik und Mechanik* **9**, 49–58.

Rollinson, H. (1996), Tonalite-trondhjemite-granodiorite magmatism and the genesis of Lewisian crust during the Archaean, *in* T. Brewer, ed., 'Precambrian crustal evolution in the North Atlantic Region', Geological Society of London, Special Publication, 112, pp. 25–42.

Royden, L., Burhfiel, B., King, R., Wang, E., Chen, Z., Shen, F. & Liu, Y. (1997), 'Surface deformation and lower crustal flow in eastern Tibet', *Science* **276**, 788–790.

Rudnick, R. (1992), Xenoliths — samples of the lower continental crust, *in* D. Fountain, R. Arculus & R. Kay, eds, 'Continental Lower Crust', Elsevier, pp. 269–316.

Rudnick, R. & Fountain, D. (1995), 'Nature and composition of the continental crust: a lower crustal perspective', *Reviews of Geophysics* **33**, 267–309.

Rudnick, R. & Jackson, I. (1995), 'Measured and calculated elastic wave speeds in partially equilabrated mafic granulite xenoliths: Implications for the properties of an underplated lower continental crust', *Journal of Geophysical Research* **100**, 10211–10218.

Rutter, E. & Brodie, K. (1990), 'Some geophysical implications of the deformation and metamorphism of the Ivrea zone, northern Italy', *Tectonophysics* **182**, 147–160.

Rutter, E. & Brodie, K. (1991), 'Lithosphere rheology — a note of caution', *Journal of Structural Geology* **13**, 363–367.

Rutter, E. & Brodie, K. (1992), Rheology of the lower crust, *in* D. Fountain, R. Arculus & R. Kay, eds, 'Continental lower crust', Elsevier, Developments in Geotectonics, 23, pp. 201–267.

Rutter, E., Brodie, K., James, T., Blundell, D. & Waltham, D. (2003), Seismic modelling of lower and mid-crustal structure as exemplified by the Massiccio dei Laghi (Ivrea-Verbano zone and Serie dei Laghi) crustal section, northwest Italy, *in* J. Goff & K. Holliger, eds, 'Heterogeneity in the crust and upper mantle', Kluwer, pp. 67–97.

Rutter, E., Holdsworth, R. & Knipe, R. (2001), The nature and tectonic significance of fault-zone weakening: an introduction, *in* R. Holdsworth, R. Strachan, J. Magloughlin & R. Knipe, eds, 'The Nature and Tectonic Significance of Fault Zone Weakening', Geological Society of London, Special Publication, 186, pp. 1–11.

Sands, D. (1969), *Introduction to crystallography*, W.A. Benjamin Inc.

Sapin, M. & Hirn, A. (1997), 'Seismic structure and evidence for eclogitisation during the Himalayan convergence', *Tectonophysics* **273**, 1–16.

Sayers, C. (1994), 'The elastic anisotropy of shales', *Journal of Geophysical Research* **99**, 767–774.

Sayers, C. (1998), 'Long-wave seismic anisotropy of heterogeneous reservoirs', *Geophysical Journal International* **132**, 667–673.

Schmid, S. & Casey, M. (1986), 'Complete fabric analysis of some commonly observed quartz c-axis patterns', *Geophysics Monograph* **36**, 263–286.

Schmid, S., Casey, M. & Starkey, J. (1981), 'An illustration of the advantages of a complete texture analysis described by the orientation distribution function (ODF) using quartz pole figure data', *Tectonophysics* **78**, 101–117.

Scholz, C. (1988), 'The brittle-ductile trnsition and the depth of seismic faulting', *Geologische Rundschau* **77**, 319–328.

Schulte-Pelkum, V., Monsalve, G., Sheehan, A., Pandey, M., Sapkota, S., Bilham, R. & Wu, F. (2005), 'Imaging the Indian subcontinent beneath the Himalaya', *Nature* **435**, 1222–1225.

Seeber, L. & Armbruster, J. (1984), 'Some elements of continental subduction along the Himalayan front', *Tectonophysics* **105**, 263–278.

Shearer, P. (1999), *Introduction to Seismology*, Cambridge University Press.

Shen, F., Royden, L. & Burchfiel, B. (2001), 'Large-scale crustal deformation of the Tibetan Plateau', *Journal of Geophysical Research* **106**, 6793–6816.

Shepherd, T. (1990), 'Geological link between fluid inclusions, dilatant microcracks, and palaeostress field', *Journal of Geophysical Research* **95**, 11115–11120.

Sheraton, J., Skinner, A. & Tarney, J. (1973), Geochemistry of the Scourian gneisses of the Assynt district, *in* R. Park & J. Tarney, eds, 'The Early Precambrian of Scotland and related rocks of Greenland', University of Keele, pp. 13–30.

Sheriff, R. & Geldart, L. (1999), *Exploration Seismology*, Cambridge University Press.

Shih, X. & Meyer, R. (1990), 'Observation of shear wave splitting from natural events: South Moat of Long Valley Caldera, California, June 29 to August 12, 1982', *Journal of Geophysical Research* **95**, 11179–11195.

Sibson, R. (1977), 'Fault rocks and fault mechanisms', *Journal of the Geological Society of London* **133**, 191–213.

Sibson, R. (1984), 'Roughness at the base of the seismogenic zone: Contributing factors', *Journal of Geophysical Research* **89**, 5791–5799.

Siegesmund, S. & Kern, H. (1990), 'Velocity anisotropy and shear-wave splitting in rocks from the mylonite belt along the Insubric Line (Ivrea Zone, Italy)', *Earth and Planetary Science Letters* **99**, 29–47.

Siegesmund, S., Helming, K. & Kruse, R. (1994), 'Complete texture analysis of a deformed amphibolite: comparison between neutron diffraction and U-stage data', *Journal of Structural Geology* **16**, 131–142.

Siegesmund, S., Takeshita, T. & Kern, H. (1989), 'Anisotropy of Vp and Vs in an amphibolite of the deep crust and its relationship to the mineralogical, microstructural and textural characteristics of the rock', *Tectonophysics* **157**, 25–38.

Sills, J. & Rollinson, H. (1987), Metamorphic evolution of the mainland Lewisian complex, *in* R. Park & J. Tarney, eds, 'Evolution of the Lewisian and Comparable Precambrian High Grade Terrains', Geological Society of London, Special Publication, 27, pp. 81–92.

Skemer, P., Katayama, I., Jiang, Z. & Karato, S. (2005), 'The misorientation index: development of a new method for calculating the strength of lattice-preferred orientation', *Tectonophysics* **411**, 157–167.

Smith, R. & Bruhn, R. (1984), 'Intraplate extensional tectonics of the eastern Basin-Range: Inferences on strucural style from seismic reflection data, regional tectonics, and thermal-mechanical models of brittle-ductile deformation', *Journal of Geophysical Research* **89**, 5733–5762.

Smithson, S. & Johnson, R. (2003), Petrological causes of seismic heterogeneity in the continental crust, *in* J. Goff & K. Holliger, eds, 'Heterogeneity in the Crust and Upper Mantle', Kluwer Academic Publishers, pp. 37–66.

Snoke, A. (1980), Transition from infrastructure to suprastructure in the northern Ruby Mountains, Nevada, *in* M. Crittenden, P. Coney & G. Davis, eds, 'Cordilleran Metamorphic Core Complexes', Geological Society of America Memoir 153, pp. 287–333.

Snoke, A. & Tullis, J. (1998), An overview of fault rocks, *in* A. Snoke, J. Tullis & V. Todd, eds, 'Fault-related Rocks: A Photographic Atlas', Princeton University Press, pp. 3–18.

Steurer, W. & Jagodzinski, H. (1988), 'The incommensurately modulated structure of an andesine (an38)', *Acta Crystallographica* **44**, 344–351.

Stünitz, H. & FitzGerald, J. (1993), 'Deformation of granitoids at low metamorphic grade II: granular flow in albite-rich mylonites', *Tectonophysics* **221**, 299–324.

Sutton, J. & Watson, J. (1951), 'The pre-Torridonian metamorphic history of the Loch Torridon and Scourie areas in the north-west Highlands, and its bearing on the chronological classification of the Lewisian', *Quarterly Journal of the Geological Society of London* **106**, 241–308.

Sutton, J. & Watson, J. (1962), 'Further observations on the margin of the Laxfordian complex of the Lewisian near Loch Laxford, Sutherland', *Transactions of the Royal Society of Edinburgh* **65**, 89–106.

Tapponnier, P., Mercier, J., Proust, F., Andrieux, J., Armijo, R., Bassoullet, J., Brunel, M., Burg, J., Colchen, M., Dupré, B., Girardeau, J., Marcoux, J., Mascle, G., Matte, P., Nicolas, A., Tingdong, L., Xuchang, X., Chenfa, C., Paoyu, L., Guangcen, L., Naiwen, W., Guoming, C., Tonglin, H., Xibin, W., Wanming,

D., Haixiang, Z., Huaibin, S., Yongong, C., Ji, Z. & Hongrong, Q. (1981), 'The Tibetan side of the India-Euraia collision', *Nature* **294**, 405–410.

Tarney, J. (1963), 'Assynt dykes and their metamorphism', *Nature* **199**, 672–674.

Tarney, J. (1973), The Scourie dyke suite and the nature of the Inverian event in Assynt, *in* R. Park & J. Tarney, eds, 'The Early Precambrian of Scotland and related rocks of Greenland', University of Keele, pp. 105–118.

Tarney, J. & Weaver, B. (1987a), Geochemistry of the Scourian complex: Petrogenesis and tectonic models, *in* R. Park & J. Tarney, eds, 'Evolution of the Lewisian and Comparable Precambrian High Grade Terrains', Geological Society of London, Special Publication, 27, pp. 45–56.

Tarney, J. & Weaver, B. (1987b), Mineralogy, petrology and geochemistry of the Scoutie dykes: Petrogenesis and crystallisation processes in dykes intruded at depth, *in* R. Park & J. Tarney, eds, 'Evolution of the Lewisian and Comparable Precambrian High Grade Terrains', Geological Society of London, Special Publication, 27, pp. 217–233.

Tatham, D. & Casey, M. (2007), Inferences from shear zone geometry: An example from the Laxfordian shear zone at Upper Badcall, Lewisian Complex, NW Scotland, *in* A. Reis, R. Butler & R. Graham, eds, 'Deformation of the Continental Crust', Geological Society of London, Special Publication, 272, pp. 47–57.

Tatham, D., Lloyd, G., Butler, R. & M.Casey (2008), 'Amphibole and lower crustal seismic properties', *Earth and Planetary Science Letters* **267**, 118–128.

Teall, J. (1885), 'The metamorphosis of dolerite into hornblende-schist', *Quarterly Journal of the Geological Society* **41**, 133–145.

Terry, M. & Heidelbach, F. (2006), 'Deformation-enhanced metamorphic reactions and the rheology of high pressure shear zones, Western Gneiss Region, Norway', *Journal of Metamorphic Geology* **24**, 3–18.

Thomsen, L. (1986), 'Weak elastic anisotropy', *Geophysics* **51**, 1954–1966.

van Calsteren, P., Harris, N., Hawkesworth, C., Menzies, M. & Rogers, N. (1986), Xenoliths from southern Africa: a perspective on the lower crust, *in* J. Dawson, D. Carswell, J. Hall & K. Wedepohl, eds, 'The nature of the lower continental crust', Geological Society of London, Special Publication, 24, pp. 351–362.

Vauchez, A., Tommasi, A., Barruol, G. & Maumus, J. (2000), 'Upper mantle deformation and seismic anisotropy in continental rifts', *Physics and Chemistry of the Earth* **25**, 111–117.

Vernik, L. & Liu, X. (1997), 'Velocity anisotropy in shales: A petrophysical study', *Geophysics* **62**, 521–532.

Voigt, W. (1928), *Lehrbuch der kristallphysik*, B.G. Tubner.

Walpole, L. (1969), 'On the overall elastic moduli of composite materials', *Journal of the Mechanics and Physics of Solids* **17**, 235–251.

Wang, Q., Zhang, P., reymueller, J., ilham, R., Larson, K. M., Lai, X., You, X., Niu, Z., Wu, J., Li, Y., Liu, J., Yang, Z. & Chen, Q. (2001), 'Present-day crustal deformation in China constrained by Global Positioning System measurements', *Science* **294**, 574–577.

Wass, S. & Hollis, J. (1983), 'Crustal growth in southeastern Australia — evidence from lower crustal eclogite and granulitic xenoliths', *Journal of Metamorphic Geology* **1**, 25–45.

Waters, C., Tikoff, B., Goodwin, L. & Little, T. (2003), Ductile instabilities and structural heterogeneity in the lower continental crust, *in* J. Goff & K. Holliger, eds, 'Heterogeneity in the Crust and Upper Mantle', Kluwer Academic Publishers, pp. 1–36.

Waters, F., Cohen, A., O'Nions, R. & O'Hara, M. (1990), 'Development of Archaean lithosphere deduced from chronology and isotope chemistry of Scourie Dykes', *Earth and Planetary Science Letters* **97**, 241–255.

Watts, A. & Burov, E, (2003), 'Lithospheric strength and its relationship to the elastic and seismogenic layer thickness', *Earth and Planetary Science Letters* **213**, 113–131.

Weaver, B. & Tarney, J. (1980), 'Rare Earth geochemistry of the Lewisian granulite-facies gneisses, northwest Scotland: Implications for the petrogenesis of the Archaean lower continental crust', *Earth and Planetary Science Letters* **51**, 279–296.

Weaver, B. & Tarney, J. (1981a), 'Lewisian gneiss geochemistry and Archaean crustal development models', *Earth and Planetary Science Letters* **55**, 171–180.

Weaver, B. & Tarney, J. (1981b), 'The Scourie syke suite: Petrogenesis and geochemical nature of the Proterozoic sub-continental mantle', *Contributions to Mineralogy and Petrology* **78**, 175–188.

Weaver, B. & Tarney, J. (1984), 'Empirical approach to estimating the composition of the continental crust', *Nature* **310**, 575–577.

Weiss, T., Seigesmund, S., Rabbel, W., Bohlen, T. & Pohl, M. (1999), 'Seismic velocities and anisotropy of the lower continental crust: a review', *Pure and applied geophysics* **156**, 97–122.

Wendt, A., Bayuk, I., Covey-Crump, S., Wirth, R. & Lloyd, G. (2003), 'An experimental and numerical study of the microstructural parameters contributing to the seismic anisotropy of rocks', *Journal of Geophysical Research* **108**, 2365.

Wenk, H. & Christie, J. (1991), 'Comments on the interpretation of deformation textures in rocks', *Journal of Structural Geology* **13**, 1091–1110.

Wernicke, B. (1981), 'Low-angle normal faults in the Basin and Range Province: nappe tectonics in an extending orogen', *Nature* **291**, 645–648.

Wernicke, B. (1985), 'Uniform-sense normal simple shear of the continental lithosphere', *Canadian Journal of Earth Science* **22**, 108–125.

Wessel, P. & Smith, W. (1998), 'New improved version of Generic Mapping Tools released', *EOS Transactions of the American Geophysical Union* **79**, 579.

Westaway, R. (1995), 'Crustal volume balance during the India-Eurasia collision and altitude of the Tibetan plateau: A working hypothesis', *Journal of Geophysical Research* **100**, 15173–15192.

Wheeler, J. (1984), 'A new plot to display the strain of ellitical markers', *Journal of Structural Geology* **6**, 417–423.

Wheeler, J. (1987), 'The determination of true shear senses from the deflection of passive markers in shear zones', *Journal of the Geological Society of London* **144**, 73–77.

Wheeler, J., Windley, B. & Davies, F. (1987), Internal evolution of the major Precambrian shear belt at Torridon, NW Scotland, *in* R. Park & J. Tarney, eds, 'Evolution of the Lewisian and Comparable Precambrian High Grade Terrains', Geological Society of London, Special Publication, 27, pp. 153–163.

White, N. (1990), Does the uniform stretching model work in the North Sea, *in* D. Blundell & A. Gibbs, eds, 'International Lithosphere Program, Tectonic Evolution of the North Sea Rifts, 181', Oxford University Press, pp. 217–239.

Willis, J. (1977), 'Bonds and self-consistent estimates for the overall properties of anisotropic composites', *Journal of the Mechanics and Physics of Solids* **25**, 185–202.

Winterstein, D. (1990), 'Velocity anisotropy terminology for geophysicists', *Geophysics* **55**, 1070–1088.

Yardley, B. (1986), 'Is there water in the deep continental crust?', *Nature* **323**, 111.

Zhang, P., Shen, Z., Wang, M., Gan, W., Bürgmann, R., Molnar, P., Wang, Q., Niu, Z., Sun, J., Wu, J., Hanrong, S. & Xinzhao, Y. (2004), 'Continuous deformation of the Tibetan Plateau from global positioning system data', *Geology* **32**, 809–812.

Zhao, W. & Morgan, W. (1985), 'Uplift of Tibetan Plateau', *Tectonics* **4**, 359–369.

Zhao, W. & Morgan, W. (1987), 'Injection of Indian crust into Tibetan lower crust: A two-dimensional finite element model study', *Tectonics* **6**, 489–504.

Zhao, W. & Yuen, D. (1987), 'Injection of Indian crust into Tibetan lower crust: A temperature-dependent viscous model', *Tectonics* **6**, 505–514.

Zhao, W., Mechie, J., Brown, L., Guo, J., Haines, S., Hearn, T., Klemperer, S., Ma, Y., Meissner, R., Nelson, K., Ni, J., Pananont, P., Rapine, R., Ross, A. & Saul, J. (2001), 'Crustal structure of central Tibet as derived from project INDEPTH wide-angle seismic data', *Geophysical Journal International* **145**, 486–498.

Zhao, W., Nelson, K. & Team, P. I. (1993), 'Deep seismic reflection evidence for continental underthrusting beneath southern Tibet', *Nature* **366**, 557–559.

Zheng, Q.-S. & Du, D.-X. (2001), 'An explicit and universally applicable estimate for the effective properties of multiphase composites which accounts for inclusion distribution', *Journal of the Mechanics and Physics of Solids* **49**, 2765–2788.

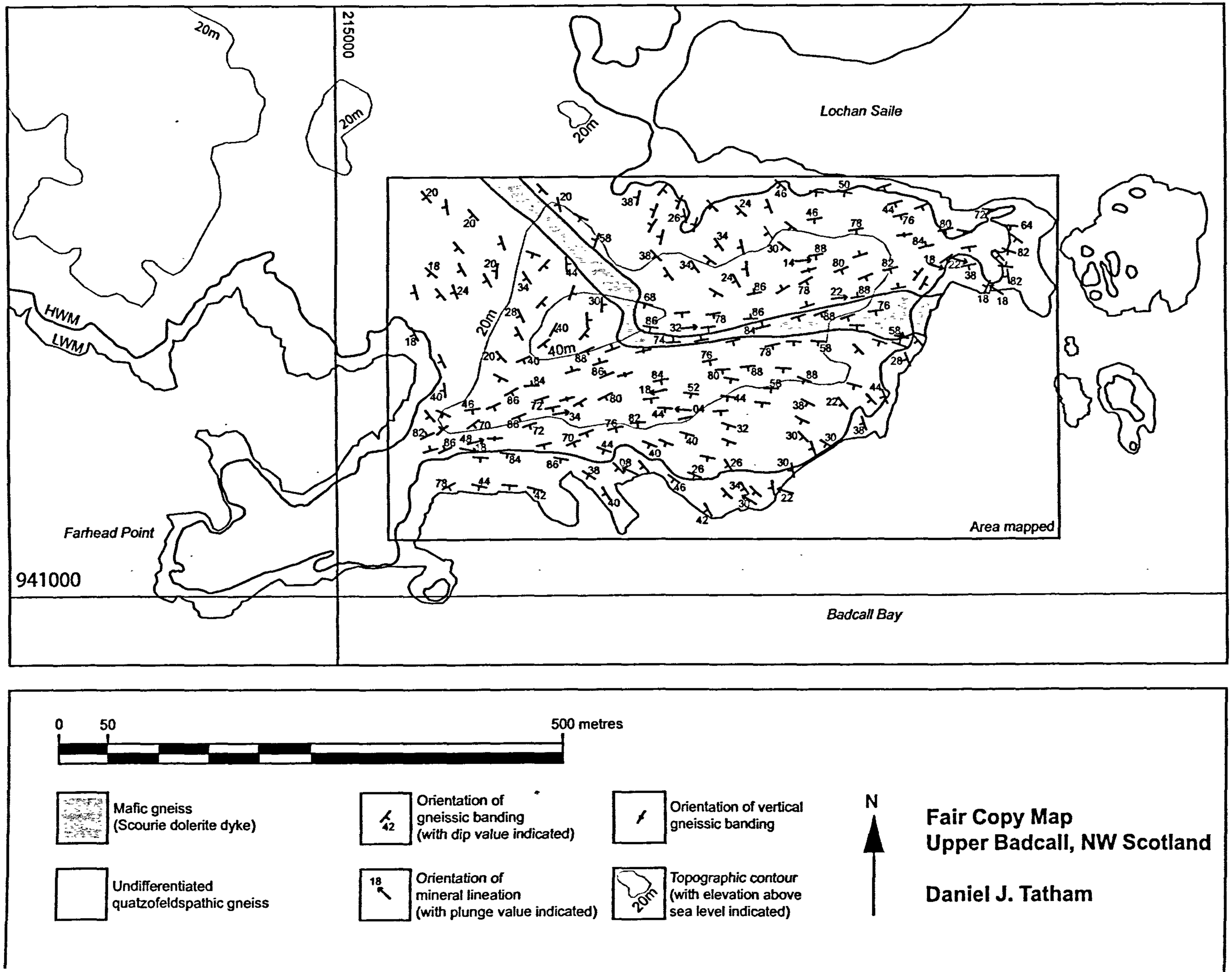

LEEDS UNIVERSITY LIBRARY

Inferences from shear zone geometry: an example from the Laxfordian shear zone at Upper Badcall, Lewisian Complex, NW Scotland

DANIEL J. TATHAM & MARTIN CASEY

Earth Sciences, School of Earth and Environment, Leeds University, Leeds LS2 9JT, UK
(e-mail: tatham@earth.leeds.ac.uk)

Abstract: This contribution presents a Laxfordian age shear zone near Upper Badcall, NW Scotland, as an example of using field data and theory to assess the kinematics and nature of deformation in a shear zone. The deformation zone includes quartzofeldspathic background gneiss and a dolerite dyke that cuts the gneissic banding at a high angle. A detailed field description of the deformation zone, which is critically discussed in terms of pure and simple shear, is presented. Analysis of gneissic banding and mineral lineation data, together with a consideration of the outcrop pattern, shows that the deformation zone is best described in terms of a simple shear zone with varying finite stretching direction. To analyse this deformation we introduce the concept of local plane strain. Although the deformation of the zone as a whole is 3D, at each point there is a direction in which it does not change its length. This direction is perpendicular to the local shear direction and so varies in orientation across the shear zone. In a reference frame defined at a point, the deformation can thus be understood in terms of conventional simple shear. Details of strain are hence determined according to this conclusion. A stereographic method for the determination of the reorientation of lines is used to calculate shear strain. The shear strain values across the shear zone are then used to restore the sheared dolerite dyke to its undeformed geometry. The success of the restoration provides supports for the strain calculation and also the conclusion of simple shear deformation.

To evaluate tests of kinematic inferences requires a field area that has undergone an extended period of successive phases of deformation separated by marker intrusions. This allows the worker to assess the nature of deformation through time in terms of its magnitude, orientation and coaxiality.

The Archaean to Proterozoic Lewisian gneiss complex of NW Scotland shows evidence of a protracted and complex history including multiple phases of deformation and intrusion (e.g. Sutton & Watson 1951). This makes it a particularly useful resource for identifying and studying the relative importance of deformation styles (pure or simple shear) in the mid- to lower crust. The Lewisian gneiss is broadly divided into the Scourian granulites (*c.* 2800 Ma, Chapman & Moorbath 1977; Hamilton *et al.* 1979) and the Laxfordian amphibolites (*c.* 1750 Ma, Moorbath *et al.* 1969; Kinny & Friend 1997), two tectonothermal events separated by a period of intrusion (2400–2000 Ma, Chapman 1979; Waters *et al.* 1990) of an approximately east–west- to NW–SE-trending suite of tabular and laterally extensive, dominantly dolerite dykes (Scourie dyke suite, Sutton & Watson 1951; Park & Tarney 1987). The Scourie dykes are locally undeformed and unaltered in the Scourian granulites and are then cut and deformed by discrete local- and regional-scale Laxfordian shear zones. The Laxfordian shear zone at Farhead Point near Upper Badcall, NW Scotland (Fig. 1), has been described by previous workers (e.g. Beach 1974) and is one that has been used to demonstrate the style or nature of shear in Laxfordian shear zones (Coward & Potts 1983) owing to interesting geometries of well-exposed deformed Scourie dykes. This contribution reassesses these early thoughts with the advantage of new and detailed field data collected by the authors. Field data analyses (including gneissic banding, lineations and outcrop geometry), together with tectonic movement directions measured from collected samples, are used in the discussion of the nature of deformation across the shear zone. The shear zone is then qualitatively and quantitatively described, based on this revised understanding of the shear.

The compatibility argument of Ramsay & Graham (1970) is reinforced with a mathematical proof of the allowable states of strain in a generalized deformation zone that permits a varying shear direction across the zone, presented in Appendix 2. Mathematical proof that the line of intersection of a plane and a generalized shear zone remains unchanged, whatever the orientation of the movement direction in the shear zone is also presented.

From: Ries, A. C., Butler, R. W. H. & Graham, R. H. (eds) 2007. *Deformation of the Continental Crust: The Legacy of Mike Coward.* Geological Society, London, Special Publications, **272**, 47–57.
0305-8719/07/$15 © The Geological Society of London 2007.

LEEDS UNIVERSITY LIBRARY

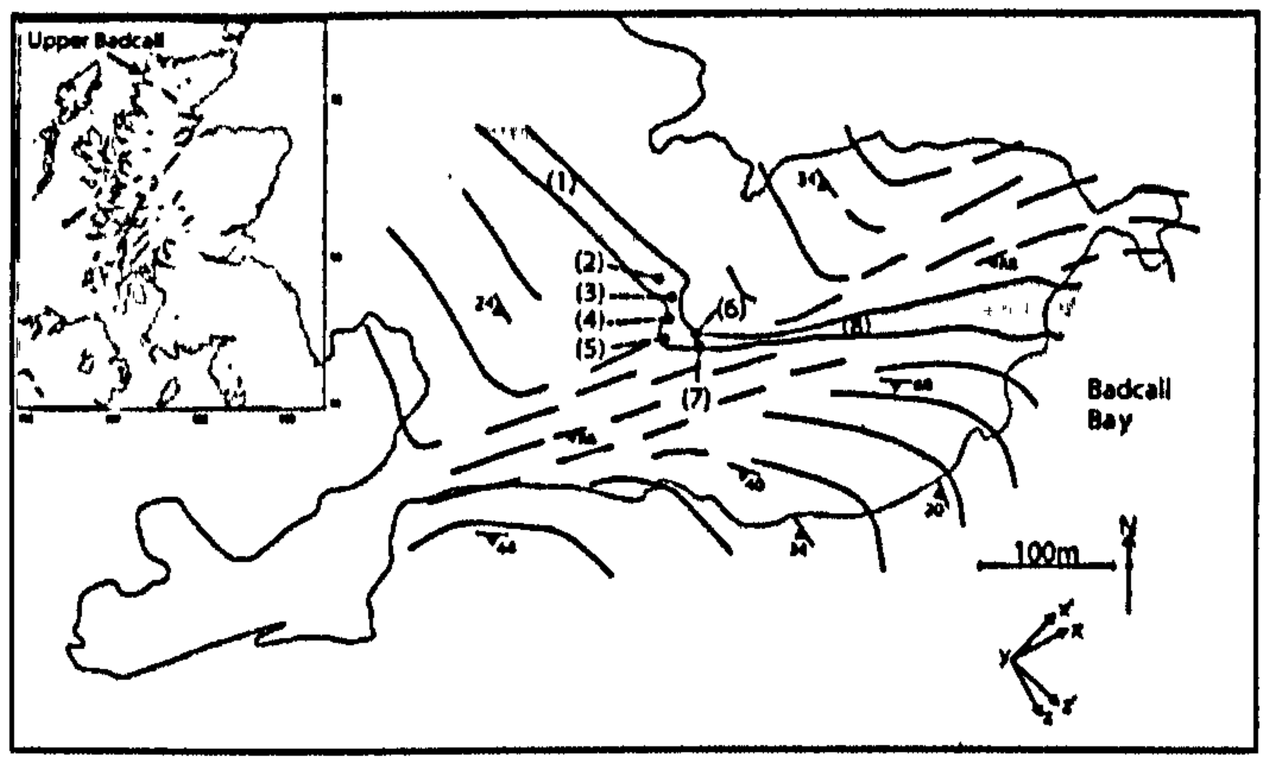

Fig. 1. Simplified structural map of Farhead Point, Upper Badcall, NW Scotland. The Scourie dyke and the orientation and formed surface gneissic banding are shown. Numbers in parentheses refer to sample locations. Both the shear zone (*xyz*) and undeformed dyke (*x'yz'*) reference frames are illustrated. This inset map of Scotland shows the location of Upper Badcall.

Field data

Gneissic banding

The poles to gneissic banding, plotted in Figure 2a, show a steady migration from the undeformed wall rock orientation at the southern coast of Farhead Point (e.g. 145/27W) to a zone of intense and subvertical fabric development (e.g. 075/84S) shown in Figure 1.

Mineral lineations

Figure 2c shows a plot of mineral lineations measured in the quartzofeldspathic gneiss between the central band of intense shear fabric development and the southern coast of Farhead Point (Fig. 1). Dyke lineations, defined by the shape fabric of plagioclase clots, are shown only for samples collected between the northern boundary of the shear zone and the band of intense shear fabric development (Fig. 2b). Poor exposure of the dyke towards the southern boundary of the shear zone prevented sample collection there.

It can be seen from Figure 2b and c that quartzofeldspathic gneiss and dyke mineral lineations can be broadly contained within a girdle that intuitively approximates the shear zone. This is most clearly developed in the dyke lineations (Fig. 2b), where the undeformed dyke material outside the shear zone is isotropic. Therefore, all mineral lineations plotted from within the dyke are the result of Laxfordian deformation. This is in contrast to mineral lineations from the quartzofeldspathic gneiss country rock, where a pre-existing mineral lineation is observed outside the shear zone; a remnant from some earlier tectonothermal event. Mineral lineations caused by the shear zone strain within the quartzofeldspathic gneiss may have some memory of an earlier orientation and progressively rotate to the orientation of the new deformation field. Hence, these data have significantly more scatter, especially away from the band of highest shear fabric development. Most of the west-plunging lineations in the gneiss refer to locations south of the zone of intense shear fabric development, including pre-existing linear fabrics and the early stages of those rotating into the shear zone orientation. East-dipping plunges mark mineral lineations from within the zone of intense fabric development, although there is scant correlation between the plunge of east-dipping lineations and the location of those data transversely across the zone. In contrast, dyke mineral lineations migrate from a subvertical plunge near the northern boundary of the shear zone to a subhorizontal plunge in the zone of intense fabric development.

Outcrop geometry

The NW–SE-trending steeply dipping dyke intersects the northern boundary of the shear zone at a high angle (Fig. 1). From this point southwards, the dyke is deflected left-laterally through the high-strain zone, in which it is offset by *c.* 190 m, before returning to an undeformed state at its most southeastern outcrop in Badcall Bay. The 'kink' in the deflection of the dyke at

LEEDS UNIVERSITY LIBRARY

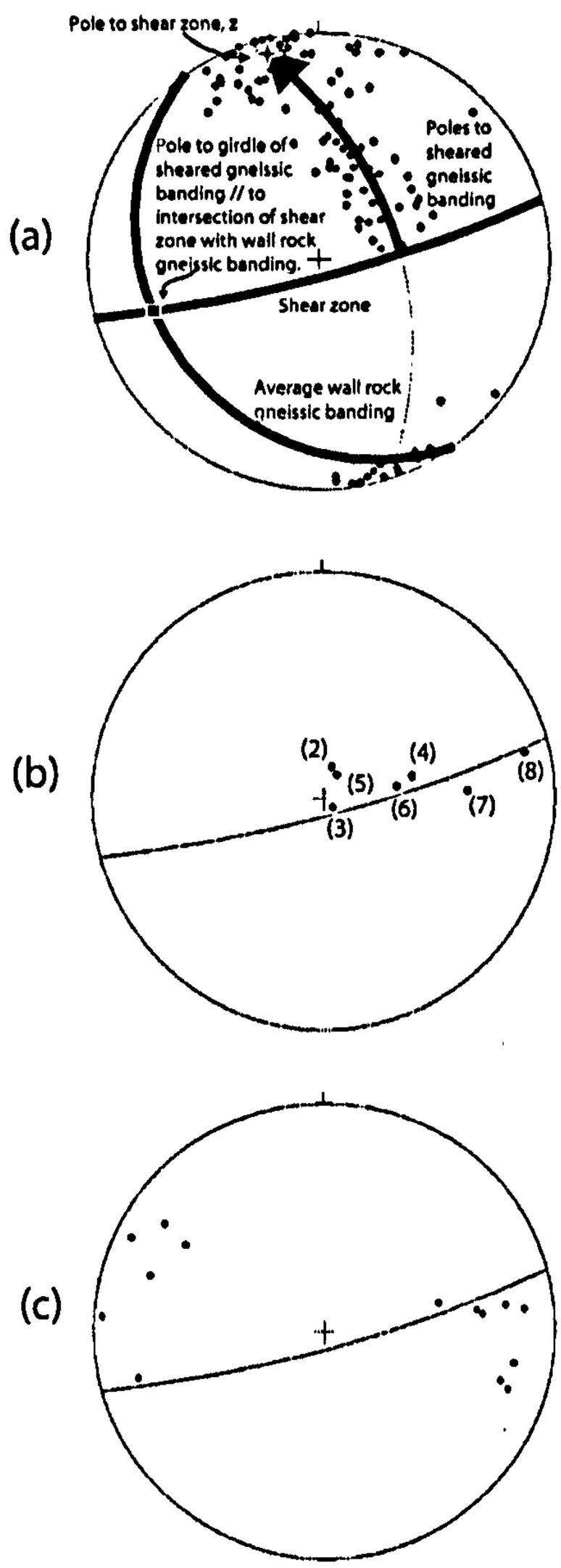

Fig. 2. Gneissic banding and lineation data. (a) Stereogram illustrating the parallelism of the point of intersection between the average shear zone orientation and the average wall rock gneissic banding orientation, and the pole to the girdle of sheared gneissic banding. This is used to indicate deformation under simple shear. The trace of the arrow indicates the migration of poles to gneissic banding with increasing deformation. (b) Lineations in the Scourie dyke. Numerical annotations refer to the sample number from which they were derived. Sample 1 is not included because of its undeformed state and therefore lack of tectonic lineation. (c) Lineations in the quartzofeldspathic gneiss.

the northern boundary of the shear zone should be noted. This is a real feature and not an artefact of topographic interference.

Discussion of field data

Although the heterogeneous strain field of a shear zone undisputedly is the result of mechanical effects, the reorientation of linear and planar features in shear zones can be studied as a consequence of the heterogeneous deformation field alone. Thus the distinction of the active or passive nature of linear or planar fabric elements is not relevant. The left-lateral sense of shear, inferred from the deflection of the dyke, is supported by the apparent deflection of gneissic banding as shown in Figure 1. According to the method of determining true shear sense from the deflection of passive markers, described by Wheeler (1987), this inference of left-lateral shear from the gneissic fabric is a correct one.

According to Ramsay (1967), hinge lines and fold axes in a simple shear zone are always parallel to the line of intersection of the shear plane with the surface being folded. Hence, the line of intersection between the undeformed gneissic banding in the wall rock and the simple shear zone itself should remain constant in spatial orientation during deformation. As shown in Figure 2a, the pole to the girdle containing poles to gneissic banding lies parallel to the line of intersection between the undeformed gneissic banding orientation and the shear zone. It should be noted also that during simple shear, poles to marker planes are deformed along a great circle that contains the pole to the shear plane (z), and they eventually approach that pole, as illustrated in Figure 2a. The field data thus support both of these tests for simple shear.

It has been shown that the behaviour of linear fabrics, such as mineral lineations, can be used to infer the kinematics of deformation prevalent in a shear zone. Wheeler (1987) suggested that passive linear markers, when deformed under simple shear, deform along great circles that contain the movement direction and ultimately approach a trend parallel to that direction. Figure 2b and c shows that to some degree of accuracy this rule can be upheld. Scatter in the data may be due to a number of factors. For example, the varying mineral lineation directions from the dyke, within a fixed foliation orientation, suggest that the tectonic movement direction across the shear zone is not constant. Undeformed dyke material in the wall rock is isotropic and shows no fabric development; however, dyke mineral lineations migrate from subvertical at the northern boundary of the shear zone to subhorizontal in

LEEDS UNIVERSITY LIBRARY

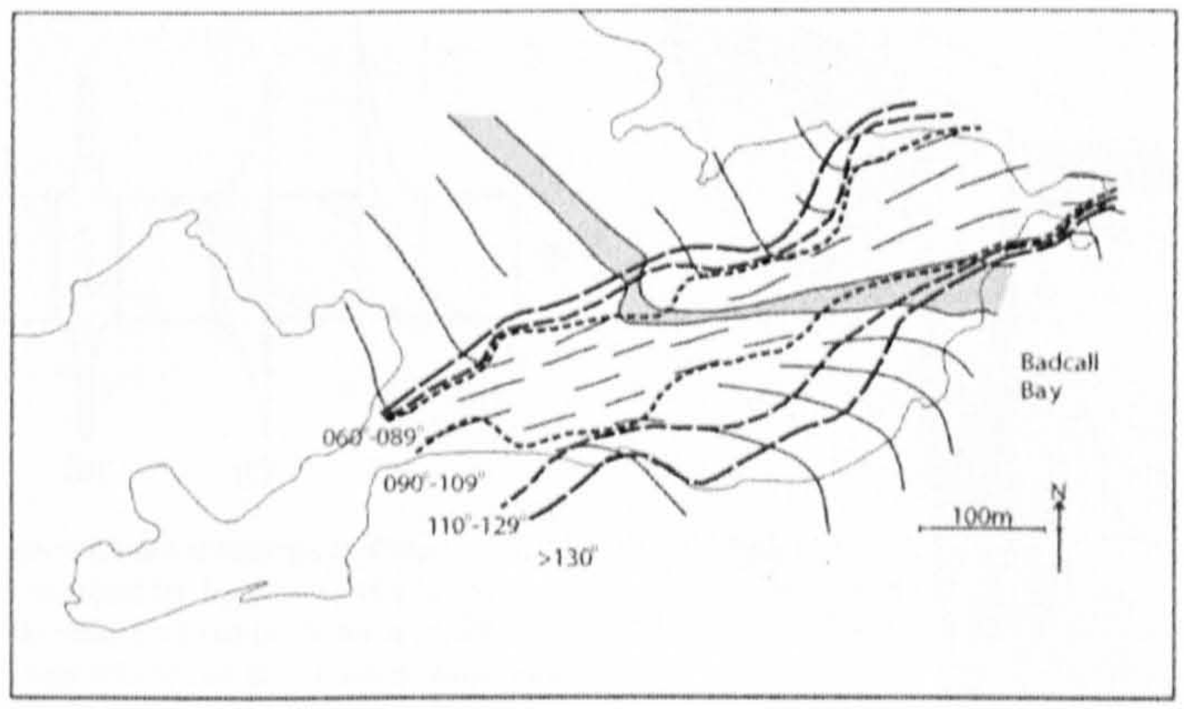

Fig. 3. Isogons of strike of gneissic banding. Isogons are parallel and laterally continuous.

the zone of intense shear fabric development. This may indicate either spatial partitioning of the strain field or temporal variations in the movement direction and magnitude of strain.

Parallelism of gneissic banding strike isogons (as measured in the field) supports the quality of the approximation of a concentrated zone deforming by simple shear (Fig. 3). This satisfies the condition that deformation is constant at each successive level transversely across the dyke, normal to the shear zone boundary.

The inference of a variable tectonic movement direction is supported by the apparently antithetic 'kink' in the deflection of the dyke at the northern boundary of the shear zone. This can be explained by a number of mechanisms. The most simple explanation is that the entire shear zone is deforming under simple shear with the tectonic movement direction spatially partitioned or temporal variation in the strain field transversely across the shear zone. The exact 3D orientation of the undeformed dyke could not be measured, although it was clear that it dipped steeply to the NE. The dyke could hence develop this kinked geometry at its northern margin under the condition that it dipped more shallowly than the mineral lineations or movement directions in, for example, Sample 5. This concept is shown schematically in Figure 4. It should be noted that the anomalously shallower plunge of Sample 4 (Fig. 2b) amongst the steep plunges of Samples 3 and 5 close to its location in the shear zone (Fig. 1) suggests that the sample may not be representative.

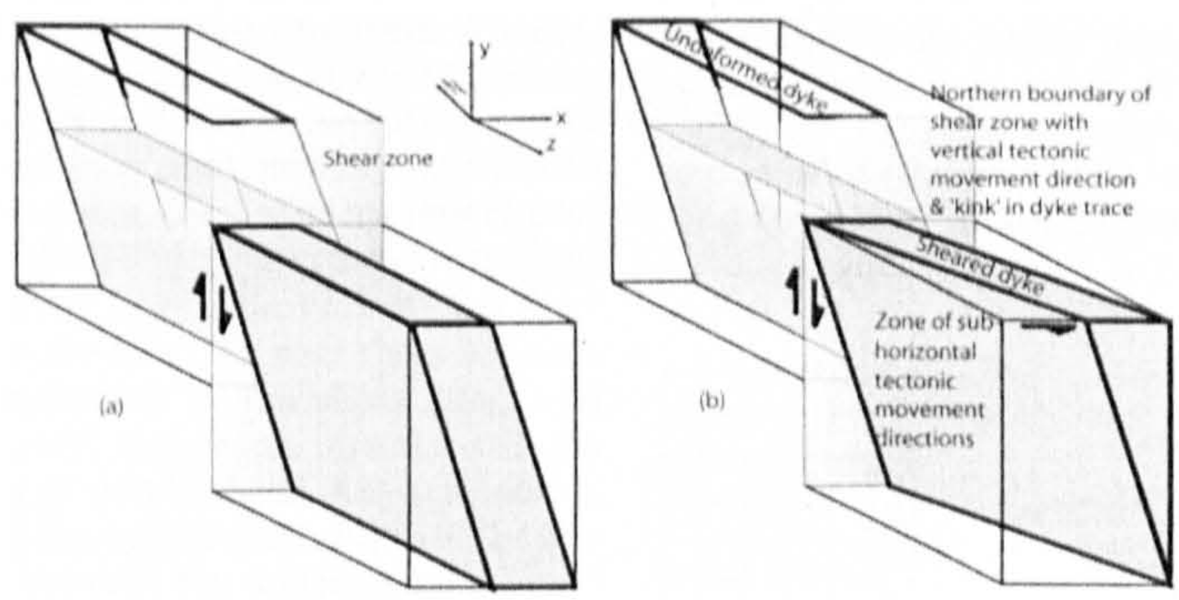

Fig. 4. (**a**) A diagram to illustrate how a steeply dipping dyke can be sheared to generate a kink in its outcrop trace. A vertical shear zone with a vertical shear direction can create an apparently right-lateral outcrop trace. (**b**) Model for the shear zone at Upper Badcall. Vertical shear on a vertical shear zone at the northern boundary of the shear zone provides the subvertical linear fabric and kink in the dyke trace observed. Simple shear with a horizontal displacement vector in the southern block gives a left-lateral offset geometry of the dyke and subhorizontal linear fabric.

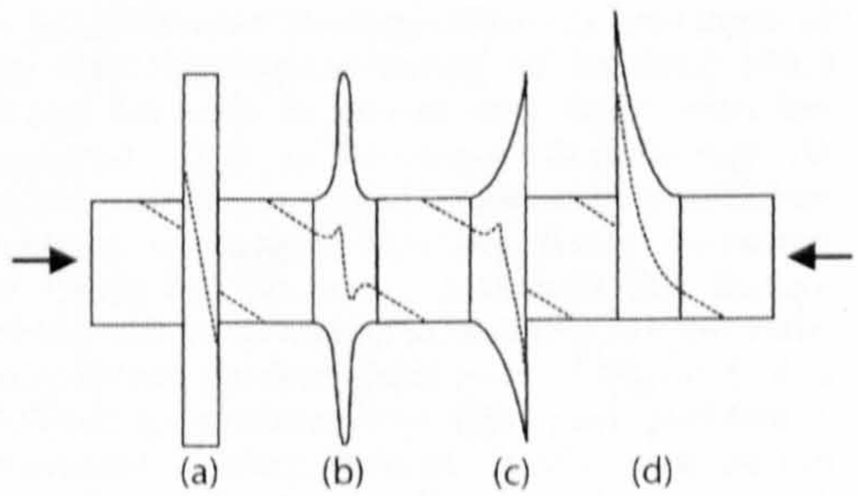

Fig. 5. Expected geometries under pure shear deformation as described by Escher *et al.* (1975). Geometries (**a**)–(**d**) refer to situations with different boundary conditions where the shear zone–wall rock interface switches between no slip and free slip.

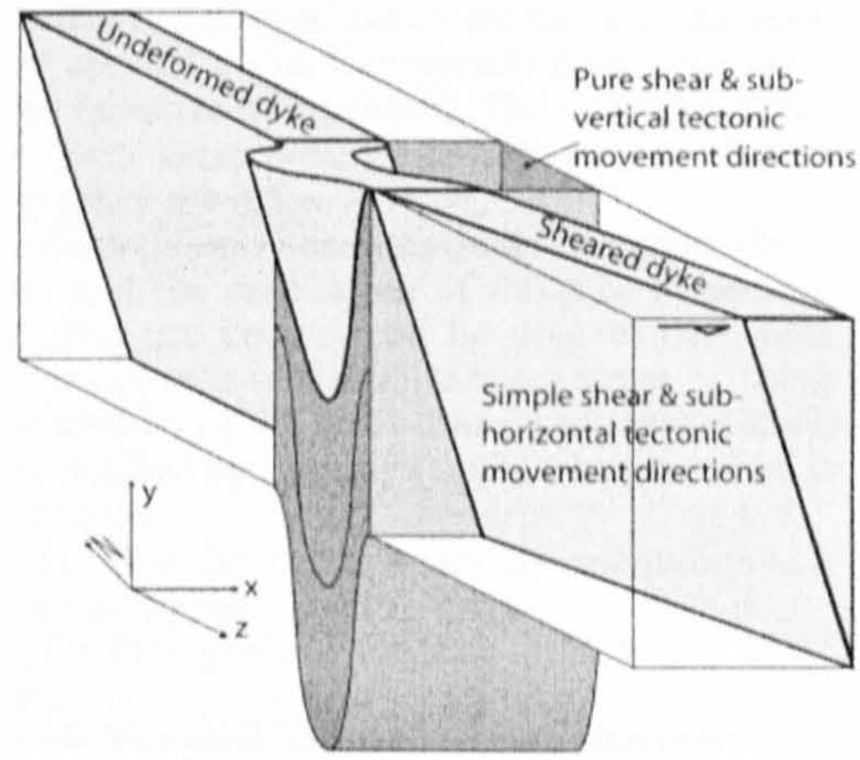

Fig. 6. An alternative hypothesis of deformation in the dyke including pure shear near the northern boundary of the shear zone.

It could be suggested that the dyke outcrop geometry developed under pure shear. Escher *et al.* (1975) depicted a selection of outcrop geometries that can prevail when a unit of rock, cross-cut by a subvertical marker, is deformed by a pure shear zone, each with different boundary conditions (Fig. 5). Upon initial inspection there is an almost convincing similarity between the unusual geometry, mapped at the northern boundary of the shear zone at Upper Badcall, and the patterns depicted in Figure 5b and c. However, there are a number of factors that invalidate this theory. The variation in lineation directions across the shear zone from subhorizontal to subvertical suggests that a single pure shear plane strain field does not exist. To generate the observed map-view outcrop pattern from the spatially consistent pure shear strain field indicated in Figure 5b and c, all mineral lineations would have to plunge horizontally; a condition that is clearly not observed. Alternatively, to a first approximation, the field outcrop and mineral lineation data can be satisfied with a model of combined and spatially partitioned pure and simple shear (Fig. 6). This model provides the subvertical finite movement directions and the apparently antithetic kink in the dyke outcrop trace in the block of pure shear towards the northern boundary of the shear zone, and subhorizontal finite movement directions in the southern region of simple shear. Any pure shear, however, would change the orientation of the line of intersection between the undeformed gneissic banding in the wall rock and the shear zone. This is not observed (Fig. 2a), and hence suggests that pure shear deformation, in any orientation, does not occur in this shear zone.

Furthermore, pure shear necessitates that the displacement and strain in the shear zone varies along its length. That is, about some centre point of the shear zone, strain and displacement increase cumulatively longitudinally outwards. Figure 7 illustrates transverse material lines deforming in a pure shear zone. This prediction is not supported by field observations. In addition, Figure 5b and Figure 5c suggest respectively, an equivalent and opposite kink in the outcrop geometry or a discrete discontinuity on the southern boundary of the shear zone. Again, these are not observed.

The problem of strain compatibility and increasing differential shear parallel to the shear zone highlights a further problem in pure shear deformation, one of space. A shear zone of finite length must show evidence for the extrusion of the 'filling' at its lateral terminations if it is to be modelled by pure shear. The main high-strain segment of the shear at Upper Badcall is considered to be of relatively finite length parallel to the zone boundary, although Beach (1974), Barber

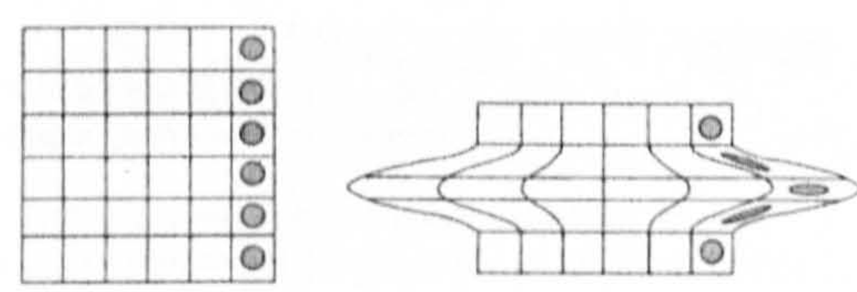

Fig. 7. Material lines deforming in a pure shear zone. The cumulative increase in displacement parallel to the shear zone walls outward from the centre-point of the deformation zone should be noted. Modified from Ramsay & Huber (1987).

et al. (1978) and the original survey field maps of the area (Geological Survey of Scotland 1892) linked the zone to one or two shears with less apparent offset to the east of Badcall Bay. At neither end of the mapped zone is there sufficient evidence to suggest that this lateral extrusion of filling has occurred. Although this feature would not be observed in outcrop for the vertically extruding pure shear zone of Figure 6, it is difficult to conceive how this space problem is overcome at deep tectonic levels, such as the amphibolite-facies conditions of Laxfordian deformation, without the presence of a free surface such as the Earth's surface (Escher *et al.* 1975).

These limitations support the inference that pure shear deformation is not prevalent in the deformation zone at Upper Badcall, which is best approximated as a simple shear zone with a transversely varying tectonic movement direction.

Shear zone with varying finite stretching direction

Ramsay & Graham (1970) demonstrated that a band of high deformation between wall rocks with no deformation can only have a heterogeneous simple shear or heterogeneous uniaxial volume change. It is simple to show with a deck of cards that this can be generalized to combinations of spatially partitioned simple shear in orthogonal directions (e.g. Treagus & Lisle 1997). Further, the finite displacement direction of the shear may vary across the shear zone. A mathematical proof of this is given in Appendix 2. The card deck thought-experiment also shows clearly that there is no deformation in the shear plane, so that the orientation of any line in this plane does not change (see also Appendix 2). An example of such a direction relevant to the current analysis is the intersection line of the gneissic banding and the plane of the shear zone. The constant orientation of this line means that it is a generator of the folded surface of gneissic banding across the shear zone and is the explanation of the observation that the poles to gneissic banding (Fig. 2a) lie on a great circle, normal to this direction.

Any general pure shear strain in the high-strain band would change the orientation of the intersection lineation and the pole to banding would no longer lie on a great circle.

Determining shear strain

A coordinate system is established with the x-axis parallel to the strike of the average orientation of the shear zone (positive to the east), y-axis positive up, and z-axis transversely across the shear zone (positive to the south). The origin lies at the northern shear zone boundary, on the western margin of the dyke.

Data points, where the finite stretching direction and the orientation of the pole to gneissic banding are known, can be used to determine the magnitude of the finite shear strain, γ, using the method of the reorientation of marker lines, as described by Ramsay (1967). The procedure is as follows:

(1) Plot shear zone boundary orientation as a plane and pole.

(2) Plot gneissic banding outside the shear zone.

(3) For each lineation (shear) direction:

(a) plot the direction;

(b) plot the great circle containing shear direction and shear zone pole;

(c) plot the gneissic banding inside the shear zone for this level;

(d) read off α and α' as the intersections of the gneissic banding and the plane constructed in (b) (see Ramsay 1967, fig. 3.23 for definition).

(e) Calculate γ.

An example is shown in Figure 8 and the results are shown in Table 1. The equation (from Ramsay 1967, equation (3–71), p. 88) is

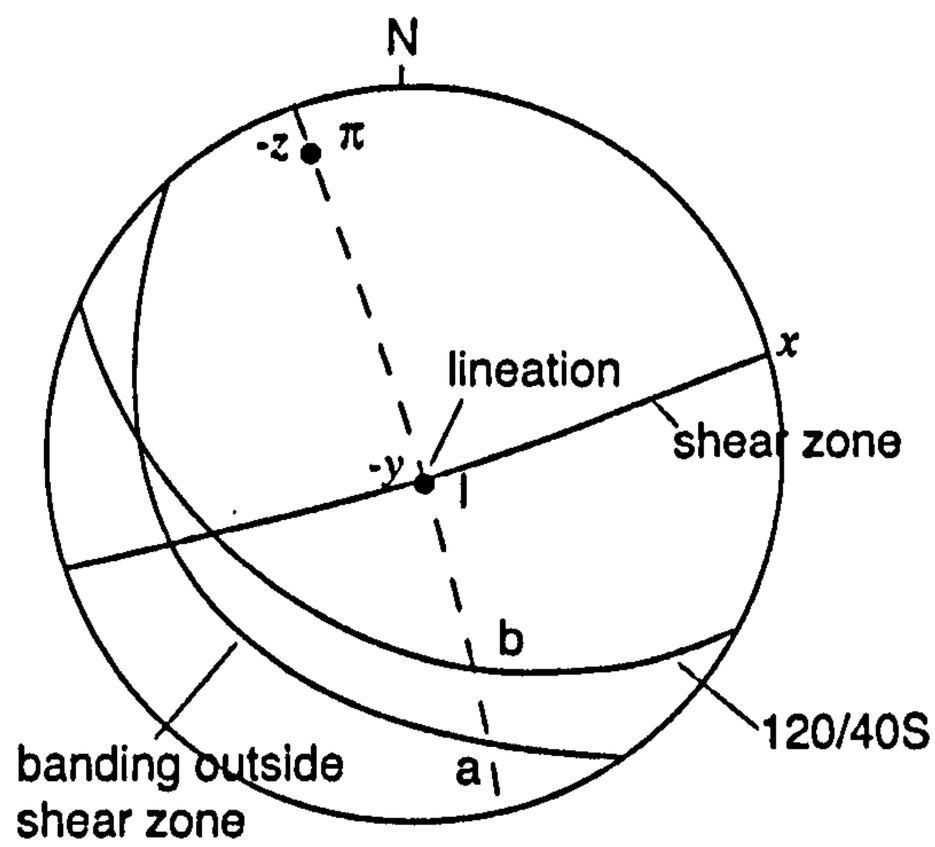

Fig. 8. Example of the stereonet determination of α and α'. Angle a–l measured in the great circle is α and angle b–l is α'. Also marked on the plot are the coordinate directions x and y. The angle x–l is θ, in this case negative because on this lower hemisphere plot the lineation is pointing downwards and $+\theta$ is defined as the anticlockwise angle from positive x to the lineation.

Table 1. *Kinematic data from points distributed across a transect transversely from north to south over the Laxfordian shear zone at Upper Badcall*

Lineation (azimuth/plunge and corresponding sample number)	Gneissic banding (dip/strike)	α (deg)	α' (deg)	γ	θ (deg)	Δz (m)	Cumulative displacement in x (m, W to E)	Cumulative displacement in y (m, vertically downwards)
135/86 (3)	120/40S	73	54	0.42	−88	23.75	0.3	10.0
080/64 (6)	100/86S	74	9	6.03	−64.1	16.25	43.1	98.1
087/38 (7)	082/84S	76	5	11.18	−39.2	11.25	140.6	177.6
087/38 (7)	078/90	76	0	15.0	−39.2	15	315.0	319.8
077/12 (8)	078/76S	65	4	13.83	−12.1	25	653.1	392.3
077/12 (8)	098/52S	65	28	1.41	−12.1	20	680.8	398.2
077/12 (8)	098/44S	65	30	1.27	−12.1	21.25	707.1	403.9
077/12 (8)	108/32S	65	38	0.81	−12.1	22.5	725.0	407.7
077/12 (8)	110/32S	65	40	0.73	−12.1	20	739.2	410.8

Each data line refers to a location transversely across the shear zone. Table lines include lineation data taken from the dyke sample closest to the shear fabric measured in the quartzofeldspathic gneiss country rock at that location, α, α', γ, Δz, and the resolved cumulative displacements in x and y. The average orientation of the gneissic banding outside the shear zone is 145/27W and the average orientation of the shear zone is 075/84SW.

$$\gamma = \cot \alpha' - \cot \alpha. \quad (1)$$

The x and y components of γ can be calculated from

$$\gamma_x = \gamma \cos \theta \quad (2)$$

$$\gamma_x = \gamma \cos \theta \quad (3)$$

where θ is the angle from positive x to the lineation measured in the x,y plane (Figure 8).

A series of points, each including a measurement of gneissic banding and an associated lineation direction related to a sample point, were taken across a transverse section of the shear zone. At each of these points γ_x and γ_y were determined according to equations (1)–(3) and considered constant across a finite width of the shear zone. The relative displacements (ΔU_x, ΔU_y) across each segment of shear zone (Δz) are calculated from

$$\Delta U_x = \gamma_x \Delta z \quad (4)$$

$$\Delta U_y = \gamma_y \Delta z. \quad (5)$$

The cumulative displacements are then obtained by summing the contributions of each segment across the shear zone from north to south (Table 1).

Restoration of the dyke

To test the method of determining shear strain, sheared dyke coordinates as seen in outcrop are restored to their pre-deformation geometry. This procedure has two purposes. First, it tests the method of γ and offset calculation via simple observation of continuity with the unsheared wall rock dyke and the restored dyke coordinates. Second, it estimates the orientation of the undeformed dyke where direct field measurements were unreliable.

Coordinates of points selected along the dyke within the shear zone were restored by removing the cumulative displacement, as calculated above, from the coordinate values at the point under consideration. In general, points moved to the west and upwards on restoration. The cumulative displacements across the shear zone totalled 739.2 m left-lateral in x and 410.8 m north-side upwards in y (Table 1). To determine the geometry of the undeformed dyke the restored coordinates were viewed in a new reference frame with the x'-axis perpendicular to the trace of the undeformed dyke outside the shear zone, the z'-axis parallel to the strike of the undeformed dyke, and y-axis up. Coordinate points were found by simple trigonometry:

$$x' = x \cos \phi + z \sin \phi \quad (6)$$

where ϕ is the angle of rotation of the x- and z-axes about the y-axis between the old (shear zone, xyz) and the new (undeformed dyke, $x'yz'$) reference frames. Restored coordinates projected onto the undeformed dyke profile plane ($x'y$) suggest a dip of *c.* 56° to the NE for the undeformed dyke outside of the shear zone (see Fig. 9). This value compares well with field data

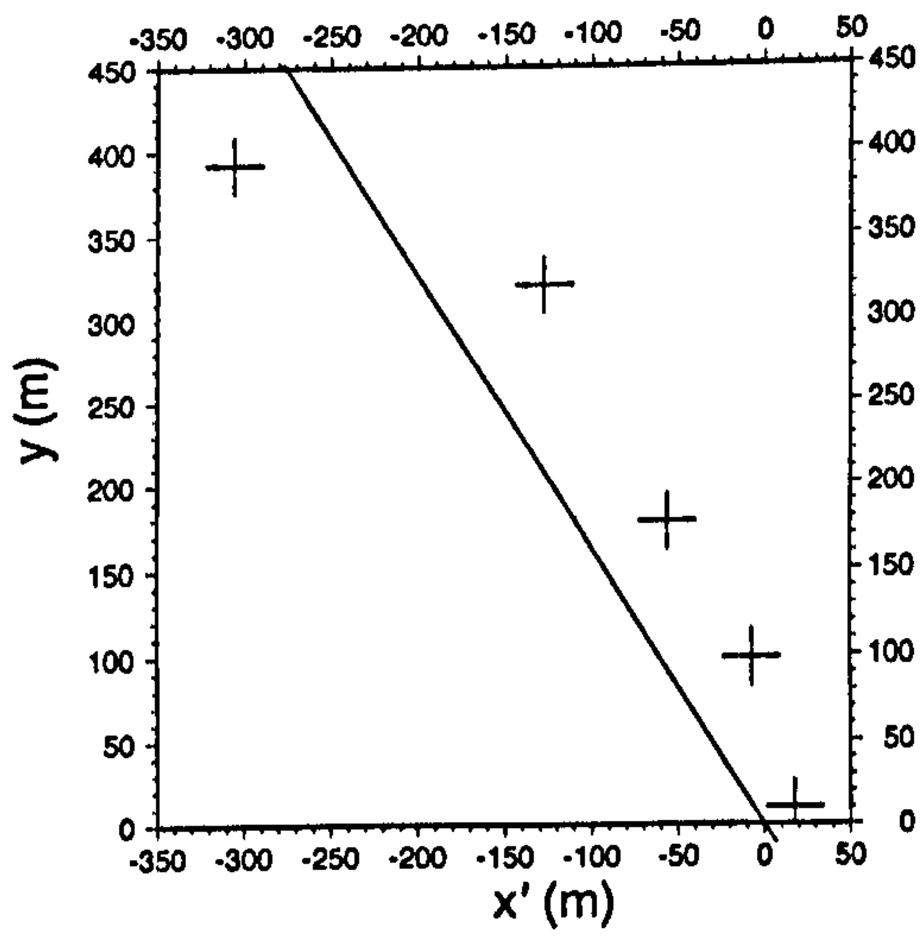

Fig. 9. Restored points on the west margin of the dyke in the section containing its dip direction. The coordinate x' is horizontal and trending perpendicular to the trace of the dyke (increasing to 044). The coordinate y is vertical, increasing upwards. The symbols are restored coordinates of points on the dyke, and the line is the best fit to these points.

of the undeformed dyke orientation, although sparse. The best-fit line of Figure 9 represents the trace of the planar dyke in the section plane that has the strike direction of the undeformed dyke as its pole. The minor deviations of the points from the lines shows that the hypothesis of simple shear with a varying shear direction is reasonable, considering the irregularity of the shear zone (see Figs 2a and 3). Furthermore, it gives support to inferences made above on the origin of the kink in the trace of the dyke, near the northern boundary of the shear zone.

Discussion and conclusions

The model of simple shear with a varying shear direction within a constant shear plane is capable of explaining the complex geometry and field data of the Badcall shear zone without recourse to varying amounts of heterogeneous pure shear. In particular, the apparently antithetic kink or fold in the dyke near the northern margin of the shear zone is seen to be an artefact of the interaction of subvertical movement direction of the shear zone in that region, as recorded in the finite stretching lineation, and the shallower dip of the dyke. Although a model of spatially partitioned pure and simple shear across the shear zone can superficially explain the observed field data and outcrop geometries, further thought regarding the geometry of pure shear and interactions of planar fabrics shows that this scenario is not possible here.

Hence, the kinematics of the Laxfordian shear zone at Upper Badcall, NW Scotland, is best modelled as a zone of local plane strain simple shear through which the finite movement direction varies from subhorizontal near its southern boundary to subvertical near its northern boundary. The temporal variation in the magnitude and direction of strain is not clear and may present an issue for future study.

The cumulative displacements across the shear zone can be compared with those calculated by Beach (1974). Parallel to x (left-lateral) and y (north-side up), respectively, the displacements of 739.2 m and 410.8 m, calculated here, are noticeably larger than the values of 250 m and 91 m, calculated by Beach (1974), in a simple geometrical problem based on a single movement direction within the shear zone, the orientation of the shear zone and a marker, and the horizontal offset of that marker. Clearly, and as discussed by Beach (1974), significant errors are introduced where shear zones have a varying movement direction.

In its simplest sense, this study supports decades of research in the Lewisian complex (e.g. Beach *et al.* 1974; Coward 1990), which suggests that the Laxfordian deformation in some part proceeded by north-block up and left-lateral shear deformation. To place this research in the wider context of regional Laxfordian deformation, a full description and re-evaluation of the tectonics and kinematics of the tectonothermal event would be necessary. Moreover, it would undoubtedly require significant fieldwork to interpret the plethora of Laxfordian shears in the Lewisian complex in accordance with the routine outlined here. This is beyond the scope of this paper, although is a very interesting project for future research.

The work was supported by NERC PhD Studentship NER/S/A/2002/10477. The authors thank J. Balfour and Scottish Natural Heritage for sample collection licence. J. Wheeler and J. Watkinson are thanked for their helpful manuscript reviews. Further details including field data or calculations included herein can be obtained from the corresponding author.

Appendix 1: Sample numbers

Scourie Dyke samples 1–8 described herein refer to the following University of Leeds, School of Earth Sciences sample catalogue numbers.

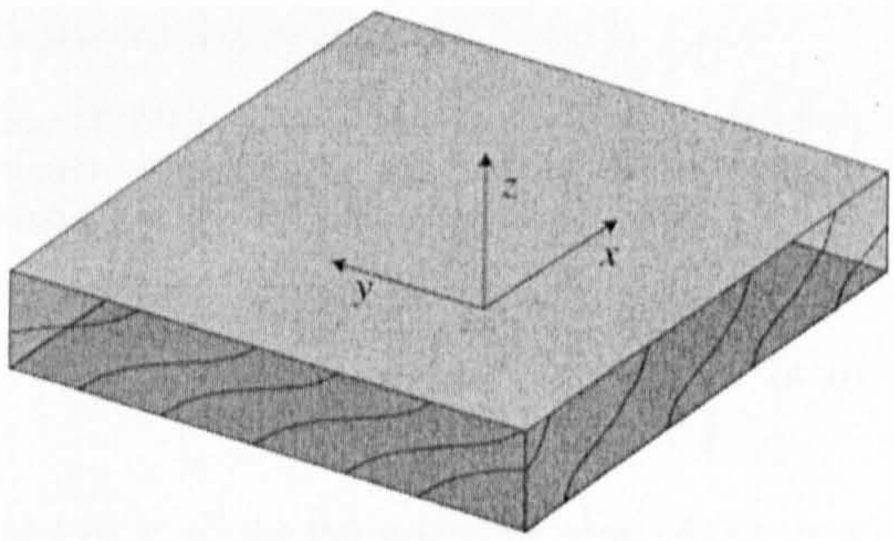

Fig. A1. General shear zone with varying strain profiles in x and y. The state of deformation is identical at points an equal height above the base of the shear zone in both the x and y directions.

1: 62485
2: 62483
3: 62484
4: 62482
5: 62481
6: 62480
7: 62479
8: 62478

Appendix 2: General shear zone

A generalized 3D shear zone is shown in Figure A1. The state of deformation is constant in x and y, but varies with position in z.

The deformation from the undeformed state to the deformed state can be defined by three functions of position giving the x, y and z components of the finite displacement, u, v, w, to the position after deformation:

$$u = u(x, y, z) \tag{A1}$$

$$v = v(x, y, z) \tag{A2}$$

$$w = w(x, y, z). \tag{A3}$$

The strains and rotations can be derived from the gradients of the displacement with respect to x, y and z, the displacement gradient matrix:

$$\begin{pmatrix} \frac{\partial u}{\partial x} & \frac{\partial u}{\partial y} & \frac{\partial u}{\partial z} \\ \frac{\partial v}{\partial x} & \frac{\partial v}{\partial y} & \frac{\partial v}{\partial z} \\ \frac{\partial w}{\partial x} & \frac{\partial w}{\partial y} & \frac{\partial w}{\partial z} \end{pmatrix}. \tag{A4}$$

Taking the term $\partial u/\partial z$ and differentiating with respect to x gives a result that can be set equal to zero because there is no variation of strain state in the x direction:

$$\frac{\partial^2 u}{\partial x \partial z} = 0. \tag{A5}$$

The order of partial differentiation does not influence the result:

$$\frac{\partial^2 u}{\partial z \partial x} = 0 \tag{A6}$$

which means that $\partial u/\partial x$ does not vary in z; that is, it is constant across the shear zone. The same argument can be applied to the terms $\partial v/\partial z$ and $\partial w/\partial z$ to show that $\partial v/\partial x$ and $\partial w/\partial x$ are constant across the shear zone. Repeating the procedure for differentiation of the terms in the third column of the displacement gradient matrix with respect to y shows that $\partial u/\partial y$, $\partial v/\partial y$ and $\partial w/\partial y$ are also constant across the shear zone, so the displacement gradient matrix becomes

$$\begin{pmatrix} c_1 & c_4 & \frac{\partial u}{\partial z} \\ c_2 & c_5 & \frac{\partial v}{\partial z} \\ c_3 & c_6 & \frac{\partial w}{\partial z} \end{pmatrix}. \tag{A7}$$

There is no condition that can be applied to the terms in the third column, so these can be functions of z, but not of x and y because of the constancy of deformation state in these directions. Further identifying that $\partial u/\partial z$ is the shear strain in x, γ_x, $\partial v/\partial z$ is the shear strain in y, γ_y, and $\partial w/\partial z$ is a uniaxial volume change in the z direction, Δ, the displacement gradient matrix becomes

$$\begin{pmatrix} c_1 & c_4 & \gamma_x(z) \\ c_2 & c_5 & \gamma_y(z) \\ c_3 & c_6 & \Delta(z) \end{pmatrix}. \tag{A8}$$

Thus the state of strain in a general shear zone can be variable shear in the x and y directions varying across the zone and a volume change, achieved by uniaxial shortening in the z direction also varying in z. No other state of strain is possible except that homogeneous strain can be added by matrix multiplication. The constant terms in equation (A4) can be subsumed into this homogeneous strain leaving zeros and the deformation gradient matrix can be formed by adding one to the diagonal terms.

$$\begin{pmatrix} 1 & 0 & \gamma_x(z) \\ 0 & 1 & \gamma_y(z) \\ 0 & 0 & 1+\Delta(z) \end{pmatrix}. \tag{A9}$$

Treagus & Lisle (1997) considered this kind of shear zone and demonstrated that there are no continuous principal planes of finite strain, but it is still possible to see continuous planes on the local scale.

Reorientation of planes

Flinn (1979) gave the following equation for the reorientation of normals to planes under the deformation described by the deformation gradient matrix:

$$\left(n_x' \; n_y' \; n_z'\right) = \left(n_x \; n_y \; n_z\right)\begin{pmatrix} D_{11}^{-1} & D_{12}^{-1} & D_{13}^{-1} \\ D_{21}^{-1} & D_{22}^{-1} & D_{23}^{-1} \\ D_{31}^{-1} & D_{32}^{-1} & D_{33}^{-1} \end{pmatrix} \quad \text{(A10)}$$

where $(n_x' \; n_y' \; n_z')$ are the direction cosines of the plane normal in the deformed state, $(n_x \; n_y \; n_z)$ are the direction cosines of the plane normal in the undeformed state and the matrix in D_{ij}^{-1} is the inverse of the deformation gradient matrix.

For a constant-volume shear zone the deformation gradient matrix is

$$\begin{pmatrix} 1 & 0 & \gamma_x(z) \\ 0 & 1 & \gamma_y(z) \\ 0 & 0 & 1 \end{pmatrix} \quad \text{(A11)}$$

which has the inverse

$$\begin{pmatrix} 1 & 0 & -\gamma_x(z) \\ 0 & 1 & -\gamma_y(z) \\ 0 & 0 & 1 \end{pmatrix}. \quad \text{(A12)}$$

Thus, equation (A6) becomes

$$\left(n_x' \; n_y' \; n_z'\right) = \left(n_x \; n_y \; n_z\right)\begin{pmatrix} 1 & 0 & -\gamma_x(z) \\ 0 & 1 & -\gamma_y(z) \\ 0 & 0 & 1 \end{pmatrix} \quad \text{(A13)}$$

or

$$(n_x' \; n_y' \; n_z') = [n_x \; n_y \; (-n_x\gamma_x - n_y\gamma_y + n_z)]. \quad \text{(A14)}$$

At any point in the shear zone the movement direction will be oriented at an angle θ to the x axis. If the amount of finite shear strain is given the symbol γ, components of shear in the x and y directions will be

$$\gamma_x = \gamma \cos\theta \quad \text{(A15)}$$

$$\gamma_y = \gamma \sin\theta. \quad \text{(A16)}$$

Hence we may write

$$(n_x' \; n_y' \; n_z') = [n_x \; n_y \; n_z - \gamma(n_x \cos\theta + n_y \sin\theta)]. \quad \text{(A17)}$$

The fact that the x and y components of the unit vector in the direction of the plane normal do not change is a consequence of there being no strain on the shear plane. If there were a varying pure shear component in the shear zone, then x and y components would vary with position in the shear zone and the intersection line of gneissic banding and the zone boundary would vary.

Normalizing equation (A13) gives the following for n_z':

$$n_z' = \frac{n_z - \gamma\left(n_x \cos\theta + n_y \sin\theta\right)}{\left\{n_x^2 + n_y^2 + \left[n_z - \gamma\left(n_x \cos\theta + n_y \sin\theta\right)\right]^2\right\}^{\frac{1}{2}}}. \quad \text{(A18)}$$

This equation can be rearranged to give an expression for γ, but the stereonet and the use of equation 1 is more practical.

References

BARBER, A. J., BEACH, A., PARK, R. G., TARNEY, J. & STEWART, A. D. 1978. *The Lewisian and Torridonian Rocks of NW Scotland.* Geologists' Association Guides, **21**.

BEACH, A. 1974. The measurement and significance of displacements on Laxford Shear Zones, Northwest Scotland. *Proceedings of the Geologists' Association*, **85**, 13–21.

BEACH, A., COWARD, M. P. & GRAHAM, R. H. 1974. An interpretation of the structural evolution of the Laxford Front, north-west Scotland. *Scottish Journal of Geology*, **9**, 297–308.

CHAPMAN, H. J. 1979. 2390 Myr Rb–Sr whole-rock age for the Scourie dykes of north-west Scotland. *Nature*, **277**, 642–643.

CHAPMAN, H. J. & MOORBATH, S. 1977. Lead isotope measurements from the oldest recognised Lewisian gneisses of north-west Scotland. *Nature*, **268**, 41–42.

COWARD, M. P. 1990. Shear zones at the Laxford front, NW Scotland and their significance in the interpretation of lower crustal structure. *Journal of the Geological Society, London*, **147**, 279–286.

COWARD, M. P. & POTTS, G. J. 1983. Complex strain patterns developed at the frontal and lateral tips to shear zones and thrust zones. *Journal of Structural Geology*, **5**, 383–399.

ESCHER, A., ESCHER, J. C. & WATTERSON, J. 1975. The reorientation of the Kangamiut Dike Swarm, West Greenland. *Canadian Journal of Earth Sciences*, **12**, 158–173.

FLINN, D. 1979. The computation of deformations. *Geological Journal*, 87–98.

GEOLOGICAL SURVEY OF SCOTLAND 1892. *Lochinver Sheet 107*, 1 inch to a mile.

HAMILTON, P. J., EVENSEN, N. M., O'NIONS, R. K. & TARNEY, J. 1979. Sm–Nd systematics of the Lewisian gneisses: implications for the origin of the granulites. *Nature*, **277**, 25–28.

KINNY, P. D. & FRIEND, C. R. L. 1997. U–Pb isotopic evidence for the accretion of different crustal blocks to form the Lewisian Complex of northwest Scotland. *Contributions to Mineralogy and Petrology*, **129**, 326–340.

MOORBATH, S., WELKE, H. & GALE, N. H. 1969. The significance of lead isotope studies in ancient,

high-grade metamorphic basement complexes, as exemplified by the Lewisian rocks of northwest Scotland. *Earth and Planetary Science Letters*, **6**, 245–256.

PARK, R. G. & TARNEY, J. 1987. The Lewisian complex: a typical Precambrian high-grade terrain? *In*: PARK, R. G. & TARNEY, J. (eds) *Evolution of the Lewisian and Comparable Precambrian High Grade Terrains*. Geological Society, London, Special Publications, **27**, 13–25.

RAMSAY, J. G. 1967. *Folding and Fracturing of Rocks*. McGraw–Hill, London.

RAMSAY, J. G. & GRAHAM, R. H. 1970. Strain variation on shear belts. *Canadian Journal of Earth Sciences*, **7**, 786–813.

RAMSAY, J. G. & HUBER, M. I. 1987. *The Techniques of Modern Structural Geology: Folds and Fractures*. Academic Press, London.

SUTTON, J. & WATSON, J. 1951. The pre-Torridonian metamorphic history of the Loch Torridon and Scourie areas in the North-West Highlands, and its bearing on the chronological classification of the Lewisian. *Quarterly Journal of the Geological Society, London*, **106**, 241–308.

TREAGUS, S. H. & LISLE, R. J. 1997. Do principal surfaces of stress and strain always exist? *Journal of Structural Geology*, **19**, 997–1010.

WATERS, F. G., COHEN, A. S., O'NIONS, R. K. & O'HARA, M. J. 1990. Development of Archaean lithosphere deduced from chronology and isotope chemistry of Scourie Dykes. *Earth and Planetary Science Letters*, **97**, 241–255.

WHEELER, J. 1987. The determination of true shear senses from the deflection of passive markers in shear zones. *Journal of the Geological Society, London*, **144**, 73–77.

Available online at www.sciencedirect.com
ScienceDirect
Earth and Planetary Science Letters 267 (2008) 118–128
EPSL
www.elsevier.com/locate/epsl

Amphibole and lower crustal seismic properties

D.J. Tatham [1], G.E. Lloyd *, R.W.H. Butler, M. Casey

Institute of Geophysics and Tectonics, School of Earth and Environment, The University, Leeds, LS2 9JT, UK

Received 29 September 2007; received in revised form 19 November 2007; accepted 19 November 2007
Available online 8 December 2007
Editor: R.D. van der Hilst

Abstract

Measurements of seismic anisotropy frequently offer insights of the deformation kinematics in-situ within the Earth. In the continental crust, seismic anisotropy is commonly ascribed to regionally aligned lattice preferred orientation (LPO) of mica crystals. However, determinations of composition suggest that the deep continental crust contains rather little mica. In this contribution, the role of amphibole, a far more plausible constituent, especially for deep continental crust of basic composition, is assessed. A field analogue approach is adopted, where the LPO are measured, correlated with the strain state of the rocks, and used to calculate the seismic properties. The seismic properties may be up-scaled through the specimen using the modal proportions of the constituent mineral phases. To examine the role of composition in controlling the intensity of seismic anisotropy, seismic properties are computed using an array of modal compositions (so-called 'rock recipes'). The case history comes from the Central Block of the Lewisian of NW Scotland, where a regional basic dyke swarm (the Scourie dykes) is locally deformed within amphibolite facies shear zones, conditions that are representative of the deep crust. Shear strain (γ) profiles across a 100 m wide shear zone, using deflected banding in the host gneisses, yield values of $0<\gamma<15$ or greater. A Scourie dyke deflected into the shear zone exhibits hornblende with distinct preferred dimensional orientations representative of such strains. In contrast, plagioclase (and quartz) clots are almost totally insensitive to deformation (due to grain-size sensitive creep deformation) and yield approximately constant apparent strains of $\gamma=1-2$. Hornblende–plagioclase–quartz LPOs, combined in their modal proportions and modulated by their individual single-crystal elastic properties, define the seismic properties of the shear zone. Rock recipe modelling demonstrates that it is the hornblende that dominates the seismic response and that plagioclase and quartz serve simply to dilute the intensity of anisotropy. The values calculated indicate significant (up to ~13%) seismic anisotropy for strongly sheared amphibolites. Thus amphibole, aligned through deformation, is likely be a major contributor to the seismic anisotropy of the deep continental crust.
© 2007 Elsevier B.V. All rights reserved.

Keywords: amphibole; LPO; seismic properties; lower crust

1. Introduction

Seismic anisotropy is becoming the investigative method of choice for mapping ductile strain patterns in-situ within the continental crust (e.g. Christensen and Mooney, 1995; Mainprice and Nicolas, 1989). For example, in Tibet and the Himalayas, seismological experiments have detected seismic anisotropy within the crust not only using teleseismic receiver functions (e.g. Ozacar and Zandt, 2004) but also from local intra-crustal earthquakes (e.g. Schulte-Pelkum et al., 2005). There is a general assumption that much of the observed anisotropy is caused by aligned mica within the crust (e.g. Shapiro et al., 2004; Mahan, 2006; Meissner et al., 2006). Acoustic measurements of rock samples (e.g. Meltzer and Christensen, 2001) indicate that foliated micaceous rocks can indeed generate the levels of seismic anisotropy observed. However, whilst foliated micaceous rocks may offer plausible explanations for some seismic anisotropy, global compilations of the composition and structure

* Corresponding author. Tel.: +44 113 343 5209; fax: +44 113 343 5259.
E-mail address: g.lloyd@earth.leeds.ac.uk (G.E. Lloyd).
[1] Now at School of Earth and Ocean Sciences, University of Liverpool, Liverpool, L69 3GP, UK.

0012-821X/$ - see front matter © 2007 Elsevier B.V. All rights reserved.
doi:10.1016/j.epsl.2007.11.042

LEEDS UNIVERSITY LIBRARY

of the continental crust suggest other options (e.g. Rudnick and Fountain, 1995; Rudnick and Gao, 2003). Global averages of crustal controlled-source and teleseismic travel times (e.g. Christensen and Mooney, 1995), volume fraction of lithologies in currently out-cropping high-grade terranes (e.g. Weaver and Tarney, 1980; Percival et al., 1992), and evidence from deep sourced xenoliths (e.g. Jackson, 1991; Rudnick, 1992; Rudnick and Jackson, 1995) indicate the importance of mafic material in accounting for the bulk properties of the lower crust. The composition therefore of much of the lower and lower-middle continental crust approximates to that of amphibolite-to-granulite facies metabasites, with amphibole and pyroxene as the dominant crystal phases and which contain little mica (e.g. Rudnick and Fountain, 1995). The question arises: what is the role of these non-micaceous minerals in generating seismic anisotropy?

Modelling the lower crust as a homogeneous mafic aggregate (Rudnick and Fountain, 1995) deforming by ductile processes and existing beneath the threshold at which cracks or fractures are prevalent (Crampin et al., 1984; Rasolofosaon et al., 2000) means that it can be considered in terms of its intrinsic properties alone (Kendall, 2000). Such petrophysical properties are independent of the seismic wavelength and are inherent to the transmitting material. The most important of these properties is the crystal lattice preferred orientation (or LPO) of the constituent mineral phases in a rock aggregate (Christensen, 1984; Mainprice and Nicolas, 1989; Siegesmund and Kern, 1990). Calibration of the seismic response of continental crust in-situ can be achieved using samples naturally occurring in rock outcrops. One approach is to make direct measurements of seismic velocity on samples (e.g. Burlini and Kern, 1994; Takanashi et al., 2001). Whilst it is well-established that micro-fracturing, especially in the upper continental crust, can dominate the seismic anisotropy (e.g. Crampin, 1981), open fractures are far less significant at depths greater than a few tens of MPa (e.g. Rasolofosaon et al., 2000). Outcrop samples that have passed through the upper crust since they developed their ductile deformation fabrics must be reloaded therefore during acoustic experiments to close up any micro-fractures. Such experimental results can yield seismic velocities comparable with those measured for the deep crust (e.g. Barruol and Mainprice, 1993; Barruol and Kern, 1996). An alternative approach is to model seismic properties using measurements of LPO. This petrofabric method has advantages because structural elements within the sample that are not believed to have formed at depth can be excluded explicitly from the model. Thus, retrogression and fracturing are not a source of uncertainty. Furthermore, the contribution of different mineral phases, domains and microstructures can be isolated and investigated. It is possible therefore to relate the petrophysical response to rock texture and deformation processes.

The aim of this paper is to model the seismic anisotropy of amphibole-dominated deformed rocks of basic composition that are representative of the deeper continental crust. The approach adopted follows that used to calibrate seismic properties of the upper mantle (e.g. Kern et al., 1996; Ben Ismail and Mainprice, 1998) by reconstructing seismic properties from measured LPO of rocks believed to be appropriate analogues for in-situ Earth materials. Compared with the continental crust, the mantle is considered to be structurally simple and xenolith samples have been used therefore to calculate its seismic response (e.g. Kern et al., 1996). Such studies have shown that the bulk seismic properties of a sample are the integrated response of the LPO for each mineral phase present (e.g. Babuska and Cara, 1991). However, xenoliths are unconstrained in terms of their original location and geological relationships from which they derive. Given the complexity of continental geology, and in contrast to the xenolith-based approach, samples from outcrop analogues of deep crustal geology are required.

There are many outcrop examples of amphibole-dominated continental crustal materials that have been exhumed as part of large, continuous terranes and hence have known structural context (e.g. Percival et al., 1992). In such cases, the amphibolitic rock LPO can be related directly to strain state as defined by variations in linear and planar fabrics over the outcrop and combined with the relevant single-crystal elastic constants to predict the whole rock seismic properties. Furthermore, because the constituent minerals are considered individually, their impact in varying modal compositions with changing finite strain can be investigated. This approach, using appropriate outcrops as proxies for in-situ deep crust, informs a discussion of the role of strain state and composition in determining seismic anisotropy in general. The key role of amphibole is examined.

2. Geological setting and sample descriptions

The choice of outcrop analogue for estimating seismic properties of the deep crust requires appropriate material deformed by a measurable amount under appropriate pressure and temperature conditions. Thus, the field setting for this study comes from the Lewisian of NW Scotland, a classic tonalitic–trondjhemite–granodioritic (TTG) gneiss complex of late Archaean to Paleoproterozoic age (e.g. Kinny et al., 2005; Fig. 1a, b). The complex is an amalgam of tracts with distinct TTG protolith ages but all parts are cross-cut by a suite of meta-igneous mafic sheets (the Scourie dyke swarm), emplaced between 2400–2000 Ma (e.g. Cohen et al., 1991). The most recent regional reworking of the Lewisian complex occurred at c. 1750 Ma (Kinny et al., 2005) during the so-called Laxfordian event. At this time, the TTG gneiss and the Scourie dykes were deformed in broad tracts and, more usefully for the current study, in discrete shear zones within which strain can be measured. The mafic dykes represent excellent lithological analogues for deep crust of basic composition. They were emplaced under conditions of 450–500 °C and 5–7 kb (e.g. Tarney, 1963), prior to the amphibolite facies deformation considered here. The specific site for this study comes from part of the 'Assynt terrane' of Kinny et al. (2005), where host granulite facies TTG gneisses are transected by amphibolite facies (Laxfordian) shear zones that deform both the gneisses and the Scourie dykes.

The study here uses the Upper Badcall Shear Zone (e.g. Coward and Potts, 1983, and references therein), an approximately 100 m wide ENE–WSW-trending structure with a

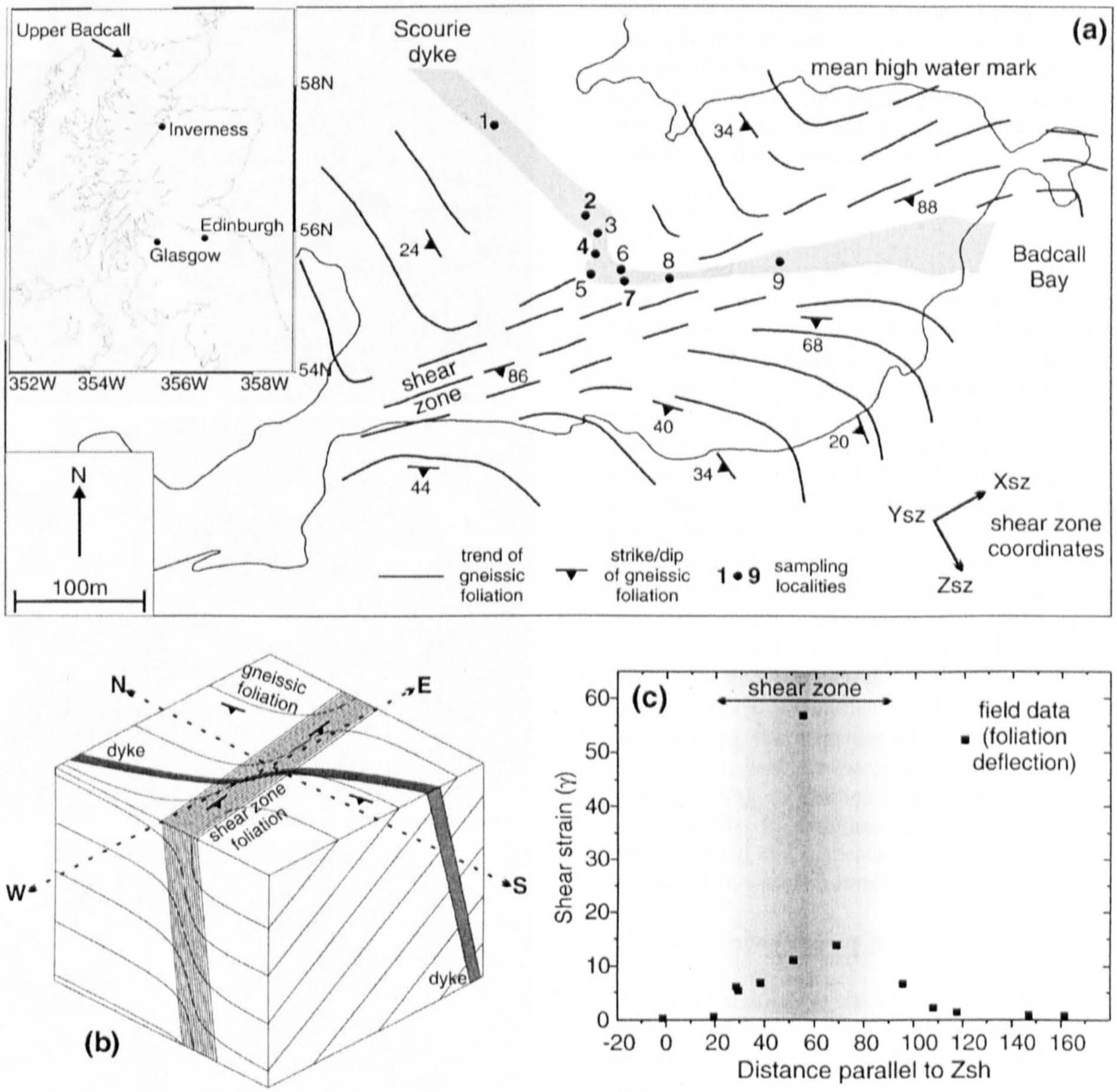

Fig. 1. Laxfordian Lewisian shear zone, Upper Badcall, NW Scotland (after Tatham and Casey, 2007). (a) Simplified structural map (inset, general location), including sample locations of Tatham and Casey (2007) — bold type are samples used in this study. (b) Schematic 3D representation. (c) Strain profile calculated from reorientation of country-rock gneissic banding. Reference frame origin is the western dyke margin at the northern shear zone boundary.

generally subvertical strain fabric in the host gneisses (Fig. 1a, b). A Scourie dyke (amphibolite sheet and analogue for deep crust of basic composition) crosses the shear zone, within which it is deflected and attenuated. Deflection of fabrics in the surrounding TTG gneisses records the strain state of both the host rock and dyke (Tatham and Casey 2007) and indicates that, in the present orientation, the Upper Badcall Shear Zone acted as a ductile zone of oblique left-lateral strike slip. Shear strains (γ) increase generally to at least $\gamma = 15$ and in some narrow tracts in the centre of the shear zone may exceed this value (Fig. 1c). However, as there are well-known problems in calibration as shear strain increases towards these higher values (e.g. Ramsay and Huber 1983), only samples from the range $0 < \gamma < 15$ have been considered in this study. The geological set-up for the Upper Badcall shear zone constitutes therefore a natural deformation rig within which the strain gradient can be tracked and samples collected directly.

Outside of the shear zone the dyke cross-cuts the host TTG gneisses and is undeformed. It contains a relict granular texture of presumed meta-igneous origin, comprising ferropargasitic hornblende and andesine plagioclase, with subordinate quartz, relict salitic clinopyroxene and accessory minerals. Within the shear zone the dyke is variably deformed and comprises typically ferropargasitic hornblende and seriticised oligoclase plagioclase, with subordinate quartz and accessory minerals (e.g. Fig. 2).

A suite of oriented samples was collected from along the dyke, from the undeformed shear zone wall into the shear zone proper, from domains of different strain state (Fig. 1a; Tatham

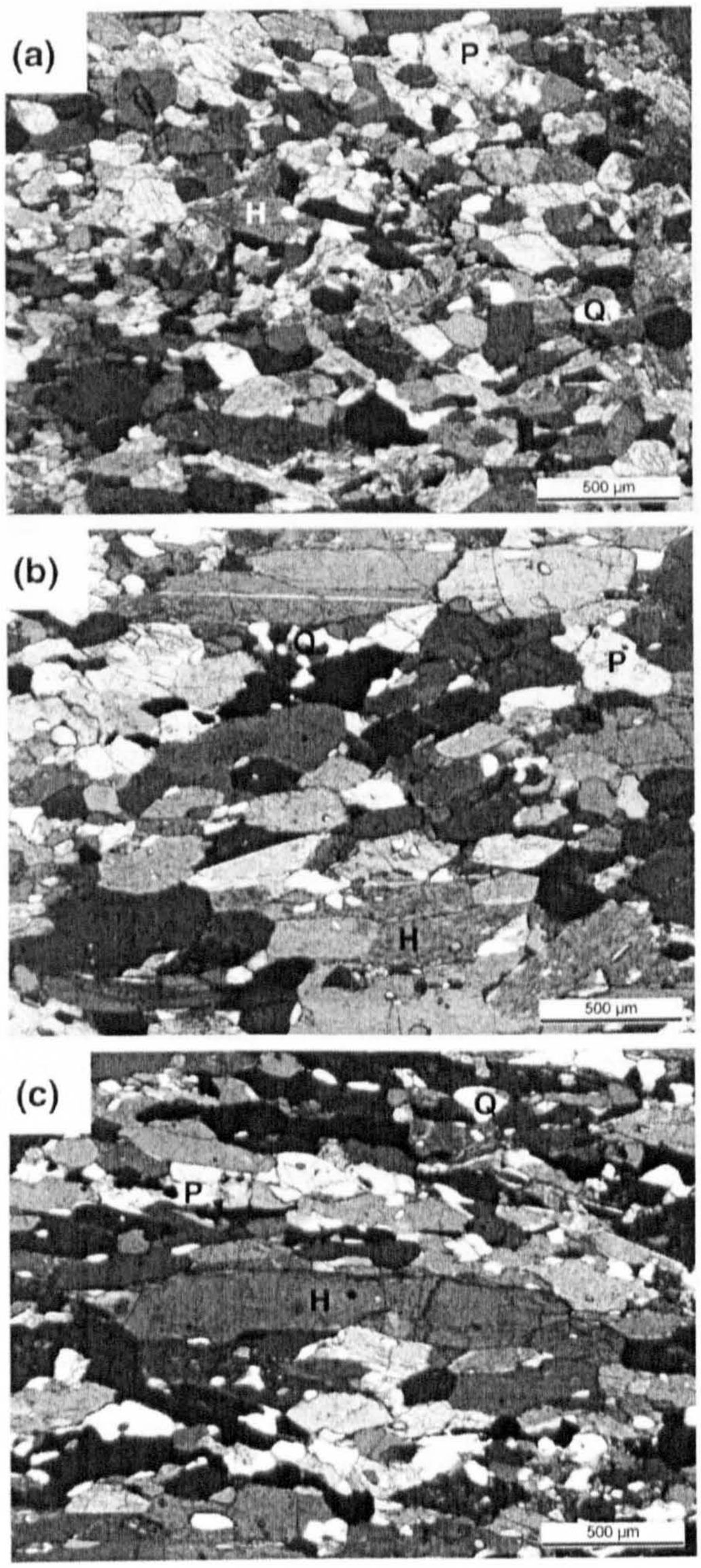

Fig. 2. Microstructures of samples used to derive seismic properties (cross-polars photomicrographs; *XZ* section with *X* horizontal and *Z* vertical; H, hornblende; P, plagioclase; Q, quartz). See Fig. 1 for sample locations. (a) Low strain (sample 2). (b) Intermediate strain (sample 4). (c) High strain (sample 7). The low strain sample has a smaller grain size for all three minerals than the other two samples, whilst there is a noticeable increase in the degree of shape preferred orientation, particularly of hornblende, from the low to the high strain samples.

and Casey, 2007). The modal proportions of the principal minerals in these samples, determined during LPO analysis (see below), are: hornblende, 60±11%; plagioclase, 25±8%; and quartz, 13±6%. Deformed samples show the progressive development with increasing strain of a shape preferred orientation (SPO) in hornblende grains (Fig. 2). Millimetric scale clots of plagioclase aggregates with a reduced grain size, representing originally undeformed individual grains, show also the development of SPO, although within the clots a granular texture of equiaxed 100–250 µm grains prevails. Quartz grains remain approximately equant and maintain a constant size somewhat smaller than the plagioclase range.

3. Methodology

Rocks are made up of different minerals, each of which may have a LPO. Every mineral has single-crystal elastic properties represented by a 6×6 symmetric elastic stiffness matrix. Orientation dependent velocities of seismic waves are a consequence of the non-isotropic nature of the elastic stiffness matrices of minerals (e.g. Babuska and Cara, 1991). Seismic velocities and polarizations for all orientations are obtained from the stiffness matrices (e.g. Ji et al., 2002). As the single-crystal elastic properties vary with pressure and temperature but the P–T derivatives are often unknown, we follow convention (e.g. Mainprice et al., 2000) and assume the elastic parameters determined under ambient conditions (i.e. quartz, McSkimin et al., 1965; plagioclase, Aleksandrov et al., 1974; and hornblende, Aleksandrov and Ryzhova, 1961). The seismic properties (Fig. 3) are given as contoured stereographic projections (e.g. Mainprice, 1990; Mainprice and Humbert, 1994) of the P-wave velocity (Vp), the velocities of the fast (Vs_1) and slow (Vs_2) shear waves, and the percentage shear wave anisotropy or splitting (AVs), as defined conventionally by Mainprice and Silver (1993). In addition, the absolute P-wave anisotropy (AVp), defined as a percentage of the average difference of the fastest and slowest P-waves is provided.

3.1. Single-crystal seismic properties

Due to variations in the single-crystal elastic properties, the single-crystal seismic properties of the constituent minerals of the dyke (i.e. hornblende, plagioclase and quartz) vary with crystal symmetry and direction (Fig. 3). In general, the relationships between crystal symmetry and seismic properties are relatively simple. Quartz has three maxima and minima in Vp (sub-parallel to the *z* and *r*-directions respectively) and three maxima (parallel to the *a*-axis) and four minima (parallel to the *c*-axis and sub-parallel to the *r*-directions) in AVs. Plagioclase (e.g. oligoclase, triclinic symmetry P-1) exhibits typically single maximum and minimum in Vp (parallel to the *b*- and *a*-axes respectively) but its AVs behaviour is more complex, with two maxima (inclined to the *c*-axis) and a single minimum (sub-parallel to the *c*-axis), although there is some variation in all of these values with Ca-content (e.g. Lloyd and Kendall, 2005). In contrast, hornblende has only a single maximum and minimum in both Vp (parallel to the *c*-axis and sub-parallel to the *a*-axis respectively) and AVs (sub-parallel to the *c*- and *a*-axes respectively). Plagioclase exhibits the most anisotropy in both AVp and AVs. Quartz and hornblende have similar but much lower AVp anisotropy, whilst hornblende has the lowest AVs anisotropy. Note that as AVp is merely the difference between the maximum and minimum in Vp, it has no azimuthal significance.

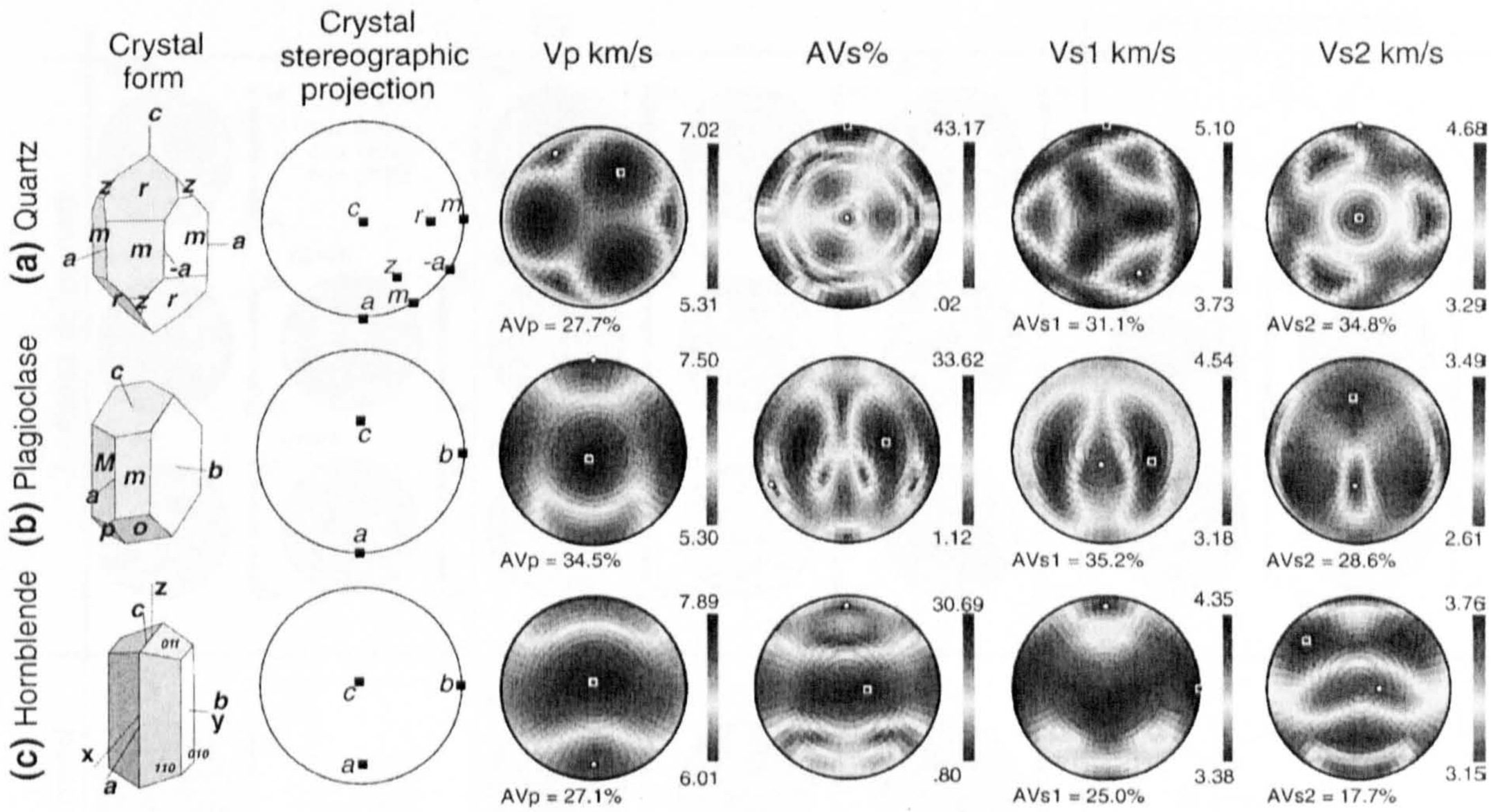

Fig. 3. Single-crystal seismic properties for the minerals in the Upper Badcall shear zone (upper hemisphere projections; contours as indicated; seismic projections plotted in the same coordinate system as the crystal stereographic projections).

3.2. Rock aggregate seismic properties

Although understanding the seismic behaviour of single crystals is crucial to the interpretation of whole rock seismic behaviour, in practice all mineral phases in a rock contribute to the overall seismic properties according to their single-crystal elastic parameters, volume fraction and LPO distribution (e.g. Mainprice and Humbert, 1994). As aggregates of randomly oriented crystals must generate isotropic bulk rocks, there must be a degree of crystal alignment (i.e. LPO) present to produce seismic anisotropy. In general, strong LPOs are induced by tectonic stresses in deformed rocks. The methodology used to calculate whole rock seismic property distributions in three-dimensions follows directly from that employed in the single-crystal calculations described previously (e.g. Mainprice and Humbert, 1994; see also Lloyd and Kendall, 2005).

3.3. Workflow: petrofabric-derived seismic properties

First, the complete LPO for each mineral in a sample is measured. This is possible both accurately and efficiently via electron backscattered diffraction (EBSD) in the SEM (e.g. Prior et al., 1999). Second, the LPOs are combined with the appropriate single-crystal elastic properties for each mineral such that for each orientation the single-crystal elastic parameters are rotated into the sample reference frame and the elastic parameters of the polycrystal are derived by integration over all possible orientations in the three-dimensional orientation distribution function. Third, the individual mineral properties, modulated according to modal proportion, are combined to determine the whole rock elastic and hence seismic properties. Due to stress/strain compatibility assumptions it is conventional to adopt the mean or Voigt–Reuss–Hill (VRH) average as the best estimate of the aggregate elastic parameters (e.g. Hill, 1952), as this has been observed to give results close to experimental values (e.g. Bunge et al., 2000). The aggregate seismic phase velocities and related anisotropy are obtained then in every direction (e.g. Mainprice and Humbert, 1994; Lloyd and Kendall, 2005).

The impact of each mineral to the whole rock seismic properties can be investigated by varying the relative proportions appropriately whilst maintaining the LPOs. This approach (termed here 'rock recipes') assumes implicitly that the microstructure (and hence deformation mechanisms) of each phase remains constant regardless of the proportion of that or the other phases present. This assumption becomes invalid probably where the recipe approaches 100% for any of the minerals present because the rock begins to behave as a monomineralic rather than polymineralic aggregate, exhibiting bulk rather than localised microstructures and textural evolution (e.g. Handy, 1994). It remains unclear for the moment at what level of recipe this transition occurs but it is likely to be dependent on a number of factors (e.g. mineralogy, strain, deformation mechanisms, etc.).

4. Results

Nine samples were collected from a transect across the Upper Badcall Shear Zone (Fig. 1). However, results are presented here for three samples only (e.g. Tatham and Casey, 2007). Sample 2 (Fig. 2a) is from the low strain ($\gamma \ll 1$) part of the shear zone margin, representative of a low deformation state with a steeply plunging lineation associated with incipient deformation of the Upper Badcall shear zone. Sample 4 (Fig. 2b) is from within the

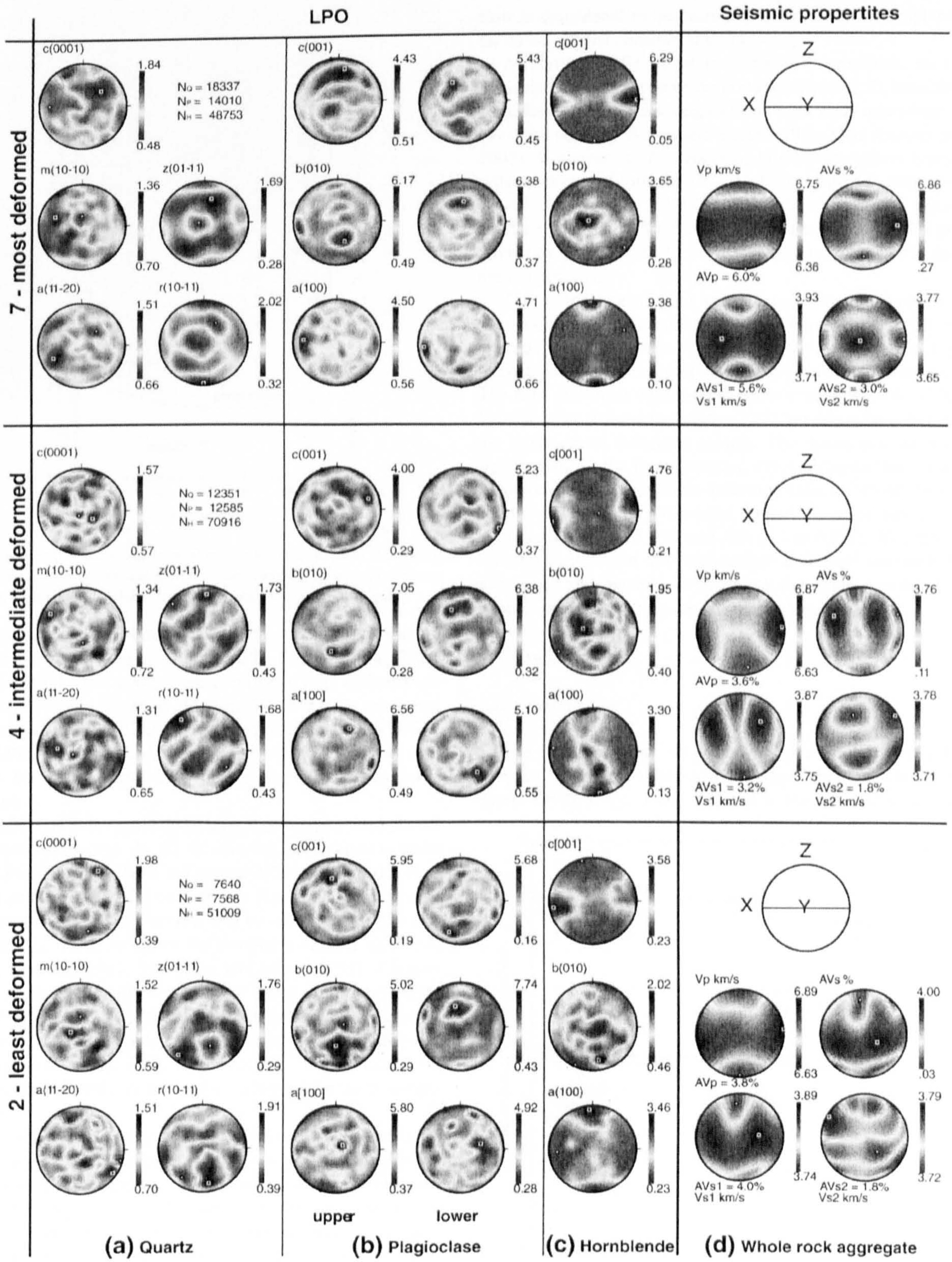

Fig. 4. LPO and seismic property distributions for the least, intermediate and most deformed samples. All projections lower hemisphere except plagioclase, which is both lower and upper; crystal directions as indicated. Contours are multiples of uniform distribution, as indicated (solid squares, maximum values; open circles, minimum values). Kinematic orientation *X*, *Y*, *Z* as indicated (n.b. these are relevant only to each sample and change geographically from sample to sample, for example with plunge of lineation, *X*).

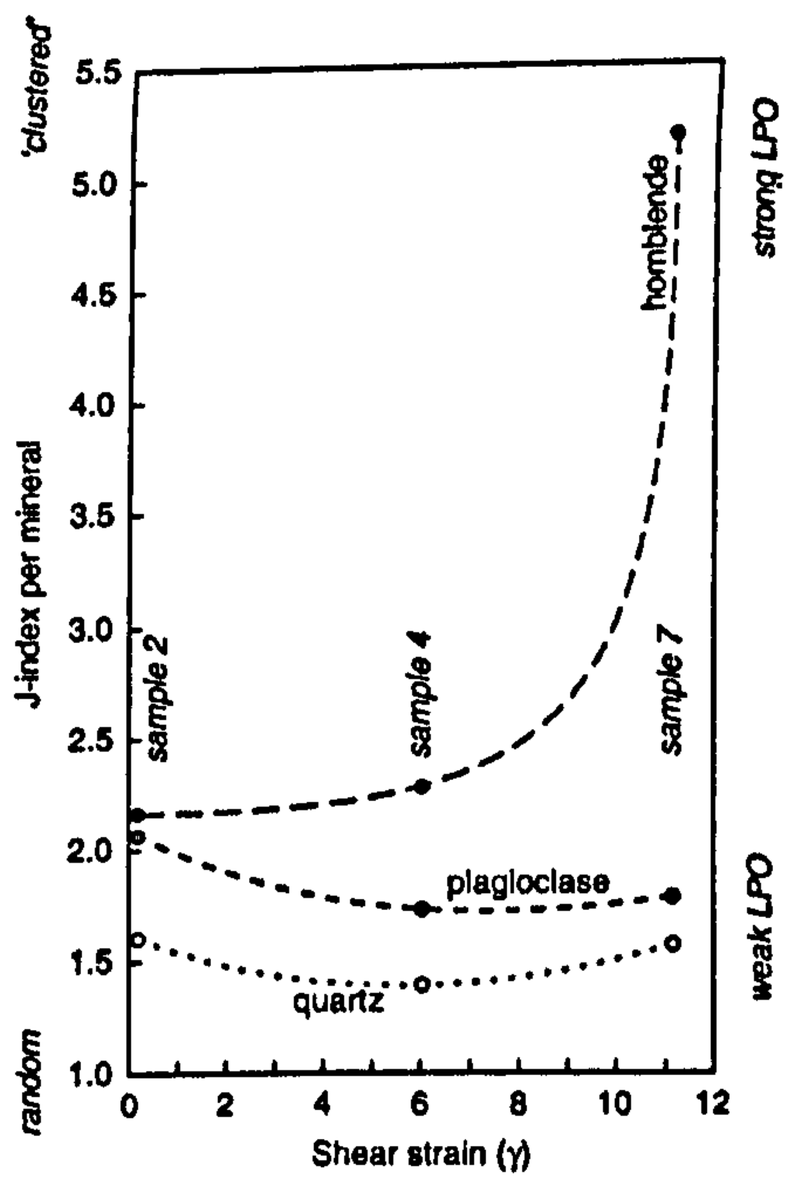

Fig. 5. Relationship of individual mineral texture index (J) to finite shear strain (γ) for the least, intermediate and most deformed samples, assuming polyphase aggregates comprising 60% hornblende, 30% plagioclase and 10% quartz.

shear zone proper, representative of an intermediate deformation state ($\gamma \approx 6$) with a lineation plunging 58°. Sample 7 (Fig. 2c) is from the central shear zone, representative of high deformation state ($\gamma \approx 11$) with a lineation plunging 38°. For each specimen, the individual mineral LPOs were determined via SEM/EBSD. These LPOs were applied then to the measured modal proportions for each specimen to derive the aggregate seismic properties.

The LPOs of both quartz and plagioclase remain weak for all deformation states (Fig. 4a, b). In contrast, hornblende exhibits strong LPOs (Fig. 4c), with the crystal c[001] and a(100) axes aligning parallel to X and Z respectively (i.e. the latter normal to the foliation, XY). Such behaviour can be quantified by the texture index (J), which measures the sharpness of LPO clustering (Bunge, 1969 and 1982; Mainprice and Silver, 1993). J is normalised so that for random fabrics $J=1$ and with increasingly clustered fabrics $J \rightarrow \infty$, although a value of $J \approx 50$ is frequently recognised for ideal 'single-crystal' fabrics (e.g. Michibayashi and Mainprice, 2004). Thus, the value of J per mineral LPO can be related directly to the strain calculated for each sample (Fig. 1c).

The J-index is essentially constant as a function of shear strain for both plagioclase and quartz (Fig. 5). In contrast, the J-index increases with shear strain for hornblende. Such behaviours indicate not only different deformation mechanisms but also a potential partitioning of the deformation between the plagioclase–quartz aggregate and hornblende. Under greenschist facies conditions, small grain size and lack of LPO development with strain in plagioclase is normally interpreted as indicating granular/grain-size sensitive creep flow of refined, originally single igneous grains (e.g. Prior and Wheeler, 1999). Grain-size sensitive flow is considered to be more important under the amphibolite facies conditions considered in this study.

As there is little direct evidence (i.e. subgrains, etc.) for intragranular crystal plastic deformation (see Fig. 2), hornblende could have achieved a strong LPO via rigid-body rotation as well as crystal slip (e.g. Berger and Stunitz, 1996; Diaz Azpiroz et al., 2007). However, as the shape of hornblende grains typically reflects its crystal form (see Fig. 1), both rigid-body rotation and crystal slip, such as (100)[001], can be expected to generate similar LPOs. Thus, hornblende LPOs, and hence seismic properties, are often likely to be insensitive to the specific deformation process.

The petrofabric-derived seismic property distributions are somewhat similar for the three samples (Fig. 4d). They all show maxima and minima in Vp aligned with the sample X (i.e. lineation) and Z (i.e. normal to foliation) directions, respectively. The least and most deformed samples exhibit a girdle of faster Vp velocities parallel to foliation (XY) but this is less obvious in the intermediate deformed sample. The distribution of AVs is similar also for the three samples, although again there is more variation in the intermediate deformed sample. Whilst there is a slight decrease in Vp with strain, there is a concomitant increase in both AVp (3.8 to 6.0%) and AVs (4.0 to 6.8%), although both actually decrease in the intermediate deformed sample before increasing significantly in the most deformed sample. These seismic property behaviours are summarised in Fig. 6.

5. Seismic models

5.1. Rock recipes

The petrofabric-derived seismic properties clearly reflect the dominant influence of hornblende rather than plagioclase and/or quartz LPOs (Figs. 3 and 4). Due to the specific relationship

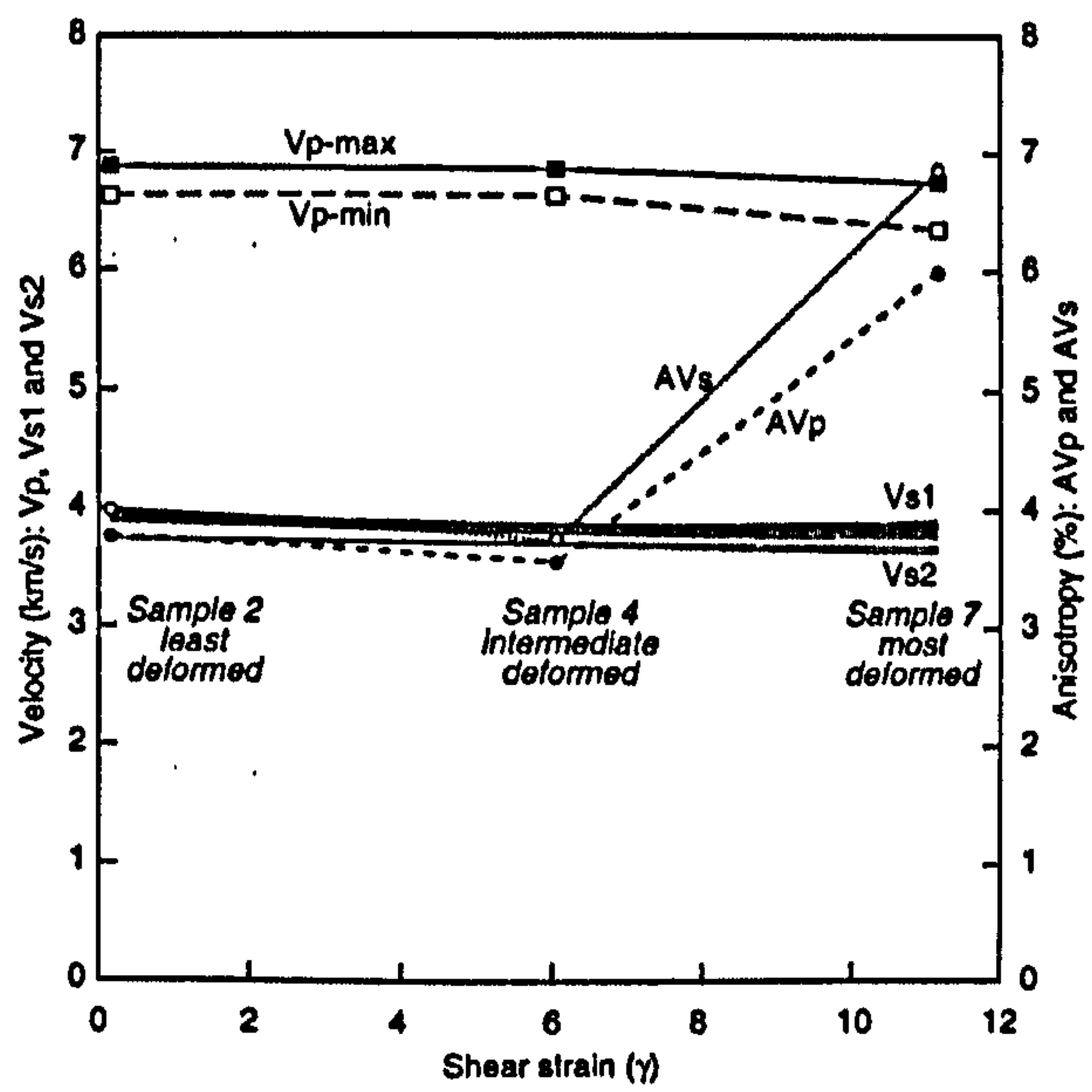

Fig. 6. Summary of seismic properties for the least, intermediate and most deformed samples.

between the hornblende LPOs and the kinematic axes, the Vp and AVs distributions reflect also the kinematic coordinate systems. Both the plagioclase and quartz LPOs are weak and essentially constant with increasing deformation (Figs. 4a, b and 5). The effective role of plagioclase and quartz therefore is to dilute the impact of the hornblende LPO away from monomineralic behaviour. This effect can be demonstrated using rock recipes in which the modal proportions of plagioclase and quartz are varied pro rata (i.e. 3:1) relative to total hornblende content (i.e. 0–100%), whilst maintaining the individual LPO of each mineral (e.g. a rock recipe with 0% hornblende comprises 75% plagioclase and 25% quartz, whilst one with 20% hornblende comprises 60% plagioclase and 20% quartz, and so on).

The rock recipes results are summarised in Fig. 7, incorporating the Vp and AVs distributions plotted at the same appropriate scales throughout. Vp increases only slightly with increasing hornblende content. In the least and intermediate deformed samples, both AVp and AVs show an initial decrease with increasing hornblende content, although there is a slight increase in both as 100% hornblende content is approached. This behaviour suggests that the weak plagioclase–quartz fabrics are diluted initially by the introduction of hornblende (see Figs. 4 and 5). In contrast, both AVp and AVs increase progressively with increasing hornblende content in the most deformed sample, reflecting the impact of the strong hornblende LPO. Thus, hornblende clearly dominates the Vp and AVs properties, even when only a few ten's of percentage of hornblende are added to the basic recipe.

5.2. The lower crust

The impact of hornblende on typical lower crustal seismic properties can now be considered. According to Rudnick and

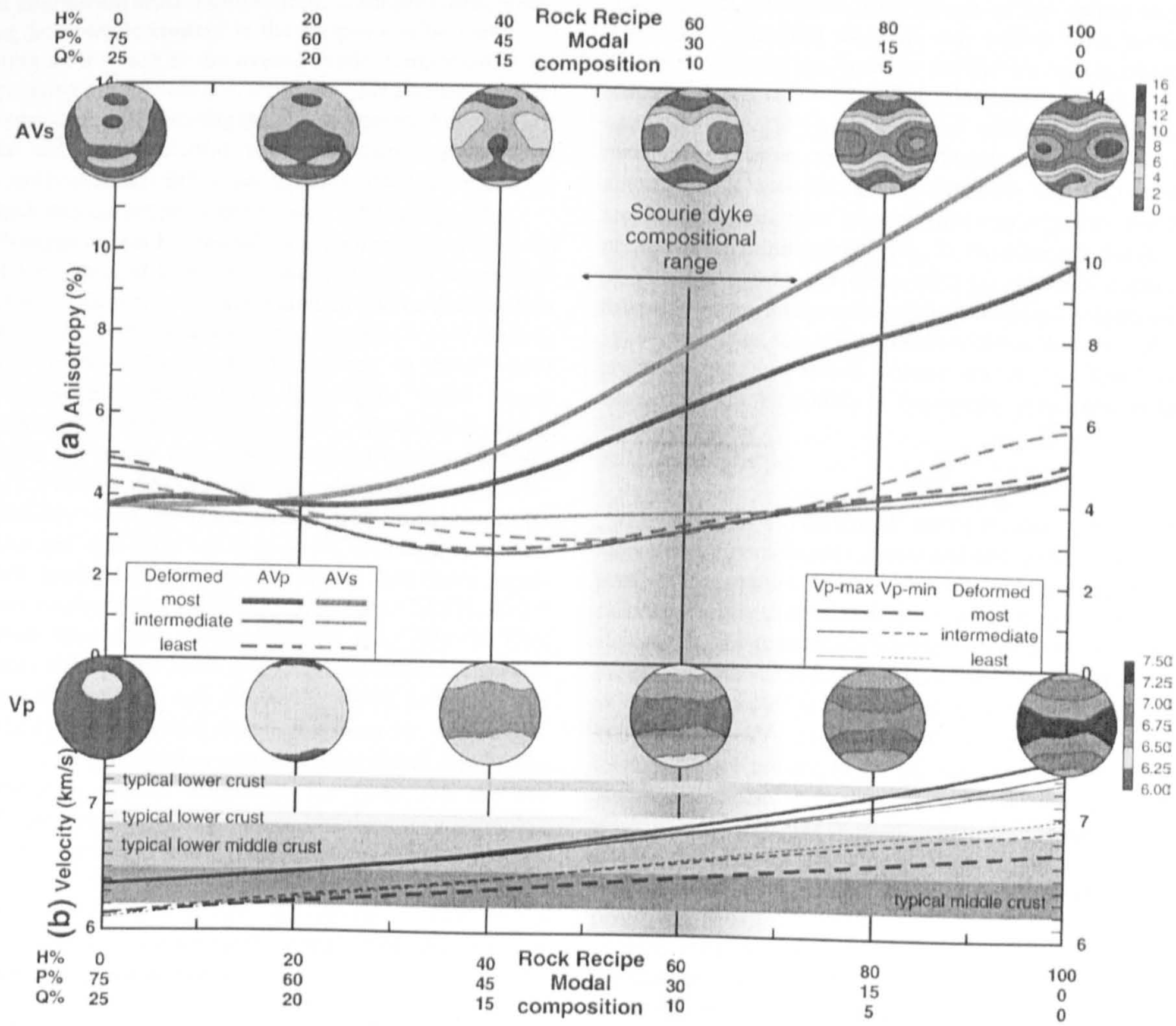

Fig. 7. Rock recipe modelling of hornblende–plagioclase–quartz rocks, based on LPO measured from the least, intermediate and most deformed samples, as indicated by variation in hornblende content from H0–H100% at 20% intervals (plagioclase–quartz content is varied concomitantly in the ratio 3:1). The curves are best-fit polynomials through the values calculated for each parameter for each recipe. Also shown are Vp and AVs distributions (plotted at the same appropriate colour-coded scales) for specific compositions of the most deformed sample (*X*, horizontal and E–W; *XY* vertical and E–W; *Z*, vertical and N–S). (a) Anisotropy (AVp and AVs). (b) Velocity (Vp); note the colour-coded lower-middle crustal Vp profile suggested by Rudnick and Fountain (1995).

LEEDS UNIVERSITY LIBRARY

Fountain (1995; see also Rudnick and Gao, 2003), increasing average P-wave seismic velocities with depth indicate increasing proportions of mafic lithologies and increasing metamorphic grade. They expect therefore that the lower continental crust (i.e. below ~20–25 km depth) is lithologically diverse but dominated by granulite facies mafic lithologies with an average composition approaching that of primitive basalt, although felsic-to-intermediate lithologies may be important locally. In contrast, the average middle crust (i.e. between 10–15 and 20–25 km depth), where P-wave velocities are too low to be explained by dominantly mafic lithologies, is considered to consist of a mixture of mafic, intermediate and felsic amphibolite facies gneisses. Amphibolite facies may be important also in the lower crust, particularly where high water fluxes occur.

The petrofabric-derived seismic property estimates (Fig. 4) obtained from a simple shear deformation profile across a Scourie dyke at Upper Badcall, NW Scotland, augmented via rock recipe models (Fig. 7), can act as a proxy for deformation in the lower continental crust. Furthermore, in simple terms, whilst increasing hornblende content in the recipes can be viewed as representing an increase in the overall mafic component in the rock, decreasing hornblende (i.e. increasing plagioclase–quartz) content represents an increasing felsic component. Accordingly, the lower and middle crustal velocity profile suggested by Rudnick and Fountain (1995) is superposed on to the hornblende rock recipes seismic property predictions for Vp (Fig. 7b).

Fig. 7b suggests that hornblende is capable of generating the values of Vp observed in most of the middle and lower continental crust, irrespective of modal content and/or deformation state. Only the highest velocity layers (i.e. where Vp > 7.0 km/s) are unlikely to be explained by hornblende as these would require almost pure hornblende lithologies. Such layers probably consist of pyroxenes (±garnet), which have higher single-crystal Vp values (e.g. 6.9–9.0 km/s) than amphiboles (e.g. 6.0–7.9 km/s). However, hornblende-dominated lithologies, particularly when deformed, exhibit significant anisotropy in both AVp and AVs (Fig. 7a). In contrast, although pyroxenes can exhibit strong LPOs when deformed, they have significantly less single-crystal anisotropy (e.g. AVp = 24.3%, AVs = 18.0%) than amphiboles (e.g. AVp = 27.1%, AVs = 30.7%), using values determined from single-crystal elastic constants for augite (Aleksandrov and Ryzhova, 1961) following the same methodology described above. Furthermore, whilst similar LPOs can be generated in amphibole by either crystal slip and/or rigid-body rotation behaviour, due to the fact that the typical prismatic shape of the grains reflect the crystallography, pyroxenes are typically 'stubby' and only the development of pyroxene LPOs via crystal slip will impact significantly on seismic anisotropy. Thus, seismic anisotropy as well as Vp values should be used to interpret the composition and structure of the continental crust at depth.

6. Discussion

The results of the petrofabric-derived seismic property estimates and rock recipe models described here indicate that much of the seismic properties of the middle-lower continental crust can be explained by amphibole in sufficient abundance and appropriate deformation state. This contrasts with the suggestion that micas (e.g. biotite and muscovite) control the seismic properties of the deeper continental crust (e.g. Meltzer and Christensen, 2001; Shapiro et al., 2004; Mahan, 2006; Meissner et al., 2006). However, Rudnick and Fountain (1995) have shown that there is little evidence for metapelite-dominated layers in the deep continental crust (although some high metamorphic grade former metapelites consisting now of kyanite and/or sillimanite, the latter having high seismic velocities and associated anisotropy (e.g. Ji et al., 2002), may represent up to ~10% of the lower crust). Micas are monoclinic and typically exhibit similar LPO distributions as amphiboles but crucially not the same crystal–kinematic–seismic orientation relationships due to their vertical transverse isotropy characteristics (e.g. Vernik and Liu, 1997). They are also the most seismically anisotropic minerals, with AVp and AVs values up to 64% and 114% (for biotite) respectively (e.g. Babuska ands Cara, 1991; Ji et al., 2002). However, their range of Vp values (e.g. 4.0–7.8 km/s for biotite) suggests that neither mica content nor deformation state can account for the Vp values observed in either the lower or lower-middle continental crust (e.g. Rudnick and Fountain, 1995). In terms of modal composition, most metabasic rocks at amphibolite facies comprise at least 50% amphibole. If such lithologies dominate the deep crust, then amphibole rather than mica is likely to represent the seismic property determining phase (Fig. 7). No other mineral (e.g. mica, plagioclase, quartz, pyroxene, etc.) is capable of imparting the full range of seismic properties observed (e.g. Siegesmund et al., 1989). However, it is the thickness of the rock mass with similar properties through which seismic waves pass that ultimately determines the magnitude of the seismic properties recognised.

7. Conclusions

Deformation in metabasic rocks produces strong mineral alignment of hornblende crystals and hence strong crystal lattice preferred orientation (LPO). The results of petrofabric-derived seismic property determinations presented here indicate that such alignments can generate significant seismic anisotropy. Based on the samples considered, the values of hornblende-induced seismic anisotropy expected at high shear strains (e.g. $\gamma \approx 10$) are ~7% in both AVp and AVs. In many cases, the impact of other common mineral phases present (e.g. plagioclase, quartz) is to dilute the amphibole effect due to the fact that these phases tend to have weak-to-random LPOs in such polyphase aggregates. Thus, the intensity of seismic anisotropy observed on the sample scale reflects both deformation intensity and hornblende modal proportion. For rock compositions and crustal depths that are unlikely to contain significant mica, hornblende is likely to be the principal contributor to the sample LPO and therefore the seismic anisotropy of the deep continental crust.

Acknowledgements

Parts of this paper were presented initially at the 2006 Fall Meeting of the AGU, San Francisco (Session T53: Crustal fabric,

seismic anisotropy and deformation). We thank the participants of this session for their input. We thank also Dave Mainprice for access to his suite of programs for calculating LPO and seismic properties (Pfch5, AnisCh5 and VpG). We are grateful to the Journal's anonymous referees and editor, Rob van der Hilst, for their comments and help in improving the original version of this manuscript. DT acknowledges receipt of a UK NERC postgraduate studentship. The EBSD data were measured using equipment provide by UK NERC grant GR9/3223 (GEL/MC).

References

Aleksandrov, K.S., Ryzhova, T.V., 1961. The elastic properties of rock-forming minerals, I: pyroxenes and amphiboles. Izv. Acad. Sci. USSR, Geophys. Ser. 9, 1339–1344 (in Russian).

Aleksandrov, K.S., Alchikov, V.V., Belikov, B.P., Zaslavskii, B.I., Krupnyi, A.I., 1974. Velocities of elastic waves in minerals at atmospheric pressure and increasing of precision of elastic constants by means of EVM. Izv. Acad. Sci. USSR, Geophys. Ser. 10, 15–24 (in Russian).

Babuska, V., Cara, M., 1991. Seismic Anisotropy in the Earth. Kluwer Academic, Dordrecht.

Barruol, G., Mainprice, D., 1993. 3-D seismic velocities calculated from lattice-preferred orientation and reflectivity of a lower crustal section: examples of the Val Sesia section (Ivrea zone, northern Italy). Geophys. J. Int. 115, 1169–1188.

Barruol, G., Kern, H., 1996. Seismic anisotropy and shear-wave splitting in lower-crustal and upper-mantle rocks from the Ivrea Zone — experimental and calculated data. Phys. Earth Planet. Inter. 95, 175–194.

Ben Ismail, W., Mainprice, D., 1998. An olivine fabric database: an overview of upper mantle fabrics and seismic anisotropy. Tectonophysics 296, 145–158.

Berger, A., Stunitz, H., 1996. Deformation mechanisms and reaction of hornblende: examples from the Bergell tonalite (Central Alps). Tectonophysics, 257, 149–174.

Bunge, H.J., 1969. Mathematische Methoden der Texturanalyse. Akademie-Verlag.

Bunge, H.J., 1982. Texture Analysis in Materials Science. Butterworths, London. 599pp.

Bunge, H.J., Kiewel, R., Reinert, T., Fritsche, L., 2000. Elastic properties of polycrystals–influence of texture and stereology. J. Mech. Phys. Solids 48, 29–66.

Burlini, L., Kern, H., 1994. *Special Issue*: seismic properties of crustal and mantle rocks — laboratory measurements and theoretical calculations. Surv. Geophys. 15, 439–672.

Christensen, N.I., 1984. The magnitude, symmetry and origin of upper mantle anisotropy based on fabric analyses of ultramafic tectonites. Geophys. J. R. Astron. Soc. 76, 89–111.

Christensen, N.I., Mooney, W.D., 1995. Seismic velocity structure and composition of the continental crust: a global review. J. Geophys. Res. 100, 9761–9788.

Cohen, A.S., O'Nions, R.K., O'Hara, M.J., 1991. Chronology and mechanism of depletion in Lewisian granulites. Contrib. Mineral. Petrol. 106, 142–153.

Coward, M.P., Potts, G.R., 1983. Complex strain patterns at the frontal and lateral tips to shear zones and thrust zones. J. Struct. Geol. 5, 383–399.

Crampin, S., 1981. A review of wave motion in anisotropic and cracked elastic media. Wave Motion 3, 242–391.

Crampin, S., Chesnokov, E.M., Hipkin, R.G., 1984. Seismic anisotropy — the state of the art: II. Geophys. J. R. Astron. Soc. 76, 1–16.

Diaz Azpiroz, M., Lloyd, G.E., Fernandez, C., 2007. Development of lattice preferred orientation in clinoamphiboles deformed under low-pressure metamorphic conditions — a SEM/EBSD study of metabasites from the Aracena metamorphic belt, SW Spain. J. Struct. Geol. 29, 629–645.

Handy, M.R., 1994. Flow laws for rocks containing two non-linear viscous phases: a phenomenological approach. J. Struct. Geol. 16, 287–301.

Hill, R., 1952. The elastic behaviour of a crystalline aggregate. Proc. Phys. Soc. Lond. A65, 351–354.

Jackson, I., 1991. The petrophysical basis for the interpretation of seismological models of the continental lithosphere. Sp. Publ. Geol. Soc. Aust. 17, 81–114.

Ji, S., Wang, Q., Xia, B., 2002. Handbook of Seismic Properties of Minerals, Rocks and Ores. Polytechnic International Press, Canada.

Kendall, J.M., 2000. Seismic Anisotropy in the boundary layers of the mantle. In: Karato, S., Forte, A.M., Liebermann, R.C., Masters, G., Stixrude, L. (Eds.), Earth's Deep Interior: Mineral Physics and Tomography from the Atomic to the Global Scale. American Geophysical Union, Washinton, DC, pp. 133–159.

Kern, H., Burlini, L., Ashchepkov, I.V., 1996. Fabric-related seismic anisotropy in upper-mantle xenoliths: evidence from measurements and calculations. Phys. Earth Planet. Inter. 95, 195–209.

Kinny, P.D., Friend, C.R.L., Love, G.J., 2005. Proposal for a terrane-based nomenclature for the Lewisian Gneiss Complex of NW Scotland. J. Geol. Soc. Lond. 162, 175–186.

Lloyd, G.E., Kendall, J.M., 2005. Petrofabric Derived Seismic Properties of a Mylonitic Quartz Simple Shear Zone: Implications for Seismic Reflection Profiling. In: Harvey, P.K., Brewer, T., Pezard, P.A., Petrov, V.A. (Eds.), Petrophysical Properties of Crystalline Rocks. Sp. Publ. Geol. Soc. Lond., 240, pp. 75–94.

Mahan, K., 2006: Retrograde mica in deep crustal granulites: implications for crustal seismic anisotropy. Geophys. Res. Lett. 33 (24) Art. No. L24301 Dec 16.

Mainprice, D., 1990. An efficient Fortran program to calculate seismic anisotropy from the lattice preferred orientation of minerals. Comput. Geotech. 16, 385–393.

Mainprice, D., Nicolas, A., 1989. Development of shape and lattice preferred orientations: application to the seismic anisotropy of the lower crust. J. Struct. Geol. 11, 175–189.

Mainprice, D., Silver, P.G., 1993. Interpretation of SKS-waves using samples from the subcontinental lithosphere. Phys. Earth Planet. Inter. 78, 257–280.

Mainprice, D., Humbert, M., 1994. Methods of calculating petrophysical properties from lattice preferred orientation data. Surv. Geophys. 15, 575–592.

Mainprice, D., Barruol, G., Ben Ismail, W., 2000. The Seismic Anisotropy of the Earth's Mantle: from Single Crystal to Polycrystal. In: Karato, S.I., Forte, A.M., Lierberman, R.C., Masters, G., Stixrude, L. (Eds.), Earth's Deep Interior; Mineral Physics and Tomography from the Atomic to the Global Scale. Geophys. Monogr., 117, pp. 237–264.

McSkimin, H.J., Andreatch Jr., P., Thurston, R.N., 1965. Elastic moduli of quartz versus hydrostatic pressure at 25 °C and −195.8 °C. J. Appl. Phys. 36, 1624–1632.

Meissner, R., Rabbel, W., Kern, H., 2006. Seismic lamination and anisotropy of the lower continental crust. Tectonophysics 416, 81–99.

Meltzer, A., Christensen, N., 2001. Nanga Parbat crustal anisotropy: implications for interpretation of crustal velocity structure and shear-wave splitting. Geophys. Res. Lett. 28, 2129–2132.

Michibayashi, K., Mainprice, D., 2004. The role of pre-existing mechanical anisotropy on shear zone development within oceanic mantle lithosphere: an example from the Oman ophiolite. J. Petrol. 45, 405–414.

Ozacar, A.A., Zandt, G., 2004. Crustal seismic anisotropy in central Tibet: implications for deformation style and flow in the crust. Geophys. Res. Lett. 31, L23601. doi:10.1029/2004GL021096.

Percival, J.A., Fountain, D.M., Salisbury, M.H., 1992. Exposed crustal cross sections as windows on the lower crust. In: Fountain, D.M., Arculus, R., Kay, R.W. (Eds.), Continental Lower Crust. Elsevier, Amsterdam, London, pp. 317–362.

Prior, D.J., Wheeler, J., 1999. Feldspar fabrics in a greenschist facies albite-rich mylonite from electron backscatter diffraction. Tectonophysics 303, 29–49.

Prior, D.J., Boyle, A.P., Brenker, F., Cheadle, M.C., Day, A., Lopez, G., Potts, G.J., Reddy, S., Spiess, R., Timms, N., Trimby, P., Wheeler, J., Zetterstrom, L., 1999. The application of electron backscatter diffraction and orientation contrast imaging in the SEM to textural problems in rocks. Am. Mineral. 84, 1741–1759.

Ramsay, J.G., Huber, M.I., 1983. The techniques of modern structural geology. Strain Analysis, vol. 1. Academic Press, London.

Rasolofosaon, P.N.J., Rabbel, W., Siegesmund, S., Vollbrecht, A., 2000. Characterisation of crack distribution: fabric analysis versus ultrasonic inversion. Geophys. J. Int. 141, 413–424.

Rudnick, R.L., 1992. Xenoliths samples of the lower continental crust. In: Fountain, D.M., Arculus, R., Kay, R.W. (Eds.), Continental Lower Crust. Elsevier, Amsterdam, London, pp. 269–316.

Rudnick, R.L., Fountain, D.M., 1995. Nature and composition of the continental crust — a lower crustal perspective. Rev. Geophys. 33, 267–309.

Rudnick, R.L., Jackson, I., 1995. Measured and calculated elastic wave speeds in partially equilibrated mafic granulite xenoliths: Implications for the properties of an under-plated lower continental crust. J. Geophys. Res. 100, 10211–10218.

Rudnick, R.L., Gao, S., 2003. The Composition of the Continental Crust, In: R.L. Rudnick (Ed.), The Crust, Treatise on Geochemistry vol. 3 (H.D. Holland and K.K. Turekian Eds.), Elsevier-Pergamon, Oxford, 1–64.

Schulte-Pelkum, V., Monsalve, G., Sheehan, A., Pandey, M.R., Sapkota, S., Bilham, R., Wu, F., 2005. Imaging the Indian subcontinent beneath the Himalaya. Nature 435, 1222.

Shapiro, N.M., Ritzwoller, M.H., Molnar, P., Levin, V., 2004. Thinning and flow of Tibetan crust constrained by seismic anisotropy. Science 305, 233.

Siegesmund, S., Kern, H., 1990. Velocity anisotropy and shear-wave splitting in rocks from the mylonite belt along the Insubric Line (Ivrea Zone, Italy). Earth Planet. Sci. Lett. 99, 29–47.

Siegesmund, S., Takeshita, T., Kern, H., 1989. Anisotropy of Vp and Vs in an amphibolite of the deeper crust and its relationship to the mineralogical, microstructural and textural characteristics of the rock. Tectonophysics 157, 25–38.

Takanashi, M., Nishizawa, O., Kanagawa, K., Yasunga, K., 2001. Laboratory measurements of elastic anisotropy parameters for the exposed crustal rocks from the Hidaka Metamorphic Belt, Central Hokkaido, Japan. Geophys. J. Int. 145, 33–47.

Tarney, J., 1963. Assynt dykes and their metamorphism. Nature 199, 672–674.

Tatham, D.J., Casey, M., 2007. Inferences from shear zone geometry: an example from the Laxfordian shear zone at Upper Badcall, Lewisian Complex, NW Scotland. Sp. Publ. Geol. Soc. Lond. 272, 47–57.

Vernik, L., Liu, X., 1997. Velocity anisotropy in shales: a petrophysical study. Geophysics 62, 521–532.

Weaver, B.L., Tarney, J., 1980. Rare Earth geochemistry of the Lewisian granulite-facies gneisses, northwest Scotland: Implications for the petrogenesis of the Archaean lower continental crust. Earth Planet. Sci. Lett. 51, 279–296.